Design of Steel Weld Deposits

By
Tracey Cool
New Hall, Cambridge

Department of Materials Science and Metallurgy
Pembroke Street
Cambridge
CB2 3QZ

A dissertation submitted for the degree of Doctor of Philosophy at the University of Cambridge

September 1996

Fabrication of metals by welding is not unlike clothesmaking, with steel plate as the cloth, welding consumables being the thread, the power sources and welding equipment being the sewing machines.

Tad Boniszewski, 1979

PREFACE

This dissertation is submitted as a PhD thesis in the University of Cambridge. The investigation described herein was carried out under the supervision of Dr H. K. D. H. Bhadeshia in the Department of Materials Science and Metallurgy, University of Cambridge, between October 1993 and September 1996.

Except where acknowledgement and reference is specifically made to the contrary, this work is, to the best of my knowledge, original, and has been carried out without collaboration. Neither this, nor any substantially similar dissertation has been or is being submitted for any degree, diploma or other qualification at any other university. The work has been presented in the following publications;

T. Cool and H. K. D. H. Bhadeshia *Materials Science and Technology* **12** (1996) 40–44.

A. J. Summerfield, T. Cool, B. R. Keville and H. K. D. H. Bhadeshia *Welding and Metal Fabrication* (January 1996) 23–24.

T. Cool, H. K. D. H. Bhadeshia and D. J. C. MacKay *Mathematical Modelling of Weld Phenomena III* edited by H Cerjak and H. K. D, H. Bhadeshia, Institute of Materials Press *in press*.

T. Cool and H. K. D. H. Bhadeshia *Science and Technology of Welding and Joining* (1996) *in press*.

T. Cool, H. K. D. H. Bhadeshia and D. J. C. MacKay *Materials Science and Engineering* (1996) *in press*.

Tracey Cool

Tracey Cool

ACKNOWLEDGEMENTS

I wish to thank Professor Alan Windle for provision of laboratory facilities in the Department of Materials Science and Metallurgy at the University of Cambridge. I am also very grateful to Dr Harry Bhadeshia for his enviable enthusiasm, encouragement and support during the course of this work. The help of technical and academic staff in the Department has been much appreciated, especially from Mark Manning, Rob Wallach, Alasdair Preston, Simon Newcomb, Graham Morgan, Kevin Roberts, Brian Barber, Carol Best and Ray Fella. I am also grateful to fellow members of my research group, past and present, for their friendship and help.

David MacKay gave invaluable guidance with the use of his neural network model. I am also grateful to Tim Auckland and Francis Davey for their assistance with computer problems.

This work would not have been possible without financial support from Parsons Turbine Generators Ltd., the EPSRC and the DTI. I am indebted to many members of the company for assistance with my work; Bill Stalker, Steve Price (now of Sheffield Forgemasters), Geoff Brown, Linda Gibson. I am especially grateful to Roger Conroy for countless useful discussions, and Jim Summerfield, Bob Hill and Dick Graham for their efficient and successful managing of the project. I would also like to thank Steve Dowd of International Research and Development Ltd. and staff from the Materials Analysis Unit at Newcastle University. I must not forget the welders, without whom none of this would be possible; Brian Liddle, Jimmy Bradley and Tom Varty.

The work was part of a larger "Link" collaboration funded by the Department of Trade and Industry, and I am grateful to Professor Gordon Brown and Dr David Driver, project coordinator, for their participation in the project and their encouragement. I have also benefited from the wisdom of Vic Wright, an independent consultant, and valuable committee member, and the thought provoking suggestions from the project monitor, Professor John Knott.

A further participating company in the Link project was Oerlikon Welding Ltd. and it has been a privilege for me to share in discussions with Barbara Keville and Chris Thornton, who have introduced me to the complexities and mysteries of welding. I am also grateful to Glyn Evans, not only for his wide ranging research which has been extremely useful in my modelling, but also for his enthusiasm for my work.

I would like to thank my friends both inside and outside of work for giving me the distractions I needed for a balanced life, especially Tim for his patience with my grumblings when work has been less than perfect, and for sharing my enthusiasm on the better days. Finally I am extremely grateful to my parents for their encouragement to take on this challenge in the first place, and for being there to remind me of the bright side of life in my more cynical moments. I deeply regret that Dad is not here to see the fruits of my labour now that the thesis is finally in print, but I gain consolation from the fact that Mam will be twice as proud.

ABSTRACT

The development of new welding alloys for power plant steels has in the past been achieved by trial and experience. The purpose of this work was to enable a significant proportion of the development procedure to be done by computation. A variety of methods have been used towards this end, ranging from physical models to other methods which rely heavily on patterns in experimental data.

The thesis begins with an introduction and literature review covering both a description of the essential features of power plant, and the steels used in constructing the plant. The reliability expected from the steels over a period of some thirty years of service is quite remarkable, and sets similarly stringent requirements on any model used for design purposes.

A thermodynamic method based on the theory of martensite nucleation has been applied to the calculation of martensite-start temperatures of highly alloyed steels. This information is necessary for welding procedures. The formation of martensite is suppressed as the strength of austenite is increased by alloying. Thus, the critical driving force necessary to trigger martensite is larger for stronger austenite.

Some confusing mechanical property data on 9Cr1Mo type steel welds have been thoroughly explained by considering the relative stabilities of δ-ferrite and austenite as a function of chemical composition. Excessive concentrations of austenite stabilising elements such as nickel cause the formation of austenite during post weld heat treatment. The austenite then transforms to untempered martensite on cooling, thereby causing a drastic increase in strength and reduction in toughness. By contrast, large concentrations of tungsten make it impossible to fully austenitise the alloy, rendering it exceptionally soft.

A weld typically might contain more than twenty important solute additions and impurities. Its properties also depend on the welding conditions and post weld heat treatment. It is a formidable task, therefore, to attempt to predict the yield and ultimate tensile strengths, elongation and Charpy toughness, all of which are elementary design parameters. A massive dataset was compiled using detailed data from the published literature, and subjected to neural network analysis. This is a highly flexible and powerful empirical method, but it is demonstrated that with care the network can be trained to recognise metallurgically sound relationships. The resulting models have been validated in a variety of ways with emphasis on data previously unseen by the models. Having done this, the models have been used to successfully design a new welding alloy. A detailed case study is presented to illustrate the design procedure and to show how both the success, and in some cases the failure, of the models can be used to advantage in efficient design.

CONTENTS

CHAPTER ONE

Introduction

1.1 Aim of the Project

A necessary requirement for success in the power plant generation industry, as in any competitive market, is to sell a reliable product meeting the desired criteria for a reasonable price. An effective way of achieving this requirement is to increase the operational capability of the plant, thus providing a better quality product than the competition. Additional benefits are reaped if the cost of manufacturing can be reduced. This then can be passed on to the customer as a reduction in price.

Traditionally, the development of a manual metal arc electrode of new composition has been based on experience and empirical experimentation. This can cost in excess of £35,000, with a typical time scale of 12 months from concept to production. The time scales involved are large because of the need to produce and test electrode variants. Technology to reduce the work load and the lead time by a factor of two could lead to an increase in sales turnover of about £75,000 per annum for each electrode variant, and also give a competitive edge in sales.

At present, there is no formal method for the design of welding alloys; their development is based on trial and error. The aim of this project was to utilise the vast range of knowledge and technology available today to develop computer models suitable for enhanced production of power plant components. A survey of the operation of the power station and theservice conditions is presented first in order to set the background for the modelling research.

1.2 Power Plant Operation

The basic function of steam power plant is to convert the energy from the steam, via mechanical energy in the turbine, to electrical energy in the generator [Graham, 1975]. Although there are several categories of plant, each has the same basic set of components independent of the type of fuel used to create the steam [Race, 1992]. A schematic plan of a power station is shown in Figure 1.1.

Water is heated to steam in the evaporator before being passed onto the steam drum, where it is collected in headers. There it undergoes a superheating stage and it is then passed into the high pressure (HP) turbine. On exit from this stage, the steam has undergone about 25% of its total expansion [Graham, 1975] and is fed back to the reheater where it is returned to the same temperature, before being introduced to the intermediate pressure (IP) turbine. The steam then flows into a maximum of three low pressure (LP) turbines, the number of which is dependent on the size of the plant. The exhaust steam from the final low pressure stage is condensed and then returned to the boiler [Race, 1992]. Typical inlet and outlet temperatures and pressures are shown in the text accompanying Figure 1.2 [Graham, 1975].

The advantage of reheating the steam after the first (HP) stage is to improve the overall efficiency of the unit. The steam is also allowed to expand to a lower pressure before becoming wet, and as a result, water droplets form at a later stage in the LP cycle which reduces the erosion and stress corrosion problems on the last few rows of turbine blades [Graham, 1975]. Some smaller machines (< 100 MW) in the past have missed out the reheat stage, but only when fuel costs have been low.

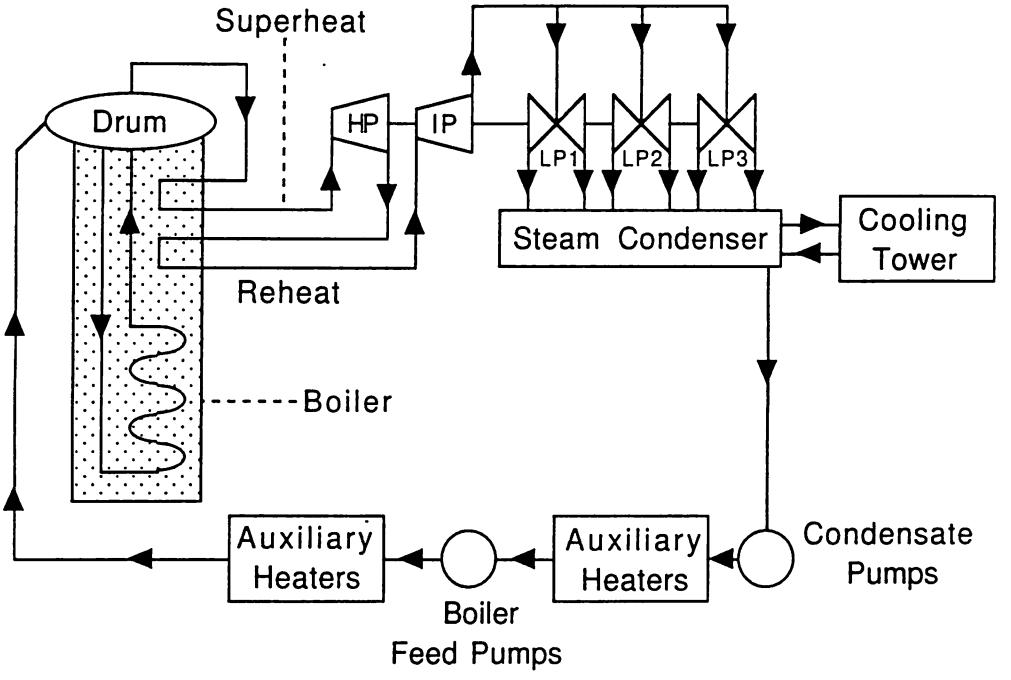

Figure 1.1: Schematic view of the components of power production. After Weisman and Eckart [1985].

An annotated artist's impression of one of the six 660 MW turbine generator sets at Drax in North Yorkshire — the largest coal fired power station in Europe is shown in Figure 1.2. Some of the notation used in this figure will be explained fully later in the chapter.

1.3 The Turbine

The turbine consists of a long cylindrical rotor to which are attached the blades which shape the path of the steam throughout the cycle. There are three types of rotor to consider; high pressure (HP), intermediate pressure (IP) and low pressure (LP). To provide an estimate of the size, the LP forging usually weighs between 17 and 34 tonnes, and the HP between 9 and 16 tonnes. The weights of these components in service are further increased by that of the turbine blading. The LP blades are considerably larger than those of the HP turbine (Figure 1.3), due to the increased volume of steam taken up at the LP end. The turbine rotors are coupled between each stage, and the final LP stage is directly coupled to the generator.

Figure 1.4 shows the coupling of the turbine rotors to each other and finally to the generator rotor for a machine with one HP, one IP and one LP turbine.

1.3.1 Turbine Rotors

There are three main methods in current use in the power industry for the manufacture of turbine rotors [Hohn, 1973]; a single forging, a shaft with shrunk on discs, and a welded rotor.

As the name suggests, a single forging is a rotor forged out of one ingot of steel. Very few steelworks have the large scale equipment necessary to satisfy these requirements. There are disadvantages linked to the manufacture of such rotors due to their vast size, and the high degree of quality required for their

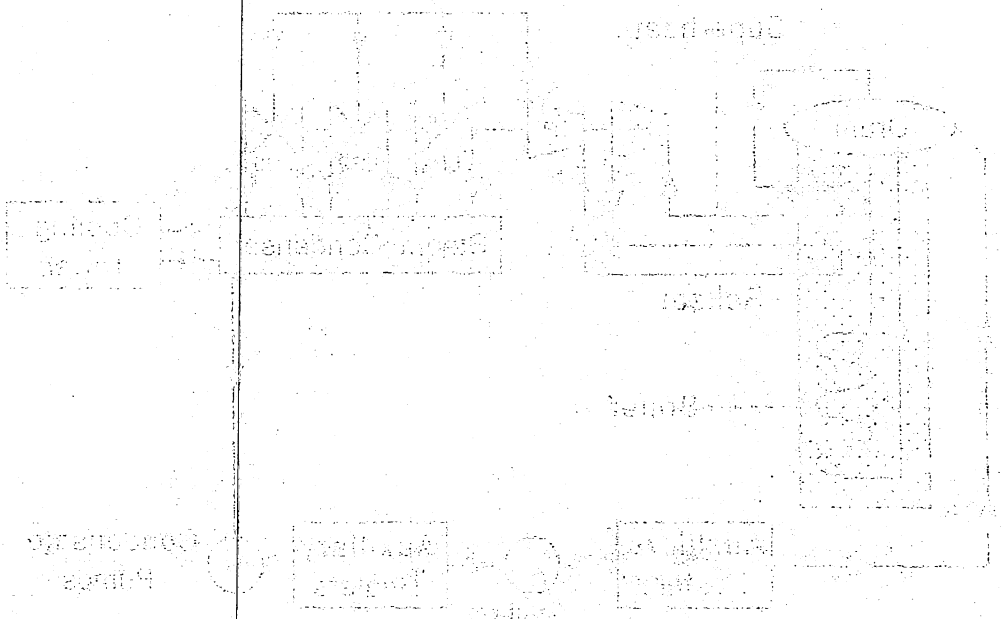

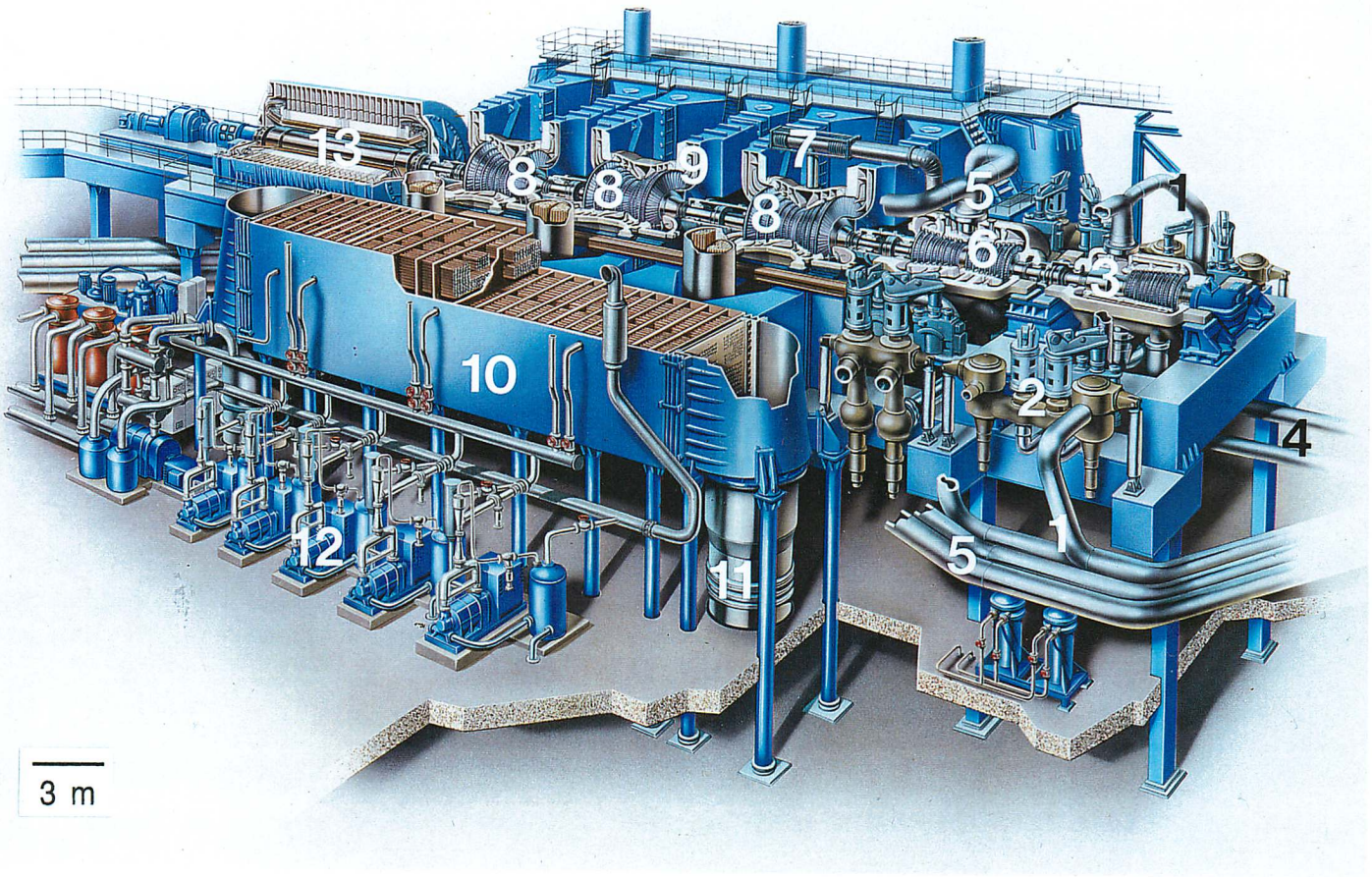

Figure 1.2

1 Pipework transporting steam at 565 °C, 15.8 MPa from the boiler to the HP turbine. $\frac{1}{2}$Cr$\frac{1}{2}$Mo$\frac{1}{4}$V steel.

2 HP Steam valves. These consist of four closed die forgings of $\frac{1}{2}$Cr$\frac{1}{2}$Mo$\frac{1}{4}$V steel welded together. Advances in technology have now reduced the need for welding, so a casting would be used in a modern power station. The valves control the steam flow, and allow stoppage in case of emergencies.

3 HP turbine. The rotor is fabricated from a single forging of 1CrMoV steel, and the blades are of 12CrMoV steel. The turbine casing is $\frac{1}{2}$Cr$\frac{1}{2}$Mo$\frac{1}{4}$V, with the upper casing attached to the lower by 1CrMoV bolts.

4 Pipework taking steam at $\sim$ 420 °C, $\sim$ 4 MPa back to the boiler for reheating.

5 Pipework transporting steam at 565 °C, 3.8 MPa to the IP turbine.

6 IP turbine. The rotor, blades and casings are made of the same materials as the HP turbine. This section is "double flow", *i.e.* the steam enters in the middle of the turbine, and flows outwards. This balances the thrust, as the forces on the turbine are equal and opposite, leaving no net forces acting on the turbine.

7 Pipework transporting the steam at $\sim$ 250–300 °C, 620 kPa from the LP turbine to the three LP turbines.

8 LP turbines. The rotors is made of a $3\frac{1}{2}$NiCrMoV steel with 12Cr steel blades. The outer casings are fabricated from a steel casting. There are three LP turbines. Technology has improved such that only two would be needed for the same output in modern power stations.

9 Pipework transporting steam at $\sim$ 80 °C from the LP turbines to the condenser.

10 The condenser. The condensers in Drax are unusual in that they are panier mounted, with one at each side of each turbine generator set. Conventional condensers are situated underneath the turbines. The outer wall of the condenser is made of mild steel. Steam travels through copper alloy tubes in the condenser, and is cooled into water before being returned to the boiler for the next cycle. It is cooled by a separate cycle of water flow. This cooling water is heated up in the process, and is what can be seen being returned to its lower temperature in cooling towers.

11 Pipe returning water to the boiler. This is a $\frac{1}{2}$Cr$\frac{1}{2}$Mo$\frac{1}{4}$V casting.

12 Cooling water pumps.

13 The generator. It can be seen from the diagram that the turbines and rotors are directly coupled together. The rotor of the generator is made from $3\frac{1}{2}$NiCrMoV steel, and the stator, the outer casing through which it rotates, holds the conductors which carry the electricity generated by the rotation of the generator, (effectively a large magnet). An aluminium (non-conducting) alloy holds the conductors in place.

Figure 1.3: The author (height 1.56 m) next to one of the LP rotors from Drax power station. Compare the blade size to HP blading, which is typically about the length of a finger.

extreme operating conditions, as well as the long lead time associated with their production.

Metallurgically, the degree of chemical segregation is increased with the size of the forging, and this could lead to a reduction in quality, or an increase in expense for improved core forging techniques. It is important to achieve consistent properties in both the rim and the core, which is a difficult goal, due to the dimensions of the forging. The tempering processes needed after the initial formation of the ingot depend upon its shape and size, and for a huge sample, the latter cannot be relied upon to be uniform. The testing of the rotor for quality could also prove problematic, as non-destructive testing procedures cannot access the core of the rotor, and although destructive methods can provide samples from trepanning, the size is usually too small to be reliable.

The shaft of the rotor with shrunk on discs is in the form of a long thin "pencil" piece forged from a single ingot, with discs shrink fitted to the body of the shaft. The turbine blading is then attached to the discs. This has similar disadvantages to the single forging in that it is of a large size. Although the volume of this thinner forged shaft is smaller, reducing the problem of segregation to an extent, there will still be the disadvantage of the huge length of the forging with relation to the availability of resources in steel producing plant.

The welded rotor is made up of a series of thick discs made from single forgings and welded together. The design of the discs produces an essentially hollow bodied rotor, with welding required only around the surface of the discs. These small forgings have a size advantage; from a production point of view they can be produced in a relatively short period of time, and metallurgically, they have

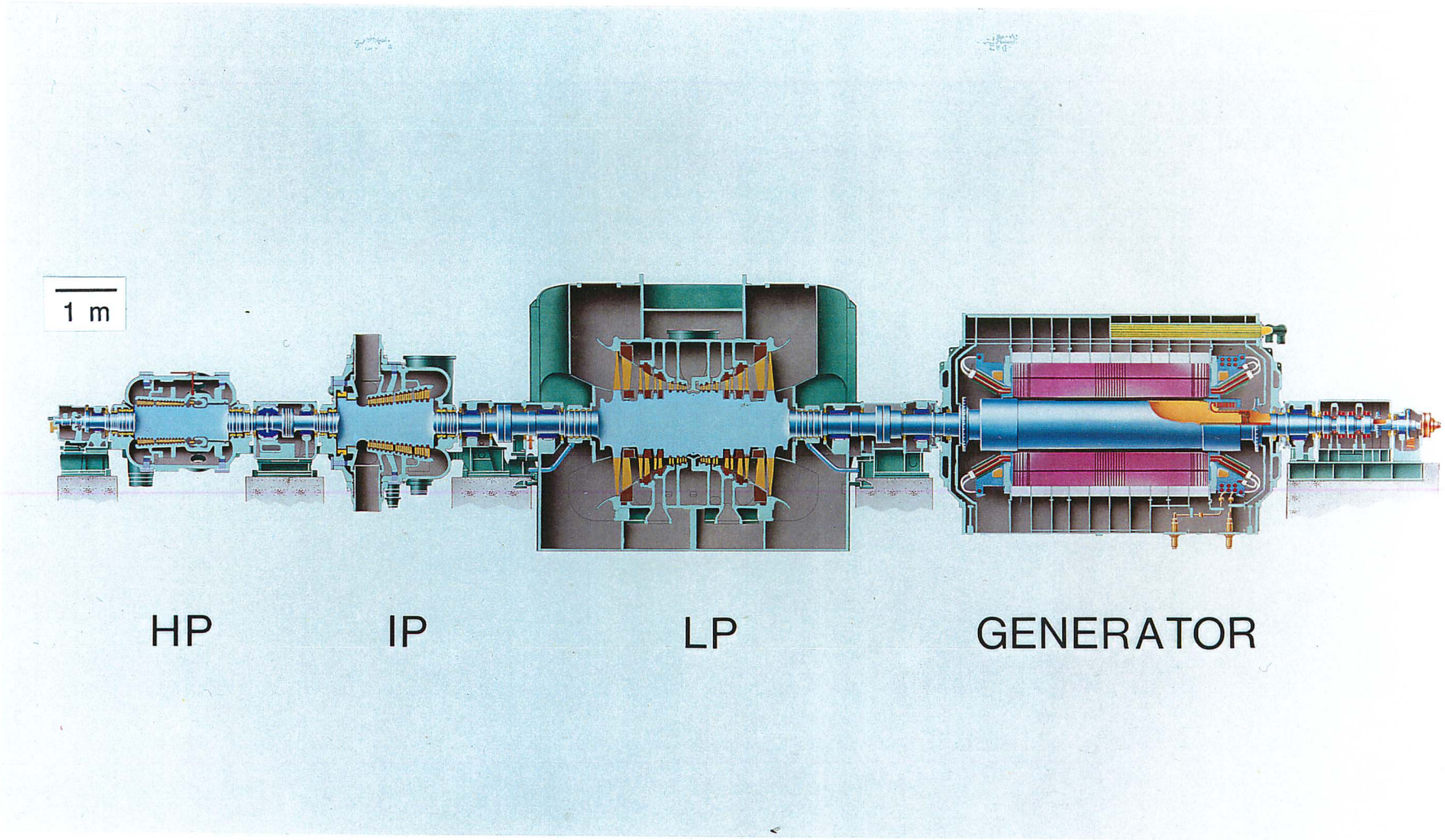

Figure 1.4: Illustration of the joining of HP, IP, LP and generator rotors to form a coupled shaft.

a lower tendency towards segregation [Lüthy, 1968], as well as an improved through hardening in the discs and shaft ends. Their smaller dimensions also allow an easier and more uniform temper and anneal, and exceptionally good access for testing both before and after the welding. Low pressure shafts are often welded for high temperature considerations [Dien, 1973], and high pressure turbine shafts are occasionally welded, but not from a size point of view. The submerged arc process is most commonly used in the manufacture of these rotors as it is fully mechanised, and therefore reliable and repeatable [Dien, 1973].

The three types of turbine needed for the power station are outlined below:

For a typical HP cylinder the high temperature steam enters the turbine through two pipes, 180° apart, then passes through a series of fixed and rotating blades. The triple casing around the turbine allows acceptable pressure and temperature gradients across cylinders. Many low alloy steels can cope with such steady state stresses across cylinder walls. During start up, however, severe thermal stresses may arise [Graham, 1975]. $\frac{1}{2}$Cr$\frac{1}{2}$Mo$\frac{1}{2}$V steels are suitable for all castings in the creep range. The rotor forgings require high creep strength to avoid excessive dimensional changes, but a balance is needed between creep strength and creep ductility in order to prevent grain boundary cracking [Graham, 1975]. A 1Cr1Mo0.2V steel which is used for high temperature rotors may have low K_{IC}[1] values at ambient temperature, but the toughness increases with temperature. Care must be taken during the manufacturing heat treatment to ensure that the creep strength is identical at opposite sides of the rotor to avoid bending during service [Graham, 1975].

The temperature of the steam at the IP inlet is the same as that of the HP, but due to its lower pressure, it occupies a higher volume. This requires a larger blade annulus, and therefore a larger diameter rotor than the HP turbine. As a result, there are higher steady state and transient stresses present. A 1Cr1Mo$\frac{1}{2}$V steel is used. The stresses in the casing are lower than that of the HP, due to the decreased pressure, and the cylinder arrangement is not so complicated [Graham, 1975].

HP and IP rotors require good creep and rupture strength at their highest operating temperature [Marriott and Greenfield, 1988]. The rotors must also remain dimensionally stable over their lifetime ($\sim$ 30 years), and must not bow in service due to differential straining round the circumference in start up or in general running. CrMoV steels have been used successfully in rotors in the range of 550–565 °C, but it is recommended that 12Cr steels are used for temperatures exceeding 600 °C.

The LP section of the turbine operates below the creep range, and the pressures are much lower. The inner cylinder can be manufactured of carbon steel, or spheroidal graphite iron, and the outer of a mild steel plate. The steam occupies a large volume by this stage in the cycle, and typical dimensions for a system with three LP units, the exhaust diameter is 3450 mm. The blades are required to be long, due to the high volume of steam, and as a result, a large rotor diameter is needed to support them. This is of the order of 1625 mm. High strength and toughness are needed, due to the high centrifugal stresses, and a 3$\frac{1}{2}$Ni1$\frac{1}{2}$CrMoV steel which has been quenched and water tempered is often used.

The rotor styles outlined above are designed to satisfy the requirements of the conventional HP, IP and LP turbines. However, developments of the steelmaking process and rotor materials have made it

[1] K_{IC} represents the fracture toughness [Knott, 1973] and is a property which can be used in design of engineering structures [Dieter, 1988].

possible to produce turbines with HP, IP and LP conditions within a single cylinder. This reduces the cost of manufacture and improves the efficiency. This is of particular interest to combined cycle work, where the cooling water temperatures are high, or the absence of water requires air cooling [Beech *et al.*, 1990]. The temperature region over which the rotor is required to operate ranges from less than 100 °C to 565 °C. In combined cycle plant, gas is used to fuel industrial gas turbines, and the waste heat exhausting from them is used to produce steam which then drives a steam turbine generator (Figure 1.5). At the inlet end of the turbine, creep and fatigue properties of a conventional HP rotor are required, and at the outlet end, the mechanical properties of a conventional LP rotor are necessary, particularly low $FATT_{50}$[2] [Bertilsson and Berg, 1980].

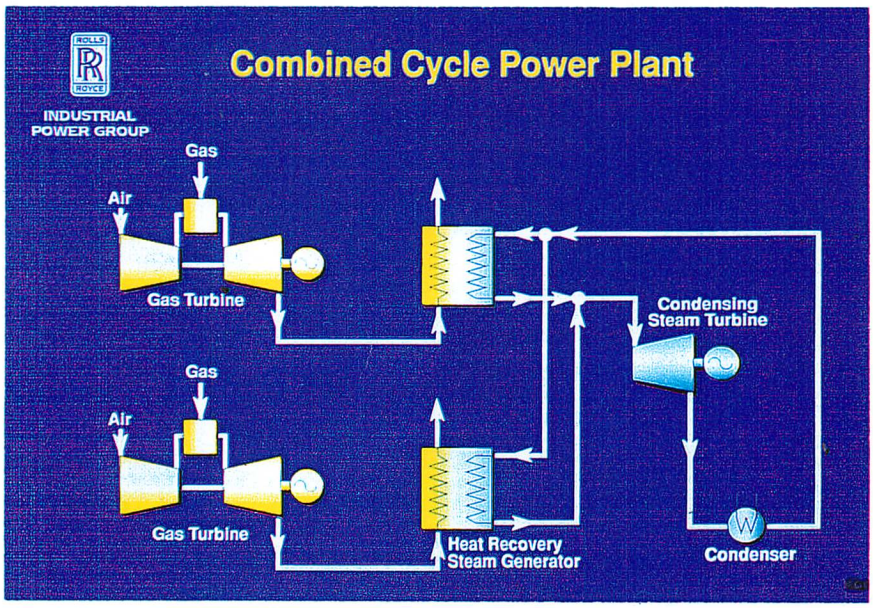

Figure 1.5: Schematic of combined cycle plant operation.

1.3.2 Turbine Blading

There are two types of blading in turbines — fixed blades and moving blades. The fixed blades are stationary during turbine operation, and are attached to the outer cylindrical casing of the turbine (Figure 1.6). The moving blades are attached to the turbine rotor, which is caused to rotate with the action of the steam on the blades. Together these blades provide a path for the steam to travel through the turbine which provides the rotation necessary for electricity generation.

Table 1.1 shows typical LP blade lengths and their associated exhaust area. Each turbine blade consists of three distinct sections; the root to align the blade into the rotor or cylinder, the tip, which may aid in supporting the blade, and the aerofoil which guides the steam to develop the power in the turbine [Graham and Barnes, 1990].

---

[2] $FATT_{50}$ is the fracture appearance transition temperature, based on 50% cleavage, 50% shear on the fracture surfaces of Charpy impact specimens [Dieter, 1988].

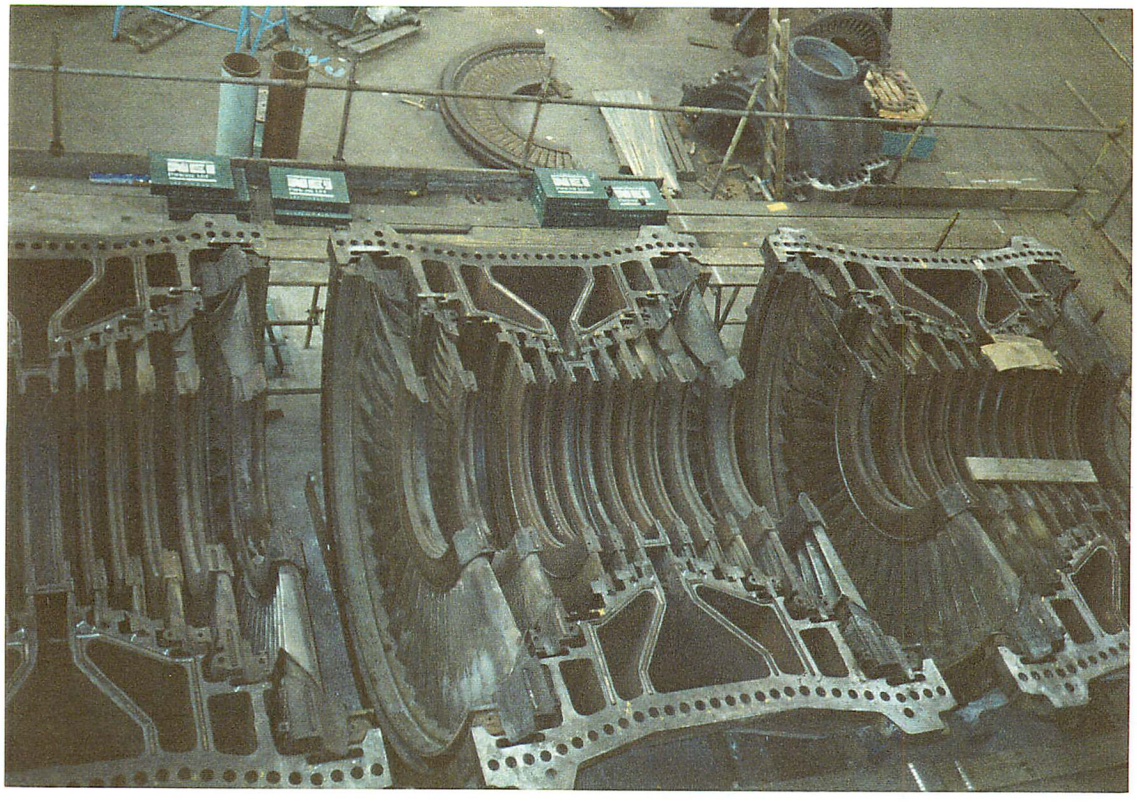

Figure 1.6: LP turbine casing at Drax showing the stationary blades.

Blade Length mm	Exhaust area m^2
635	7.60
762	10.94
914	14.58
1070	19.08

Table 1.1: Typical exhaust areas of LP turbines [Graham, 1975].

The root of the blade provides the necessary constraint to keep the blade in position in the turbine. This must be secure, to maintain the steam path. There are several styles of root, depending on the position of the blade in the turbine. Small HP blades may use a "fir tree" root with serrations on the blade which fit into corresponding slots on the rotor/cylinder. Larger blades may use a "forked straddle root" where the root of the blade is shaped like the tines of a fork, fitting into slots on the rotor. The largest LP blades use a "side entry fir tree root" where the serrated blades are inserted at an angle to the circumference of the rotor (Figure 1.7).

The tip of the blade is generally a long thin edge, designed to minimise contact between the blade and the cylinder or rotor, if rubbing were to occur during service. It should also ensure minimum steam leakage in order to get the maximum work out of the steam in turning the rotor. In HP blading the

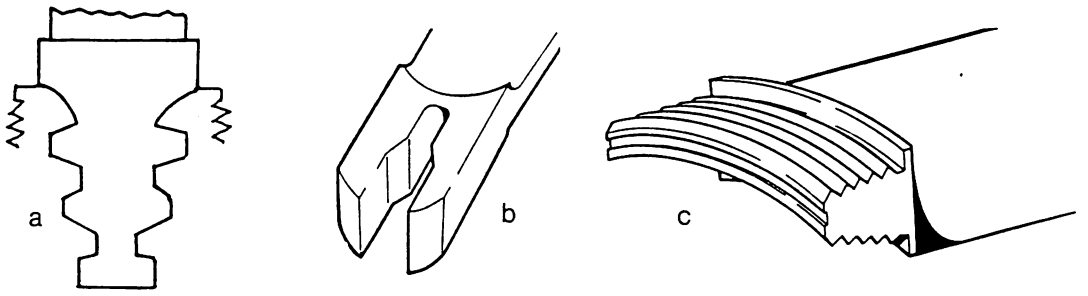

Figure 1.7: Typical blade roots. (a) fir tree root, (b) forked straddle root, (c) side entry fir tree root [Westinghouse, 1981].

tips tend to be shrouded together in groups which are then interconnected. For larger, LP, blading, the tips of rotating blades are required to be strong to maintain their rigidity against the centrifugal forces during rotation, which would alter the geometry of an unconstrained blade. They are often joined with lacing wire (Figure 1.8).

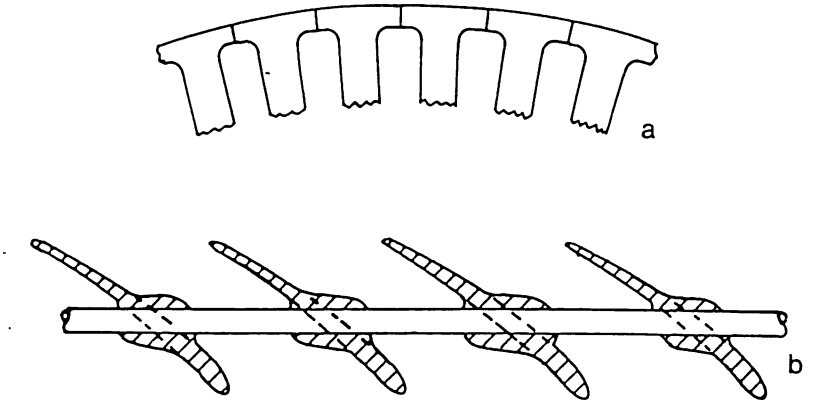

Figure 1.8: Typical blade tips. (a) integral shroud, (b) lacing wire [Westinghouse, 1981].

The shape of the aerofoil transforms the steam energy into torque. Blades can be machined from a solid billet or formed into shape by roll forming or pressing, the latter leading to enhanced mechanical properties. The blades may also require snubs or lacing wire holes, and due to these complex geometries, cannot be rolled. They are instead produced by drop forgings. The advances of computer numerical controlled (CNC) machining has allowed the complex machining necessary to produce more advanced blades [Graham and Barnes, 1990]. A stylus follows a copymaster which embodies the blade geometry, enabling an exact replica to be produced (Figure 1.9).

The general material requirements of blading are resistance to corrosion, and fatigue, as well as good hot working and machinability [Graham, 1975]. The degree to which these properties are required is a factor of the position of the blade in the turbine, and whether it is a stationary or a moving blade. Final and penultimate LP blades are positioned in a region of the turbine where steam is wet, and are susceptible to erosion on their leading edge. The leading edge of the blade is the edge of the aerofoil that hits the steam first. It is usually very thin to minimise turbulence. Shields made of tungsten tool

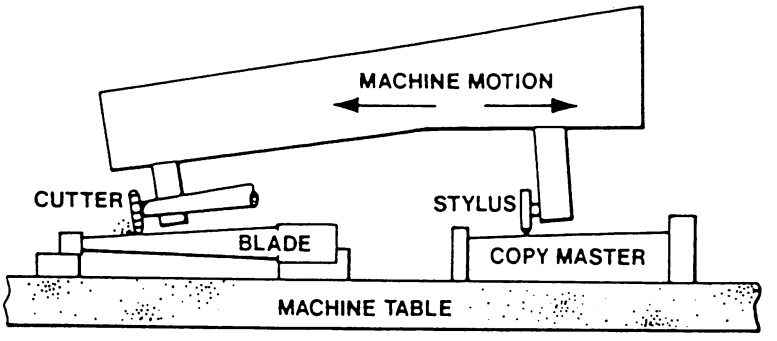

Figure 1.9: Schematic of copy milling [Graham and Barnes, 1990].

steel are brazed onto the edge of these blades to protect from erosion. As HP blading is considerably shorter than the LP blading it therefore receives less centrifugal force. The forces on the moving blades are much higher than the forces on the stationary blades, and are as such required to be of a tougher material. 12Cr steels hardened by alloy carbides satisfy all the mechanical requirements, as they have the high creep resistance necessary at the HP end and the very high tensile strength required at the last row of HP blades.

1.4 Material Requirements

The choice of material for each of the components is governed by the operating conditions which are dictated by the design and the type of fuel used [Graham, 1975] together with availability and cost. Wyatt [1976] has stated that the capital cost of a nuclear power station accounts for 70 % of the cost of the electricity sold, as compared to 40 % for a conventional fossil fuel fired plant. The material must be able to be reliably fabricated to the shape and size required. The component must also be resistant to the environment in which it will be expected to operate, either intrinsically, or with protective treatment (*e.g.* a coating). The typical service life of a power station is $\sim$ 30 years and steels used for this length of time at elevated temperature must retain their mechanical properties. The majority of steels used in power plant are low in carbon, with chromium, molybdenum and vanadium as the major alloying elements. Due to the high service temperature, creep resistance is important. These bainitic steels have good formability and weldability, and are fortunately not very expensive. As the steels are held at high temperatures for a number of years, the microstructure must be resistant to graphitisation, which is not directly related to creep properties. Because of this, the aluminium concentration is kept low ($<$0.015 weight %), and chromium and molybdenum are used together. Molybdenum alone can lead to graphitisation [Hrivňák, 1987]. Typical steel compositions are summarised in Table 1.2, and outlined in more detail in the next section.

1.5 Typical Steels Used For Power Plant Applications

1.5.1 1CrMoV Steels

These steels have been used extensively for superheater tubing [Day, 1965], steam turbine castings and turbine rotor forgings since the 1960s [Buchi *et al.*, 1965]. Their creep strength is due to fine uniformly dispersed precipitates of vanadium carbide particles in irregular ferrite grains. Poorer creep strength

Element	$\frac{1}{2}Cr\frac{1}{2}Mo\frac{1}{4}V$		2CrMoNiWV	$3\frac{1}{2}$NiCrMoV	
Carbon weight %	0.10–0.18	0.10–0.15	0.20–0.26	0.20–0.30	0.20–0.30
Silicon weight %	0.14–0.40	0.15–0.45	<0.25	<0.30	0.10–0.30
Manganese weight %	0.40–0.70	0.40–0.70	0.60–0.80	<0.40	<0.40
Sulphur weight %	<0.025	<0.03	<0.015	<0.015	<0.015
Phosphorus weight %	<0.030	<0.03	<0.015	<0.015	<0.015
Nickel weight %	<0.30	<0.30	0.65–0.85	3.25–3.75	3.00–3.75
Chromium weight %	0.30–0.60	0.30–0.50	2.00–2.20	1.25–1.80	1.25–1.75
Molybdenum weight %	0.50–0.70	0.40–0.60	0.75–0.95	0.40–0.60	0.40–0.60
Vanadium weight %	0.22–0.28	0.22–0.28	0.28–0.37	0.05–0.20	0.05–0.20
Tungsten weight %	—	—	0.55–0.75	—	—
Yield Strength MPa	>300	280–495	>600	>700	>750
Ultimate Tensile Strength MPa	460–610	460–650	730–850	800–950	850–1000
Elongation %	>18	>16	>15	>15	>10.
Impact Energy J			<25	>54	>35

Table 1.2a: Typical specifications for steels used in power plant fabrication.

is observed in samples with coarser irregularly dispersed precipitates and polygonal matrices. These differences in microstructure can even be observed in the cross section of a single casting, as they are due to the effects of the different cooling rates from the austenitisation temperature. Maximum creep strength is obtained in a tempered upper bainite structure. Carbon concentrations in excess of that required for alloy carbide forming result in cementite, which lowers the creep strength of the alloy.

The optimum balance of tensile, creep and creep rupture properties of this steel is achieved by heat treatment to granular bainite [Batte *et al.*, 1978]. Studies of heat treatment practise have lead to better microstructure, with the development of oil and water spray quenching to control the cooling rate, as well as vertical heat treatment of rotor forgings to ensure symmetrical properties. For large castings, if the quenching rate is reduced in order to prevent martensite and promote granular upper bainite at the rim, then there is a danger of a ferritic core. The cooling is sometimes interrupted to prevent quench cracking on the surface, but this has little effect on the core properties, as the amount of ferrite formed depends on the cooling time spent in the ferrite transformation range, rather than total cooling, much of which will be spent in the austenite range. The presence of ferrite influences the mechanical properties, mainly controlling the hardness and tensile strength, but concentrations in excess of 50 % also influence the creep rupture strength.

The hardenability of the steel can be controlled without upsetting the C, Cr, Mo balance required for good creep properties if Mn and Ni are increased.

Element	high temperature		low temperature		diaphragms
Carbon weight %	0.09–0.15	0.10–0.15	0.08–0.15	0.08–0.15	0.09–0.15
Silicon weight %	<0.50	<0.60	<0.50	<0.50	<0.80
Manganese weight %	<0.70	0.30–0.70	<1.00	0.50–1.00	<1.00
Sulphur weight %	<0.03	<0.03	<0.03	<0.03	<0.03
Phosphorus weight %	<0.04	<0.03	<0.03	<0.03	<0.04
Nickel weight %	<0.60	<0.80	1.50–3.00	2.00–3.00	<1.00
Chromium weight %	11.5–13.00	11.00-12.50	11.00–12.50	11.00–12.00	11.50–13.50
Molybdenum weight %	0.40–0.80	0.40–0.80	0.70–2.00	1.00–2.00	
Vanadium weight %		0.10–0.25	0.05–0.40	0.05–0.40	
Niobium weight %			<0.40	<0.40	
Yield Strength MPa	>465	>615	<770	>880	>340
Ultimate Tensile Strength MPa	620–770	740–900	930–1080	1030–1190	540–700
Elongation %	>18	>15	>15	>12	>20
Impact Energy J		>34	>34	>34	

Table 1.2b: Typical specifications for 12Cr steels used for turbine blading applications.

Carbide precipitation is responsible for the creep strength of these low alloy steels. For optimum results, a carbon concentration of $\sim$ 0.1–0.2 weight % is required, as well as an upper bainitic structure [Cornwell and Pollard 1971].

1.5.2 $2\frac{1}{4}$Cr1Mo Steels

This alloy has the high creep resistance required for use in power plant, which is provided by a fine and highly stable dispersion of alloy carbides. Despite the value of these carbides, the carbon concentration of the steels is kept low, in order to allow a proportion of molybdenum (a strong alloy carbide forming element) to remain in solid solution, thus contributing to the strengthening [Lundin, *et al.*, 1982]. Solid solution strengthening increases with importance for longer service at high temperatures, as annealing effects reduce the microstructural effects [Bhadeshia, 1992].

1.5.3 9Cr Steels

The 9Cr steels used in power plant are ferritic [Aplin and Middleton, 1990]. Such a microstructure gives the steels several advantages over their austenitic counterparts. These are more resistant to stress corrosion cracking at higher temperatures and are considered useful at temperatures up to 600 °C. They have a lower expansion coefficient and higher thermal conductivity and ductility, which combined, result in improved thermal fatigue properties. A further advantage is their reduced cost compared to austenitic steels.

Element	WCr tool steel	carbon steel
Carbon weight %	0.65–0.70	0.15–0.20
Silicon weight %	<0.40	<0.60
Manganese weight %	<0.50	0.50–1.10
Sulphur weight %	<0.035	<0.050
Phosphorus weight %	<0.035	<0.050
Nickel weight %	<0.50	<0.40
Chromium weight %	5.80–6.50	<0.25
Molybdenum weight %	0.20–0.50	<0.15
Vanadium weight %	0.20–0.50	—
Tungsten weight %	18.50–20.00	—
Cobalt weight %	0.20–0.50	—
Yield Strength MPa		215–340
Ultimate Tensile Strength MPa		40–540
Elongation %		>22
Impact Energy J		>45

Table 1.2c: Typical specifications for steels used in power plant. Mechanical properties are not stated for the WCr tool steel, as it is not used under stress, and is merely required to provide corrostion resistance.

An addition of 1 weight % molybdenum to the 9 weight % chromium basic steel renders a fully martensitic structure [Barnes, 1994]. Common applications of these 9Cr1Mo steels in the power station are in heat exchanger tubing and headers of steam plant. These steels have better high temperature properties than their $2\frac{1}{4}$Cr1Mo counterparts, allowing higher stresses on components of a given thickness, thus reducing cost as well as enhancing performance. The precipitation strengthening of Mo modified 9 (or 12) Cr steels is predominantly by $M_{23}C_6$[3] carbides [Foldyna and Kuboň, 1993]. Vanadium and/or niobium additions improve the creep resistance and high temperature creep strength of the steels due to VN and/or Nb(C,N) precipitation. These elements (V, Nb and high Cr) which are essential for the creep characteristics of the material have an adverse effect on the toughness of the steel. They are unable to be reduced because of the high toughness requirements [Dittrich and Heuser, 1986]. Oxidation resistance is also improved by these additions. Strengthening of the solid solution during creep of these steels is caused by the presence of Mo and/or W content in solid solution. In nitrogen containing steels, the carbides are likely to be replaced by complex carbonitrides. Aluminium also interacts with nitrogen to form AlN. The factors influencing solid solution strengthening change

[3] Here, M represents metallic elements, including iron.

with time, as the carbide precipitation depletes the lattice of solutes. For example, creep strength in these steels can only be improved by addition of molybdenum equivalent (Mo + 0.5 W wt. %) up to a maximum of about 1 weight %, as higher contents cause the precipitation of M_6C carbides and the Fe_2Mo intermetallic which remove Mo and W from the solid solution [Abe and Nakazawa, 1992]. After aging at low temperature, precipitations of Laves phases occur in the structure. These from large particles, principally on the prior grain boundaries [Foldyna and Kuboň, 1993]. To minimise these phases, the silicon content of the steels is kept to a minimum.

1.5.4 10CrMoV Steels

These steels are suitable for steam conditions with temperatures up to 600 °C. Although austenitic steels can be used for such conditions, these are susceptible to thermal fatigue [Berger *et al.*, 1994] because of their large thermal expansion coefficient. These steels are typically used for critical components such as forged turbine rotors and blades, and castings for turbines and valve casings.

1.5.5 12Cr Steels

These alloys are useful in power plant applications, as the high quantities of chromium control the oxidation resistance [Irvine, Crowe and Pickering, 1960]. They are completely austenitic at a solution temperature in the region of 1050 °C, and have a martensite-start temperature such that they will be completely martensitic at room temperature. Nickel is kept at below 2 weight % to keep the Ac_1[4] temperature high enough to ensure no reversion to δ-ferrite on tempering. This may be deviated from if sufficient ferrite stabilising elements (*e.g.* Si, Al, Mo and V) are present. The transformation characteristics of the steel show that carbide precipitation precedes the pearlite reaction, and the bainite reaction is completely suppressed. Secondary hardening can occur within the temperature range 400–500 °C, by precipitation of a Cr-rich carbide of the type M_2X. Carbon and nitrogen in the steels are very effective in accentuating the secondary hardening, but nickel and manganese are less effective, and increase the softening rate of the steels. Overaging produces the precipitation of $M_{23}C_6$ at grain boundaries, accompanied by a slow reabsorbsion of the M_2X. The ferrite forming elements such as Mo, W, V, and Si cause solid solution hardening of the steel and also intensify the secondary hardening reaction. Vanadium's main contribution is to stabilise M_2X, so that higher hardnesses are produced at higher tempering temperatures Mechanically, the secondary hardening is accompanied by poor impact properties. This results because of the coherency straining due to the M_2X formation. Additions of Mo up to 2 weight % improve both the strength and the impact resistance. At greater concentrations, it affects the M_2X precipitate, which outweighs these benefits. Vanadium increases the tensile strength, although only small amounts can be used without deleterious effects on the impact properties. For the best combination of strength and impact, a composition of 0.1 weight % carbon, 12 weight % chromium, 2 weight % nickel, $1\frac{1}{2}$ weight % molybdenum and 0.3 weight % vanadium is recommended. For improved ductility and impact properties in an application where reduced tensile strength is acceptable, then a reduction of nickel to $1\frac{1}{2}$ weight % can be used.

1.5.6 $3\frac{1}{2}$Ni Steels

These alloys are used for thick section (LP) rotor forgings in the power plant [Elsender *et al.*, 1978,

[4] Ac_1 is the temperature at which austenite first begins to form on heating.

Ridley *et al.*, 1994, Iwanaga *et al.*, 1990]. They have excellent hardenability, along with high strength and good toughness.

These steels are used in the "superclean" condition. Such steels are free of impurities and also of the additions which are usually added to standard steels to counteract the effects of impurities [Jaffee, 1989]. For example, manganese is usually added to steels to counteract the effects of sulphur, but in superclean steels, sulphur is removed through reducing slags in ladle furnaces so manganese is not required. Similarly, silicon and aluminium are not necessary for the steels, as carbon is used for deoxidation by the vacuum carbon deoxidation process. The gases hydrogen, oxygen and nitrogen are removed from the steel by vacuum processing. There are no proven processes of removing tin, arsenic or antimony from the steel, so these must be controlled by scrap selection. As a result these steels have no inclusions, no impurities and only the intended alloying elements.

Superclean $3\frac{1}{2}$NiCrMoV steel is found to be immune to temper embrittlement, and it benefits from improved ductility, toughness and creep properties as compared to steels of conventional purity. These advantages outweigh the extra cost required for its production ($\sim$ 10 % higher for the price of the scrap, and $\sim$ 8 % higher for the longer processing times involved).

These steels have satisfactory weldability. However, low sulphur levels lead to low weld penetration due to the negative surface tension coefficients. This can be improved upon by raising the heat input (defined later, in section 1.6.6).

1.5.7 Future Development

Tried and tested ferritic steels used in earlier applications are no longer of use at the higher temperatures and pressures needed to achieve higher efficiency, as their useful limit is 560 °C [Adam *et al.*, 1995]. Austenitic steels may be used at temperatures up to 600 °C, although they may have unfavourable physical properties, *e.g.*, low thermal conductivity and higher thermal expansion [Adam *et al.*, 1995]. They are also more expensive than their ferritic counterparts.

1.5.8 Steelmaking Techniques for Advanced Material Quality

The electroslag refining process is used in the production of high temperature rotor forgings, allowing control of non-metallic inclusion formation, and increasing the usable weight of the ingot. Creep rupture strengths of steels produced in this manner are comparable with those produced by the basic electric arc method, with slightly lower creep rupture properties. However, chemical analysis of the steels showed that the aluminium content of electroslag refined rotors was increased compared to conventional rotors (0.017–0.066 weight %, compared to 0.003 weight %), which is known to reduce creep ductility [Viswanathan and Beck, 1975]. Care must therefore be exercised to control the aluminium content. However, the electroslag refining process reduces the probability of large inclusions or excessive segregation.

As the use of remelted scrap has continued in the manufacture of steel, concern has arisen that the level of residual elements in the steel may increase to unacceptable levels, especially in the use of high integrity components [Batte and Murphy, 1979]. Trace elements such as aluminium, arsenic and antimony can be deleterious to the high temperature performance of steels. Basic oxygen steelmaking with blast furnace hot metal as the charge is a viable method of controlling the quantities of residual elements present in the steel. Batte and Murphy [1979] illustrate that this method of production could

be used to lower the phosphorus, arsenic, antimony, tin and aluminium contents of a 1CrMoV steel, with respect to a basic electric steel forging from the same initial cast. Due to the lower concentration of major elements added to the steels in the basic oxygen process, the nickel concentration was found to be lower, which consequently reduced the proof strength and creep rupture strength of the steel, though kept them within an acceptable range. The creep rupture and ductility properties of the steels were comparable, as was the weldability, but the basic oxygen steel had an above average strength.

Vacuum carbon deoxidation gives improved control of silicon and manganese levels, and reduces the segregation in large forgings [Sawada *et al.*, 1977]. It is also applicable to 1%CrMoV forgings without detriment to their creep resistance [Schinn and Schieferstein, 1970]. Silicon deoxidation reduces the FATT of the steel, which is termed "semikilled" [Dieter, 1988]. Silicon and aluminium deoxidation reduces the FATT further, producing a "killed" steel.

1.6 Welding in the Power Station

Joints in the power station are required to have mechanical properties matching those of the parent materials. In order to achieve this, the materials joined together are required to have good "weldability". This is a very broad term, best defined as "the capacity of a metal or a combination of metals to be welded under the fabrication conditions imposed into a specific suitably designed structure and to perform satisfactorily in the intended service. The better the weldability, the easier these requirements may be met" [Gorton, 1975].

1.6.1 Background on Weld Microstructure

The action of the process of welding not only provides new solidified weld material, but also influences the structure of the parent steel adjacent to the weld. This is called the heat affected zone (HAZ). For a single pass weld, a heat affected zone structure is produced which consists of four major regions [Slater, 1993], each region having been subject to a different range of peak temperatures, T_i during the act of welding. In all, seven different zones exist in the cross section of the single pass weldment, each having their own range of microstructure and properties [Easterling, 1983, Honeycombe and Bhadeshia, 1995] (Figure 1.10).

1. The solidified weld.
   This region consists mainly of the deposited weld metal, though some dilution with the parent is likely to occur in certain cases. It is essentially a cast structure, with long thin grains. However, in contrast to a casting, the grains are nucleated from the neighbouring parent material, and there is no shrinkage.
2. The solid/liquid transition zone.
   This is a very thin layer which has experienced a peak temperature approximately equal to the melting temperature of the parent steel.
3. Coarse grained heat affected zone.
   This region has received a peak temperature greater than $\sim$ 1100 °C, up to the melting point of the steel. The material is austenitic, and consists of large grains. It is also known as the "grain growth zone" [Easterling, 1983].
4. Fine grained heat affected zone.

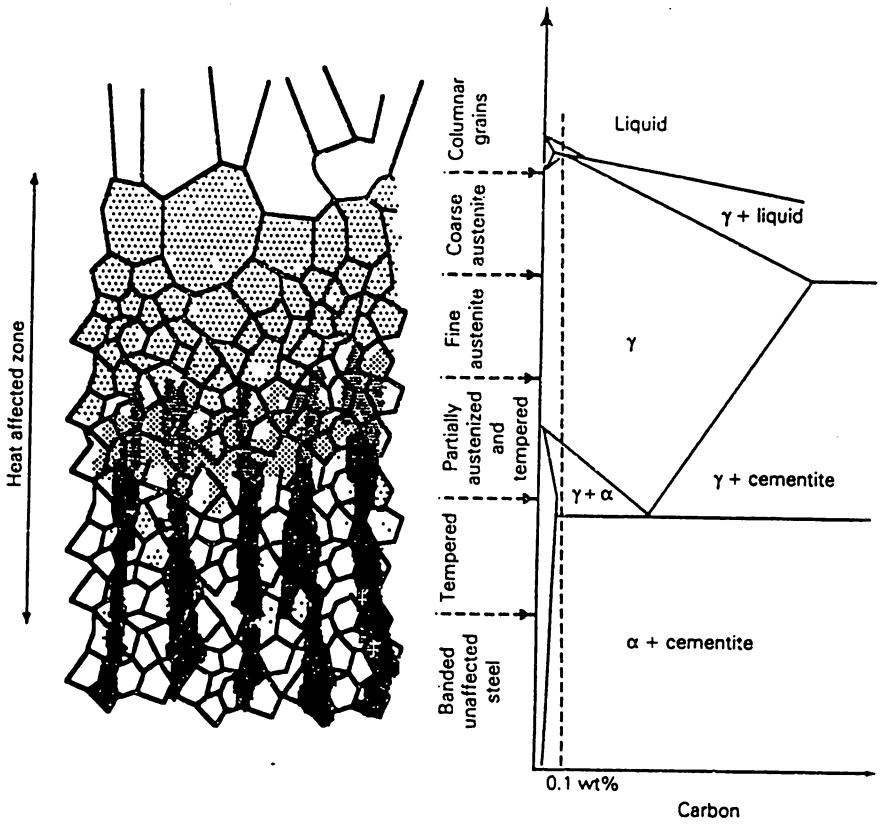

Figure 1.10: Schematic illustration of the microstructural variation to be expected in the heat affected zone of steel welds [Honeycombe and Bhadeshia, 1995].

Otherwise known as the "grain refined HAZ" [Slater, 1993]. This region is defined by a peak temperature between 1100 °C and the Ac_3 temperature of the steel. Ac_3 is the temperature at which austenite formation is completed during heating.

5. Intercritical heat affected zone.

   The intercritical heat affected zone is defined by the temperature range $Ac_1 < T_i < Ac_3$. Both ferrite and austenite are stable, so the microstructure is mixed. On heating, steel with a low carbon content remains in the ferritic state and carbon enriched regions transform to austenite [Slater, 1993]. On cooling, the stable phases would be ferrite and pearlite (ferrite + cementite).

6. Subcritical heat affected zone.

   This area of the HAZ has received a T_i of less than Ac_1, but greater than $\sim$ 600 °C. No phase change happens, but at this reasonably high temperature diffusion is easier, and partial spherodisation of pearlite may occur [Slater, 1993]. This is also known as the tempered zone [Easterling, 1983].

7. Unaffected parent material.

   At temperatures less than $\sim$ 600 °C, diffusion is less able to occur, and so the heat affected zone ends, leaving the parent material in its original state [Easterling, 1983].

Multipass welds are often used in the power station, as they cause both an improvement in

toughness, and a reduction in residual stress as compared to single pass welds [Easterling, 1983]. Using more than one pass, however, causes reheat of the heat affected zone and weld metal of previous welds, modifying the simple weldment regions outlined above. The reheated weld metal, deposited in earlier runs, experiences recrystallisation and grain growth. The latter, however, is unlikely to be extensive, as the heat input for mulipass welds is lower than for a single pass. Reheating of the HAZ has the effect of refining the microstructure. However, only a relatively small part of the HAZ is reheated to T_i, the rest receiving a milder heat treatment.

1.6.2 Rôles of Welding in Power Plant

Welding plays a wide range of important rôles in the construction of power plant [Harris and Lee, 1962]. An application of this is the simple concept of joining together two smaller castings or forgings, to produce a larger unit, as in the forgings for the HP valves for Drax (Figure 1.2). This can reduce the problems associated with the casting of large components. This process can be extended to composite turbine cylinders. Because of the gradation in temperature and pressure along the length of the component, a less highly alloyed and therefore cheaper material can be used for the lower temperature end. Another important use is to attach an extension stub to the cylinder or a steam chest for site welding, where this is not possible in the cast used. An illustration [Harris and Lee, 1962] of how welded components add to the efficiency of power plant, can be found in welded steam turbine diaphragms. These are superior to diaphragms produced by a riveted construction for the following reasons:

1. They are stronger for given dimensions.
2. Construction is simpler.
3. Steam leakage is reduced.
4. Integral steam guides can be used.

However, despite these advantages, some service failures in power plant have been encountered in weldments [Parker and Parsons, 1994]. Such failures have been classified in the following manner [Schuller *et al.*, 1974]:

Type I — cracking in the weld metal.
Type II — cracking originating in the weld metal, but extending into the HAZ.
Type III — cracking in the coarse grained region of the HAZ.
Type IV — cracking in the intercritical region of the HAZ.

It has been found that the majority of weldments reach their design life without damage, but there are trends in those which do fail. The study of performance of low alloy steel weldments has revealed that Type III damage was more likely to occur early in service life, with Type I more common at service lives of 40 000–60 000 hours (4–7 years). Both of these types of crack initiate because of relaxation of welding residual stresses in relatively brittle microstructures [Parker and Parsons, 1994]. Type IV damage becomes more prominent at lives of about 60 000–100 000 hours, which is the normal design life of the plant. This develops because of high system loading in a region of low creep strength.

Tests show that as the weld microstructure ages, micro-hardness across the HAZ tempers to a homogeneous level. Long term aging, (100 000–210 000 hours service) leads to carbon depletion in the

HAZ. The width of this decarburised zone for any time and temperature combination can be calculated using a model developed by Race [1992]. The carbides provide creep resistance to the low alloy steel, and this decarburised zone has an increased rate of creep deformation [Parker and Parsons, 1994].

1.6.3 Welding Techniques

As expected, the type of welding taking place in power plant varies according to individual requirements. Fabrication welds may well be processed in a different way to site repairs even if they are for welds on the same component. The commonly used processes are outlined below.

Manual metal arc welding is a simple and convenient method for the majority of applications, and where required, the work can rotated on a manipulator, so that welding may be carried out in the flat position [Harris and Lee, 1962]. "U" and "V" type notches are both in common use for weld preparations, and backing plates are used, which are later machined out, to leave a sound root. This process has the advantage that it can be used in all positions (horizontal, vertical and overhead), but a lower heat input can be attained than if an automated process is used, for the safety of the welder.

Submerged arc welding is also used in many applications, with the "step pass" method, used to avoid rotation of components [Harris and Lee, 1962], or a rotating method. This is an automated process, and as such produces reliable and reproducible results. A higher heat input can be used, as the operator is well away from the heat source when the welding is taking place.

1.6.4 The use of Preheat

Preheating of a weldment helps to minimise the risk of cold cracking, as it affects the microstructure of the HAZ and the weld metal as well as aiding hydrogen diffusion away from the joint zone [Hrivňák, 1985]. Hydrogen removal for welded steel with no danger of HAZ martensite can more effectively be achieved with a post weld heating. Evans [1982a] frequently uses a treatment of 250 °C for 14 hours for this purpose. The preheat temperature must not exceed the M_S temperature of the steel as this can result in the stabilisation of residual austenite [Hrivňák, 1985]. Harris and Lee [1962] illustrated that the preheating of a CrMoV sample to 200 °C before welding resulted in a marked improvement in impact strength, and reported similar results for other power plant alloys. Preheating is therefore necessary to increase crack propagation resistance, which is a necessary property for the high wall thicknesses often present in power plant components. With the $2\frac{1}{4}$Cr1Mo steel, preheating provides a dual function of reducing the underbead hardness, as well as maintaining an adequate toughness. British Standard recommended preheat levels for a hydrogen controlled[5] weld metal with parent material thickness > 12 mm are:

1.6.5 The Interpass Temperature

The interpass temperature is only becomes an important factor when multipass welds are considered [Hrivňák, 1985]. It is usually lower than the preheat temperature, as the dilution of subsequent weld runs never reaches the degree of that in the root zone. A range ought to be provided for the interpass temperature, as heat removal is low in multipass welds, and so, unrestrained, the temperature gradually increases with the number of passes.

---

[5] Hydrogen controlled weld metal contains < 15 mL of diffusible hydrogen per 100g of deposited weld metal [British Standard EN499, 1995].

Alloy	Minimum Preheat Temperature °C
1Cr$\frac{1}{2}$Mo	150
1$\frac{1}{4}$Cr$\frac{1}{2}$Mo	150
$\frac{1}{2}$Cr$\frac{1}{2}$Mo$\frac{1}{4}$V	200
2$\frac{1}{4}$Cr1Mo	200
9Cr1Mo	200
12CrMoV	150
3$\frac{1}{2}$Ni	150

Table 1.3: Common preheat levels [British Standard 2633, 1987].

The martensite transformation ought to be taken into account when choosing the interpass temperature. If a weld is carried out at an interpass temperature above the martensite-start temperature, M_S, then the weld structure will be totally austenitic during deposition. On cooling, this austenite will transform into an untempered martensitic structure, which will be brittle and liable to crack.

If the interpass temperature is less than the martensite-finish temperature, M_F, then the deposition of the weld will produce 100 % martensite, and no transformation will take place on further cooling. Again, a completely martensitic structure will result and the weld will be susceptible to cracking.

The ideal scenario would be for the interpass temperature to be chosen between M_S and M_F, where some, but not all of the austenite will transform to martensite during welding. Once the weld is completed, it can be heated to a higher temperature to temper the martensite in the mixed microstructure of martensite and austenite. This tempered martensite is composed of Fe_3C and cubic ferrite which is only slightly supersaturated with carbon [Bain and Paxton, 1961]. On further cooling to ambient temperature, the remaining austenite will transform to untempered martensite, which will be supported by the more ductile tempered martensite. This represents the best welding procedure, with approximately 50 % tempered martensite, providing ductility to support the remaining 50 % untempered martensite. The higher the tempering temperature, the more spheroidal the carbide particles become, and the greater the improvement in ductility [Bain and Paxton, 1961].

1.6.6 Heat Input

The heat input is a measure of energy provided by the welding process, and can be defined by the equation

$$\text{heat input} = \frac{\text{current} \times \text{voltage}}{\text{welding speed}} \tag{1.1}$$

Heat input is one of the most important welding variables as it influences heating rates, cooling rates and weld pool size [Lancaster, 1993]. A high cooling rate can lead to hydrogen-induced cracking. Metallurgically, the cooling rate governs the size of the grains in the resolidified region of the weldment. In ferritic steels, coarse grains are associated with a reduction in notch ductility. Böhler Welding [1993] similarly report that Charpy impact toughness values from a weld metal sample built up of thin layers

were a distinct improvement on measured values from a thick layered specimen. As well as reducing the heat input (usually by reducing current), these improved properties could also be obtained by using smaller diameter electrodes, or using a "weave bead" technique of depositing the weld.

Typical heat inputs for a variety of welding processes are provided in Table 1.4 [Easterling, 1983].

Welding Process	Typical heat input range kJ mm^{-1}
Electroslag	5–50
Submerged arc	1.0–10
Gas-metal arc	0.5–3
Manual metal arc	0.5–3
Gas-tungsten arc	0.3–1.5
Electron beam	0.1–0.6
Laser beam	0.1–0.6

Table 1.4: Typical heat inputs (after Easterling [1983]).

Evans [1980] studied the effect of heat input variations on multi pass C Mn welds. These variations were achieved by adjusting the welding speed, keeping current and voltage constant. Research showed that as the heat input was increased, the size of the weld beads increased, which caused variation in the number of beads deposited per layer, hence making standardisation between the different heat inputs used difficult. This was accompanied by an increase in width of the columnar grains in the deposit. A decrease in the hardness, yield strength and tensile strength of the weld was also observed. The reheated regions of the weld were also influenced, and grain growth took place in both the coarse and fine grained zones as the speed was decreased.

These results show that a lower heat input provides enhanced mechanical properties. This explains why multipass welding techniques are often chosen, because many small layers with low heat input produce a better weldment than one large deposition from a single pass weld.

1.6.7 Post Weld Heat Treatment

Completed welds are, where possible, transported to the stress-relieving furnace without cooling. Stress-relieving of cold weldments brings the additional risk of cracking, because of the addition of thermal stresses to the already high levels of residual welding stress [Harris and Lee, 1962]. British Standard recommendations for the post weld heat treatment temperatures for these particular steels are outlined below:

During the post weld heat treatment, both heating and cooling must be carried out slowly, to avoid temperature differences across the component. This would cause thermal stresses, thus counteracting the desired effect of reducing the stress.

1.6.8 Weld Metal Composition

Despite intuition, selecting a weld metal composition matching that of the parent is not always the most

Alloy	Post Weld Heat Treatment Temperature °C	Minimum Post Weld Heat Treatment Time minutes
1Cr$\frac{1}{2}$Mo	630–670	120
1$\frac{1}{4}$Cr$\frac{1}{2}$Mo	630–670	120
$\frac{1}{2}$Cr$\frac{1}{2}$Mo$\frac{1}{4}$V	680–720	180
2$\frac{1}{4}$Cr1Mo	680–720	180
9Cr1Mo	710–750	120
12CrMoV	720–760	180
3$\frac{1}{2}$Ni	580–620	60

Table 1.5: Common post weld heat treatment levels. [British Standard 2633, 1987].

practical of cases. In CrMo alloys, such a selection has been found to produce satisfactory results for those alloys of lower creep strength [Harris and Lee, 1962]. In contrast, it is found in CrMoV steels of higher creep strength, that the risk of cracking of the base metal during stress relieving is increased. This is still observed, even when the stress relief is carried out immediately after welding, with no allowance for cooling. However, if a 2$\frac{1}{4}$Cr1Mo electrode is used on the CrMoV steel, then a much sounder joint is produced. Residual stresses in such a weld are much lower than for weld matched to the parent [Harris and Lee, 1962].

Weld metals, therefore, are chosen on a basis of matching the *physical properties* rather than the composition to that of the parent steel or steels. A prime example of this is the development of filler metals for use with P91, a 9Cr creep resistant steel [Adam *et al.*, 1995]. Three basic types of filler metal are now available for this steel; 9CrMoVNb, 10CrMoWVNb and 9CrMoWVNb. In developing these compositions, the effects of the individual alloying elements were considered.

1.6.9 Dissimilar Metal Welds

If the different types of steel outlined in the sections above are to be used to their best advantage in the manufacture of power plant, it is evident that there will have to be some fabrication of dissimilar steel welded joints. This phenomenon brings with it some associated problems. Carbon diffusion across the welded joint occurs at elevated temperatures, such as a post weld heat treatment, or during service in one of the hotter regions of the power station, and is greatest across a weld where the difference in activity of the carbon between the two parents is greatest. The diffusion is an act of equilibration. Race [1992] has outlined the major problem of carbon diffusion, providing calculations for the carbon depleted zone and the carbon enriched zone width. As chromium has a large influence on the carbon activity, diffusion will then be greater between steels with a contrasting chromium concentration, for example a weld between 12Cr and 2$\frac{1}{4}$CrMoV steels. Nickel based weld metals may eliminate carbon migration [Eaton and Glossop, 1970] but they provide hard lamellar phase precipitation at the interface and in diluted regions on post weld heat treatment. 12Cr steel parent metals are also prone to hydrogen induced hard zone cracking if they are welded without adequate preheat or are allowed to cool before

tempering. This risk is lessened if welds are carried out by the TIG process, as this is associated with a lower quantity of hydrogen. 9Cr welds fortunately do not suffer from this problem.

It can be seen that the selection of welding consumable compositions, process conditions and post weld heat treatments is an important process, critical to the mechanical properties and integrity of the weld. Historically, this has been achieved by a "trial and error" process, which requires experienced researchers and is costly in both time and consumables. The work described in subsequent chapters takes a look at the prediction of the effect of varying these parameters on the mechanical properties of welds and parent material, with a view to optimisation of the weld properties. This would enable new welds to be developed more rapidly and cheaply.

CHAPTER TWO

Experimental Materials and Techniques

2.1 Introduction

A variety of specimens typical of power plant applications were provided for the tests described later in this thesis. They consisted of both wrought alloys and weld deposits. The alloys used and the experimental techniques employed are described below.

2.2 Experimental Alloys — Wrought Steels

The wrought steels were provided by Parsons Power Generation Systems Ltd. They were chosen from the range of steels used in manufacturing power plant. Their chemical compositions are listed in Table 2.1, the steels being identified by their proprietary designations.

Sample	B158	4HSG	HYE	97	P91	F	ADQ
Carbon	0.20	0.29	0.25	0.14	0.093	0.13	0.11
Silicon	0.084	0.22	0.34	0.20	0.41	0.19	0.26
Manganese	0.64	0.85	0.28	0.52	0.49	0.55	0.44
Sulphur	0.003	0.009	0.007	0.009	0.003	0.006	0.002
Phosphorus	0.009	0.011	0.008	0.011	0.015	0.013	0.018
Nickel	0.76	0.73	3.51	0.084	0.23	0.62	0.043
Chromium	2.12	0.97	1.60	0.30	9.08	10.2	2.01
Molybdenum	0.83	0.65	0.46	0.56	0.92	1.51	0.94
Vanadium	0.32	0.26	0.13	0.23	0.25	0.21	0.008
Cobalt	0.013	0.021	0.069	0.021	0.012	0.010	0.008
Tungsten	0.63	0.011	0.017	0.007	0.000	0.000	0.009
Niobium	0.020	0.017	0.020	0.010	0.000	0.000	0.022
Nitrogen	0.006	0.012	0.009	0.011	0.035	0.060	n/a

Table 2.1: Composition of the wrought samples. All elements are in weight %.

2.2.1 B158: 2CrMoNiWV Steel

This steel is used for high temperature (up to 565 °C) turbine rotors of the HP and combined HP/IP single cylinder type. HP rotors are supplied in the oil quenched and tempered condition for optimum creep properties. The steel has improved toughness over the 1% CrMoV steel normally used in this application. For single cylinder applications, this material is supplied in the "dual" heat treated

condition, *i.e.* simulated oil quench at the HP end, and a water quench at the LP end. A simulated oil quench uses water sprays for quenching at the correct rate to mimic a quenching received by oil. This procedure gives optimum creep properties where they are needed and improved strength and toughness, as required for the LP end of the shaft. It also enables the LP rotor diameter to be significantly increased without promoting ferrite formation in the core region of the forging.

2.2.2 4HSG: 1CrMoV Steel

This steel has been in use for approximately 35 years for high temperature rotors operating at conventional temperatures (538–565 °C). It was developed to give optimum creep strength and rupture density.

2.2.3 HYE: $3\frac{1}{2}$NiCrMoV Steel

This is the "industry standard" steel for LP turbine rotor and generator rotor forgings. Problems with embrittlement restrict the temperature of operation to below 350 °C. The steel is designed for optimum strength and toughness, rather than for creep strength.

2.2.4 97: $\frac{1}{2}Cr\frac{1}{2}Mo\frac{1}{4}V$ Steel

This is the conventional creep resistant steel that has been used in the UK for the last 20 years for the manufacture of cast turbine cylinders and steam chests, forged components and steam pipework (to British Standard 3605 [1991] grade 660) for turbines operating at 538–565 °C.

2.2.5 P91: Modified 9Cr1Mo Steel

This steel is now being used in the manufacture of pipework, forgings and castings for steam turbine plant where operating temperatures are greater than 565 °C, up to about 620 °C, where the conventional materials no longer have creep strengths high enough for them to be used in thicknesses that are practical or economical. It is also being used to replace conventional materials at the lower operating temperatures where reductions in thickness are advantages from a flexibility point of view (pipework), or there is an economical advantage [Orr and Burton, 1993]. Steel P91 has superior creep rupture properties to $2\frac{1}{4}$CrMo and X20 CrMoV steels [Naylor, 1993]. It has high creep strength with good ductility in test durations up to 80 000 hours, high resistance to thermal fatigue cracking, good weldability and good corrosion and cracking resistance in both aqueous and gaseous environments [Naylor, 1993]. Sufficient data and experience of this steel are held to justify its use at temperatures up to 600 °C.

2.2.6 F: 10CrMoWNbVN Steel

This steel is one of the "12Cr" steel variants produced under the COST 501[1] development programme for advanced steam cycle turbine rotors, operating at temperatures above 600 °C. The steel is designed for optimum creep strength and creep ductility at these higher operating temperatures. Long term testing of the material is still in progress in a collaborative European development programme.

2.2.7 ADQ: $2\frac{1}{4}$Cr1Mo Steel

This is a creep resistant steel that has been used internationally for many years as the standard material for cast turbine cylinders and steam chests, forged components and steam pipework (to ASTM A335

[1] COST 501 is a collaborative committee comprising representatives from European countries working together for improved properties of power plant components.

grade P22) for turbines operating at 538–565 °C. It has slightly lower creep strength than the "97" type of material (Section 2.2.4).

2.3 Experimental Alloys — Weld Deposits

The weld deposits studied as part of this work were provided from the COST 501 programme, to study the effect of alloying elements on modified 9Cr1Mo weld deposits. They form a systematic series beginning with a basic 9Cr1Mo composition, with additions of nickel, cobalt and tungsten individually up to a level of 3 weight %. Some samples with mixtures of these alloying elements were also provided, combining the effects of nickel with both tungsten and cobalt. The welds were made to match a parent material from the COST 501 project - NF616, a high strength 9Cr1Mo wrought steel. The deposits from which the samples were taken were multi-run welds prepared to ISO 2560 geometry, which ensures minimal dilution so that all-weld metal samples can easily be machined. The welds were made using 4 mm diameter electrodes at a heat input of 1 kJ mm^{-1} and an interpass temperature of 175 °C. Welding was followed by a post weld heat treatment of 750 °C for 8 hours, defining the condition in which the samples were received. The compositions and mechanical properties of the samples are presented in Table 2.2, along with data for NF616.

Three further welded alloys were produced by Oerlikon as being typical of power plant steel welds. They were manufactured using the manual metal arc process, with 4 mm diameter electrodes. Their chemical composition, welding conditions and mechanical properties are outlined in Table 2.3.

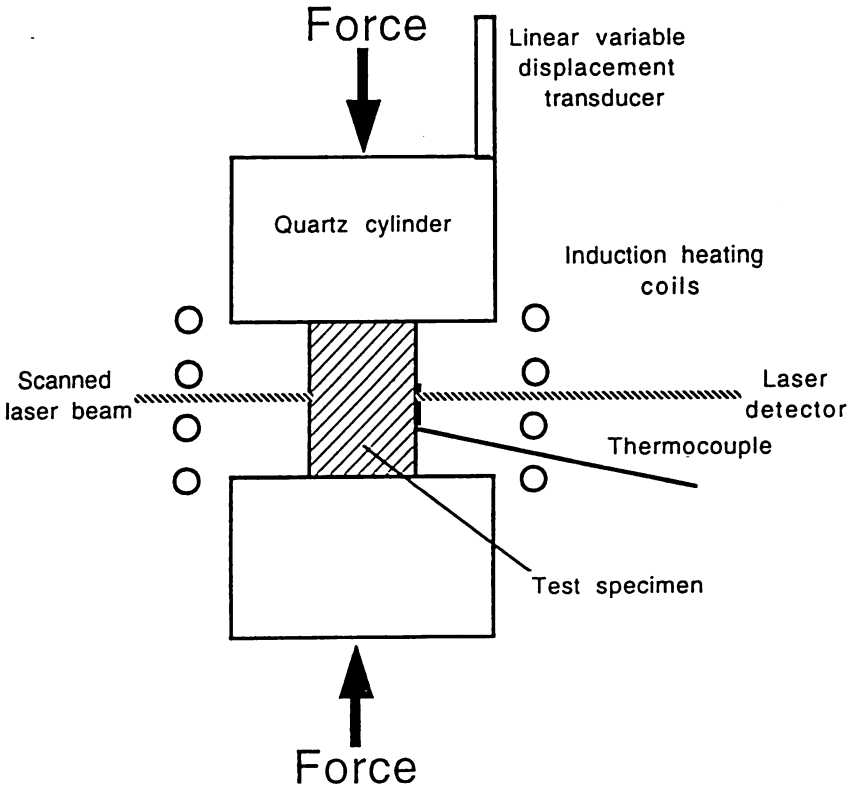

Figure 2.1: Schematic of the thermomechanical simulator.

Sample	Base	1Ni	2Ni	3Ni	1Co	2Co	3Co
Carbon	0.099	0.093	0.101	0.095	0.096	0.094	0.091
Silicon	0.17	0.16	0.17	0.16	0.16	0.18	0.16
Manganese	1.01	1.03	1.02	1.02	1.01	1.00	1.00
Sulphur	0.007	0.008	0.008	0.007	0.007	0.008	0.008
Phosphorus	0.012	0.012	0.012	0.012	0.013	0.017	0.015
Nickel	0.08	0.98	1.92	3.01	0	0	0
Chromium	9.30	9.08	9.12	9.17	9.16	9.31	9.30
Molybdenum	1.00	0.98	1.00	0.96	0.99	0.98	0.98
Vanadium	0.20	0.19	0.19	0.19	0.19	0.19	0.19
Cobalt	0	0	0	0	0.95	1.89	2.80
Tungsten	0	0	0	0	0	0	0
Niobium	0.046	0.043	0.047	0.045	0.045	0.043	0.041
Nitrogen	0.0539	0.0515	0.0494	0.0489	0.0552	0.0517	0.0520
Oxygen	0.0634	0.0651	0.0664	0.0610	0.0672	0.0687	0.0666
Yield Strength MPa	617	551	672	920	525	526	481
UTS MPa	762	751	866	1151	696	690	672
Elongation %	18.4	19.6	13.6	10.6	19.8	21.9	23.7
Reduction of Area %	61.2	64.5	56.8	47.6	64.4	66.0	66.7

Table 2.2a: Composition and mechanical properties of the welded samples. All elements are in weight %.

2.4 Thermomechanical Simulator

A thermomechanical simulator is a programmable piece of equipment with the ability to simulate a specified thermal cycle on a sample of the alloy to be studied. The *Thermecmastor Z* simulator was used to study phase transformations during heating and cooling conditions. The control of the machine, and data collection are both via a computer. It is possible to monitor temperature, stress and dilation of the specimen with respect to time. Heating is achieved using high frequency induction, and cooling using a gas (N_2 or He) or water quench. Helium was used for all of the experiments.

The temperature of the specimen is monitored using a platinum/platinum-rhodium thermocouple, which is spot welded to the specimen. The accuracy of the temperature measurements obtained in this way is ± 3 °C [Fuji Electronic Industrial Co. Ltd., 1986].

The diametrical dilation of the specimen is monitored without contact to the specimen using a He-Ne laser beam, with an accuracy of $\pm$ 1 μm. The laser beam scans and moves with the ram in order

Sample	1W	2W	3W	1W1Ni	1W1Co	1W2Co	NF616
Carbon	0.095	0.096	0.094	0.097	0.091	0.090	0.12
Silicon	0.18	0.20	0.20	0.18	0.18	0.17	0.02
Manganese	1.04	0.99	1.03	1.00	0.99	0.97	0.47
Sulphur	0.008	0.007	0.008	0.007	0.008	0.008	0.006
Phosphorus	0.015	0.015	0.015	0.015	0.015	0.015	0.011
Nickel	0	0	0	0.93	0	0	0
Chromium	9.35	9.25	9.26	9.10	8.94	9.20	9.07
Molybdenum	1.00	0.91	0.84	0.96	0.97	0.96	0.46
Vanadium	0.19	0.19	0.19	0.19	0.18	0.18	0.19
Cobalt	0	0	0	0	0.92	1.87	0
Tungsten	1.03	1.92	2.99	0.98	0.98	0.97	1.78
Niobium	0.051	0.053	0.058	0.046	0.044	0.045	0.06
Nitrogen	0.0544	0.0526	0.0537	0.0529	0.0509	0.0523	0.043
Oxygen	0.0656	0.0669	0.0640	0.0667	0.0695	0.0662	n/a
Yield Strength MPa	526	515	489	531	492	524	525
UTS MPa	702	698	686	738	673	701	680
Elongation %	19.6	18.9	18.7	17.3	21.8	20.7	22
Reduction of Area %	59.3	59.0	49.6	58.1	65.3	63.7	72

Table 2.2b: Composition and mechanical properties of the welded samples, along with NF616 [Hald, 1994], a wrought steel. All elements are in weight %.

to ensure that the same location is monitored irrespective of deformation. The scanning frequency of the laser is approximately 1000 Hz [Fuji Electronic Industrial Co. Ltd., 1986].

The specimens were machined into cylinders of 8 mm diameter, by 12 mm long, and their configuration in the simulator is illustrated in Figure 2.1.

Alloys were heated at a variety of rates to a temperature within the austenite phase field, and soaked isothermally before gas quenching to room temperature. A helium quench gives a cooling rate of $\sim$ 50 °C s^{-1}, which can be measured accurately by the Thermecmastor. The experiments carried out allowed the Ac_1, Ac_3 (austenite formation on heating) and M_S (martensite-start) temperatures to be measured.

2.5 Optical Microscopy

Specimens for optical analysis were hot mounted in conductive Bakelite, then ground to a smooth finish using silicon carbide papers followed by diamond paste on cloth. They were thoroughly cleaned

Variable	$2\frac{1}{4}$Cr1Mo	9Cr	$3\frac{1}{2}$Ni
Carbon weight %	0.07	0.10	0.13
Silicon weight %	0.39	0.38	0.37
Manganese weight %	0.90	1.14	1.47
Sulphur weight %	0.007	0.007	0.007
Phosphorus weight %	0.010	0.008	0.010
Nickel weight %	0.02	0.00	2.97
Chromium weight %	2.64	9.00	1.07
Molybdenum weight %	1.18	1.14	0.66
Vanadium weight %	0.02	0.22	0.049
Copper weight %	0.00	0.00	0.00
Cobalt weight %	0.00	0.00	0.00
Tungsten weight %	0.00	0.00	0.00
Oxygen p. p. m. w.	410	460	200
Titanium p. p. m. w.	0	0	0
Boron p. p. m. w.	0	0	0
Niobium p. p. m. w.	60	600	50
Nitrogen p. p. m. w.	60	460	60
Heat Input kJ mm^{-1}	1.605	1.12	1.20
Interpass Temperature °C	300	300	300
Tempering Temperature °C	700	760	700
Tempering Time hours	3	2	3
Yield Strength MPa	568	752	920
UTS MPa	676	872	1000
Elongation %	18	13	14
Reduction of Area %	70	56	51
Charpy Impact Energy J	180, 168, 163	34, 57, 38	8, 5, 8

Table 2.3: Chemical composition, welding process and heat treatment data for the three test welds. The abbreviation p. p. m. w. stands for parts per million by weight.

between each stage in the preparation process, and were then etched in Vilella's reagent or nital.

2.5.1 Vilella's Reagent

Vilella's reagent was prepared by the mixture of 1000 ml methyl alcohol (CH_3OH), 50 ml hydrochloric acid (HCl), and 10 g of picric acid (2, 4, 6 trinitrophenol).

2.5.2 Nital

A 2 % nital etchant was prepared by mixing 980 ml of methyl alcohol with 20 ml of nitric acid ($HN0_3$). Different concentrations were prepared by altering the proportions appropriately.

2.6 Scanning Electron Microscopy

Facilities at both Cambridge and Newcastle University were employed. Polished and etched specimens as described in the optical section were used, together with unprepared specimens in order to view the fracture surfaces.

2.7 Hardness Testing

The hardness of the samples was measured using a Vickers diamond indent hardness machine with a 10 kg or 20 kg load.

2.8 Mechanical Properties Testing

The testing of the mechanical properties of the experimental welds was carried out by Oerlikon prior to the commencement of this research, and the data were obtained from their reports [Evans, 1994a; Davin 1994]. However, welds manufactured as part of this work were tested by International Research and Development Ltd., using the following techniques.

2.8.1 The Tensile Test

This test enables several properties to be determined which provide information on the strength and ductility of a material, including the yield strength, ultimate tensile strength, elongation and reduction of area. For the purpose of the test, the weldment was machined into a standard sample shape (Figure 2.2). It was important that the test piece consisted entirely of deposited weld metal, and no HAZ or parent material was included, in order to ensure the the properties of the weld metal were being measured.

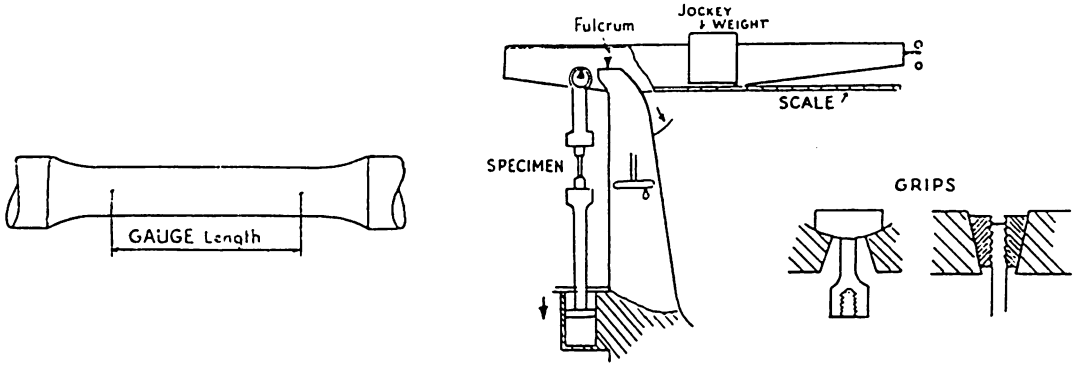

Figure 2.2: The standard proportions for a tensile test piece, and schematic of tensile testing machine [Rollason, 1961].

Two sizes of sample were used for the testing programme. Each was the largest available for the particular test weldment. Size TMP3 had a specimen diameter of 4 mm and a gauge length of 20 mm. The corresponding dimensions for size TMP4 were 5.65 mm and 28 mm.

The samples were inserted into a tensile testing machine (Figure 2.2), and subjected to a continuous strain of 0.015 min^{-1} until the proof load was reached, and then 0.15 min^{-1} until fracture occurred. Plots of load versus extension were recorded.

The 0.2 % proof stress was determined from the stress/strain plot as the stress at which the permanent extension of the sample was 0.2 % (Figure 2.3). The ultimate tensile strength was measured to be the maximum engineering stress experienced by the sample.

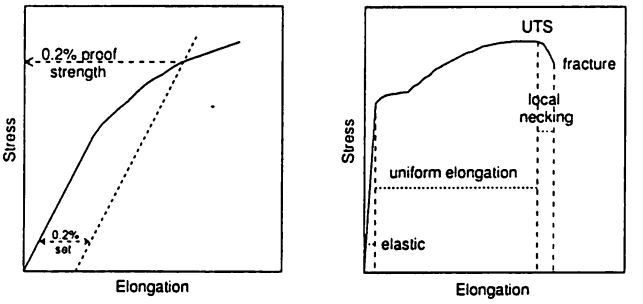

Figure 2.3: Measurement of the proof strength and UTS from the stress-strain curve.

The elongation was determined from the broken tensile specimen as the ratio of the extension to the original gauge length of the sample (Figure 2.4).

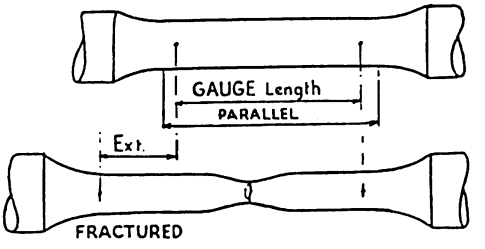

Figure 2.4: Measurement of the elongation from the broken tensile specimen [Rollason, 1961].

The reduction of area was also determined from the broken specimen, and was calculated as

$$\text{reduction of area} = \frac{\text{original area} - \text{final area}}{\text{original area.}}$$

2.8.2 Charpy "V" Notch Test

The Charpy "V" notch test is an empirical measure of the impact toughness of a material. 55 mm long samples of 10 mm × 10 mm cross sectional area were notched half way along their length

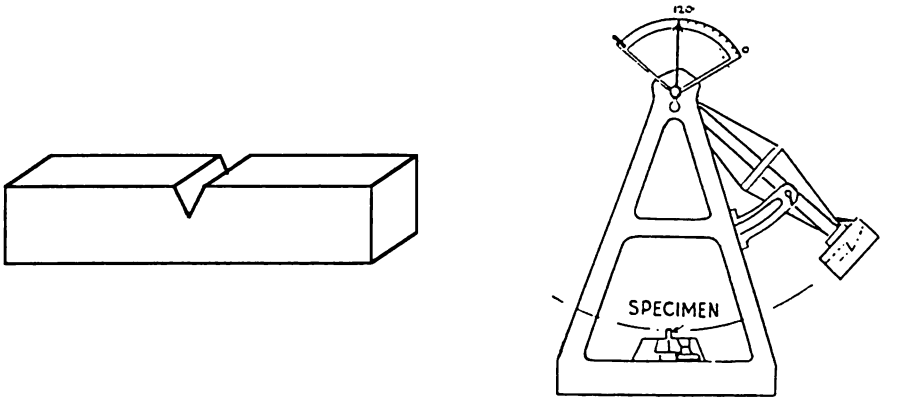

Figure 2.5: Charpy specimen and schematic impact testing machine [Rollason, 1961].

(Figure 2.5). Specimens were mounted on the testing machine, and then struck using a weighted pendulum. The energy required for the fracture of the specimen was recorded.

2.9 Chemical Analysis

Chemical analysis was carried out by International Research and Development Ltd. The following methods were employed.

2.9.1 Quantovac Analysis

Although not a non-destructive technique, only a small sample is required. The analysis removes only $\sim$ 1 mm depth of material on a 10 mm $\times$ 10 mm specimen. The material to be tested is placed near an anode, and a large positive potential ($\sim$3000 V) is applied across the small gap. This causes a spark and a small amount of the material is vapourised. The electrons of the atoms present are excited to higher shells, and as they fall to their equilibrium state light is emitted. This light is directed into a spectrometer with mirrors, and split into different wavelengths with a diffraction grating. The intensity of the different wavelengths reveals the quantity of each element. From the spectrometer the light is fed into a photomultiplier where light is converted to a voltage and then to a frequency. This frequency is used to identify the elements present.

2.9.2 LECO Analysis

LECO analysis similarly makes use of emission spectroscopy to determine the quantities of elements such as nitrogen and oxygen present in the sample [LECO Corporation, 1979]. Electrons of the elements are provided with enough energy to shift into a higher shell, and the energy of their return to their standard state is measured via light emission, enabling identification of the element and determination of the proportions present.

2.10 Thermodynamic Analysis

The computer based package used for thermodynamic predictions in the analysis was the National Physical Laboratory's MTDATA[2] [1996]. This package is used for the calculation of phase diagrams in multiphase and multicomponent systems. It can access several databases which use critically assessed

[2] Metallurgical and Thermochemical **DATA**bank

thermodynamic data. Many of these databases are provided by the "Scientific Group Thermodata Europe" (SGTE). The "solution" database was used for the purpose of this research.

An equilibrium phase diagram shows which single phase or mixture of phases is stable at each temperature for any given alloy composition. Such a diagram is generated from the free energy data at a variety of temperatures. The equilibrium phase(s) exist in order to minimise the free energy at the temperature considered. Materials do not always exist in their equilibrium state, for example martensite in steels, which is metastable [Porter and Easterling, 1993].

2.10.1 Elements

Studies using MTDATA were carried out using a selective dataset containing the elements and phases appropriate to the alloys studied. Overspecification of alloying elements is avoided, as the appropriate data may not be available in the database, forcing the program into making approximations. The composition of the alloy being studied is presented to the program as its weight fraction. All components in the dataset which are not present in the alloy chemistry are classified as absent. For the iron based alloys studied here, only the weight fraction of the alloying elements was required — the weight fraction of iron is automatically calculated to be the balance. The set of alloying elements used alongside iron for the database for this research are presented in Table 2.4.

ID	Element	ID	Element	ID	Element
1	Carbon	5	Molybdenum	9	Tungsten
2	Silicon	6	Chromium	10	Niobium
3	Manganese	7	Vanadium	11	Nitrogen
4	Nickel	8	Copper	12	Cobalt

Table 2.4: Alloying elements present in the MTDATA database used for this research.

2.10.2 Phases

The phases chosen for the dataset are selected from an available range in the solution database. Not all the phases allowed by the database were chosen. This was because MTDATA was designed for universal applications, and whereas $Cu_{87}Si_{13}$ may be a vitally important phase in some circumstances, it is extremely unlikely to occur at all in an alloyed steel. The set of phases included in the database for this research are presented in Table 2.5.

Once the dataset is established, it is possible to exclude selected phases from the analysis without the need to redefine the dataset. This may even mean "forcing" the alloy into a metastable state. Those phases required to be ignored for the purpose of the calculation are simply classified absent.

ID	Phase	ID	Phase	ID	Phase
1	Liquid	5	hcp* Iron	9	ksi-carbide
2	Ferrite (α and δ)	6	M_7C_3	10	M_3C_2
3	Cementite	7	$M_{23}C_6$	11	Sigma phase
4	Austenite	8	M_6C	12	Laves phase

Table 2.5: Alloying elements present in the MTDATA database used for this research.
* hexagonal close packed

CHAPTER THREE

Prediction of the Martensite-Start Temperature

3.1 Introduction

It is planned that future power stations will be designed to operate with steam temperatures in excess of 600 °C. The steels currently being developed to cope with these requirements contain a total solute concentration which is often in excess of 14 weight %. The main solutes include strong carbide forming elements such as chromium and molybdenum, with the chromium also providing the necessary corrosion and oxidation resistance for prolonged elevated temperature service. The key alloys under consideration include numerous variants of the classical "12Cr1Mo" and "9Cr1Mo" steels [Sikka *et al.*, 1983, Alberry and Gooch, 1985, Panton-Kent, 1989]. These alloys have a high hardenability and a microstructure which is predominantly martensitic on cooling from the austenitisation temperature. Their martensite-start temperatures are therefore of considerable importance in deciding on the exact welding conditions necessary to avoid cracking [Sikka *et al.*, 1983, Alberry and Gooch, 1985, Panton-Kent, 1989].

The consequences of the relationship of the interpass temperature of a weld to the martensite transformation temperatures has been discussed earlier (1.6.5), showing that an ideal weld will have an interpass temperature, T_I, such that $M_F < T_I < M_S$.

Martensite-start temperatures are usually relatively easy to calculate using empirical equations [Steven and Haynes, 1956, Payson and Savage, 1944, Carapella, 1944, Rowland and Lyle, 1945, Grange and Stewart, 1946, Nehrenberg, 1946, Andrews, 1965, Irvine, Pickering and Garstone, 1960] as long as the steels have a *low* alloy content. Even though empirical equations exist for high-alloy steels, they are not sufficiently general and are known to give inaccurate answers for the new power plant alloys, even when these alloys are fully austenitic (without δ-ferrite or undissolved carbides) [Bhadeshia and Middleton, 1982].

3.2 Empirical Models for M_S Prediction

The existing empirical equations for calculation of M_S are listed below. The terms in squared brackets provide a modification to incorporate cobalt data [Kung and Rayment, 1982]. Table 3.1 summarises the compositional limits over which these models have been tested.

Payson and Savage (1944)

$$M_S(°\mathrm{C}) = 499 - 308x_C - 32.4x_{Mn} - 27x_{Cr} - 16.2x_{Ni} - 10.8x_{Si} - 10.8x_{Mo} - 10.8x_W[+10x_{Co}] \tag{3.1}$$

Carapella (1944)

$$M_S(°\mathrm{C}) = 496(1 - 0.62x_C)(1 - 0.092x_{Mn})(1 - 0.033x_{Si})(1 - 0.045x_{Ni})(1 - 0.07x_{Cr})(1 - 0.029x_{Mo})(1 - 0.018x_w)[1 + 0.12x_{Co}] \tag{3.2}$$

Rowland and Lyle (1946)

$$M_S(°\mathrm{C}) = 499 - 324x_C - 32.4x_{Mn} - 27x_{Cr} - 16.2x_{Ni} - 10.8x_{Si} - 10.8x_{Mo} - 10.8x_W[+10x_{Co}] \tag{3.3}$$

Grange and Stewart (1946)

$$M_S(°C) = 538 - 350x_C - 37.7x_{Mn} - 37.7x_{Cr} - 18.9x_{Ni} - 27x_{Mo}[+10x_{Co}] \quad (3.4)$$

Nehrenberg (1946)

$$M_S(°C) = 499 - 292x_C - 32.4x_{Mn} - 22x_{Cr} - 16.2x_{Ni} - 10.8x_{Si} - 10.8x_{Mo}[+10x_{Co}] \quad (3.5)$$

Steven and Haynes (1956)

$$M_S(°C) = 561 - 474x_C - 33x_{Mn} - 17x_{Cr} - 17x_{Ni} - 21x_{Mo}[+10x_{Co} - 7.5x_{Si}] \quad (3.6)$$

Andrews (1965) sum

$$M_S(°C) = 539 - 423x_C - 30.4x_{Mn} - 12.1x_{Cr} - 17.7x_{Ni} - 7.5x_{Mo}[+10x_{Co} - 7.5x_{Si}] \quad (3.7)$$

Andrews (1965) product

$$M_S(°C) = 512 - 453x_C - 16.9x_{Ni} - 9.5x_{Mo} - 217x_C^2 - 71.5x_C x_{Mn} + 15xCr - 67.5x_C x_{Cr}[+10x_{Co} - 7.5x_{Si}] \quad (3.8)$$

	P & S, C	R & L	G & S	N	S & H	A	I
C	0.44–0.55	0.35–1.03	0.29–1.02	0.17–1.28	0.09–0.55	0.06 max	0.09-0.55
Mn	0.30–4.87	0.31–0.50	0.29–1.85	0.18–1.85	0.20–1.54	–	0.20–1.54
Cr	0.00–4.61	0.22–1.48	0.40–1.41	0.05–8.81	0.08–3.34	5.0 max	0.08–12*
Ni	0.00–4.83	0.27–1.76	0.20–3.41	0.20–3.41	0.15–4.95	5.0 max	0.15–4.95
Mo	0.00–5.40	0.00–0.24	0.11–0.33	0.01–0.33	0.00–0.65	5.4 max	0.00–0.65
Si	0.26–1.06	0.21–0.30	0.15–0.70	0.15–1.89	0.11–1.74	–	0.11–1.74
W	0.00–4.78	–	–	–	–	4.1 max	–
V	–	–	0.16 max	0.16 max	0.20 max	–	0.20 max

Table 3.1: Compositional limits for the models used to calculate M_S. * No 12Cr steels were used in the development of the model, but the equation was found to provide acceptable results for such steels.

An alternative approach is to use thermodynamic theory [Kaufmann and Cohen, 1958, Bhadeshia, 1981(a),(b)], which has the advantage that any solute combination can be considered as long as thermodynamic data are available. In the thermodynamic approach, martensite is said to be triggered

Irvine, Crowe and Pickering (1960)

$$M_S(°C) = 300 - 474x_C - 33x_{Mn} - 17x_{Ni} - 17x_{Cr} - 21x_{Mo} - 11x_W - 11x_{Si} \quad (3.8)a$$

when the chemical driving force for composition-invariant transformation of austenite to martensite of the same composition achieves some critical value at the M_S temperature:

$$\Delta G^{\gamma\alpha'}\{M_S\} = \Delta G_C^{\gamma\alpha'} \tag{3.9}$$

where $\Delta G^{\gamma\alpha'}\{T\}$ is the free energy change accompanying the transformation of austenite to martensite of the same composition at a temperature T. This differs from the corresponding term $\Delta G^{\gamma\alpha}$ for the transformation of austenite to ferrite of the same composition because the latter does not allow for the Zener ordering of the carbon atoms [Zener, 1946, Fisher, 1949]. $\Delta G_C^{\gamma\alpha'}$ is the critical value of the driving force needed to trigger martensitic transformation. The method is illustrated in Figure 3.1. This method has been used successfully for low-alloy steels where it has been possible to rationalise experimental data by allowing $\Delta G_C^{\gamma\alpha'}$ to assume either a constant value of about -1100 J mol^{-1} or by allowing it to vary slightly with the carbon concentration, the exact variation defined empirically [Bhadeshia, 1981(a),(b)].

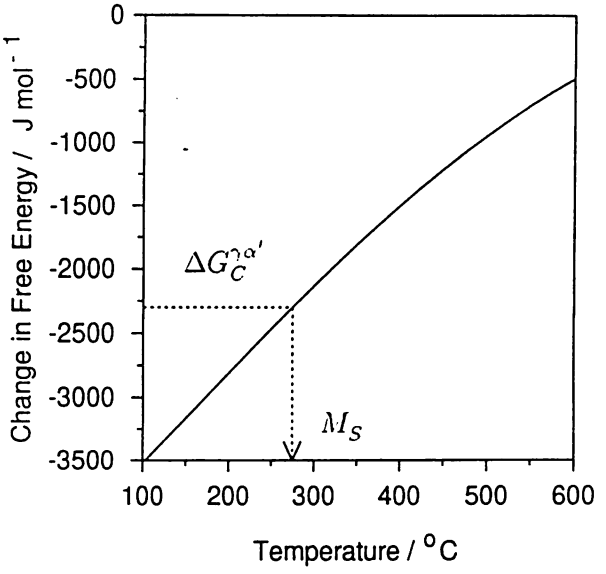

Figure 3.1: An illustration of how the martensite-start temperature may be calculated as the point where the chemical driving force for the transformation of austenite without a composition change achieves a critical value.

Neither of these methods work well when applied to high alloy steels. The purpose of this work was to see whether a new model developed by Ghosh and Olson [1993, 1994], which takes into consideration the strengthening of austenite caused by solute additions, can be applied to the calculation of the M_S temperatures of highly alloyed power plant steels. The model is tested against published data as well as new experimental measurements.

3.3 The Ghosh & Olson Model

Olson and Cohens' model [1976] for the nucleation of martensite relies on barrierless nucleation, in which there are no heterophase fluctuations as in conventional nucleation theory, but the nucleation

event is defined by the faulting caused by the dissociation of a pre-existing array of dislocations. Consequently, the activation energy for nucleation is that associated with the motion of the partial dislocations. The dislocations migrate against a frictional stress τ_O which consists of the sum of a thermal (τ_{th}) and athermal (τ_μ) term. The dislocations must therefore experience a force per unit length which is given by:

$$(\tau_\mu + \tau_{th})bn \tag{3.10}$$

before they can migrate. In this expression, b is the magnitude of the Burgers vector and n is the number of planes over which the faulting occurs (*i.e.* the number of dislocations in the array). This is the force which opposes the motion of the array. However, when transformation is favoured, the faults created by the dissociation are energetically favoured — *i.e.* the fault energy per unit area (γ_f) becomes negative. This gives a total change in energy due to faulting as:

$$\gamma_f = n\rho_A(\Delta G^{\gamma\alpha'} + G_S) + 2\sigma \tag{3.11}$$

where ρ_A is the density of atoms in the fault plane, G_S is the strain caused by the embryo and σ is the interface energy per unit area of embryo; the energies, G, are expressed here in Joules per unit volume.

The embryo becomes unstable (*i.e.* becomes a nucleus) when the force on the dislocations due to the negative fault energy overcomes the frictional force:

$$-\gamma_f = (\tau_\mu + \tau_{th})bn \tag{3.12}$$

It follows from the previous equations that

$$n\rho_A(\Delta G^{\gamma\alpha'} + G_S) + 2\sigma = -(\tau_\mu + \tau_{th})bn \tag{3.13}$$

If we now set $\Delta G^{\gamma\alpha'} = \Delta G_C^{\gamma\alpha'}$ and assume that the τ_{th} can be neglected due to the high temperatures involved, then

$$\Delta G_C^{\gamma\alpha'} = -\rho_A^{-1}(b\tau_\mu - 2\sigma) - G_S \tag{3.14}$$

which has the form

$$\Delta G_C^{\gamma\alpha'} = K_1 + K_\mu\phi\{c\} \tag{3.15}$$

where K_1 includes the combined effects of the interfacial and strain energy terms, and K_μ is a coefficient, which when multiplied by the function ϕ of composition c incorporates the effect of solid solution strengthening by alloying additions on τ_μ.

This is an important equation because it explicitly defines the critical driving force $\Delta G_C^{\gamma\alpha'}$ in terms of solute concentration. Ghosh and Olson used solid solution theory to obtain the form of the relationship, and experimental data to obtain the coefficients K_μ:

$$\begin{aligned} -\Delta G_C^{\gamma\alpha'} =& K_1 + 4009c_C^{0.5} + 1879c_{Si}^{0.5} + 1980c_{Mn}^{0.5} \\ &+ 172c_{Ni}^{0.5} + 1418c_{Mo}^{0.5} + 1868c_{Cr}^{0.5} + 1618c_V^{0.5} \\ &+ 752c_{Cu}^{0.5} + 714c_W^{0.5} + 1653c_{Nb}^{0.5} + 3097c_N^{0.5} - 352c_{Co}^{0.5} \end{aligned} \tag{3.16}$$

The coefficients were obtained by establishing the $c^{\frac{1}{2}}$ dependence and fitting over a wide range of compositions: the maximum concentrations were approximately 2 weight % for carbon and nitrogen, 0.9 weight % of vanadium and up to 20 weight % for all the other alloying elements [Ghosh and Olson, 1993, 1994, private communication to H. K. D. H. Bhadeshia]. Ghosh and Olson quoted a value of K_1 = 1010 J mol^{-1}. It was intended in the present work to use this equation to attempt to predict the martensite-start temperatures of power plant alloys.

3.4 Calculation of the Free Energy Change

The free energy change $\Delta G^{\gamma\alpha}$ for the transformation of austenite to ferrite of the same composition can be estimated as a function of temperature using MTDATA [1996].

However, to calculate $\Delta G^{\gamma\alpha'}$ also requires an estimation of the Zener ordering energy, which arises because carbon atoms in ferrite can in some circumstances order on one of the three available sub-lattices of octahedral interstitial sites, thereby changing the symmetry of the lattice from body-centred cubic to body-centred tetragonal.

The ordering temperature T_C is a function of the carbon concentration [Fisher, 1949]:

$$T_C\{\mathrm{K}\} = \frac{T(1-x)}{28080x} \tag{3.17}$$

where x is the mole fraction of carbon. If the M_S temperature exceeds T_C then the martensite is body-centred cubic, but when it is below T_C, the ordering energy G_{Zener} is a complicated function of temperature and carbon concentration, and was calculated as in Fisher [1949].

The required free energy is then given by:

$$\Delta G^{\gamma\alpha'} = \Delta G^{\gamma\alpha} + G_{Zener} \tag{3.18}$$

3.5 Experimental Technique

The martensite-start temperature of each of the seven Parsons wrought alloys (Chapter 2, Table 2.1) and the thirteen Oerlikon weld deposits (Chapter 2, Table 2.2) was obtained by heating the sample to 1100 °C for 600 s in the thermomechanical simulator, followed by quenching at about 50 °C s^{-1} using helium gas. On plotting the strain versus temperature, the M_S temperature could easily be found at the point where the curve deviated from the straight line corresponding to the thermal contraction of austenite. This is illustrated for a typical case in Figure 3.2.

It was verified, using MTDATA, that the austenitisation temperature of 1100 °C is sufficiently high for all carbides to be dissolved. These calculations were carried out allowing the austenite, ferrite, cementite, M_2C, $M_{23}C_6$, M_6C, M_7C_3, M_3C_2, sigma and Laves phases to exist.

3.6 Comparison Between Calculated and Measured M_S

3.6.1 Published Data

An initial comparison was made of the calculated M_S temperatures against the vast range of low-alloy steels studied by Steven and Haynes [1956] and some other higher alloy samples (12CrMoV and

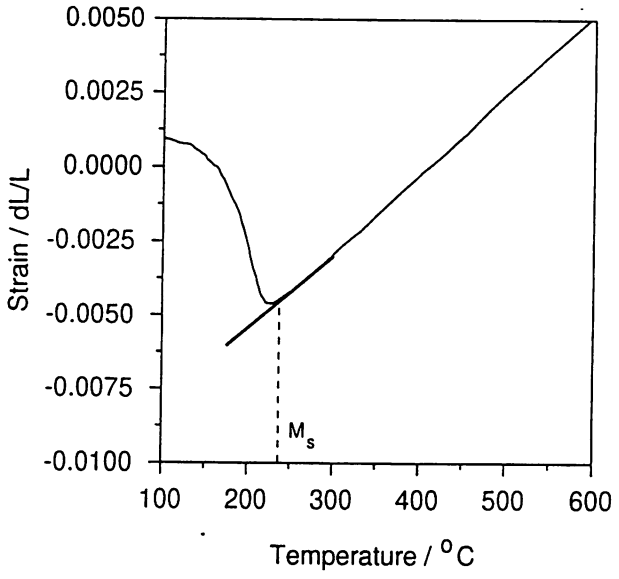

Figure 3.2: An illustration of how the martensite-start temperature is determined from the recorded strain versus temperature curve obtained using a thermomechanical simulator.

9Cr1Mo) investigated by Bhadeshia and Middleton [1982]. Figure 3.3 shows the results; the theory tended to systematically underestimate the transformation temperature, indicating that the value of K_1 was probably too large.

K_1 was therefore varied, and a value of 683 J mol^{-1} was found to give optimum agreement, as indicated in Figure 3.3. The accuracy for the lowest of M_S temperatures is relatively poor, but this cannot be attributed to Eq. 3.16 since the concentration range covered by the relation is greater than utilised in the present work. This modified value was used in all subsequent calculations.

3.6.2 New Experimental Data

Figure 3.4 shows a comparison of calculated M_S temperatures of the alloys listed in Chapter 2, Tables 2.1 and 2.2, versus their measured transformation temperatures. There is in general good agreement, but the observed scatter is larger than in Figure 1.4. The reasons for this are not clear, but there are some special difficulties the tungsten-containing samples.

The tungsten-containing 9Cr alloys are presented in more detail in Figure 3.5; it appears that large concentrations of tungsten lead to poor predictability.

Further investigation revealed that the 3 weight % W alloy does not become fully austenitic at 1100 °C (or at higher austenitisation temperatures); metallography revealed the presence of δ-ferrite (Figure 3.6), consistent with the fact that the hardness of the 3 weight % W alloy was also much lower than that of the other W-containing alloys (340 compared with 400 HV). It is therefore not surprising that the calculated martensite-start temperature does not agree with that measured. In fact, thermodynamic calculations [MTDATA, 1996] revealed that at equilibrium, all of the alloys containing 1 weight % or more of tungsten should contain some ferrite at 1100 °C. The data from all such alloys have been identified in Figure 3.4, and might explain the additional scatter apparent in Figure 3.4 when compared with Figure 3.3.

The Ghosh and Olson method was always intended to apply to fully austenitic alloys, and relies

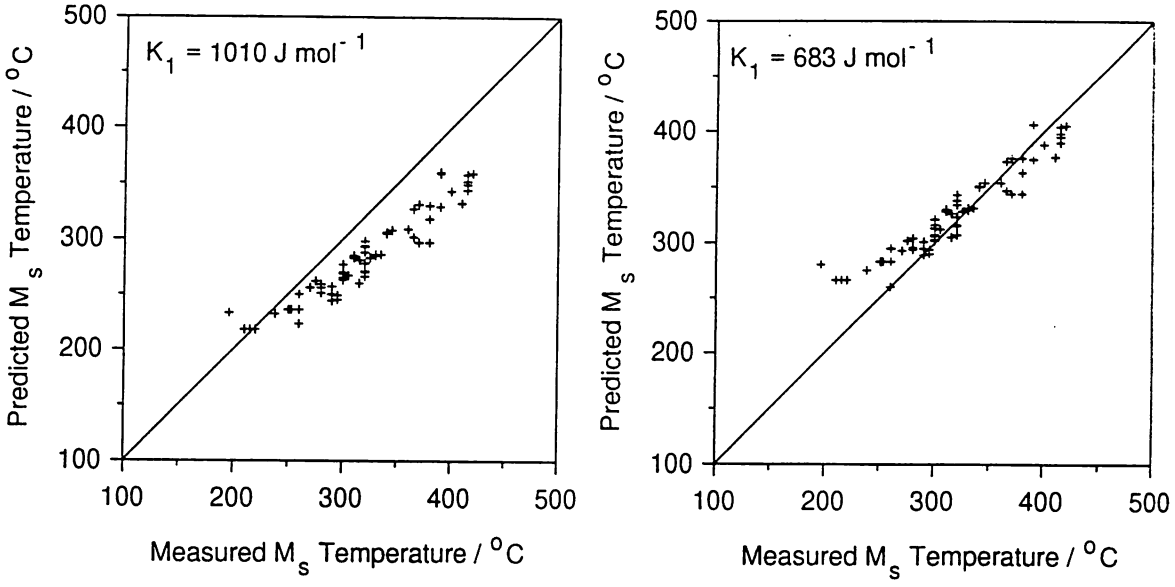

Figure 3.3: Comparison of calculated M_S temperatures versus those measured (published data). The line has a unit slope and zero intercept, so that any point on the line indicates perfect agreement between experiment and theory. The analysis uses the equation due to Ghosh and Olson for $\Delta G_C^{\gamma\alpha'}$, with $K_1 = 1010$ J mol^{-1} and with a modified value of K_1 = 683 J mol^{-1}.

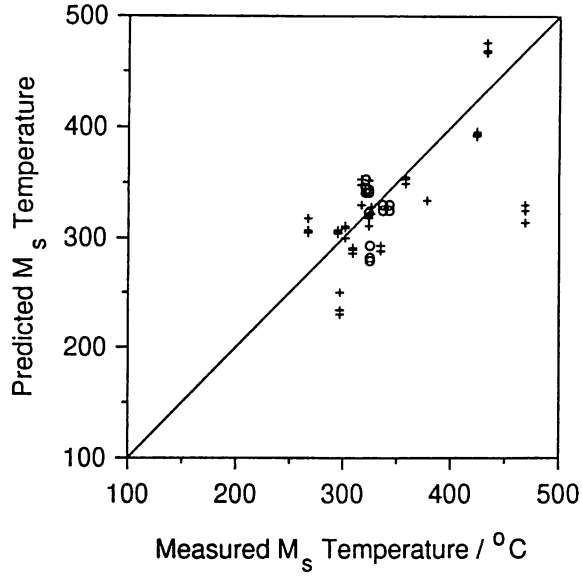

Figure 3.4: Comparison of calculated M_S temperatures versus those measured for the experimental alloys listed in Table 1. The circles identify alloys which are likely to contain δ-ferrite after heat treatment at 1100 °C. The line has a unit slope and zero intercept, so that any point on the line indicates perfect agreement between experiment and theory. The analysis uses the equation due to Ghosh and Olson for $\Delta G_C^{\gamma\alpha'}$, with K_1 = 683 J mol^{-1}.

on the availability of accurate thermodynamic data. Care must therefore be exercised in the application of the method to power plant steels in particular.

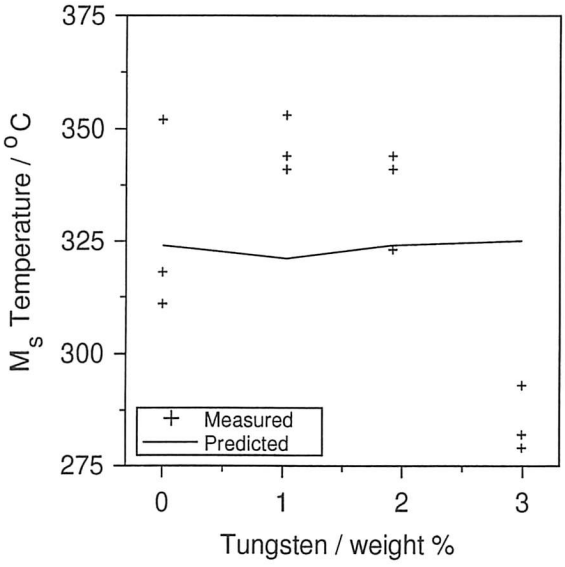

Figure 3.5: Comparison of calculated M_S temperatures versus those measured for the tungsten-containing experimental alloys listed in Table 2.2b

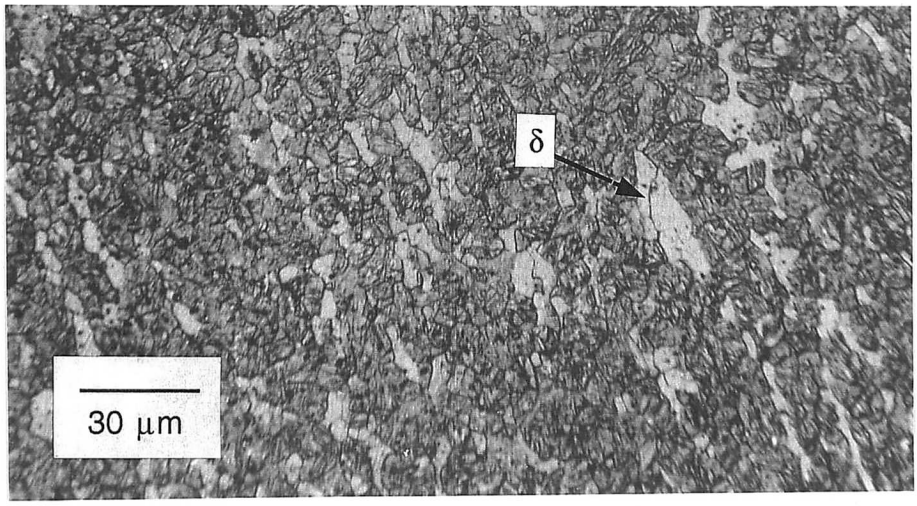

Figure 3.6: Scanning electron micrograph showing the presence of δ-ferrite in the 3 weight % tungsten-containing alloy (Table 2.2b) after quenching from 1100 °C.

3.7 Conclusions

In the Ghosh and Olson method for the calculation of the martensite-start temperature, the critical value of the driving force needed to trigger martensitic transformation is a function of the solid-solution hardening ability of alloying elements. It has been demonstrated here that the method can be used reliably to predict the martensite-start temperatures of a wide range of power plant steels, including those which are rich in alloying elements. Consequently, it is now possible to estimate the M_S temperature for the whole range of power plant steels to an accuracy of ± 20 °C as a function of alloy chemistry. This method can therefore be used in the design of welding procedures for these steels.

CHAPTER FOUR

Austenite Formation in 9Cr1Mo Type Power Plant Steels

4.1 Introduction

Further studies were carried out on the thirteen 9Cr1Mo type manual metal arc weld deposits introduced in Chapter 2 and studied in the previous chapter. The alloy series was designed particularly to show the effects of nickel, cobalt and tungsten. Evans [1994a] conducted a systematic set of experiments in which the series of weld deposits were studied to reveal their mechanical properties after post weld heat treatment of 750 °C for 8 hours. He reported some strange variations; for example, increasing the tungsten or cobalt concentrations led to a large reductions in strength, whereas an increase in the nickel concentration led to a corresponding large increase in the strength.

It was suspected that the observed changes in strength might be due to the effect of alloying elements on the stability of austenite. This chapter deals with an experimental and theoretical investigation of austenite formation in the 9Cr1Mo type alloys with a view to explaining the anomalous variations in strength following post weld heat treatment. The work is of importance in placing limits on the extent to which 9Cr1Mo steels can be alloyed with elements other than chromium or molybdenum.

4.2 Experimental Technique

The chemical compositions of the alloys studied by Evans and the commercial wrought alloy NF616 are given in Chapter 2, Table 2.2. This latter alloy is of particular interest because of its exceptionally low silicon concentration. Some of the relevant mechanical properties of the welds, as reported by Evans [1994a] are presented in Figure 4.1.

The same samples as were prepared for the martensite experiments were used to analyse the austenite transformation characteristics in thermomechanical simulation experiments. Transformation experiments were performed using the *Thermecmastor-Z* thermomechanical simulator. The transformation temperatures were obtained by heating the sample to 1100 °C at three different heating rates, 5, 10 and 20 ° s^{-1}. On plotting the recorded strain versus temperature, the Ac_1 temperature could easily be found at the first point where deviation from the straight line was observed, corresponding to a contraction on transformation from body centred cubic ferrite to the more closely packed face centred cubic austenite structure. The Ac_3 temperature can similarly be measured at the point where the austenite expansion begins to be linear. This is illustrated for a typical case in Figure 4.2.

4.3 Results and Discussion

The measurements using dilatometry are presented in Figure 4.3; these were used to estimate the Ac_1 and Ac_3 temperatures listed in Table 4.1.

As expected for any thermally activated transformation, an increase in the heating rate leads to a corresponding increase in the transformation temperatures — Ac_1 and Ac_3 (Table 4.1). An infinitely slow heating rate would provide the lower limits corresponding to the equilibrium transformation temperatures; Ae_1 and Ae_3.

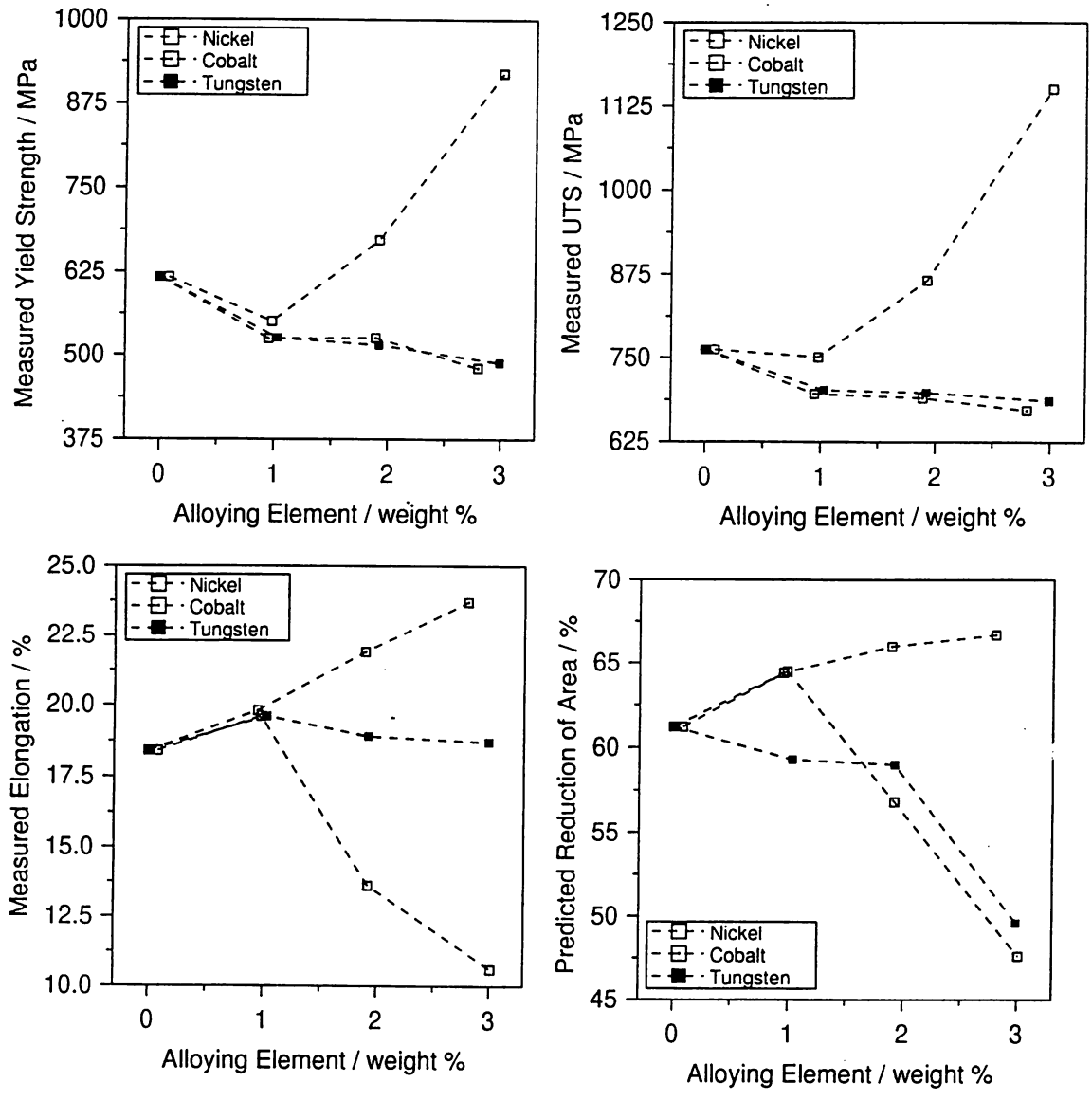

Figure 4.1: The reported [Evans, 1994a] mechanical properties of 9Cr1Mo type welds which have been post weld heat treated at 750 °C for 8 hours. The chemical compositions are given in Table 4.0. (a) yield strength; (b) ultimate tensile strength; (c) elongation, and (d) reduction of area.

4.4 Effect of Nickel

The data for the slowest heating rate of 5 °C s^{-1}, for all the alloys, are illustrated in Figure 4.4. As might be expected, an increase in the nickel concentration leads to a reduction in both the Ac_1 and Ac_3 temperatures, since nickel is an austenite stabilising element [Honeycombe and Bhadeshia, 1995].

Evans found a dramatic increase of both yield strength and ultimate tensile strength, accompanied by a reduction in elongation and reduction of area, for alloys with nickel in excess of 1 weight % (Figure 4.1). These results can be explained if austenite forms during the post weld heat treatment (PWHT). The austenite would then decompose to untempered martensite on cooling from the PWHT temperature, thereby leading to an increase in strength, in stark contrast to the intended effect of PWHT,

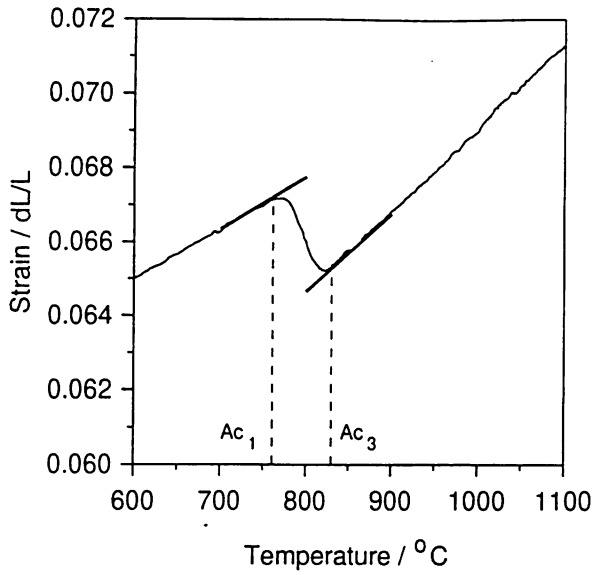

Figure 4.2: An illustration of how the austenite transformation temperatures on heating are determined from the recorded strain versus temperature curve obtained using a thermo-mechanical simulator.

which is to soften the microstructure. This hypothesis is consistent with Figure 4.4, where the Ac_1 temperature is low when compared with the PWHT temperature (the Ae_1 temperature is expected to be even lower).

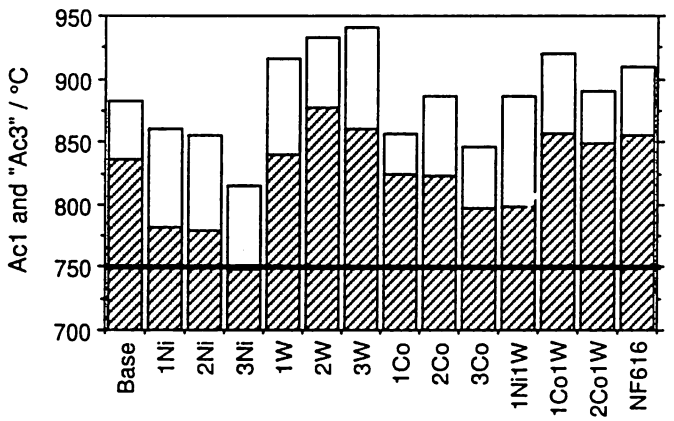

Figure 4.4: The Ac_1 and "Ac_3" temperatures measured at a heating rate of 5 °C s^{-1}. It will be seen later that the measured "Ac_3" temperature does not necessarily correspond to 100 % austenite, but the temperature at which austenite formation stops. The horizontal line indicates the post weld heat treatment temperature of 750 °C.

Additional experiments were carried out to confirm the hypothesis. The nickel series of samples (Base, 1Ni, 2Ni and 3Ni) were austenitised at 1000 °C for 10 minutes and then quenched in water, followed by tempering at 700 °C and 750 °C for 8 hours and a further water quench. The hardness of these samples was measured with a Vickers hardness testing machine using a 20 kg load (Figure 4.5).

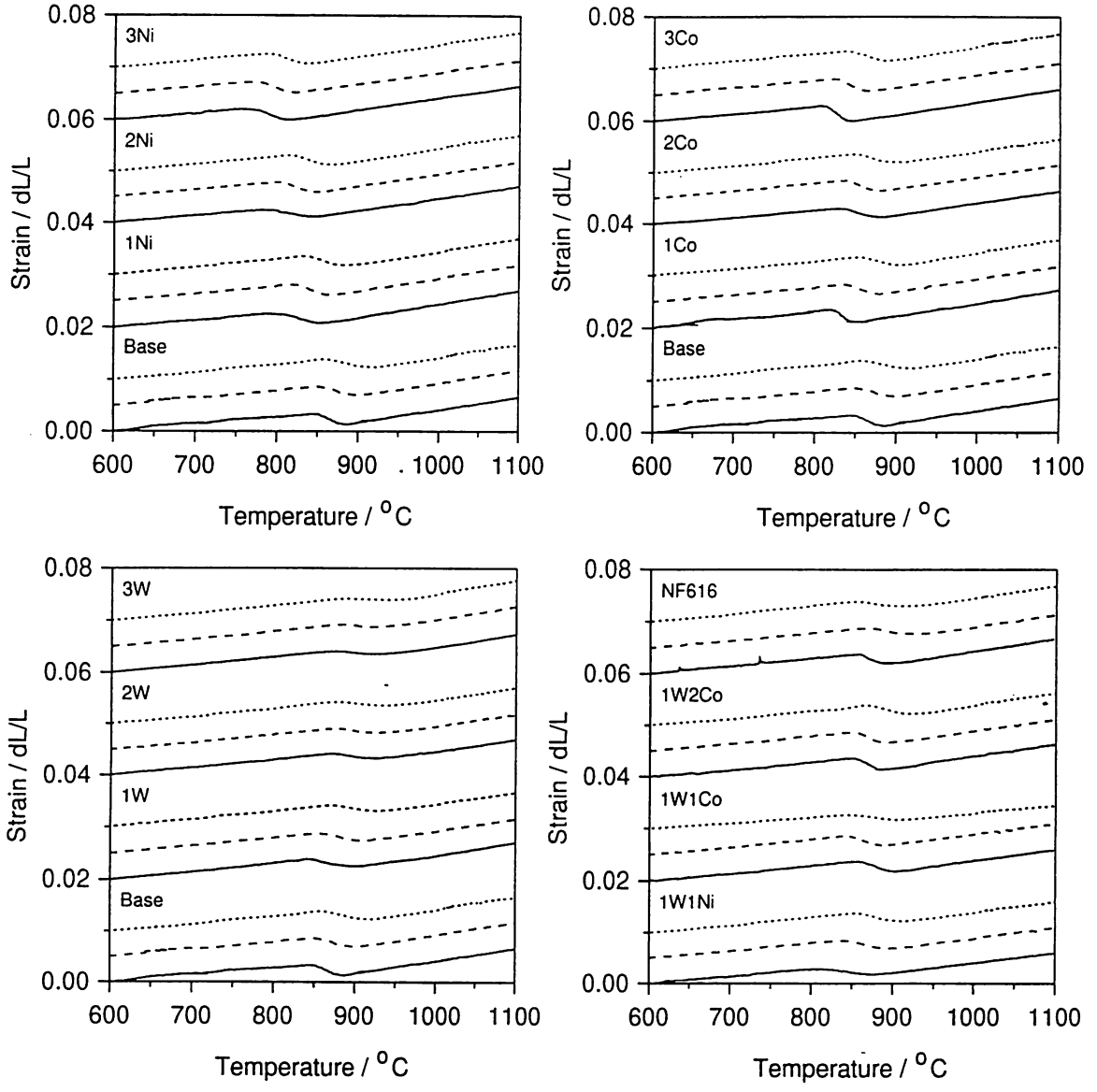

Figure 4.3: Measured dilatometry curves for the ferrite → austenite transformation of the 9Cr1Mo alloys with (a) nickel additions, (b) cobalt additions, and (c) tungsten additions (d) welds with mixed alloying, and wrought NF616. The different heating rates are represented as follows; 5 °C s^{-1} solid line, 10 °C s^{-1} dashed line and 5 °C s^{-1} dotted line.

As might be expected for the base alloy without nickel, the hardness of the sample tempered at the lower temperature of 700 °C is higher, but exactly the opposite is true for all the samples containing nickel. This is because more austenite forms at 750 °C than at 700 °C.

4.5 Effect of Tungsten

Unlike nickel, Evans found that the addition of tungsten actually leads to a decrease in the strength (Figure 4.1). As can be seen from Figure 4.4, tungsten in all cases leads to an increase in the Ac_1 and "Ac_3" temperatures when compared with the base material. There is, therefore, no danger of austenite

Sample	Ac_1			Ac_3		
	5 °C s^{-1}	10 °C s^{-1}	20 °C s^{-1}	5 °C s^{-1}	10 °C s^{-1}	20 °C s^{-1}
Base	836	849	857	882	907	924
1Ni	782	807	840	860	861	899
2Ni	779	790	823	855	849	887
3Ni	748	761	782	815	840	849
1Co	824	836	849	857	891	916
2Co	823	840	849	887	891	912
3Co	797	820	834	847	875	898
1W	840	857	866	916	924	950
2W	878	857	870	933	958	971
3W	861	874	784	941	933	966
1Ni1W	798	728	858	887	908	924
1Co1W	857	840	845	920	983	924
2Co1W	849	853	866	891	908	950
NF616	855	861	843	910	939	935

Table 4.1: Measured austenite transformation temperatures of the 9Cr1Mo samples.

formation during PWHT. A closer examination of the dilatometric curves (Figure 4.3) reveals some interesting data about the maximum contraction associated with the transformation during heating at 5 °C s^{-1} from room temperature. The strains are measured by taking the difference between the very high and very low temperature segments of the dilatometric curves extrapolated to 1000 °C. The maximum contraction should be an indication of the maximum amount of austenite that forms. Tungsten increases the lattice parameter of ferrite [Arnfelt, 1928]; it also has a lower solubility in austenite than in ferrite, consistent with its ferrite stabilising effect. Consequently, the addition of a small amount of tungsten leads to an increase in the contraction associated with a specified amount of austenite, as observed in Figure 4.6. However, further increases in tungsten lead to a decrease in the maximum observed contraction; this can be explained if the high tungsten alloys never transform completely to austenite. This would also explain the decrease in strength as the tungsten concentration increases, because the alloys can then never be fully martensitic (they will always contain δ-ferrite).

The presence of δ-ferrite in the high tungsten alloys was confirmed metallographically, as has been shown in Chapter 3, Figure 3.6. The δ-ferrite undermines the strength of the alloy by reducing the amount of martensite; this effect is greater than any solid solution strengthening associated with increasing tungsten.

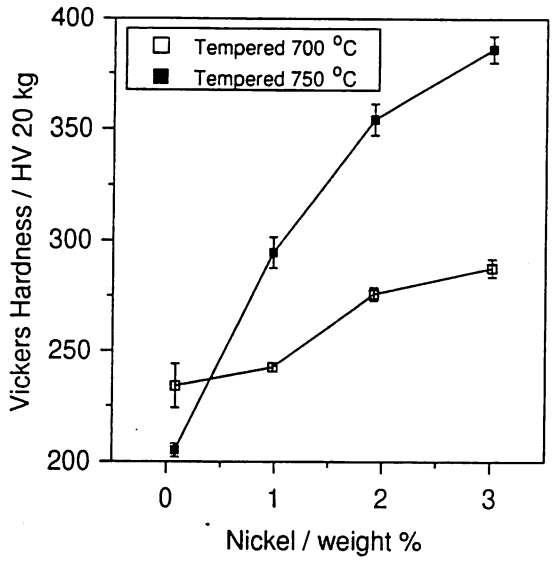

Figure 4.5: The hardness of samples which were austenitised at 1000 °C, water quenched and then tempered at the indicated temperature for 8 hours before finally quenching into water.

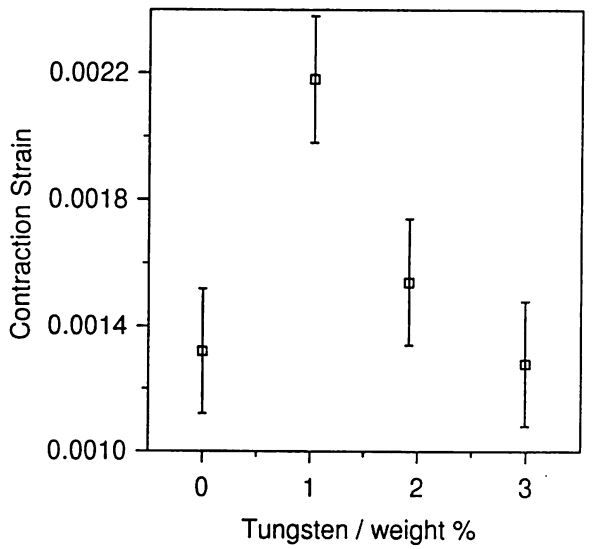

Figure 4.6: Contraction associated with the formation of austenite during heating at 5 °C s^{-1}. The strains are measured by taking the difference between the very high and very low temperature segments of the dilatometric curves extrapolated to 1000 °C.

4.6 Effect of Cobalt

The reason for adding cobalt in the original set of alloys studied by Evans was that it might lead to a reduction in the δ-ferrite content. The maximum contraction strains (measured as described for the tungsten alloys) observed during dilatometric experiments are illustrated in Figure 4.7. The extent of contraction increases with the cobalt concentration.

These results are, however, difficult to interpret. Cobalt causes a decrease in the lattice parameter of austenite [Dyson and Holmes, 1970]; clear data are not available for ferrite but the indications are that cobalt reduces the lattice parameter of ferrite and increases its expansion coefficient [Yokoyama, 1959]. It is possible, therefore, that unlike tungsten, the contraction associated with the ferrite to austenite transformation should increase with the cobalt concentration. This could hide any incomplete transformation to austenite as the cobalt concentration is increased.

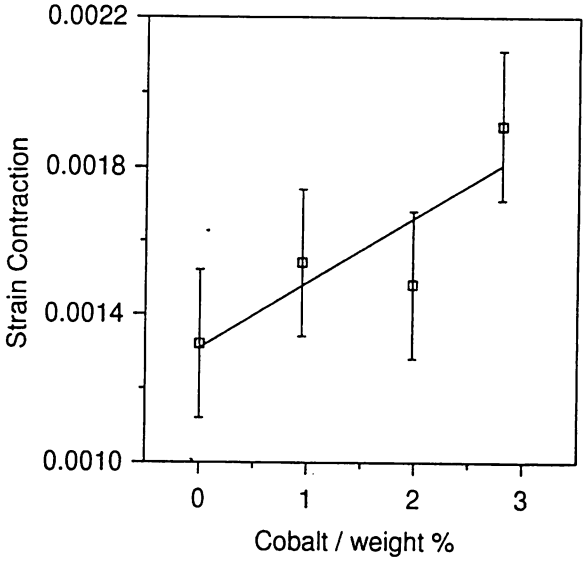

Figure 4.7: Contraction associated with the formation of austenite during heating at 5 °C s^{-1}. The strains are measured by taking the difference between the very high and very low temperature segments of the dilatometric curves extrapolated to 1000 °C.

The mechanical property data (Figure 4.1) are similar for cobalt and for tungsten, in that both lead to a decrease in the strength. Metallographic examination (Figure 4.8) revealed the presence of δ-ferrite in the high cobalt samples, both for the PWHT welds and for the samples which were austenitised at 1100 °C for ten minutes and then helium quenched to room temperature. This would explain the decrease in strength as cobalt is increased given that the fraction of martensite in the microstructure would be reduced.

4.7 Consistency with Phase Diagrams

The interpretations discussed above were examined using phase diagram calculations conducted with MTDATA [1996].

The occurrence of δ-ferrite in the microstructure was examined by calculating the equilibrium fractions of austenite and ferrite in the microstructure at elevated temperatures (Figure 4.9). As discussed previously, the method predicts that the high-tungsten alloys never become fully austenitic.

However, the cobalt alloys are predicted to be fully austenitic but not found to be so in practice. It will be necessary to investigate this further; either the thermodynamic data on which the calculations are based are flawed or the experimental observations represent non-equilibrium effects.

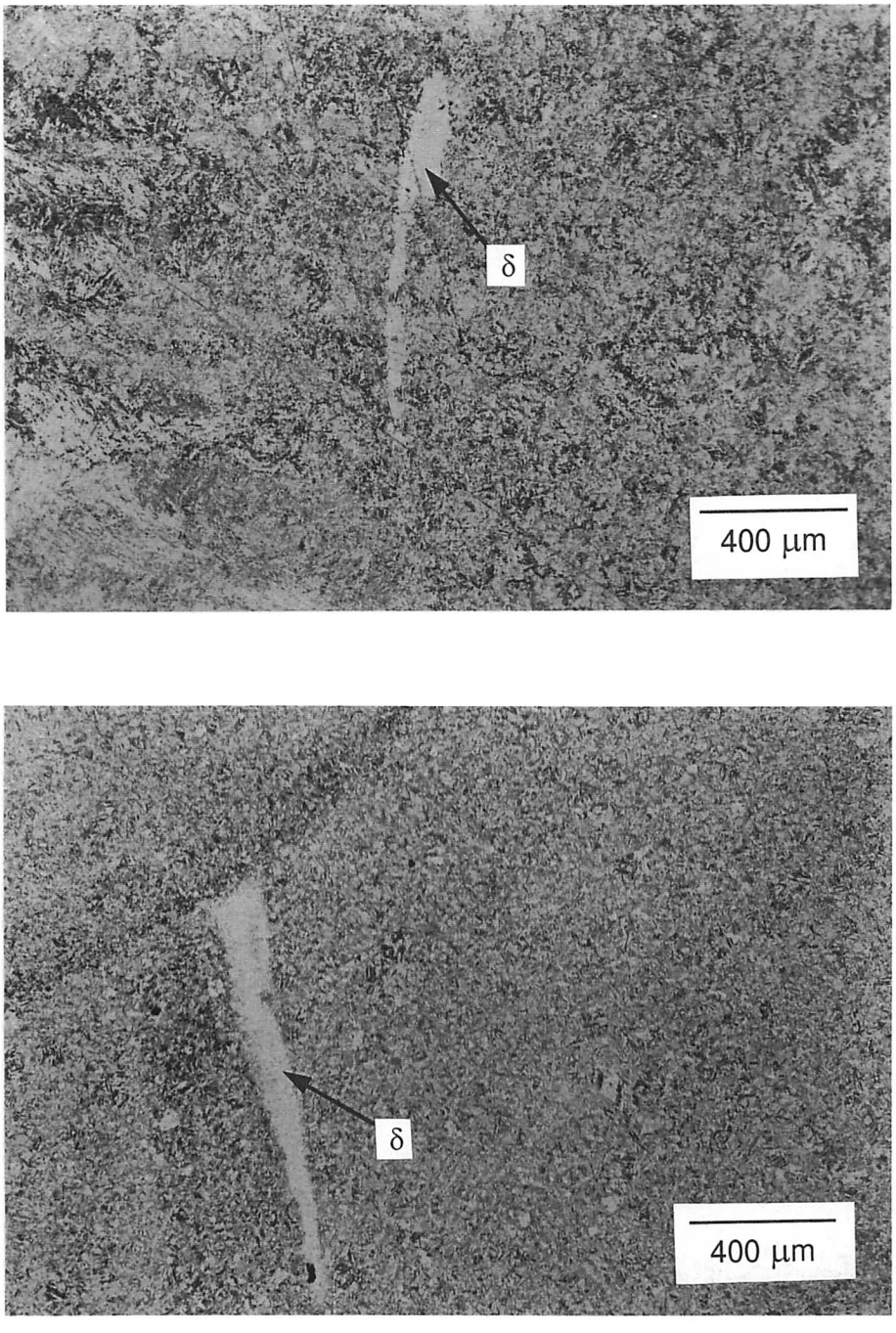

Figure 4.8: Optical micrographs for the 3Co samples. (a) The post weld heat treated weld. (b) The weld metal sample which was reheated to 1100 °C for ten minutes and helium quenched.

The wrought steel NF616 is well known in industry to be free from δ-ferrite; this is confirmed by the MTDATA [1996] analysis (Figure 4.9). It was therefore surprising when δ-ferrite was found in the 2W weld which has a very similar chemical composition to NF616. However, NF616 has an exceptionally low silicon concentration. Figure 4.10 shows that it is this low silicon concentration

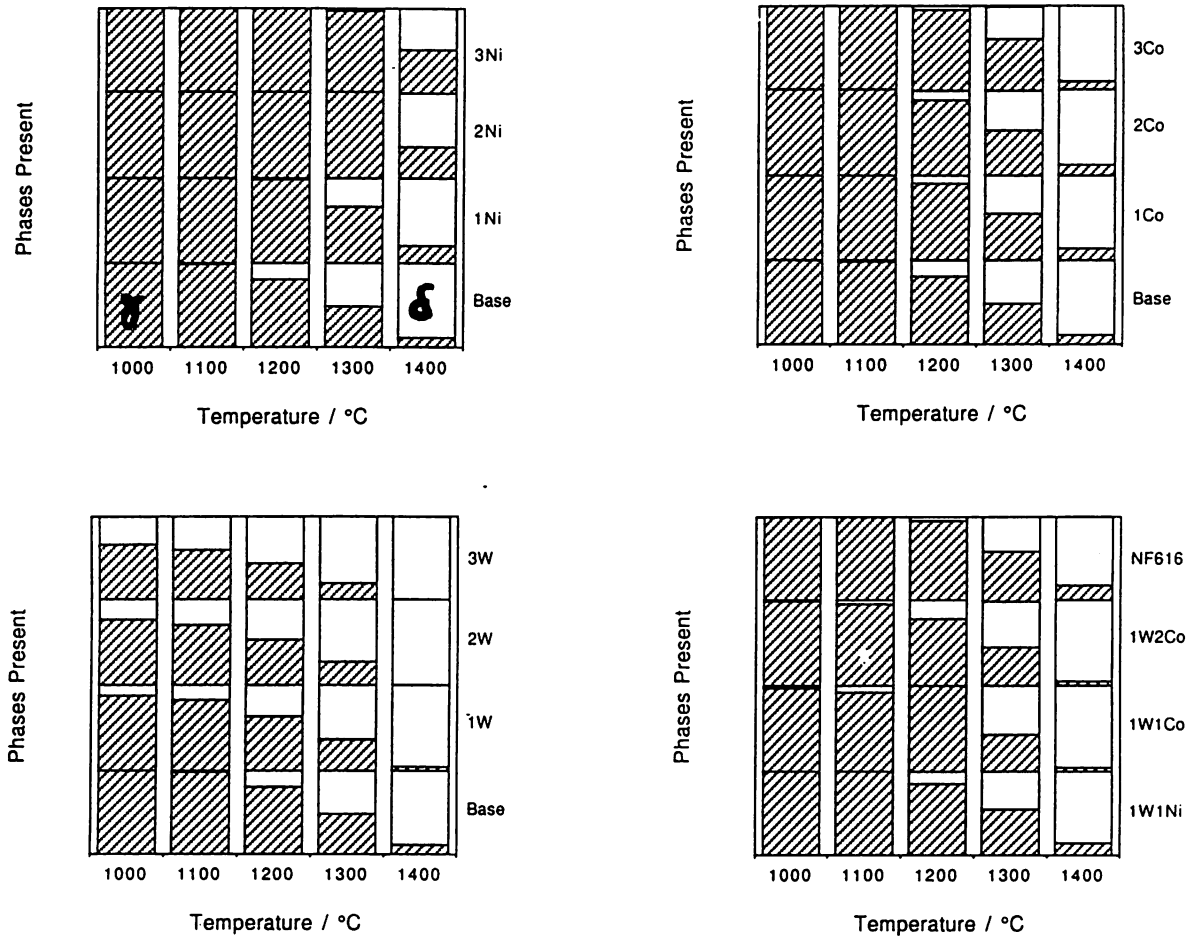

Figure 4.9: The MTDATA predicted phases for the 14 steels at different temperatures. The striped regions represent austenite, and the plain regions represent ferrite. (a) Nickel series (b) Cobalt series (c) Tungsten series. and (d) Mixed alloying weld deposits and NF616.

(0.02 weight %) which distinguishes NF616 from the 2W weld; a concentration comparable to the 2W weld (0.2 weight %) would lead to the retention of a considerable quantity of δ-ferrite in the NF616 microstructure. From the point of view of the weld, the manufacturers have stated that it does not seem possible to reduce the silicon concentration reliably to the concentration needed to avoid δ-ferrite.

Finally, the opportunity is taken here to examine whether the empirical equation proposed by Patriarca [1976], for the estimation of the δ-ferrite content is consistent with the thermodynamic calculations which are based on a vast quantity of reliable, assessed data. It is proposed [Patriarca, 1976] that the δ-ferrite correlates with a chromium-equivalent defined as follows:

$$\begin{aligned} Cr_{eq} = x_{Cr} + 6x_{Si} + 4x_{Mo} + 1.5x_{W} + 11x_{V} + 5x_{Nb} + 12x_{Al} \\ +8x_{Ti} - 40x_{C} - 2x_{Mn} - 4x_{Ni} - 2x_{Co} - 30x_{N} - x_{Cu} \end{aligned} \quad (4.1)$$

The chromium equivalents for the 14 steels studied here are presented in Table 4.2, along with the MTDATA [1996] predictions for the equilibrium quantities of δ-ferrite present. There is broad

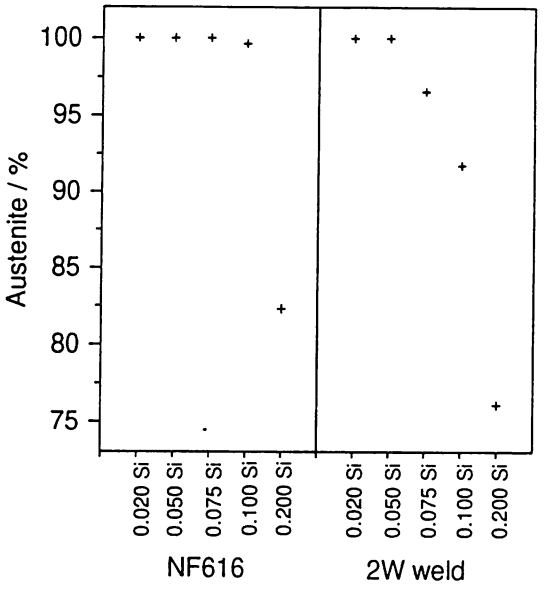

Figure 4.10: Calculated equilibrium percentage of austenite in NF616 and the 2W weld deposit, a function of the silicon concentration. The data are for a temperature of 1000 °C.

agreement between the two methods. NF616 is, however, incorrectly assessed to be susceptible to δ-ferrite formation. It is not possible from these data to suggest a minimum value of chromium equivalent to prevent the occurrence of δ-ferrite.

4.8 Conclusions

Whereas conventional creep resistant steels can be tempered and austenitised with confidence, it is evident that the heat treatments are not as easy to define for the 9Cr1Mo type alloys. This is because they routinely contain substantial quantities of solute elements; further alloying can therefore greatly affect the stability of the austenite and ferrite phases.

It has been demonstrated here that an excessive use of austenite stabilising alloying elements such as nickel, render the alloys susceptible to austenite formation during post weld heat treatment whose aim may simply be to relive residual stresses. Because of the high hardenability of the alloys, any austenite that does form during tempering transforms into untempered martensite during cooling to ambient temperature, leading to a large and possibly unacceptable increase in the strength and a deterioration in the toughness.

By contrast, an excessive use of ferrite stabilising elements such as tungsten makes it impossible to fully austenitise the 9Cr1Mo type steels. The microstructure then consists of a mixture of martensite (which forms from austenite) and relatively soft δ-ferrite; the latter increases in proportion with the tungsten concentration. Consequently, the strength actually decreases substantially as the tungsten concentration is increased.

Many of the alloys have been found to be extremely sensitive to the silicon concentration. A change from 0.05 to 0.2 weight % silicon introduces significant quantities of δ-ferrite in the microstructure.

Steel	Cr_{eq}	1000 °C	1100 °C	1200 °C	1300 °C	1400 °C
Base	8.833	99.26	99.85	18.55	50.55	87.64
1Ni	5.020	–	–	1.23	33.63	79.88
2Ni	1.223	–	–	–	–	63.15
3Ni	-3.062	–	–	–	2.95	50.13
1Co	6.979	–	–	10.23	44.60	86.77
2Co	5.524	–	–	12.09	46.72	87.09
3Co	3.675	–	–	4.15	39.60	90.03
1W	10.808	12.67	17.92	36.01	64.75	96.04
2W	11.927	23.92	29.49	46.64	72.84	100
3W	13.254	33.96	40.29	56.35	79.43	100
1W1Ni	6.623	–	0.54	15.93	45.38	85.45
1W1Co	8.583	3.97	7.68	–	57.23	95.41
1W2Co	6.971	0.19	3.63	20.80	55.30	95.63.
NF616	9.060	–	–	4.82	41.01	81.06

Table 4.2: Chromium equivalents and δ-ferrite calculations for the 14 steels.

By considering the silicon concentration, it has been possible to explain why alloys such as NF616 are free of δ-ferrite whereas others of nominally the same composition are not. A number of contradictory reports in the published literature can also be rationalised on the basis of the silicon concentration of the steel.

CHAPTER FIVE

The Yield and Ultimate Tensile Strength of Steel Welds

5.1 Introduction

The design of new welding alloys to match the ever advancing properties of newly developed steels is not an easy task. It is traditionally attained by experimental trial and error, modifying compositions and welding conditions until a satisfactory result is discovered. Enormous savings in cost and time might be achieved if the trial process could be eliminated and a weld with the desired properties could be produced without the preliminary steps.

Such an ideal is within reach with the use of an artificial neural network technique. This work outlines the use of such a tool to model the yield and ultimate tensile strengths of weld deposits from their chemical composition, welding conditions and heat treatments, drawing on extensive experimental results. The development of the models is described, as is the confirmation of their metallurgical accuracy. Finally, a test on previously unseen data illustrates their success in extrapolation and their versatility.

The tensile test provides the basic design data essential in both the specification and acceptance of welding materials. The test itself is simple but nevertheless gives reproducibly the parameters describing the onset of plastic deformation (the yield strength), the maximum load that can ever be supported (the ultimate tensile strength) and a variety of measures of ductility. Although the measurements involved are straightforward, their values depend in a complicated way on the chemical composition, the welding parameters and any heat treatment. There is, therefore, no general fundamental or empirical model capable of estimating the tensile parameters as a function of all these variables [Bhadeshia and Svensson, 1993, Bhadeshia, 1995b]. This is in spite of the fact that a great deal is known about the mechanisms of strengthening.

The difficulty limiting progress is the complexity of the problem. The physical models for strengthening mechanisms are not sufficiently sophisticated [Svensson, 1994], and the linear regression methods used traditionally [Es-Souni *et al.*, 1990, Evans, 1978, 1979, 1980, 1982b, 1983, 1989, 1990a–b, 1991a–b, 1992a, b, 1994a–c, 1995] are not capable of representing the real behaviour which is far from linear when all the factors are taken into account.

The aim of this work was to use an artificial neural network to empirically model and interpret the dependence of the yield and ultimate tensile strength of steel weld deposits as a function of many variables. A neural network is capable of realising a great variety of nonlinear relationships of considerable complexity. Data are presented to the network in the form of input and output parameters, and the optimum non-linear relationship found by minimising a penalised likelihood. As in regression analysis, the results then consist of a series of coefficients (called weights) and a specification of the kind of function which in combination with the weights relates the inputs to the outputs. To prevent overfitting, MacKay [1992a–c] has developed a Bayesian framework to control a neural network's complexity. This framework also provides quantified error bars on the network's predictions and makes it possible to automatically identify which of many possibly-relevant input variables are in fact important factors in the regression.

The creation of a model using the neural network method requires data; a large database of experimental measurements was therefore assembled for analysis.

5.2 The Experimental Database

The definition of strength in any model ideally requires a complete description of the chemical composition, the welding parameters, the heat-treatment and various features of the microstructure. A search of the literature [Es-Souni *et al.*, 1990, Evans, 1978, 1979, 1980, 1982b, 1983, 1989, 1990a–b, 1991a–b, 1992a–b, 1994a–c, 1995, Alekseev *et al.*, 1991, Blondeau *et al.*, 1984, Chandel *et al.*, 1985, Cunha *et al.*, 1982, Dittrich and Große-Wordemann, 1986, EPRI, 1989, ESAB, 1981, 1982, Garland and Kirkwood 1975a–b, Haigh, 1996, Hunt *et al.*, 1994, Ichikawa *et al.*, 1992, Inagaki *et al.*, 1966, Jorge *et al.*, 1993, Kikutake *et al.*, 1984, Kluken *et al.*, 1994, Koçak *et al.*, 1994, Martinez *et al.*, 1990, Natsume and Gotoh, 1990, Panton-Kent, 1990, Park and Svensson, 1990, Patterson, 1981, Raiter and Gonzalez, 1989, Still and Rogerson, 1978, Surian *et al.*, 1991, Svensson and Gretoft, 1990, Swift and Rogers, 1973, Watson *et al.*, 1981, Wolstenholme, 1974] showed that most of the reported data are not as detailed as these requirements. Given that the neural network technique used cannot cope with missing values, it was necessary to limit the number of variables to take maximum advantage of the 1652 individual cases studied.

Table 5.1a shows the list of nineteen input variables used for the yield strength analysis. It was possible to find 770 cases where all of these variables have been reported, with the exception, in a small number of cases, of phosphorus and sulphur concentrations. It would have been unreasonable to set these latter concentrations to zero when their values are not reported; welds inevitably contain these impurity elements in practice. For cases where the P and S values were missing, their concentrations were set to the mean values calculated for the 1652 case database. For the other elements, such as Mn, Ni, *etc.* , the concentrations can truly be set to zero when they are not reported. This is because they would not then be deliberate additions and would have concentrations close to the limits of chemical analysis with the techniques generally used.

The same rationale was applied to the dataset for the ultimate tensile strength analysis (Table 5.1b). Unlike the yield strength, the UTS can be sensitive to the inclusion content since there are much larger plastic strains associated with the UTS. Failure mechanisms such as void formation (at inclusions) may then contribute to the formation of a maximum in the load-extension curve. For this reason, the oxygen concentration was included as an additional variable. It is well established that the UTS correlates strongly with the yield strength [Ashby and Jones, 1980]; in addition, the UTS must always be larger than the yield strength. It was found that the latter condition was best satisfied during modelling by including the yield strength as a variable in the UTS analysis. Because of the inclusion of oxygen as a variable, the UTS dataset consisted of fewer cases (520 in all), each with twenty-one input variables. Of these 520 cases, eighteen did not report the yield strength values — this was resolved by substituting values calculated using the yield strength model.

Variable	Range	Mean	Standard Deviation
Carbon weight %	0.029–0.16	0.074	0.024
Silicon weight %	0.040–1.14	0.34	0.124
Manganese weight %	0.27–2.25	1.20	0.39
Sulphur weight %	0.001–0.14	0.0097	0.0069
Phosphorus weight %	0.004–0.25	0.013	0.011
Nickel weight %	0.00–3.50	0.22	0.63
Chromium weight %	0.00–9.35	0.734	2.07
Molybdenum weight %	0.00–1.50	0.17	0.35
Vanadium weight %	0.00–0.24	0.018	0.049
Copper weight %	0.00–1.63	0.074	0.224
Cobalt weight %	0.00–2.80	0.011	0.147
Tungsten weight %	0.00–2.99	0.0115	0.146
Titanium p. p. m. w.	0–690	40.86	79.9
Boron p. p. m. w.	0–69	1.17	5.78
Niobium p. p. m. w.	0–1000	57.4	151
Heat Input kJ mm^{-1}	0.6–7.9	1.85	1.47
Interpass Temperature °C	20–300	207.7	48.93
Tempering Temperature °C	0–760	320.4	257
Tempering Time hours	0–24	5.72	6.29
Yield Strength MPa	315–920	507.3	92.8

Table 5.1a : The variables used in the analysis of the yield strength. The abbreviation p. p. m. w. stands for parts per million by weight.

5.3 A Brief Description of the Neural Network

The aim of this work was to be able to estimate the yield strength or UTS as a function of the variables listed in Table 5.1. Both the input and output variables were first normalised within the range ± 0.5 as follows:

$$x_N = \frac{x - x_{min}}{x_{max} - x_{min}} - 0.5 \tag{5.1}$$

where x_N is the normalised value of x which has maximum and minimum values given by x_{max} and x_{min} respectively. This normalisation is not necessary for the analysis, but enables an easier subsequent comparison of the significance of each of the variables.

Variable	Range	Mean	Standard Deviation
Carbon weight %	0.029–0.160	0.076	0.018
Silicon weight %	0.04–1.14	0.35	0.14
Manganese weight %	0.27–2.22	1.23	0.36
Sulphur weight %	0.004–0.14	0.010	0.007
Phosphorus weight %	0.004–0.25	0.012	0.012
Nickel weight %	0.00–3.15	0.16	0.53
Chromium weight %	0.00–9.35	0.62	1.91
Molybdenum weight %	0.00–1.50	0.18	0.36
Vanadium weight %	0.00–0.24	0.02	0.04
Copper weight %	0.00–1.63	0.07	0.23
Cobalt weight %	0.00–2.80	0.02	0.18
Tungsten weight %	0.00–2.99	0.02	0.18
Oxygen p. p. m. w.	132–1650	441	152
Titanium p. p. m. w.	0–690	49	91
Boron p. p. m. w.	0–69	1.15	6.18
Niobium p. p. m. w.	0–985	62	165
Heat Input kJ mm^{-1}	1–7.9	1.9	1.5
Interpass Temperature °C	100–300	205	51
Tempering Temperature °C	0–760	317	243
Tempering Time hours	0–16	6.1	6.2
Yield Strength MPa	329–920	503	88
Ultimate Tensile Strength MPa	447–1151	599	92

Table 5.1b : The variables used in the analysis of the factors influencing the ultimate tensile strength. The abbreviation p. p. m. w. stands for parts per million by weight.

Several neural network models were created using the data; the models varied in terms of their complexity and in terms of the random seeds used to start the training process.

Each network consisted of input units (one for each variable x), a number of hidden units (controlling the complexity of the model) and an output unit (representing either the yield or ultimate tensile strength, Figure 5.1). Linear functions of the inputs x_j are operated on by a hyperbolic tangent transfer

function:

$$h_i = \tanh\left(\sum_j w_{ij}^{(1)} x_j + \theta_i^{(1)}\right) \tag{5.2}$$

so that each input contributes to every hidden unit. The bias is designated θ_i and is analogous to the constant that appears in linear regression. The strength of the transfer function is in each case determined by the weight w_{ij}. The transfer to the output y is linear:

$$y = \sum_i w_{ij}^{(2)} h_i + \theta^{(2)} \tag{5.3}$$

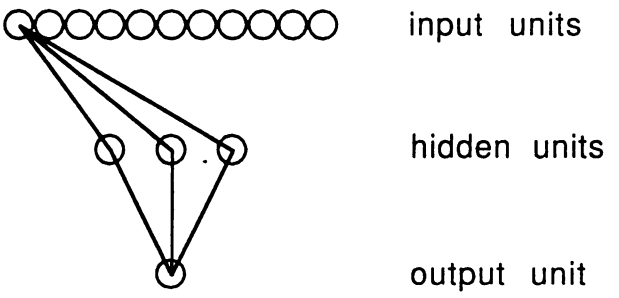

Figure 5.1: A typical network used in the analysis. Only the connections originating from one input unit are illustrated, and the two bias units are not illustrated.

The specification of the network structure, together with the set of weights is a complete description of the formula relating the inputs to the output. The weights are determined by training the network [MacKay, 1992a–c, 1993]. The training involves a minimisation of the regularised sum of squared errors. The term σ_ν used below is the framework estimate of the noise level of the data.

5.4 The Yield Strength Model

The method was applied to the yield strength data (Table 5.1a). The complexity of the model is controlled by the number of hidden units (Figure 5.1), and the values of the regularisation constants (σ_w), one associated with each of the inputs, one for biases and one for all the weights connected to the output. Figure 5.2 shows that as expected, the inferred noise level decreases monotonically as the number of hidden units increases. However, the complexity of the model also increases with the number of hidden units. A high degree of complexity may not be justified if the model attempts to fit the noise in the experimental data. MacKay has made a detailed study of this problem and has defined a quantity (the *evidence*) which comments on the probability of a model [MacKay, 1992c]. In circumstances where two models give similar results over the known dataset, the more probable model would be predicted to be that which is simpler. The evidence framework was used to control the regularisation constants and σ_ν. In addition, the experimental data were partitioned equally and randomly into a *test* dataset and a *training* dataset. Only the latter was used to train the model, whose ability to generalise was examined by checking its performance on the unseen test data. The test error (T_{en}) is a reflection of the ability of the model to predict the yield strength values in the test data:

$$T_{en} = 0.5 \sum_n (y_n - t_n)^2 \tag{5.4}$$

where y_n is the set of predictions made by the model, and t_n is the set of target (experimental) values.

It can be seen that the calculated test error for this yield strength model goes through a minimum at 3 hidden units (Figure 5.2b). This would be the optimum model if a single model were to be used for the analysis.

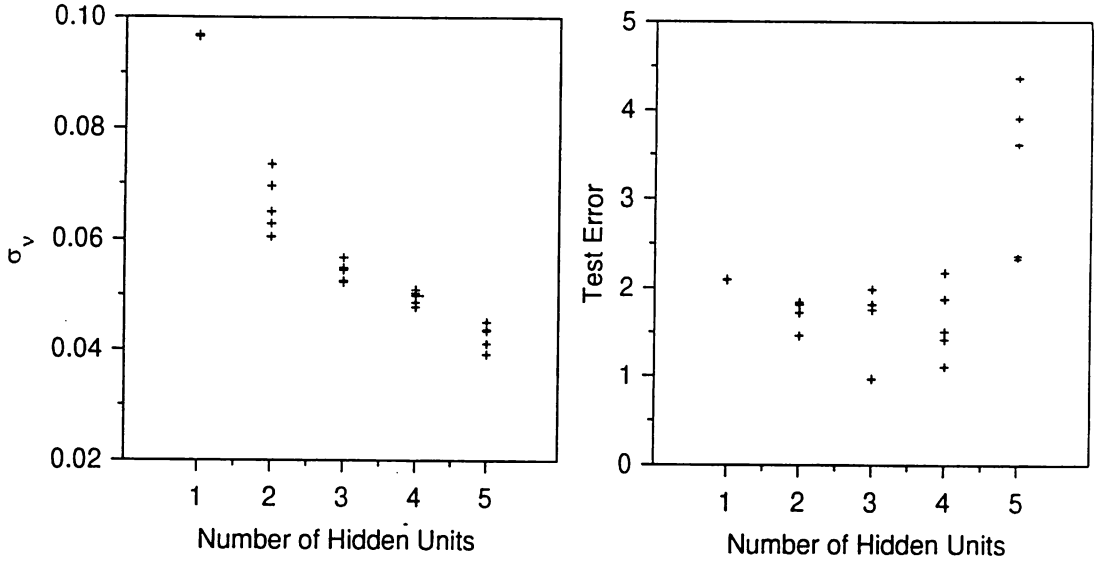

Figure 5.2: Variation in σ_ν and in test error as a function of the number of hidden units. Several values are presented for each set of hidden units because the training for each network was started with a variety of random seeds.

However, it is possible that a *committee* of models can make a more reliable prediction than an individual model. The best models were ranked using the values of their test errors (Table 5.2 and Figure 5.3). Committees could then be formed by combining the predictions of the best L models, where $L = 1, 2, \ldots$; the size of the committee is therefore given by the value of L.

Ranking	Hidden Units	Seed	Test Error	Ranking	Hidden Units	Seed	Test Error
1	3	35	0.9631	6	2	100	1.4566
2	3	50	0.9699	7	4	100	1.5045
3	4	35	1.1063	8	2	15	1.7185
4	4	5	1.4146	9	3	100	1.7550
5	2	50	1.4556	10	2	35	1.8094

Table 5.2: Ranking of ten best models by test error.

The test error of the predictions made by a committee of L models, ranked 1,2,...l,... L, each

with n lines of test data, is calculated in a similar manner to the test error of a single model.

$$T_{en} = 0.5 \sum_{n} (\overline{y}_n - t_n)^2 \qquad \text{where} \qquad \overline{y}_n = \frac{1}{L} \sum_{l} y_n^{(l)} \tag{5.5}$$

The test errors for the first ten committees (with ever increasing size) are listed in Table 5.3 and plotted in Figure 5.3. The two plots in Figure 5.3 are drawn to the same scale to emphasise the reduction in test error, and hence improved predictions, by using the committee model approach.

Models in Committee	Test Error	Models in Committee	Test Error
1	0.96311	6	0.89120
2	0.96482	7	0.90606
3	0.89200	8	0.92398
4	0.89998	9	0.94423
5	0.86223	10	0.97597

Table 5.3: Test errors of the first ten committees.

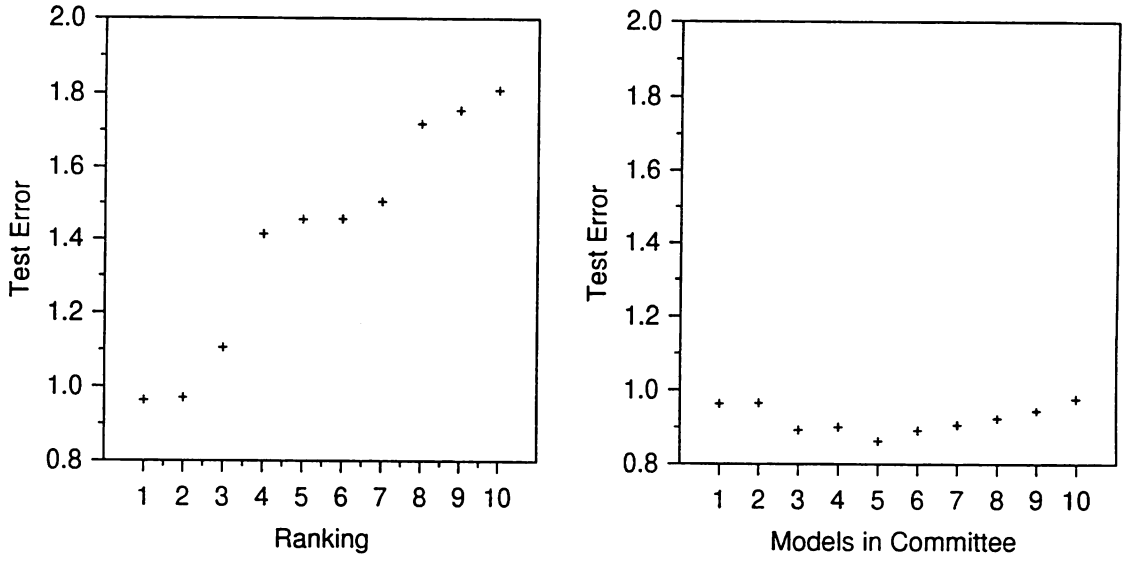

Figure 5.3: Test error of the top ten ranked yield strength models, and test error of the committees of yield strength models.

It is evident that the test error for the committee analysis goes through a minimum for the committee made up of five models. These models were used in calculating the optimum model. The comparison between the predicted and measured values of the yield strength for the training and test data are shown for the best single model, and the best committee (consisting of five best models) in figures 4 and 5.

For this purpose, the committee prediction is given by the mean value of its components:

$$\overline{y} = \frac{1}{L}\sum_{l} y^{(l)} \tag{5.6}$$

and the committee variance is given by [MacKay, 1995]:

$$\sigma^2 = \frac{1}{L}\sum_{l} \sigma_y^{(l)^2} + \frac{1}{L}\sum_{l} (y^{(l)} - \overline{y})^2 \tag{5.7}$$

It is notable that the committee is more realistic than the single model in the sense that there are very few *outliers*, *i.e.* for the test data there are few points for which the predictions are out of the 1σ error bar range.

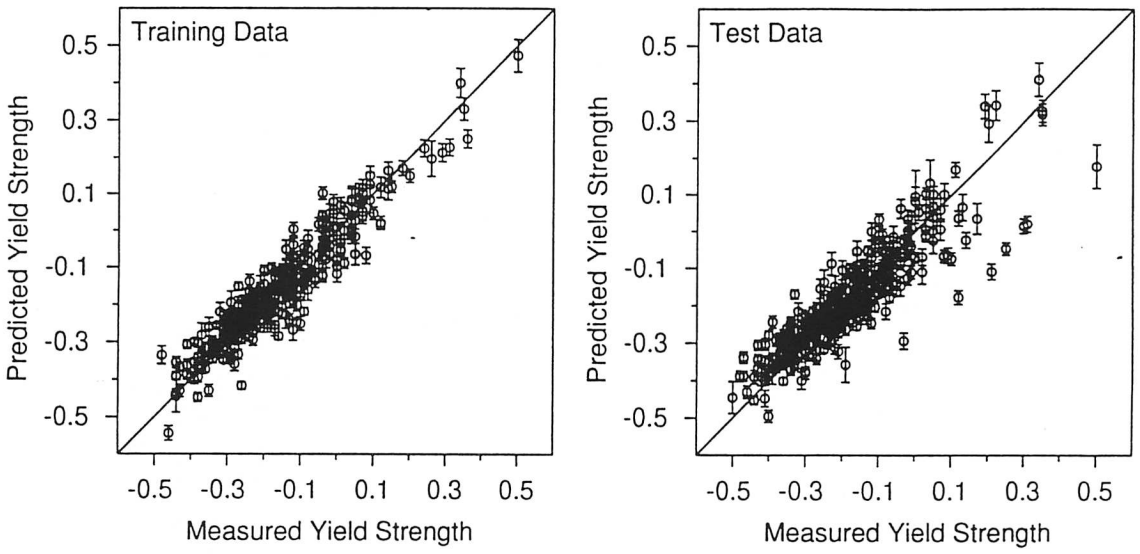

Figure 5.4: Training and test data for the single highest ranked model.

Having chosen the best committee, its five component models were retrained on the entire dataset, the retraining procedure beginning with the weights already determined. The results from this ultimate committee model are shown in Figure 5.6. It is satisfying that outliers are virtually absent.

The final weights of all models in the committee having been retrained on all data are presented in Appendix One.

5.5 Model for the Ultimate Tensile Strength

The technique discussed above was then applied the the UTS dataset (Table 1b). The plots of σ_ν, test errors and the appropriate plots for the committee investigation are shown in Figure 5.7. Numerical data are shown in Table 5.4.

The estimates for the training and test data for the best single model, and the best committee (consisting of four of the best models) are shown in Figure 5.8.

Finally, the four models making up the committee were retrained on all data, giving the final committee model as shown below in Figure 5.9.

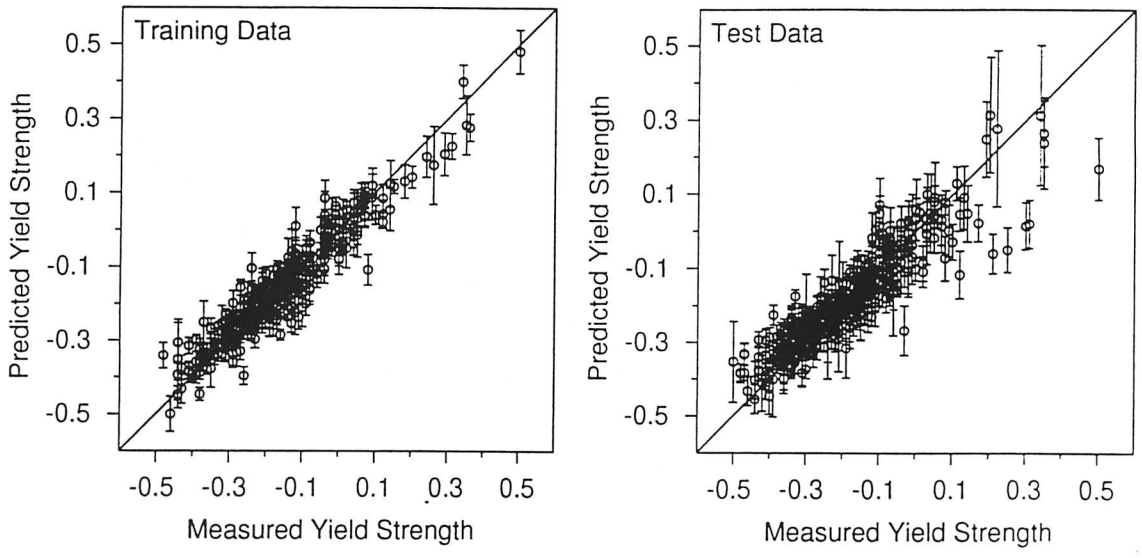

Figure 5.5: Training and test data for the committee consisting of the five highest ranking models.

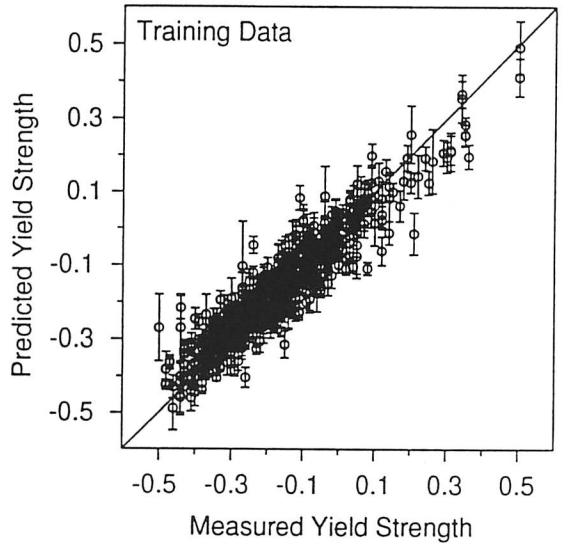

Figure 5.6: Training data for the committee produced from the five highest ranking models, trained on the *whole* data set.

5.6 Application of the Models

In this section the influence of each of the variables on the yield and tensile strengths of three welding alloys is examined. Their actual compositions and mechanical properties were listed in Table 2.3. The welds, which were fabricated by Oerlikon, cover a range of applications in power plant construction, being referred to in brief as $2\frac{1}{4}$Cr1Mo, 9Cr and $3\frac{1}{2}$Ni deposits. The purpose of the analysis presented below was to test the neural network models to see whether the relationships recognised are as expected from metallurgical considerations.

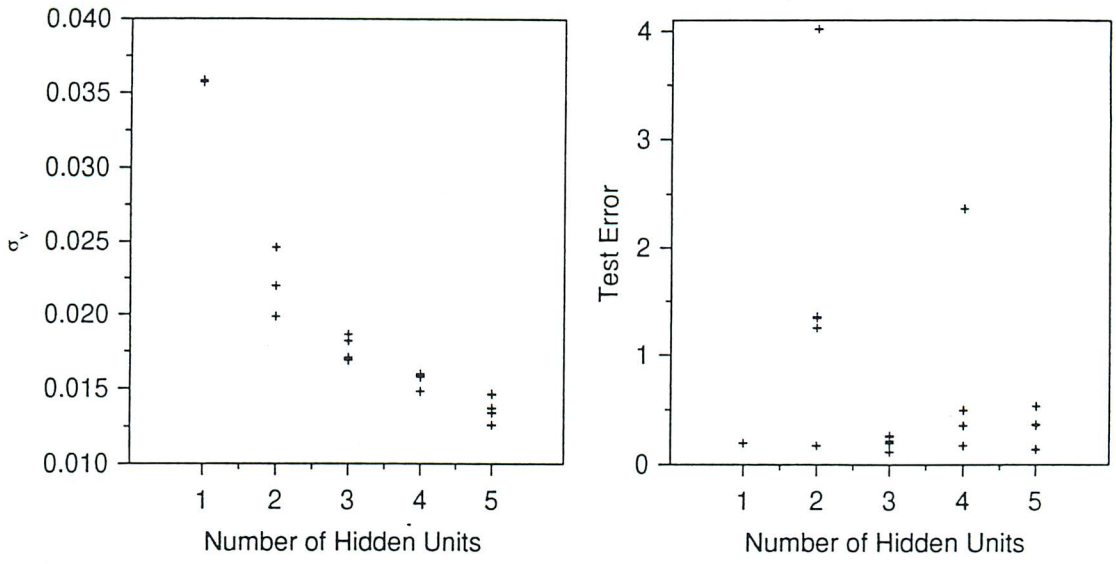

Figure 5.7a: Variation in σ_ν and in test error as a function of the number of hidden units. Several values are presented for each set of hidden units because the training for each network was started with a variety of random seeds.

Ranking	Hidden Units	Seed	Test Error	Ranking	Hidden Units	Seed	Test Error
1	3	35	0.11567	6	4	5	0.17275
2	5	35	0.13617	7	1	50	0.19463
3	5	5	0.14095	8	1	100	0.19490
4	2	35	0.17228	9	1	35	0.19504
5	4	100	0.17271	10	1	15	0.19515

Table 5.4a: Ranking of ten best models by test error.

Committee models are used for all the predictions that follow; the calculation of the error bar for the committee, from the corresponding errors for each model within the committee, has already been discussed. However, the UTS model requires the yield strength for one of its inputs, which in turn is calculated using the yield neural network committee. Errors in the calculation of yield strength must therefore add to the estimate of UTS:

$$\sigma_u^2 = \frac{1}{L_u}\sum_{l_u} \sigma_{y_u}^{(l_u)^2} + \frac{1}{L_u}\sum_{l_u}(y_u^{(l_u)} - \overline{y}_u)^2 + \sigma_s{}^2\left(\frac{\partial y_u}{\partial x_s}\right)^2 \qquad (5.8)$$

where the notation is as before, with the exception of the final term which represents the error in the yield calculation multiplied by the sensitivity of the UTS to yield. The subscripts s and u refer to the yield strength and UTS respectively.

The calculated yield and UTS of the three experimental weld deposits (Chapter 2, Table 2.2) are compared to the measured values in Table 5.5. These three welds had been included in the training

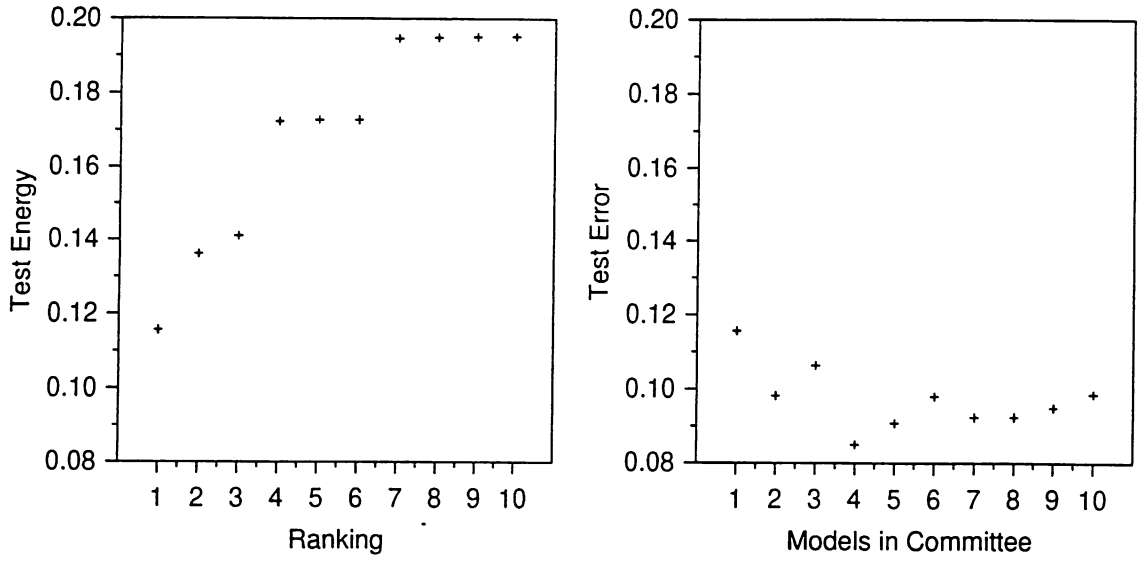

Figure 5.7b: Test error of the top ten ranked UTS models, and test error of the committees of UTS models.

Models in Committee	Test Error	Models in Committee	Test Error
1	0.11567	6	0.09804
2	0.09526	7	0.09238
3	0.10636	8	0.09238
4	0.08497	9	0.09492
5	0.09079	10	0.09857

Table 5.4b: Test errors of the first ten committees.

data. There are two calculated values for the UTS: one using the measured yield strength and the other a calculated yield value as an input in the UTS model. As might be expected, the latter method has larger uncertainty associated with it. It is evident that the predictions are all rather good, so further calculations were carried out to check the effects of each of the inputs.

5.7 Major Alloying Elements

The $2\frac{1}{4}$Cr1Mo welds have a bainitic microstructure on deposition, whereas the 9Cr and $3\frac{1}{2}$Ni are martensitic on deposition; the effect of the tempering heat treatment is to precipitate carbides. Consequently, carbon is in these circumstances expected to raise the strength, although the rise in strength should not be very large since the welds are all severely tempered. This general behaviour is exactly what the model predicts, as illustrated in Figure 5.10. The error bars in all cases get larger as the carbon concentration increases beyond the levels typically employed in welds (<0.16 weight %), since such data do not exist in the training dataset. It is well known that the ratio of the yield strength to the tensile strength decreases as the former increases; this is correctly reproduced by the model

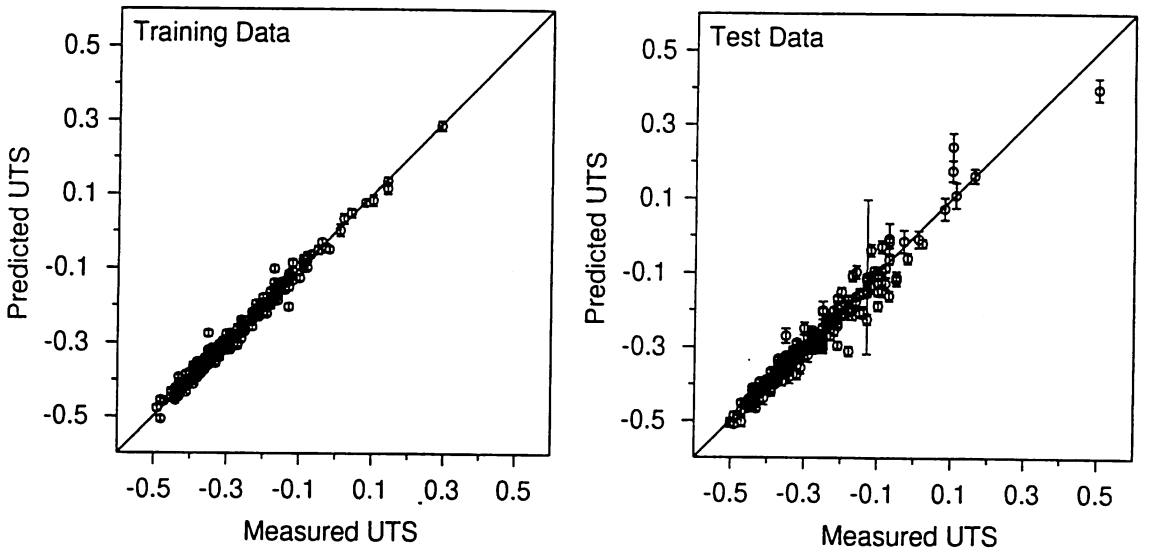

Figure 5.8a: Training and test data for the highest ranked model.

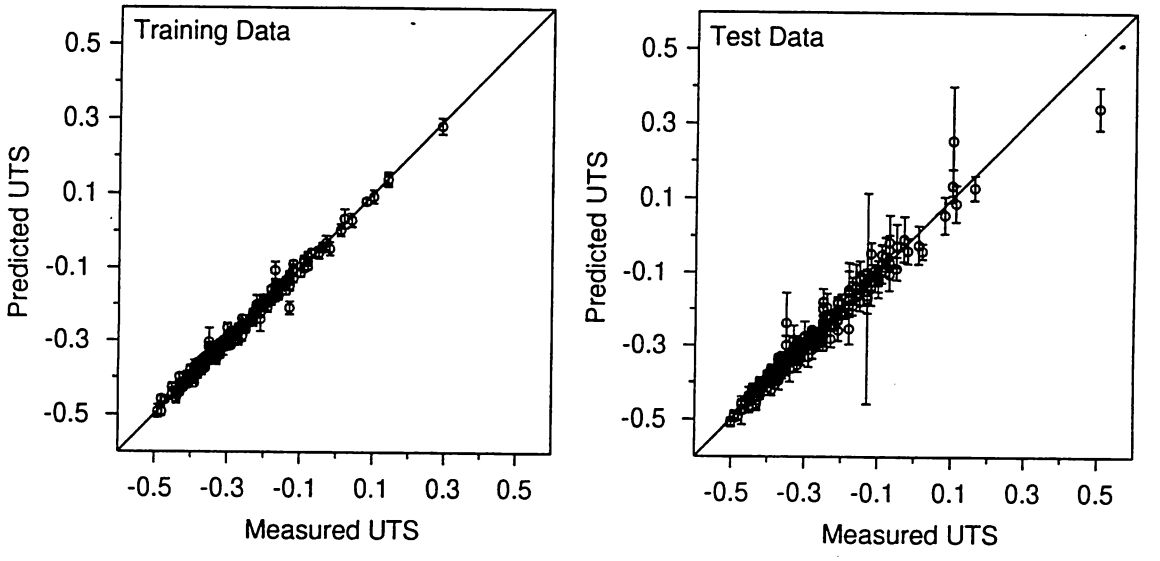

Figure 5.8b: Training and test data for the committee produced from the four highest ranking models.

(Figure 5.10).

The model also indicates that the yield strength is virtually a linear function of the carbon concentration, as assumed in most linear regression models [Svensson, 1994, Es-Souni *et al.*, 1990, Evans, 1978, 1979, 1980, 1982b, 1983, 1989, 1990a–b, 1991a–b, 1992a, b, 1994a–c, 1995]. In fact, the gradients of all the yield strength plots in Figure 5.10 are very similar so that the linear relationship is valid across the alloys. This is illustrated in Figure 5.11 where the difference between the predicted yield strength for a specific carbon concentration and the predicted yield strength at zero carbon (Δ yield strength) is plotted against the carbon concentration. These slopes are effectively identical to each

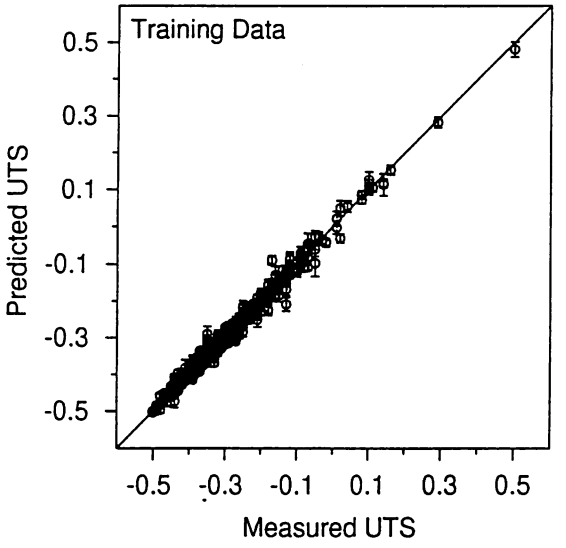

Figure 5.9: Training data for the committee produced from the four highest ranking models, trained on the *whole* data set.

Steel	Measured Yield Strength MPa	Predicted Yield Strength MPa	Measured UTS MPa	Predicted UTS MPa (Measured YS)	Predicted UTS MPa (Calculated YS)
$2\frac{1}{4}$Cr	568	561 ± 29	676	685 ± 8	685 ± 21
9Cr	752	704 ± 36	872	875 ± 13	838 ± 27
$3\frac{1}{2}$Ni	920	915 ± 43	1000	998 ± 10	994 ± 32

Table 5.5: Measured and predicted yield strength and UTS values for the three steels described in Table 2.3, and used as a basis for the predictions. The error limits represent 1σ ($\pm 65\%$).

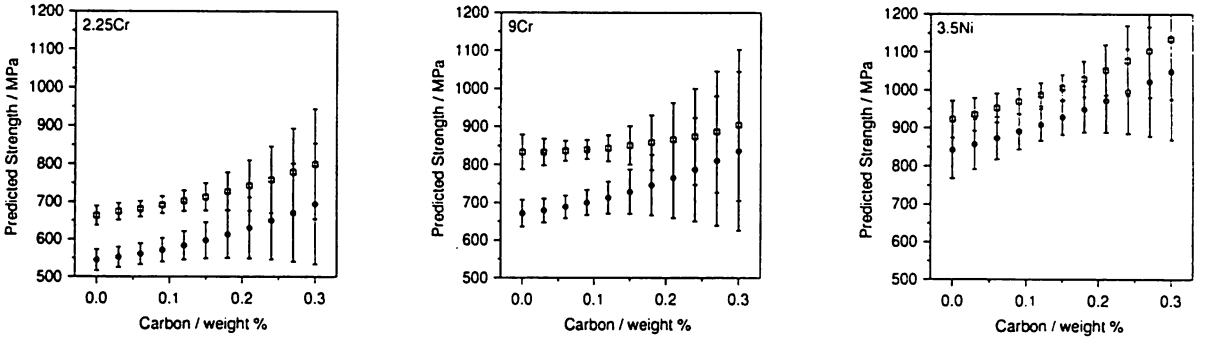

Figure 5.10: Predicted variations in yield strength and UTS with carbon variation.

other for the three steels within the error limits of the analysis.

The predicted effect of silicon is shown in Figure 5.12; the calculations for large silicon concen-

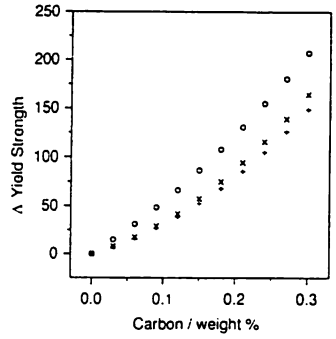

Figure 5.11: Plot showing the predicted yield strength minus the predicted yield strength for zero carbon for the three alloys. + represents the $2\frac{1}{4}$Cr weld, × the 9Cr weld and o the $3\frac{1}{2}$Ni weld.

trations are too uncertain to be useful. However, for concentrations less than about 0.5 weight % the silicon clearly raises the yield strength, by an amount which within the error bounds is consistent with solid solution strengthening at about 105 MPa per weight % [Honeycombe and Bhadeshia, 1995, page 313; Philip, 1983]. Silicon is also known to retard the formation of cementite (Fe_3C) [Bhadeshia, 1992] but the severe tempering heat treatments used here take the steels well beyond cementite into the secondary hardening regime so that this particular effect must be negligible. Silicon does decrease the lattice parameter of the ferrite matrix which increases the intensity of secondary hardening [Pickering, 1978; Chapter 7], but the severe tempering again rules this out as an important factor since the carbide particles are expected to be beyond the stage of coherency. It is therefore concluded that the major effect of silicon in these welds is via solid solution strengthening, consistent also with the fact that it does not precipitate or partition into the carbides.

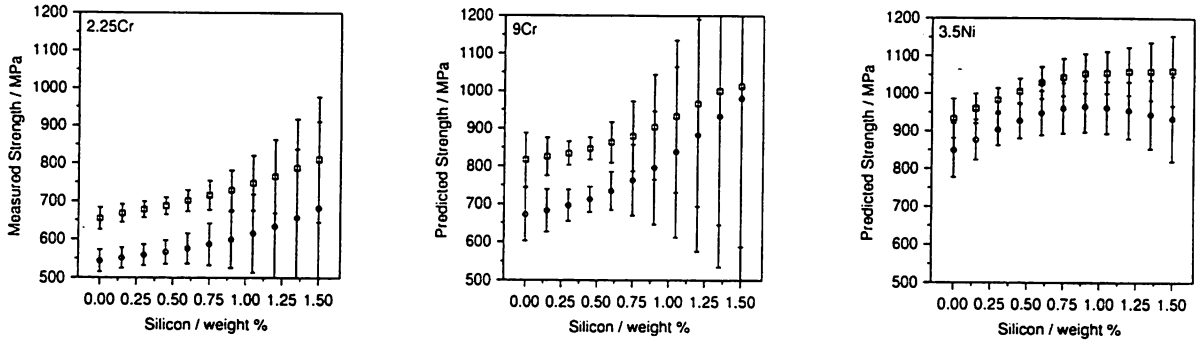

Figure 5.12: Predicted variations in yield strength and UTS with silicon variation.

Manganese has a much smaller solid solution strengthening effect (45 MPa per weight %) [Leslie, 1981], which is consistent with the results for the $2\frac{1}{4}$Cr1Mo and $3\frac{1}{2}$Ni welds (Figure 5.13). However, the yield strength of the 9Cr weld seems insensitive to the manganese concentration. It is speculated that this may be due to the large overall solute content of this alloy.

Nickel has an even smaller solid solution strengthening effect than manganese, and yet it appears to greatly strengthen all of the welds (Figure 5.14). The work presented in Chapter 4 demonstrated that

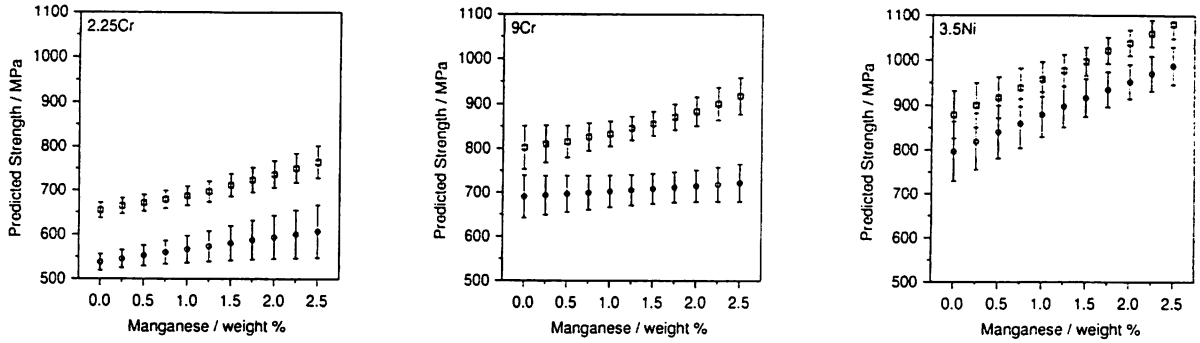

Figure 5.13: Predicted variations in yield strength and UTS with manganese variation.

austenite can unintentionally form in welds which are post weld heat treated in cases where the nickel concentration is large.

Nickel is an austenite stabiliser. MTDATA [1996], was used to predict the phases present at the tempering temperatures for the three welds, for a variety of nickel concentrations Figure 5.14. It can be seen that as the nickel concentration is increased, the amount of austenite (γ) in the weld at the post weld heat treatment temperature also increases. The important point is that this austenite subsequently decomposes to untempered martensite on cooling to room temperature and hence leads to an abnormal increase in strength [Bain and Paxton, 1961]. Comparing the two sets of graphs it can be seen that the rate of rise of yield strength and UTS is related to that of austenite fraction in the weld.

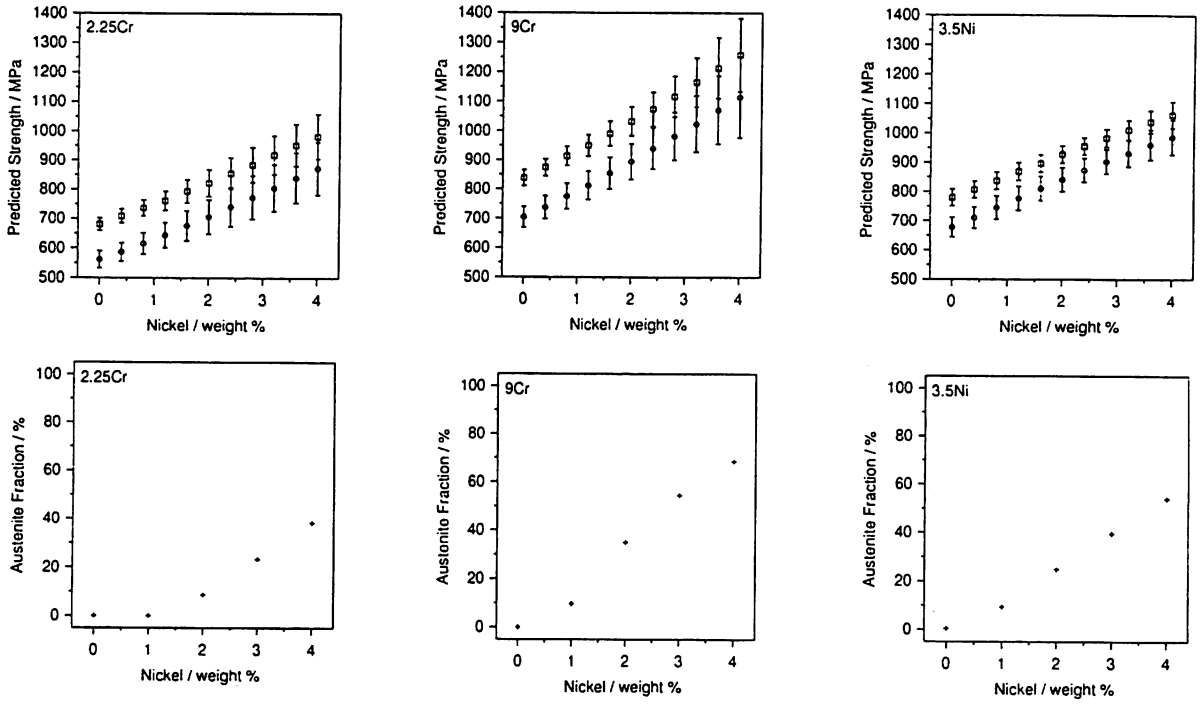

Figure 5.14: Predicted variations in yield strength and UTS with nickel variation compared to MTDATA calculated phases present at the tempering temperature for the $2\frac{1}{4}$Cr (700 °C), 9Cr (760 °C) and $3\frac{1}{2}$Ni (700 °C) weld deposits with varying nickel concentration.

5.8 Carbide-Forming & Other Elements

Figure 5.15 shows that the addition of chromium in general causes an increase in strength, though there are detailed differences between the three kinds of welds. The $3\frac{1}{2}$Ni steel is the most sensitive to changes in chromium concentration whereas the yield strength of the 9Cr steel is increased slightly but then levels off at about 5 weight %. The phase stability calculations presented in Table 5.6 provide some of the explanation for the differences between the alloys. For the 9Cr steel, there is little variation in the total fraction of carbides beyond about 6 weight % chromium, explaining the predicted lack of increase in strength. There is a large increase in the fraction of carbides present in the $3\frac{1}{2}$Ni alloy up to a chromium concentration of about 4 weight %. This is again consistent with the calculations presented in Figure 5.15c, where the rate of increase in the yield strength is significantly smaller beyond about 4 weight %, although the calculated values become unreliable at the larger chromium concentrations. For the $2\frac{1}{4}$Cr1Mo alloy, the calculations presented in Figure 5.15a are at first sight inconsistent with those presented in Table 5.6, where the carbide fraction does not change greatly as the chromium concentration is increased. However, $M_{23}C_6$ precipitation is known to be notoriously slow [Baker and Nutting, 1959] in this alloy for reasons described elsewhere [Robson and Bhadeshia, 1996]. The tempering treatment of 700 °C for 3 hours is certainly not sufficient to induce $M_{23}C_6$ precipitation [Baker and Nutting, 1959]. The data in Table 5.6 are, on the other hand, equilibrium data and therefore do not represent the microstructural state of $2\frac{1}{4}$Cr1Mo after the prescribed tempering heat treatment. This is not the case for the 9Cr alloy, where $M_{23}C_6$ is known to precipitate very rapidly indeed [Thomson and Bhadeshia, 1992] . Unfortunately, the detailed precipitation behaviour in the $3\frac{1}{2}$Ni alloy has never been experimentally characterised, so it is not possible to comment on its microstructural state; the good correlation between the equilibrium carbide fractions and strength calculations therefore is in this case unconfirmed.

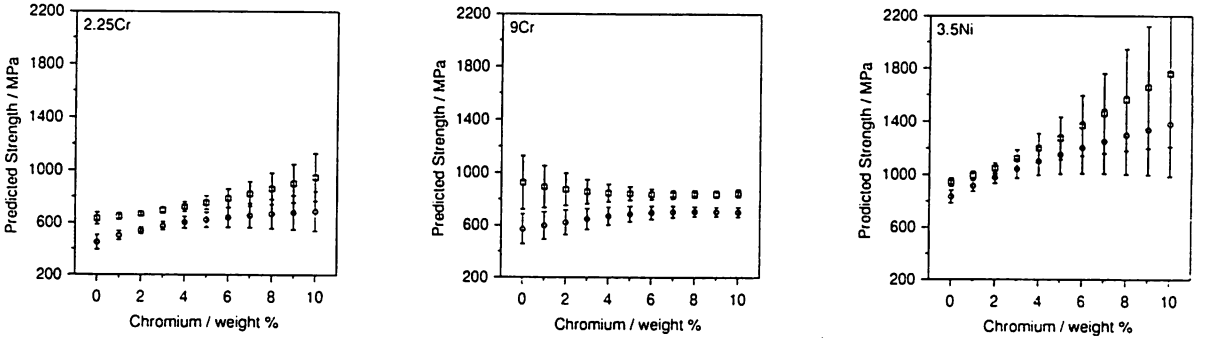

Figure 5.15: Predicted variations in yield strength and UTS with chromium variation.

The effect of molybdenum is illustrated in Figure 5.16. The effects illustrated are experimentally established [Pickering, 1978] in the regions where the magnitudes of the error bars are reasonable. The metallurgical reason for this behaviour is not understood despite having conducted equilibrium calculations.

Predictions were also made for other carbide forming elements such as vanadium, tungsten and niobium over typical ranges of concentrations; all the calculations appeared well-behaved from a metallurgical point of view. For example, the addition of vanadium produced increases in strength due

Cr	$2\frac{1}{4}$CrlMo					9Cr						$3\frac{1}{2}$Ni				
wt. %	α	MC	M_7C_3	M_2X	$M_{23}C_6$	α	γ	MC	M_2X	$M_{23}C_6$	M_7C_3	α	γ	M_2X	$M_{23}C_6$	
0	99.07	—	0.93	—	—	82.85	16.28	—	0.87	—	—	54.84	44.80	0.36	—	
2	98.59	0.03	—	—	1.38	94.85	3.72	—	1.43	—	—	61.80	36.19	0.04	1.97	
4	98.60	0.03	—	—	1.37	88.11	10.99	—	—	—	0.90	61.57	36.06	0.04	2.32	
6	98.58	—	—	0.05	1.37	97.85	—	0.23	—	1.91	—	59.35	38.23	—	2.42	
8	98.54	0.09	—	—	1.37	97.68	—	—	0.40	1.92	—	58.46	39.09	—	2.45	
10	98.54	0.10	—	—	1.36	97.84	—	0.23	—	1.93	—	59.09	38.44	—	2.47	

Table 5.6: MTDATA calculated phases present at the tempering temperature for the $2\frac{1}{4}$Cr (700 °C), 9Cr (760 °C) and $3\frac{1}{2}$Ni (700 °C) weld deposits with varying chromium concentration.

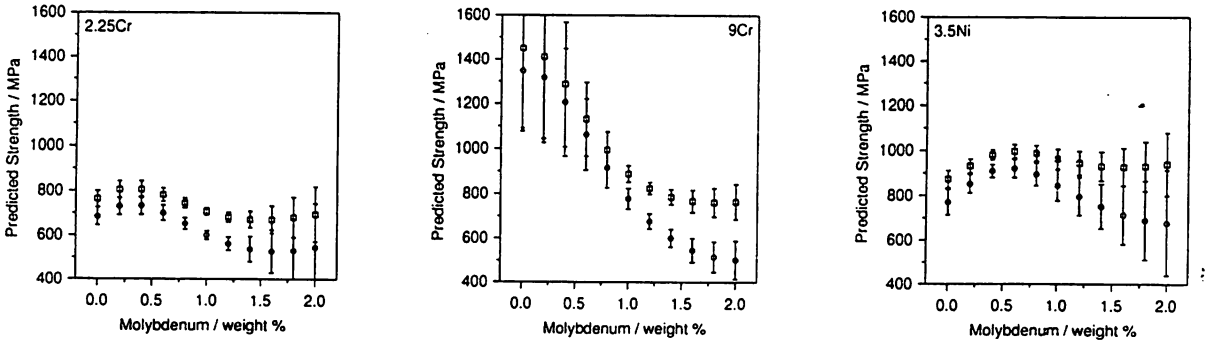

Figure 5.16: Predicted variations in yield strength and UTS with molybdenum variation.

to the precipitation of fine vanadium carbonitrides of the form $V_4(N,C)_3$. These are known to increase the strength of steels [Ridley *et al.*, 1994]. Tungsten, on the other hand, reduced strength, a well known effect originating in the fact that it induces the retention of soft, high-temperature δ-ferrite (Chapters 3 and 4). Niobium caused insignificant changes in strength for the concentrations studied (less than 1000 p.p.m.w), except in the 9Cr alloy where the resulting increase in strength is expected [Orr, *et al.*, 1992].

Finally, it was confirmed that trace impurities such as sulphur and phosphorus have no significant effect on strength. The effect of titanium, boron and copper cannot be discerned reliably in the type of welds studied here.

5.9 Heat Treatment

The effects of tempering temperature and time are as expected, that an increase in either leads to a decrease in the strength (Figure 5.17a, b). The strength does not collapse after prolonged heat treatment because all of the alloys concerned contain strong carbide-forming elements designed to provide secondary hardening and resist tempering.

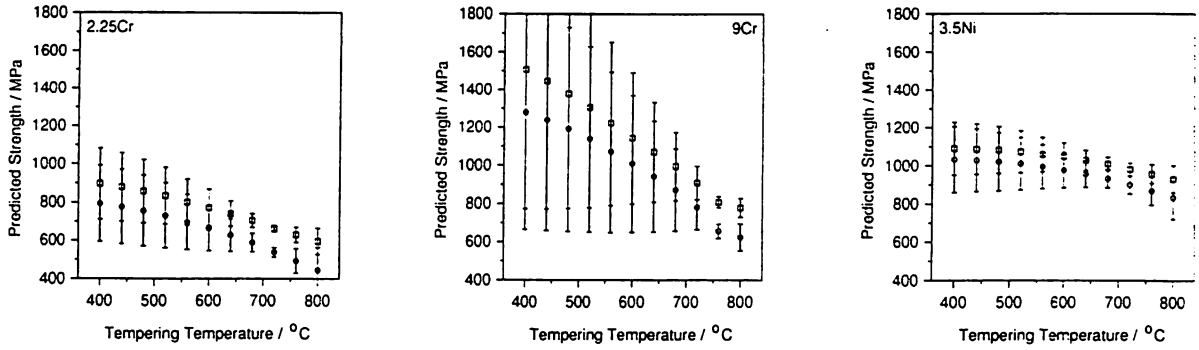

Figure 5.17a: Predicted variations in yield strength and UTS with tempering temperature variation.

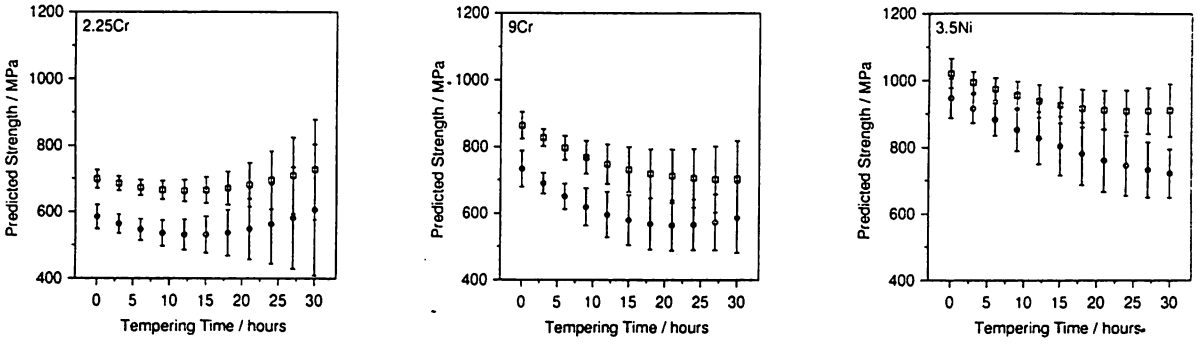

Figure 5.17b: Predicted variations in yield strength and UTS with tempering time variation.

5.10 Further Application

Experiments conducted by Lord [1996] provided further yield strength data which were not included in the original dataset. The welds were made using the manual metal arc welding process with an interpass temperature of 250 °C. The flux used is not known. The welds were all given a degassing post weld heat treated of 250 °C for sixteen hours followed by air cooling. The strength was in each case measured for an all-weld deposit.

The calculations were carried out using the trained neural network for the welds listed in Table 5.7, the model being capable of handling all the variables listed, together with the heat treatment.

Figure 5.18 shows that the calculated values for both yield strength and UTS agree well with those measured, confirming the validity of the method used. This is very encouraging, especially as in some of the cases the model has made predictions with the nickel input exceeding the maximum value with which training took place (3.5 weight %). This not only gives confidence in the technique, but permits future experimental programmes to be reduced in size and the alloys designed more rationally.

Despite the model's success, a complete solution to the problem of strength modelling has not been achieved, although the number of variables has been greatly reduced. The model is limited by the information available for training and testing. It has already been demonstrated that there was a reduction in the quantity of data available for prediction of UTS as compared to yield strength, due to the necessity of oxygen for one of the inputs. However, there are other important variables which many authors omit from their publications, because they are difficult or expensive to measure. Such an important variable is the cooling rate after PWHT.

ID	H1	H2	H3	H4	H5	H6	H7
Carbon weight %	0.049	0.037	0.045	0.026	0.025	0.022	0.102
Silicon weight %	0.29	0.27	0.29	0.23	0.22	0.17	1.63
Manganese weight %	2.09	2.13	1.11	0.97	0.85	0.78	2.18
Sulphur weight %	0.012	0.006	0.006	0.010	0.009	0.011	0.005
Phosphorus weight %	0.005	0.010	0.008	0.010	0.010	0.010	0.009
Nickel weight %	3.04	3.03	3.91	4.00	3.91	4.25	2.07
Chromium weight %	0.43	0.46	0.43	0.44	0.03	0.03	0.02
Molybdenum weight %	0.59	0.60	0.58	0.61	0.60	0.13	0.23
Vanadium weight %	0.19	0.19	0.16	0.15	0.15	0.11	0.19
Copper weight %	0.03	0.03	0.03	0.03	0.03	2.18	0.03
Titanium p. p. m. w.	140	140	140	120	120	100	390
Boron p. p. m. w.	5	6	4	2	1	—	7
Oxygen p. p. m. w.	267	307	310	348	299	423	205
Nitrogen p. p. m. w.	118	143	101	143	148	125	113
Heat Input kJ mm^{-1}	1.046	1.081	1.038	1.118	1.109	1.155	1.019

Table 5.7: Chemical compositions and heat input values for the welds [Lord, 1996].

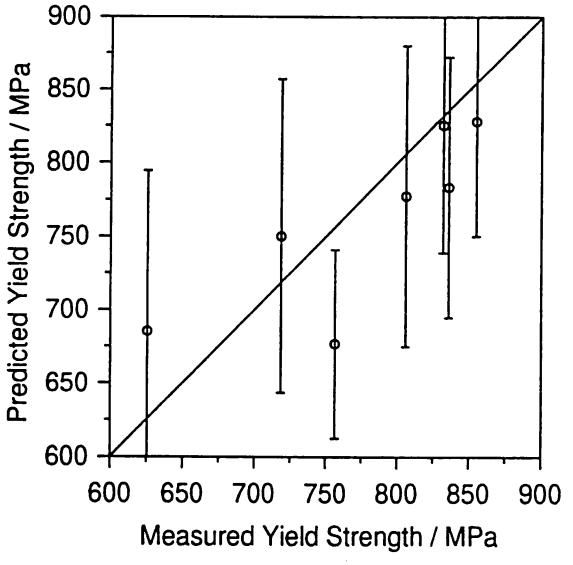

Figure 5.18a: Comparison of the yield strength as predicted using a neural network model against measured data from Lord. The error limits correspond to $\pm 1\sigma$.

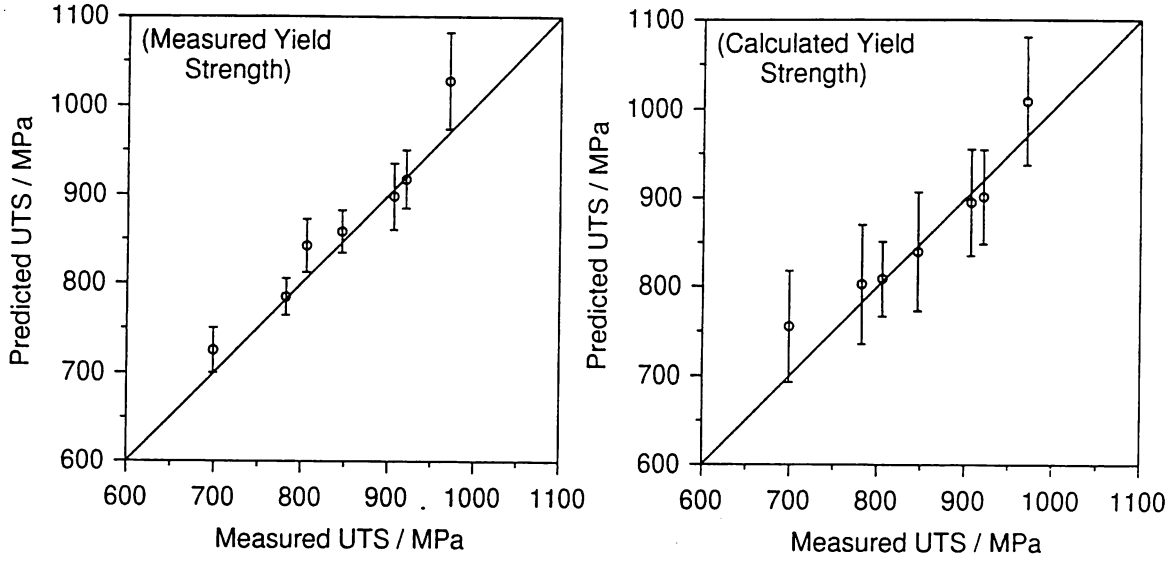

Figure 5.18b: Comparison of the UTS as predicted using a neural network model against measured data from Lord. The two sets of predictions correspond to the UTS predicted using the measured yield strength as an input, and the predicted yield strength as an input respectively.

The cooling rate from the heat treatment temperature can be critical to the microstructure, and hence to the properties of the weld. The severe consequences of the cooling rate are illustrated in the following example relating to the Oerlikon $3\frac{1}{2}$Ni weld studied in this chapter.

Initially, samples of the weld were heat treated using a heating rate of 15 °C hour^{-1}, and then immediately cooled at a rate of 60 °C s^{-1} [Davin, 1994]. This resulted in a very low Charpy impact value of 7 J at 20 °C, which was too brittle to be of any practical use in power plant. Scanning electron microscopy revealed an angular fracture surface indicative of intergranular cracking with respect to the prior austenite grains (Figure 5.19).

Such fracture is characteristic of embrittlement caused by the weakening of grain boundaries by impurity (*e.g.* phosphorus) segregation [Honeycombe and Bhadeshia, 1995]. This "temper embrittlement" is commonly found in martensitic steels. The impurity atmosphere at the boundaries evaporates at temperatures in excess of 600 °C, the segregation being most prominent during tempering in a lower range at about 500–575 °C. Consequently, it was suspected that the segregation (of phosphorus) occurred during slow cooling from the stress-relieving heat treatment temperature.

An alternative heat treatment of 640 °C for 10 minutes followed by an oil quench was therefore carried out on further samples [Davin, 1995], and succeeded in removing the temper embrittlement. The Charpy energy recovered to 60 J after this heat treatment, and the scanning electron microscopy analysis shows mainly ductile fracture.

It is therefore apparent that the poor toughness data obtained for the $3\frac{1}{2}$Ni weld deposit were due to impurity induced embrittlement which could be eliminated by cooling rapidly from the stress-relief temperature. This shows the dependence of the mechanical properties on the cooling rate.

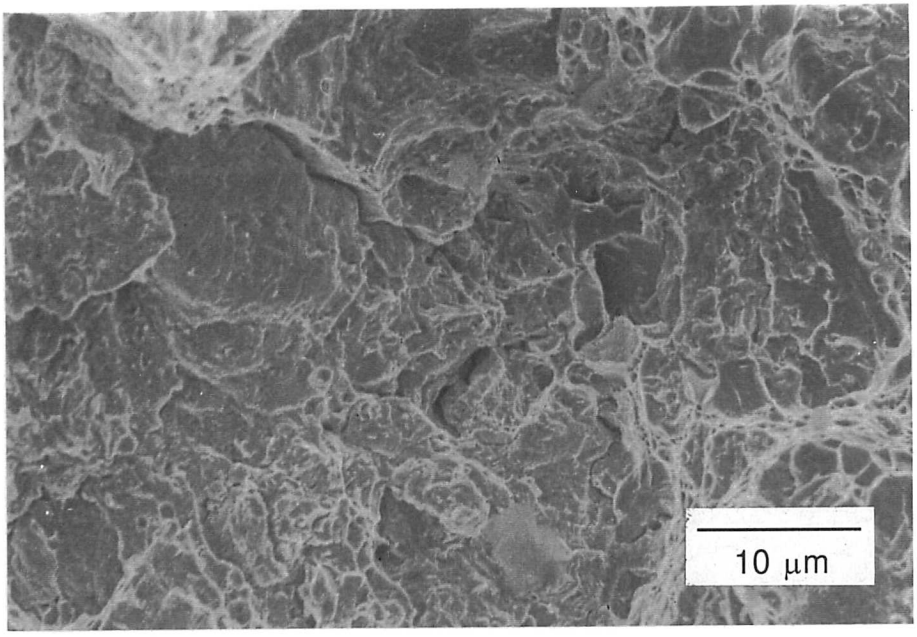

Figure 5.19: Scanning electron micrograph of the first specimen showing exposed prior austenite grain boundaries, and clear evidence for intergranular fracture.

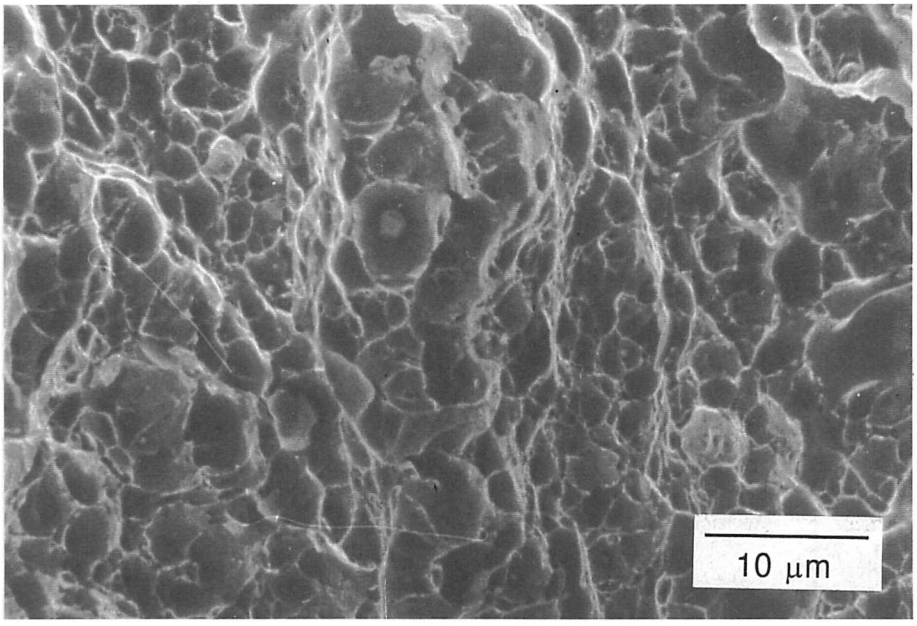

Figure 5.19: Scanning electron micrograph of the rapidly cooled specimen, showing the ductile dimpled surface.

5.11 Conclusions

A neural network method based within a Bayesian framework has been used to rationalise an enormous quantity of published experimental data on the yield and tensile strengths of steel weld deposits. It is now possible therefore, to estimate the strength as a function of the chemical composition, welding conditions and a variety of heat treatment parameters.

The models formulated have been applied towards the understanding of alloys used typically in the construction of power plant. It has been demonstrated that the models not only give good estimates of the strength, but also identify areas which require detailed investigation. The latter is a feature of the Bayesian method which permitted the expression of model-perceived uncertainty as a function of position in the input space.

Although the model has here been applied to power plant alloys, it has much wider applicability since the data used for training purposes included all varieties of welding materials.

CHAPTER SIX

Analysis of Elongation and Toughness

6.1 Introduction

Elongation is a measure of ductility in a tensile test. Its value depends on the gauge length over which the elongation is measured, because the strain is not distributed uniformly over the length of the tensile specimen. The total extension consists of two components; the uniform extension and the intense localised deformation associated with the necking. (Figure 6.1).

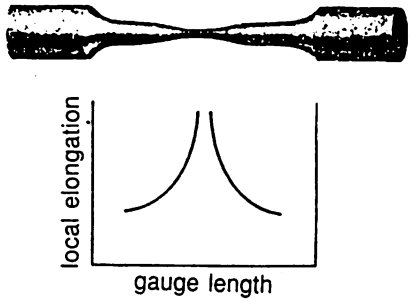

Figure 6.1: Schematic drawing of variation of local elongation with position along gauge length of tensile specimen [Dieter, 1988].

In order to compare elongation measurements from specimens of different sizes, the gauge length is taken to be $5.65\sqrt{A}$ for sheet specimens and $5.0\sqrt{A}$ for round sectioned specimens, where A is the cross sectional area [Deiter, page 295, 1988]. Although it is not clear whether the data reported in the literature are consistent with these values, it might reasonably be assumed that most industrial tests are done to these or similar specifications.

A test used to characterise toughness is the Charpy test, in which a square sectioned, notched bar is fractured under specified conditions [Knott, 1973]. The energy absorbed during fracture is taken as a measure of toughness. The Charpy test is empirical in that the data cannot be used directly in engineering design. For welded samples there are particular difficulties with Charpy tests, since most welds are inhomogeneous on many scales. The test is nevertheless a useful quality control procedure which is specified widely in international standards and in the ranking of samples in research and development experiments.

The work presented here is an attempt to understand the elongation and Charpy toughness as a function of the variables such as the chemical composition, test temperature and welding conditions. This list of variables is by no means exhaustive in determining the ductility and toughness, but it is a pragmatic approach given the nature of the data available in the reported literature.

6.2 The Elongation Model

The neural network methods described in the previous chapter were applied to a dataset prepared for the prediction of elongation. This dataset consisted of 482 cases, and contained the same inputs as the UTS model, as well as including the UTS itself as a variable (Table 6.1).

Variable	Range	Mean	Standard Deviation
Carbon weight %	0.029–0.16	0.077	0.017
Silicon weight %	0.04–1.14	0.35	0.15
Manganese weight %	0.27–2.22	1.22	0.36
Sulphur weight %	0.004–0.140	0.010	0.008
Phosphorus weight %	0.004–0.25	0.012	0.012
Nickel weight %	0.00–3.15	0.16	0.55
Chromium weight %	0.00–9.35	0.66	1.97
Molybdenum weight %	0.00–1.50	0.18	0.37
Vanadium weight %	0.00–0.24	0.02	0.05
Copper weight %	0.00–1.63	0.08	0.24
Cobalt weight %	0.00–2.80	0.02	0.02
Tungsten weight %	0.00–2.99	0.02	0.02
Oxygen p. p. m. w.	132–1650	446	156
Titanium p. p. m. w.	0–690	51	94
Boron p. p. m. w.	0–69	1	6
Niobium p. p. m. w.	0–985	61	169
Heat Input kJ mm^{-1}	1–4.8	1.7	1.1
Interpass Temperature °C	100–300	207	45
Tempering Temperature °C	0–760	322	241
Tempering Time hours	0–14	6	6
Yield Strength MPa	329–920	500	89
Ultimate Tensile Strength MPa	447–1151	598	93
Elongation %	10.6–36.4	25.8	4.9

Table 6.1: The variables for the elongation model. The abbreviation p. p. m. w. stands for parts per million by weight.

As in the case of the yield strength analysis, several neural network models were created. Their noise levels (σ_ν) and test errors (T_{en}) are shown in Figure 6.2.

Again, the committee approach was adopted, and the models were ranked in order of test error (Table 6.2 and Figure 6.3). The calculated values of the first twenty-six committees for this analysis are

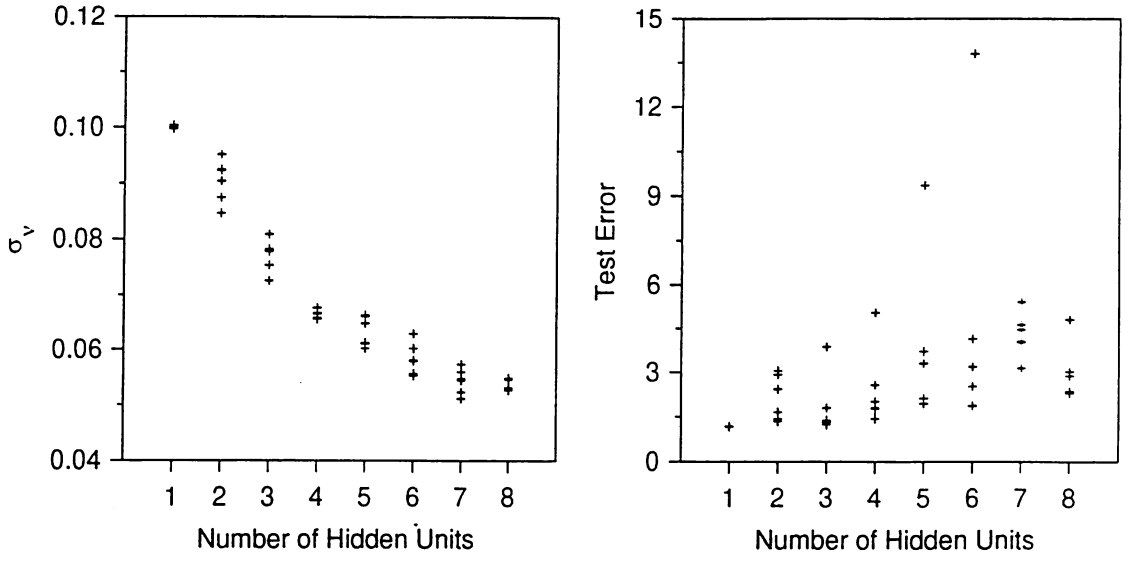

Figure 6.2: Variation in σ_ν and in test error as a function of the number of hidden units. Several values are presented for each set of hidden units because the training for each network was started with a variety of random seeds.

shown in Figure 6.3. The two plots in this figure are drawn to the same scale to emphasise the reduction in test error brought about by using the committee approach.

Ranking	Hidden Units	Seed	Test Error	Ranking	Hidden Units	Seed	Test Error
1	1	50	1.1677	14	2	15	1.6544
2	1	15	1.1678	15	4	35	1.7624
3	1	35	1.1680	16	3	35	1.7930
4	1	40	1.1693	17	4	40	1.8025
5	1	5	1.1730	18	6	5	1.8698
6	1	100	1.1772	19	5	40	1.9445
7	3	100	1.2365	20	4	15	2.0114
8	3	50	1.3207	21	5	5	2.1173
9	3	40	1.3335	22	2	5	2.4292
10	2	50	1.3457	23	6	15	2.5182
11	3	5	1.3811	24	4	100	2.5663
12	2	40	1.4276	25	2	35	2.9189
13	4	5	1.4333	26	2	100	3.0457

Table 6.2: Ranking of the twenty-six best models by test error.

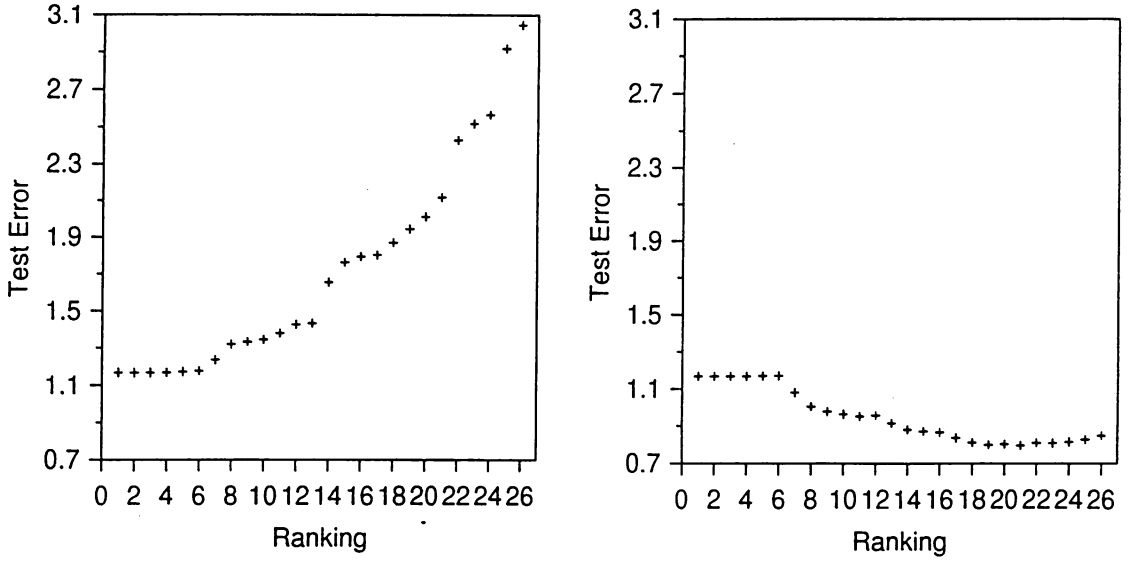

Figure 6.3: Test error of the top twenty-six ranked elongation models, and test error of the committees of these models.

The test error goes through a minimum for the committee made up of twenty-one models (Table 6.3). It is this committee which was used in all subsequent analyses.

Models in Committee	Test Error	Models in Committee	Test Error
1	1.1677	14	0.8801
2	1.1674	15	0.8713
3	1.1674	16	0.8658
4	1.1678	17	0.8359
5	1.1687	18	0.8114
6	1.1698	19	0.7988
7	1.0805	20	0.8027
8	1.0038	21	0.7951
9	0.9780	22	0.8096
10	0.9633	23	0.8091
11	0.9512	24	0.8143
12	0.9573	25	0.8269
13	0.9147	26	0.8462

Table 6.3: Test errors of the first twenty-six committees.

Using the method described previously, the twenty-one best models were used to form a committee

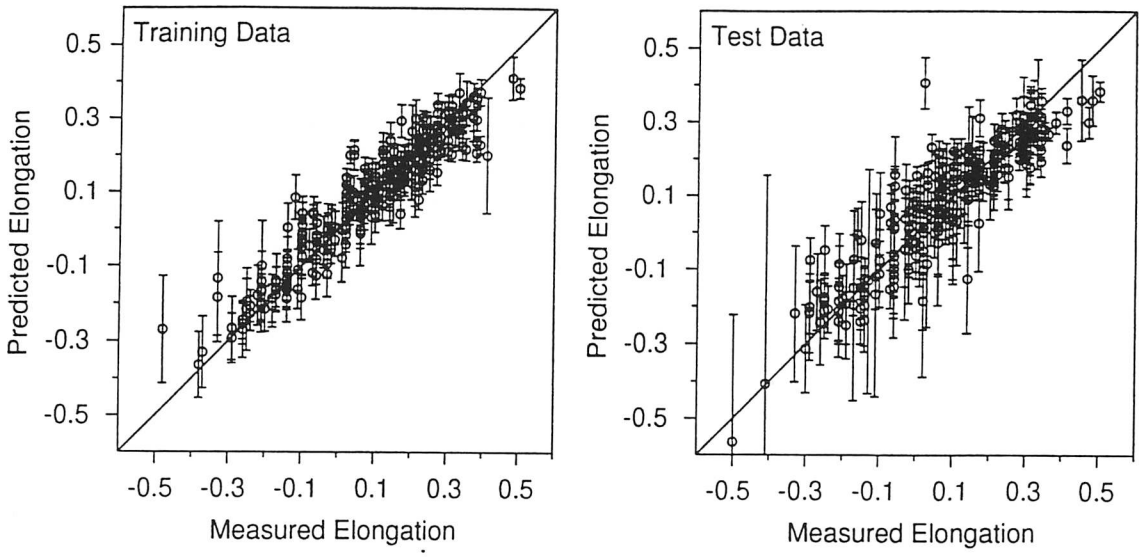

Figure 6.4: Training and test data for the committee produced from the twenty-one highest ranking models.

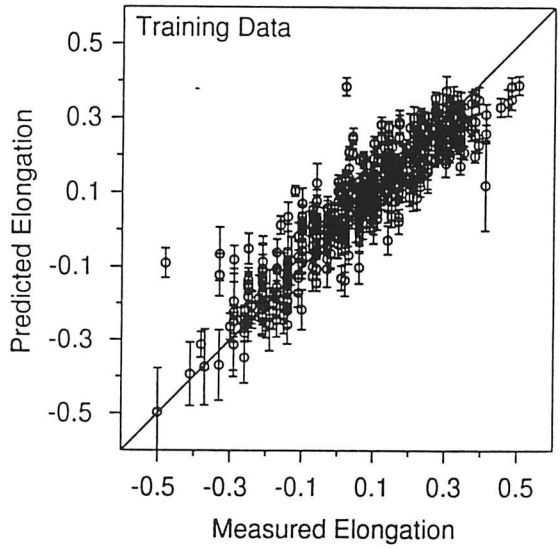

Figure 6.5: Training data for the committee produced from the twenty-one highest ranking models, trained on the *whole* data set.

model, whose training and test data are shown in Figure 6.4.

Finally, the twenty-one models making up the committee were retrained on all data, giving the final committee model as shown in Figure 6.5. As was demonstrated in the case of the UTS model, errors from predictions used as inputs to the model need to be combined with the errors associated with the model itself for a true representation of the uncertainty associated with the prediction. Hence, using notation introduced previously (Chapter 5), the errors for the elongation model are given by:

$$\sigma_e^2 = \frac{1}{L_e}\sum_{l_e} \sigma_{y_e}^{(l_e)^2} + \frac{1}{L_e}\sum_{l_e} (y_e^{(l_e)} - \overline{y}_e)^2 + \sigma_s^{\,2}\left(\frac{\partial y_e}{\partial x_s}\right)^2 + \sigma_u^{\,2}\left(\frac{\partial y_e}{\partial x_u}\right)^2 \qquad (6.1)$$

Where the subscript s refers to the yield strength, u to the UTS, and e to the elongation.

6.3 Further Assessment of the Elongation Model

The predicted values for the elongation of the three Oerlikon weld deposits (Chapter 2, Table 2.3) are compared against the actual values in Table 6.4. There are two values for the predicted elongation; one set made with the experimentally measured yield strength and UTS as inputs, and the other with the calculated yield strength and UTS as inputs. The agreement is found to be rather good in this case.

Steel	Measured Elongation %	Predicted Elongation % (Real YS and UTS)	Predicted Elongation % (Calculated YS and UTS)
$2\frac{1}{4}$Cr	18	21.3 ± 1.2	21.0 ± 1.5
9Cr	13	13.4 ± 2.2	13.9 ± 2.2
$3\frac{1}{2}$Ni	14	13.9 ± 2.7	14.1 ± 2.8

Table 6.4: Measured and predicted elongation values for the three steels described in Table 2.3, and used as a basis for the predictions. The error limits represent 1σ ($\pm 65\%$).

Figure 6.6 shows the model perceived significance of each of the input variables. The parameter σ_w is rather like a partial correlation coefficient in that it represents the amount of variation in elongation that can be attributed to any particular input parameter. It is emphasised that it does not necessarily represent the sensitivity of the elongation to each input.

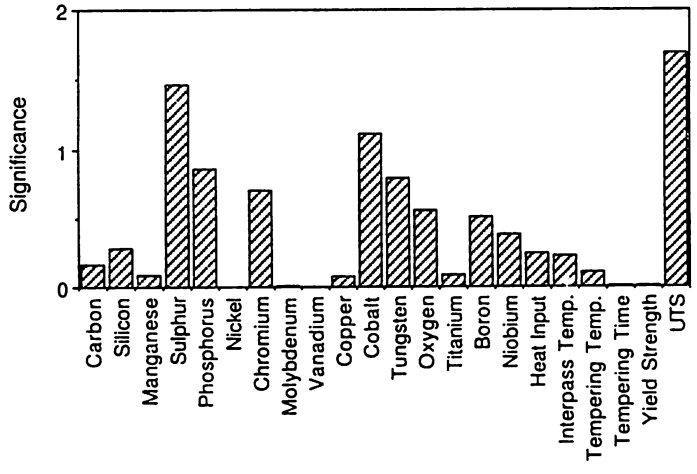

Figure 6.6: σ_w, the model-perceived significance of the input parameters to the elongation for the highest ranked model in the committee, trained on all data.

It is evident that the ultimate tensile strength has the largest σ_w value, whereas yield strength hardly features in the plot. This is an artifact of the method, since the yield strength correlates strongly with the UTS; the two are not sufficiently independent variables for the purposes of elongation. The model has therefore ascribed the variation of elongation to the UTS rather than the yield strength because that leads to a better representation of the experimental data. The fact that the yield strength has contributed to the calculation of the UTS (Chapter 5) shows that this is the better of the two choices, as the UTS

will contain information about both itself and the yield strength. In fact it is extremely well established in the literature [Dieter, pp 320-321, 1988] that in general the elongation decreases as the strength is increased.

These trends are confirmed in the present analysis as illustrated in Figure 6.7. It is emphasised that these calculations are done without permitting any of the other variables to change. They are impossible to reproduce in practice.

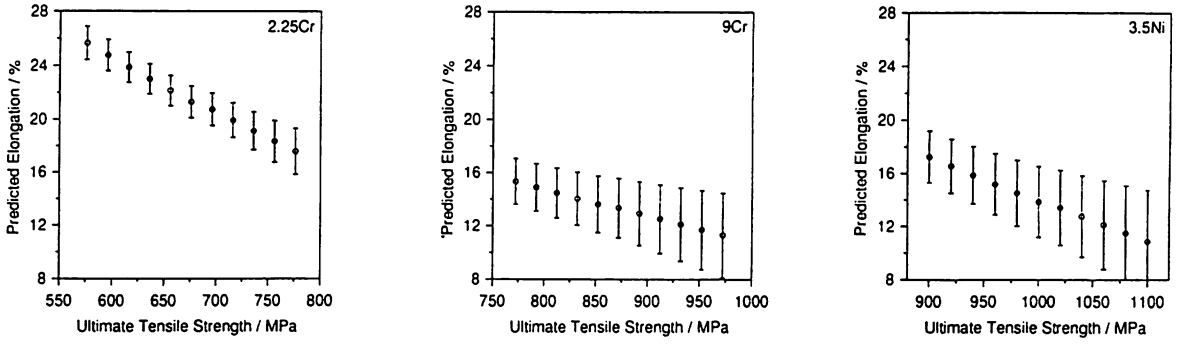

Figure 6.7: Predicted variations elongation with UTS variation.

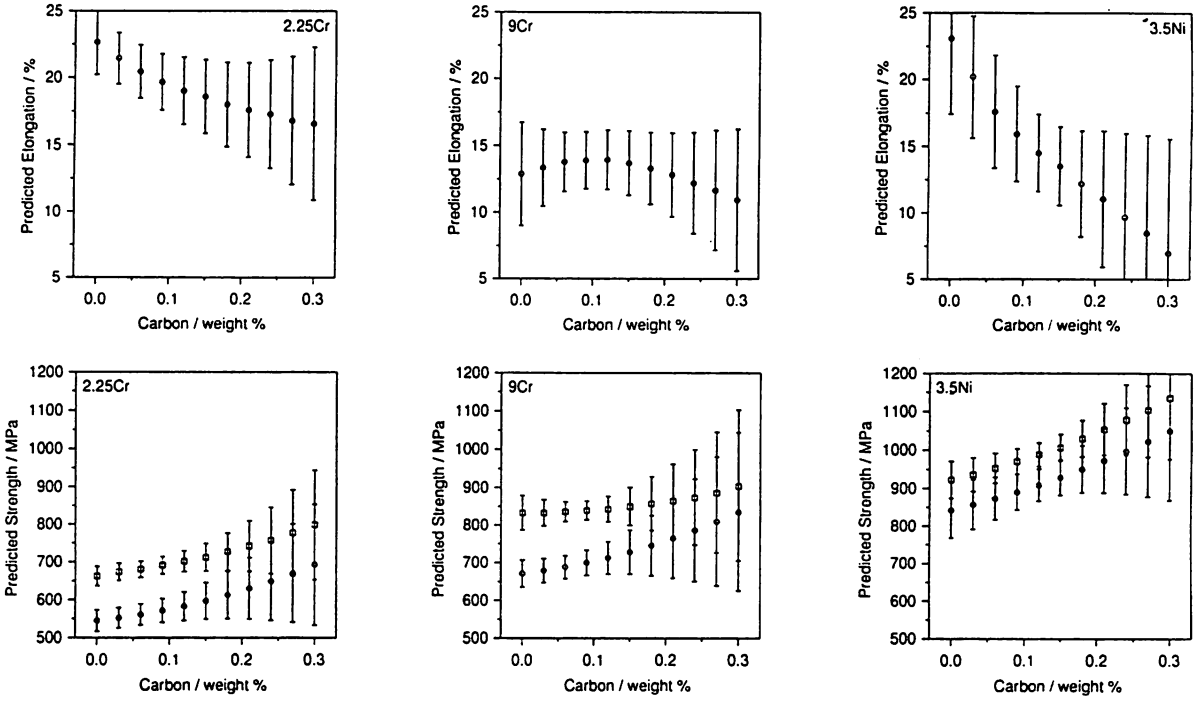

Figure 6.8: Predicted variations in the elongation as a function of the carbon concentration. The yield strength and UTS calculations are reproduced from Chapter 5 for comparison purposes.

Further analysis was carried out to examine the effect of changing each of the inputs on the elongation for the $2\frac{1}{4}$Cr, 9Cr and $3\frac{1}{2}$Ni alloys. In general only those cases for which trends are statistically meaningful are illustrated.

Figure 6.8 shows the influence of carbon on elongation; the lower set of figures represent strength and are reproduced from Chapter 5. It is clear that the elongation decreases as the strength increases. For the 9Cr steel, there is no statistically significant variation in the strength with carbon concentration — consequently, there is no statistically meaningful variation in the elongation, either.

By way of contrast, nickel in all cases significantly increases the strength and therefore significantly reduces the elongation (Figure 6.9).

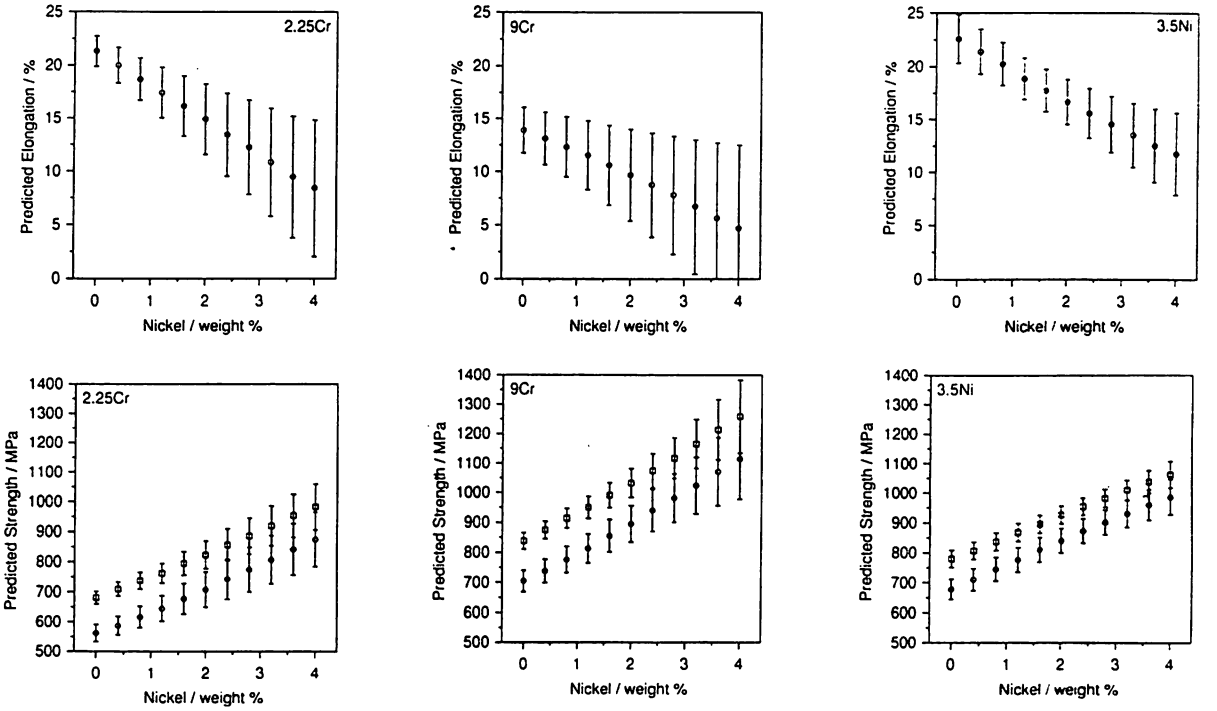

Figure 6.9: Predicted variations in the elongation as a function of the nickel concentration. The yield strength and UTS calculations are reproduced from Chapter 5 for comparison purposes.

This general trend was found to be true for all of the major alloying elements studied and for tempering time and temperature, so the results are not reproduced here. However, it is interesting to examine the rôle of trace impurities. As might be expected, the model could not perceive any meaningful effect of phosphorus. This is because phosphorus has its main effect on toughness by segregation to the grain boundaries. It does not affect the slow strain rate tensile test except when failure occurs at grain boundaries, which is rare in all commercial welds of the type included in the database. It is also suspected that there must be large inaccuracies in the reported values of phosphorus concentrations.

It was, on the other hand, possible for the model to perceive that both sulphur and oxygen reduce ductility (Figure 6.10). It is well established that both of these elements are present in precipitates which help nucleate voids. It is the linking up of these voids which leads to tensile failure and loss of ductility. Indeed, there is a semi-empirical equation describing the non uniform component of elongation as follows;

$$\text{non-uniform elongation \%} = 100 \times \beta \frac{A_0^{0.5}}{L_0} \tag{6.2}$$

Where β is Barba's constant, and A_0 and L_0 represent the cross sectional areas and gauge lengths respectively. Barba's constant is expressed as a function of the oxygen and sulphur concentrations.

$$\beta \simeq 1.239 - 9.372 \times [(\text{wt.\% O}) + (\text{wt.\% S})] \tag{6.3}$$

so that both elements reduce elongation.

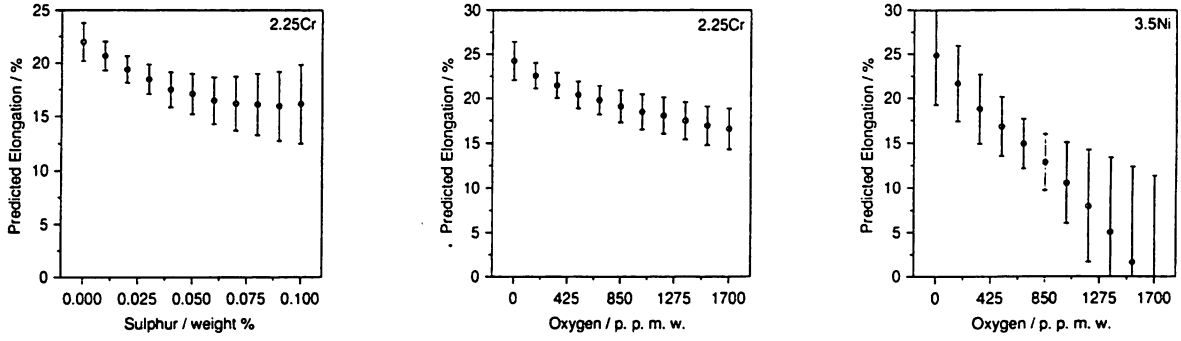

Figure 6.10: Predicted variations in elongation with oxygen and sulphur variation. These three examples illustrate the sets of predictions for which trends are statistically significant.

In summary, a reasonable model has been obtained for elongation. It appears that this parameter is affected largely by the strength and weld inclusion content, as might be expected from a metallurgical point of view.

6.4 Toughness Model

The database for the impact toughness model is summarised in Table 6.5. Its 662 cases contain similar inputs to the previous models. Nitrogen is an important variable in the analysis of toughness, so only those data having nitrogen present were included. Unfortunately, all the lines in the database containing tungsten were lacking in nitrogen, which necessitated the removal of tungsten from the database. However, the influence of tungsten would to some extent be included, as it makes a contribution to the yield strength. A further input variable was added — the temperature at which the impact test had been carried out.

As was the case for the previous analyses, several neural network models were created. Their noise levels (σ_ν) and test errors (T_{en}) are shown in Figure 6.11.

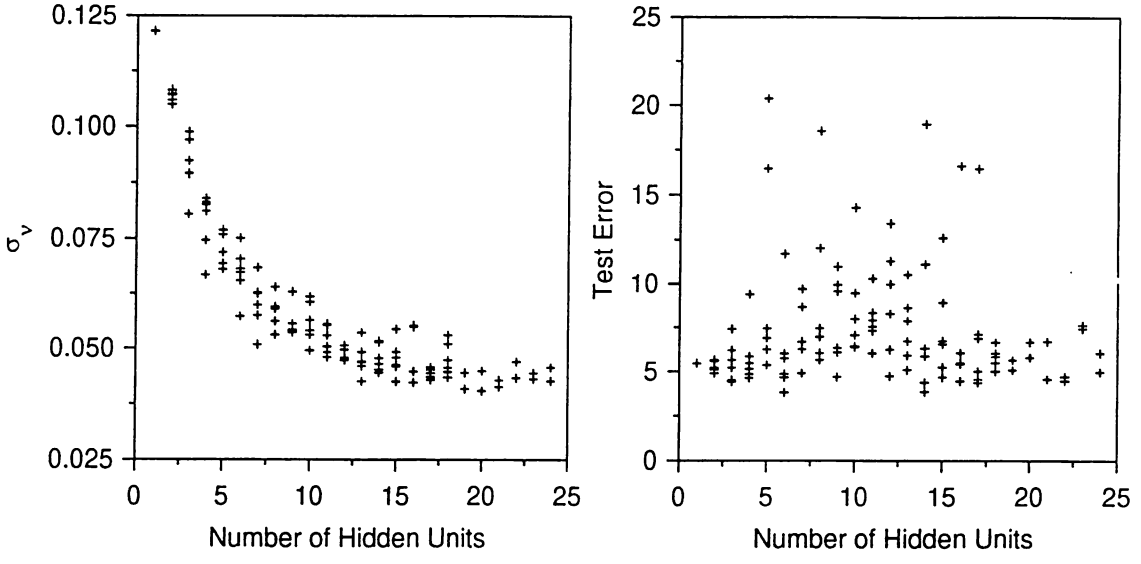

Figure 6.11: Variation in σ_ν and in test error as a function of the number of hidden units. Several values are presented for each set of hidden units because the training for each network was started with a variety of random seeds.

During their training, the models try to minimise both σ_ν and T_{en}. It is known that Charpy toughness measurements are prone to noise, an excessive reduction in the σ_ν value could result in the modelling of this noise rather than the data. It is possible to adjust the model so that σ_ν is kept constant for the training, and T_{en} is minimised for this value of σ_ν. Two sets of models with fixed σ_ν of 0.10 and 0.15 respectively were trained, and their test errors are plotted in Figure 6.12.

Again, the committee approach was taken, and all three sets of models were ranked in order of test error (Table 6.6). Committees of increasing size were examined for each set of models, ranked in order of test error. The calculated values of the first ten committees for the three analyses are shown in Figure 6.13 and Table 6.7. The three plots in Figure 6.13 are drawn to the same scale so the success of fixing of the two different values of σ_ν can be compared.

It can be seen from Figure 6.13 that the committees formed from the set of models with the free σ_ν give a lower test error compared to the models with fixed σ_ν. The test error goes through a minimum

Variable	Range	Mean	Standard Deviation
Carbon weight %	0.03–0.14	0.08	0.02
Silicon weight %	0.08–0.68	0.32	0.10
Manganese weight %	0.58–2.25	1.24	0.38
Sulphur weight %	0.002–0.14	0.010	0.016
Phosphorus weight %	0.004–0.25	0.014	0.028
Nickel weight %	0.00–3.15	0.15	0.52
Chromium weight %	0.00–9.10	0.90	2.16
Molybdenum weight %	0.00–1.30	0.22	0.42
Vanadium weight %	0.00–0.27	0.03	0.07
Copper weight %	0.00–1.63	0.07	0.24
Cobalt weight %	0.00–0.01	0.0001	0.011
Oxygen p. p. m. w.	132–922	437	131
Titanium p. p. m. w.	0–460	53	82
Nitrogen p. p. m. w.	21–480	103	83
Boron p. p. m. w.	0–69	1	8
Niobium p. p. m. w.	0–985	63	181
Heat Input kJ mm^{-1}	1–4.8	1.6	1.2
Interpass Temperature °C	100–300	198	32
Tempering Temperature °C	0–760	253	295
Tempering Time hours	0–14	4	5
Yield Strength MPa	329–920	502	94
Test Temperature °C	−114–70	−36	36
Charpy Impact Energy J	3–212	79	45

Table 6.5: The variables for the toughness model.

for this set with a committee formed of five models.

Using the method described previously, these five best models were combined to give a committee model, whose training and test data are shown in Figure 6.14a. Finally, the five models making up the committee were retrained on all data, giving the final committee model as shown in Figure 6.14b.

This model, trained on all the available data, was used for the predicting the trends which follow.

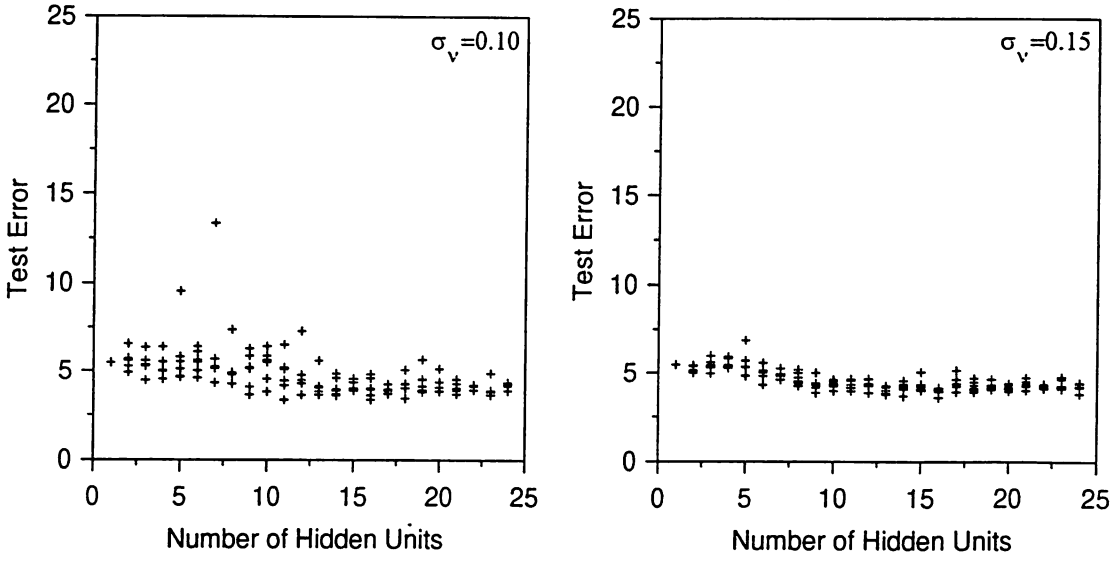

Figure 6.12: Variation in test error as a function of the number of hidden units for neural network runs with fixed σ_ν values.

	"free" σ_ν			$\sigma_\nu = 0.10$			$\sigma_\nu = 0.15$		
Ranking	Hidden Units	Seed	Test Error	Hidden Units	Seed	Test Error	Hidden Units	Seed	Test Error
1	6	100	3.8243	11	5	3.3475	16	100	3.578
2	14	40	3.8569	16	100	3.3776	14	40	3.6654
3	17	5	4.3854	18	100	3.4494	13	100	3.7477
4	14	50	4.3981	14	5	3.6026	24	5	3.7934
5	3	50	4.4235	16	5	3.6196	13	5	3.8219
6	16	40	4.4725	12	50	3.6256	12	50	3.8521
7	22	40	4.5044	23	50	3.6377	9	50	3.8531
8	3	35	4.5274	9	50	3.6394	18	100	3.8795
9	17	40	4.5612	13	5	3.6407	17	35	3.9077
10	21	40	4.5927	23	100	3.6515	16	35	3.9153

Table 6.7: Ranking of ten best models for the three sets of σ_ν values by test error.

Models in Committee	Test Error, "free" σ_ν	Test Error, σ_ν= 0.10	Test Error, σ_ν= 0.15
1	3.8243	3.3475	**3.5780**
2	3.3802	**3.1728**	3.5805
3	3.2225	3.2513	3.6171
4	3.2269	3.2613	3.6631
5	**3.1688**	3.2986	3.6752
6	3.2106	3.2607	3.6940
7	3.1878	3.2657	3.7034
8	3.1927	3.2864	3.7181
9	3.2025	3.3067	3.7310
10	3.2067	3.3217	3.7418

Table 6.7: Test errors of the first ten committees for all sets of σ_ν. Bold type indicates the minimum test error for each set of committees.

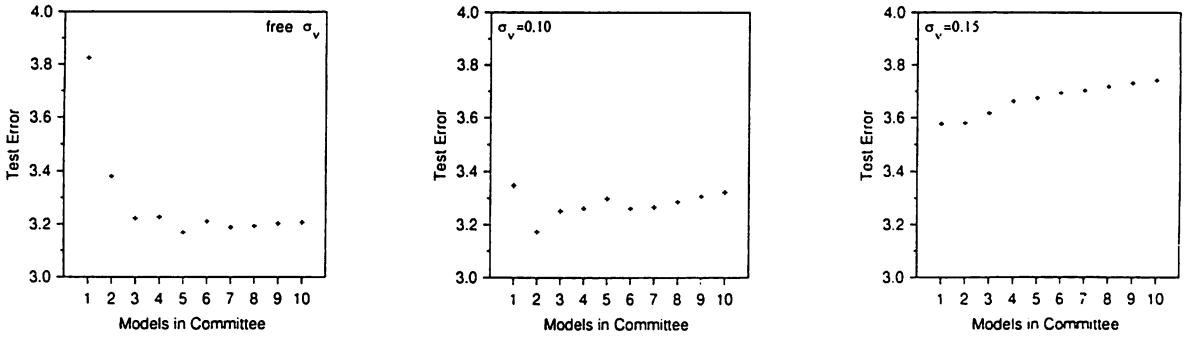

Figure 6.13: Test error of the top ten committee models for a free σ_ν, a fixed σ_ν of 10 %, and 15 %.

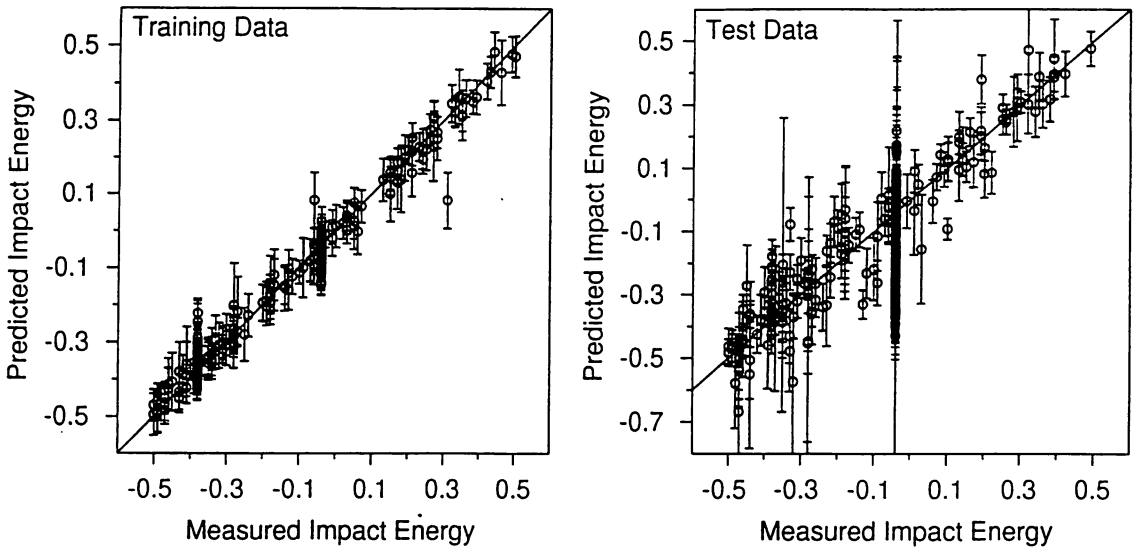

Figure 6.14a: Training and test data for the committee produced from the five highest ranking models.

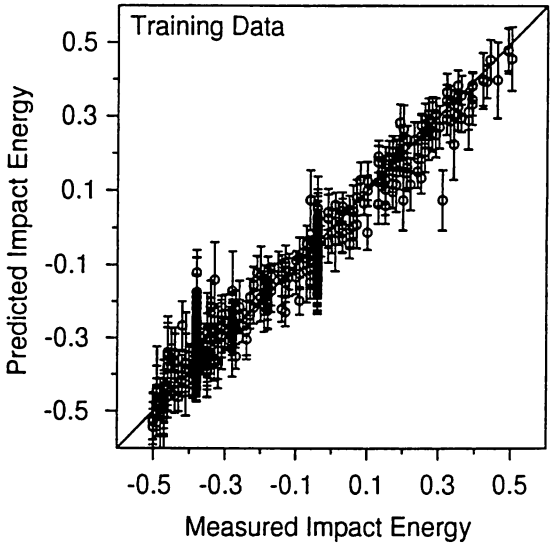

Figure 6.14b: Training data for the committee produced from the two highest ranking models, trained on the *whole* data set.

6.5 Application of the Model

As was demonstrated in the UTS and elongation models, errors from predictions used as inputs to the model need to be combined with the errors associated with the model itself for a true representation of the uncertainty associated with the prediction. Hence, using notation introduced previously, the errors for the toughness model are expressed by:

$$\sigma_t^2 = \frac{1}{L_t}\sum_{l_t} \sigma_{y_t}^{(l_t)^2} + \frac{1}{L_t}\sum_{l_t} (y_t^{(l_t)} - \overline{y}_t)^2 + \sigma_s{}^2 \left(\frac{\partial y_t}{\partial x_s}\right)^2 \tag{6.4}$$

where the subscript s refers to the yield strength, u to the UTS, and t to the toughness.

Figure 6.15 shows the significance attached by a typical member of the committee, to each of the input variables. The vertical axis can be thought of as a partial correlation coefficient for each input. The test temperature, yield strength and tempering conditions feature strongly as might be expected.

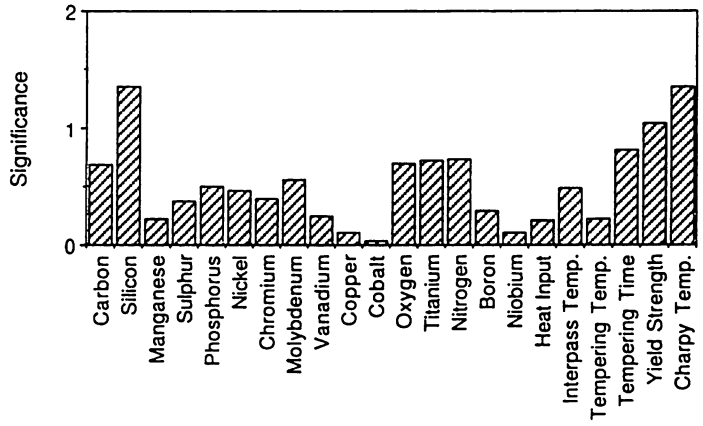

Figure 6.15: σ_w, the model-perceived significance of the input parameters to the toughness for the highest ranked model in the committee trained on all data.

The toughness values for the three Oerlikon welds are presented in Table 6.8. It can be seen that the model provides excellent predictions for these cases.

Steel	Measured Impact Energy J	Predicted Impact Energy J (Real YS)	Predicted Impact Energy J (Calculated YS)
$2\frac{1}{4}$Cr	180, 168, 163	171 ± 9	171 ± 14
9Cr	34, 57, 38	43 ± 9	48 ± 55
$3\frac{1}{2}$Ni	8, 5, 8	7 ± 9	11 ± 48

Table 6.8: Measured and predicted Charpy impact energies for the three steels described in Chapter 2 Table 2.3. The error limits represent 1σ ($\pm 65\%$).

The metallurgical significance of the model was examined for a carbon manganese steel which had not been included in the weld training database, taken from the literature [Evans, 1982a]. The composition of this weld is shown in Table 6.9. It was examined in the as-welded condition.

The effect of the temperature is shown in Figure 6.16. It is satisfying that the curve has the expected sigmoidal shape, since steels undergo a ductile-brittle transition. Fracture at high temperature is ductile by a void nucleation and coalescence mechanism, whereas at low temperature cleavage takes place.

Carbon weight %	0.098	Oxygen p. p. m. w.	400
Silicon weight %	0.32	Nitrogen p. p. m. w.	90
Manganese weight %	1.05	Yield Strength MPa	477
Sulphur weight %	0.007	Heat Input kJ mm^{-1}	1
Phosphorus weight %	0.009	Interpass Temperature °C	200

Table 6.9: Evans' C-Mn weld deposit used for the toughness analysis.

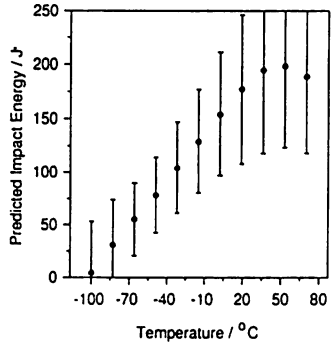

Figure 6.16: Plot showing the predicted variation in toughness with temperature for the C-Mn weld.

An increase in the carbon concentration increases both the strength and the inclusion content via the precipitation of cementite. Both of these factors contribute to a decrease in the upper shelf energy of the impact transition curve[1] [Pickering, 1978, page 118]. The failure mechanism there is by void nucleation at inclusions and void coalescence; the cementite particles nucleate voids. Calculations for Charpy tests at 20 °C are consistent with this (Figure 6.17) in that there is a downward trend, but the results are not statistically meaningful.

For cleavage fracture, the effect of carbon is first to cause an improvement in the microstructure from one which is dominated by coarse allotriomorphic ferrite to one which is predominantly acicular ferrite [Evans, 1982a, Bhadeshia and Svensson, 1993]. As the carbon concentration is increased further, the accompanying increase in strength overcomes any smaller changes in microstructure so that the resistance to cleavage fracture becomes smaller. Consequently, the cleavage toughness is expected to peak as a function of carbon concentration [Bhadeshia *et al.*, 1995]. The calculations for a test

[1] The impact transition curve is a plot of energy absorbed versus test temperature.

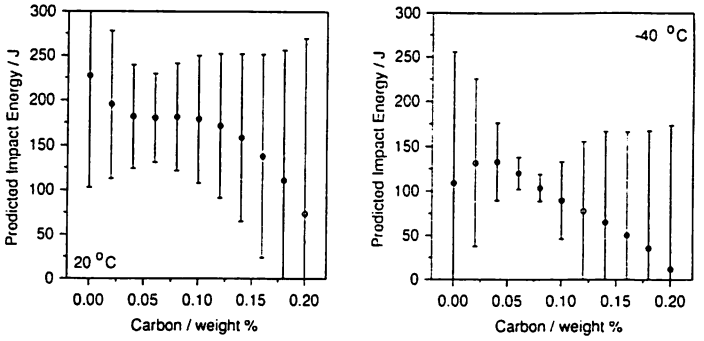

Figure 6.17: Predicted variations in toughness of the C-Mn weld with carbon concentration at two temperatures, 20 °C and −40 °C.

temperature of −40 °C again confirm the trends (Figure 6.17b), though the uncertainties are again rather large.

The results for phosphorus and sulphur are illustrated in Figure 6.18. It has not been possible to perceive significant trends.

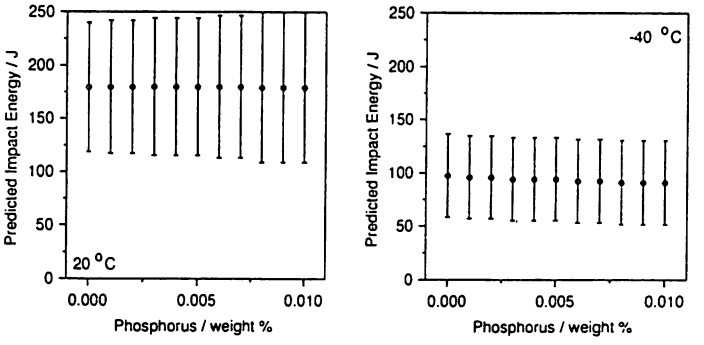

Figure 6.18a: Predicted variations in toughness with phosphorus concentration at two temperatures, 20 °C and −40 °C.

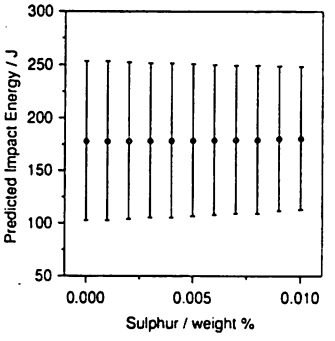

Figure 6.18b: Plot showing the predicted variation in toughness with changes in the sulphur concentration for the C-Mn weld.

6.6 Summary

It has been found possible to model the Charpy toughness of steel welds as a function of many variables. The model also seems to recognise metallurgically correct relationships, for example, the ductile-brittle transition temperature. Nevertheless, there remains a great deal of uncertainty in the prediction of toughness. This is not because there is an inordinate amount of noise in the experimental data. Judging from the σ_ν values, the reproducibility of the Charpy data is, for 95 % confidence limits, about ± 15 %. The fact that in many cases the error bars obtained for the predictions are much larger implies that there are insufficient data on which the models have been trained. Finally it is likely that the noise level in some of the inputs is larger than the ± 15 % discussed above. For example, it is conceivable that the spectroscopically determined minute concentrations of phosphorus have errors of 100 %.

CHAPTER SEVEN

A Design Process Illustrated

7.1 Introduction

Many of the phenomena treated in this work are complex in the extreme. Consequently, a great deal of effort has been expended in validating the models produced. This is both to inspire confidence in the techniques used, and to assess whether the panoply of "tools" created is actually sufficient to provide a complete engineering solution. This chapter deals with the latter problem; a novel welding alloy has been designed for a specific application beginning with nothing but engineering design criteria and the models. Although the details of the application are proprietary, the design process can nevertheless be illustrated without sacrificing any of the inherent originality and value.

7.2 Validated Models

The models that now exist include a capability for estimating the yield and ultimate tensile strengths, the tensile elongation and Charpy toughness. These have been validated on vast quantities of "test" data, on additional blind data provided in various challenges, and on experimental programmes in progress at the University of Cambridge. These models have also been assessed to ensure, as far as is possible, that they comply with known metallurgical principles. There also exists a full capability for estimating the martensite-start temperature of steels. Finally, there is an awareness of the rôle of solute elements in inducing the formation of austenite during stress relief heat treatments, and of the need to avoid δ-ferrite formation.

7.3 The Task

It is often the case in power plant that steels of different chemical composition have to be joined together by welding, using the manual metal arc (MMA) and submerged arc (SA) welding processes. The particular task here was to design a welding alloy to join a 2CrMoNiWV steel to a $3\frac{1}{2}$NiCrMoV steel (Table 7.1), taking into account dilution effects and ensuring that the mechanical properties of the weld are consistent with the plates joined, both in the as-welded and in the post weld heat treated conditions. Table 7.1 shows the compositions of the base steels and the proposed weld along with the tolerance limits needed for manufacture. Mechanical properties are also provided — design specifications for the parent steels and targets for the weld. The heat treatment rows give information on the stress relieving heat treatment for the weld, along with the final tempering heat treatments from the manufacturing process for the base steels.

7.4 Detailed Design Criteria

1. It was specified that the strength of the weld should be comparable to the weaker of the two base steels; any additional strength would not be useful in the engineering design, with the additional disadvantage that toughness might be reduced.
2. The proposed composition and heat treatment should not be overly sensitive to small changes of the kind inevitable in practice. Nor should the composition be unnecessarily ambitious with respect to the control of impurity elements, in order to minimise manufacturing costs.

Variable	2CrMoNiWV wrought steel	Proposed Weld	Tolerance limits	$3\frac{1}{2}$NiCrMoV wrought steel
Carbon weight %	0.23	0.07	0.06–0.1	0.25
Silicon weight %	0.25	0.4	0.35–0.45	0.3
Manganese weight %	0.7	1.0	0.9–1.1	0.4
Sulphur weight %	0.015	0.01	<0.01	0.015
Phosphorus weight %	0.015	0.01	<0.01	0.015
Nickel weight %	0.75	2	1.8–2.2	3.5
Chromium weight %	2.1	1.6	1.6–1.8	1.6
Molybdenum weight %	0.85	0.6	0.55–0.7	0.5
Vanadium weight %	0.32	–	minimal	0.13
Copper weight %	0.20	–	minimal	0.20
Tungsten weight %	0.65	–	minimal	0
Oxygen p.p.m.w.	n/a	300	<350	n/a
Nitrogen p.p.m.w.	n/a	50	<150	n/a
Aluminium weight %	0.015	0.015	<0.02	0.015
Yield Strength MPa	>600	>650		>700
Ultimate Tensile Strength MPa	730–850	>750		800–950
Elongation %	>18	>18		>18
Charpy Toughness J	<25	>54		>54
Heat Treatment °C	650	650		620
Heat Treatment hours	5	8		22.54

Table 7.1: Mean chemical compositions of 2CrMoNiWV and $3\frac{1}{2}$NiCrMoV, together with mechanical property data. The weld composition is new, and its mechanical properties are targets, not measured values.

3. The chemical potential of carbon will not be uniform across the dissimilar metal weld. There is a possibility that carbon may migrate over long distances during post weld heat treatment, creating carbon-rich regions with a deterioration in mechanical properties. The welding alloy should be such as to minimise this problem.
4. The post weld heat treatment should not adversely affect the properties of the parent plates. The industrial requirement was at first a temper of 700 °C for 3 hours, but this was later changed to 650 °C for 8 hours to allow large assemblies to achieve thermal equilibrium.

5. Creep properties are not relevant in the design process.

7.5 Chemical Composition

An original suggestion was that a classic $2\frac{1}{4}$Cr1Mo weld should be adequate for the suggested design criteria, but this was demonstrated by calculation to be too weak. Comparative data for $2\frac{1}{4}$Cr1Mo welds are included in the results that follow. To minimise dilution effects and minimise carbon migration problems, it was decided to see whether a composition approximately intermediate to the 2CrMoNiWV and the $3\frac{1}{2}$NiCrMoV met all the design criteria.

This emphasises the fact that the models cannot be interrogated to automatically select a chemical composition, since the latter is a starting point in the calculation of mechanical properties. Indeed, it is possible that there are no unique solutions to achieve a given set of mechanical properties; it is the absence of a unique solution which makes design interesting [Bhadeshia, 1995a].

The carbon concentration of the weld metal cannot be as high as that of the base materials (Table 7.1) since that would lead to extremely brittle welds, highly susceptible to hydrogen and other embrittlement phenomena. As will be seen later, a small amount of carbon is nevertheless necessary to ensure strength.

The suggested silicon and manganese concentrations were typical for weld deoxidation purposes; the manganese should also contribute beneficially to the hardenability of the weld given the low carbon concentration. It was important to keep the sulphur and phosphorus concentrations below 0.01 weight% to reduce the effect of temper embrittlement in the weld.

An intermediate nickel concentration was selected; nickel as an alloying element in steel is intrinsically good for toughness. However, weld metals containing too large a concentration of nickel would be susceptible to gross chemical segregation [Gretoft *et al.*, 1986]. Similar amounts of nickel to that proposed for this weld have been observed to reduce the Ac_1 temperature in 9Cr weld deposits (Chapter 4). This resulted in an excessive strength after post weld tempering, due to austenite formation. However, the post weld heat treatment for 9Cr welds is more severe than is required for this weld, so any reduction in the transformation temperature will not be problematic.

The chromium concentration was maintained at the same level as the $3\frac{1}{2}$NiCrMoV parent steel. This base plate can contain a very large carbon concentration so the choice of a matching Cr content would avoid dilution problems on that side of the weld. A similar rationale was applied to the molybdenum concentration.

Vanadium and tungsten were eliminated from the weld metal. Vanadium leads to welds with properties which are less reproducible, probably because it also combines with nitrogen whose concentration cannot be carefully controlled. Vanadium is also known to reduce the weld metal toughness [Levine and Hill, 1977a, 1977b, Bosansky and Evans, 1992]. Tungsten carbides tend to be coarse [Sahay *et al.*, 1992]; consequently, they should contribute little to the overall properties after the severe post weld heat treatments typical in the power plant industries.

A typical MMA weld oxygen concentration of 300 parts per million by weight (p.p.m.w) was assumed for the purpose of the calculations.

The welding conditions chosen were considered to be typical for manual metal arc welding; a heat input of 1 kJ mm^{-1} and an interpass temperature of 200 °C, well below the predicted M_S tempperature

(Chapter 3) for the proposed composition.

The post weld heat treatment temperature was chosen to be 650 °C with a tempering time of eight hours. This was selected because stress relief is not very effective at lower temperatures, and a time period which is long enough for large components to reach equilibrium was required. Other tempering treatments with temperatures in the range 600–700 °C were also carried out to investigate the sensitivity to tempering conditions.

In order to ensure that the properties in the as-welded condition were adequate, predictions were also made without high temperature heat treatment.

7.6 Application of Models

The neural network committee models analysed in previous chapters were used to predict the yield strength, UTS, elongation and Charpy impact values of the proposed weld, to ensure that the expected mechanical properties were within the target limits specified in Table 7.1. Mechanical properties were predicted for an as-welded deposit, and for three different heat treatments. These results are presented in Figure 7.1, along with the $2\frac{1}{4}$Cr1Mo data.

Figure 7.1a shows the predicted yield strength for the alloy. The dotted lines indicate the *minimum* yield strengths for the parent materials for comparison. Details of these predictions are presented, along with the error bars in Table 7.2. It is apparent from Figure 7.1a that the $2\frac{1}{4}$Cr1Mo steel has too low a strength for the application. Although the chosen tempering temperature of 650 °C gave a slightly higher yield strength than was necessary, it was decided that this was acceptable. For power plant components in service, it is not an unusual requirement to carry out repairs, which would necessitate a further heat treatment, thus reducing the strength. The lower strength weld tempered at 700 °C may not be able to accommodate such repairs. The higher strength weld tempered at 600 °C is overly strong compared to the parent steels, and the risks of an associated reduction in toughness apply in this case.

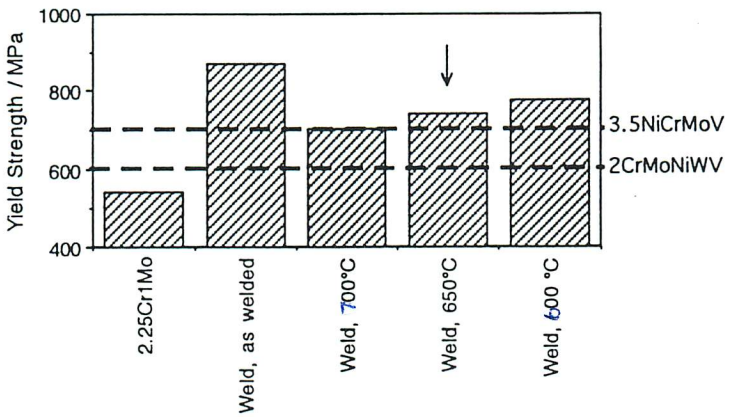

Figure 7.1a: Predicted yield strength for the proposed weld with variations in heat treatment.

Figure 7.1b illustrates the UTS of the $2\frac{1}{4}$Cr1Mo weld, and the proposed weld in the different tempered conditions. The dotted lines indicate the minimum strength of the two parent steels. Again, it can be seen that the $2\frac{1}{4}$Cr1Mo weld is inadequate for the strength needed for this application.

Temperature °C	Time hours	Yield Strength MPa	UTS MPa	Elongation %
as-welded	—	870 ±152	967 ±150	14.7 ±4
600	8	777 ±54	871 ±62	13.6 ±6
650	8	740 ±68	834 ±72	15.5 ±5
700	8	704 ±111	793 ±102	17.8 ±5

Table 7.2: Predicted mechanical properties for the steel weld at the different heat treatments. Error limits are 2σ.

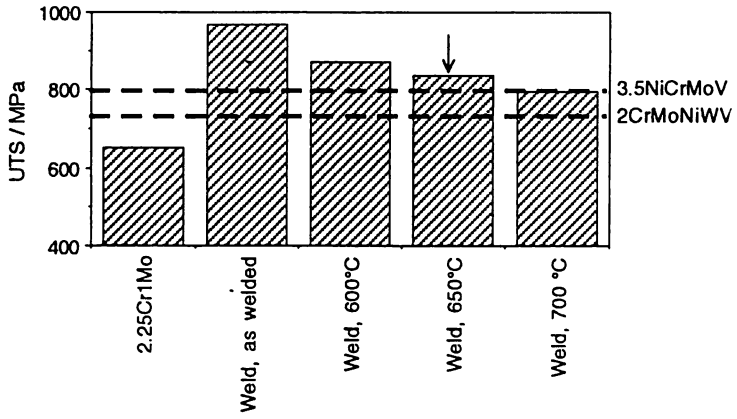

Figure 7.1b: Predicted UTS for the proposed weld with variations in heat treatment.

Figure 7.1c shows how the elongation varies with heat treatment. The dotted line represents the elongation of both parent materials. It is apparent that a heat treatment of 600 °C would provide too low an elongation.

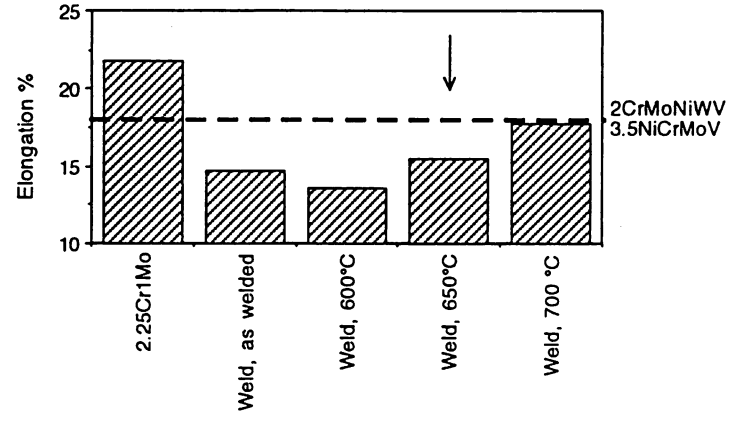

Figure 7.1c: Predicted elongation for the proposed weld with variations in heat treatment.

As was discussed in Chapter 6, error bars for the calculation of toughness are large, and hence do not provide reliable results. For this reason, toughness is not discussed here. However, calculations predicted that the impact energy of the proposed weld, tempered at 650 °C would be $\sim$ 75 J.

7.7 Sensitivity Analysis

Calculations were carried out to examine the sensitivity of the weld to reasonable variations in chemical composition. As can be seen from Figure 7.2, it was predicted to be insensitive to such variations.

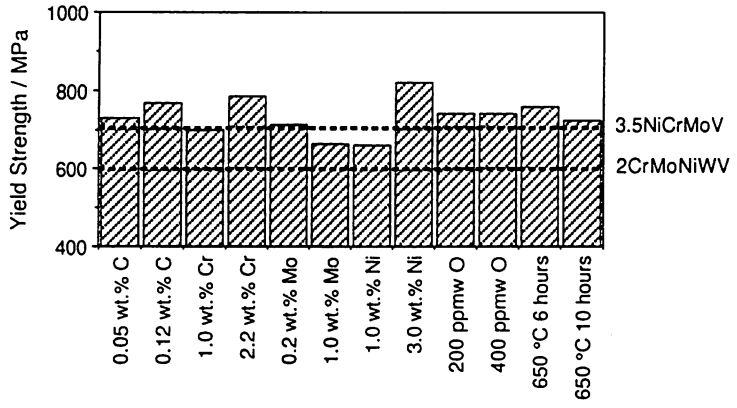

Figure 7.2a: Bar chart showing the sensitivity of the yield strength of the weld to variations in chemical composition and heat treatment.

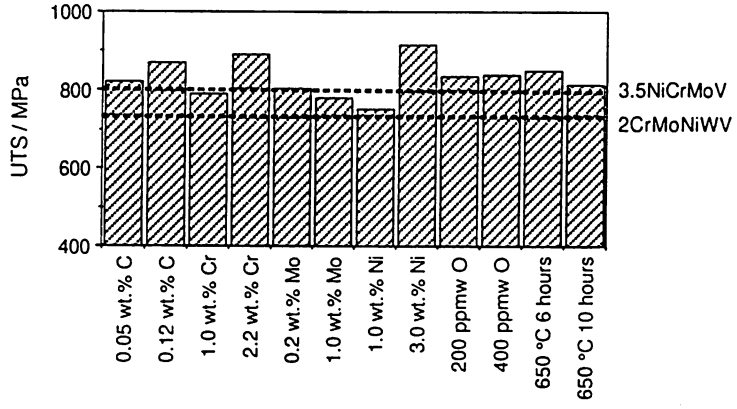

Figure 7.2b: Bar chart showing the sensitivity of the UTS of the weld to variations in chemical composition and heat treatment.

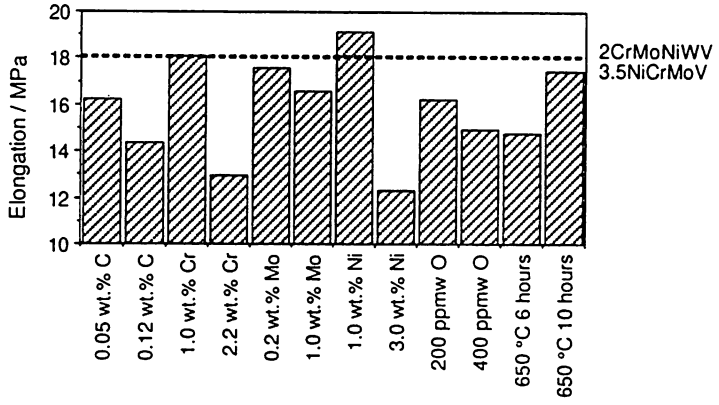

Figure 7.2c: Bar chart showing the sensitivity of the elongation of the weld to variations in chemical composition and heat treatment.

7.8 Sensitivity to Process

Should preliminary MMA tests be successful, it is intended that a weld of similar composition be produced using the submerged arc process with a much higher heat input. Calculations have shown that the effect of increasing heat input would be to reduce the strength and increase the elongation of the weld tempered at 650 °C. It was predicred that heat inputs of up to 4 kJ mm^{-1} would not reduce the strengths below their target values. This reduction of strength with increased heat input justifies the choice of this heat treatment temperature, as lower tempering temperatures would result in a weaker weld.

7.9 Physical Model

The weld composition considered here can be analysed using a model based on phase transformation theory [Bhadeshia and Svensson, 1993]; this model can be applied only to the as-welded condition, as there are no facilities for tempering effects. The predicted cooling curve is illustrated in Figure 7.3. The time to cool between 800-500 °C is found to be 11.2 s. The columnar austenite grain width $\overline{L}_{tn}$ is found to be reasonable at 98 μm. The weld metal microstructure is, as expected, predicted to be martensitic for manual metal arc welds, with a martensite-start temperature of 407 °C. The non-uniform part of the elongation is predicted to be about 15 %. The weld is predicted to be mechanically homogeneous, so that the scatter in mechanical properties should be minimal in the as-welded condition.

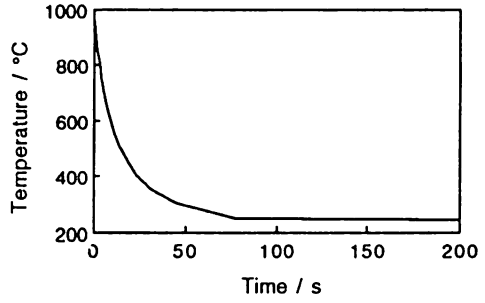

Figure 7.3: Predicted cooling curve for the weld.

7.10 Thermodynamic Analysis

Equilibrium phase stability calculations from MTDATA [1996] are presented in Table 7.3. They essentially indicate that there should not be severe problems with respect to carbon redistribution during post weld heat treatment.

7.11 Effect on Base Plates

The post weld heat treatment which is carried out will affect the properties of the base plate. A model has been developed [Cool *et. al.*, 1996] which will analyse the effects of heat treatment on the yield strength in the regions of the heat affected zone which experience a temperature greater than Ac_1 or less than Ac_3, although it does not accommodate the intercritically annealed region of the HAZ ($Ac_1 < T_i < Ac_3$). This model predicts that the proposed heat treatment will not reduce the strength of either parent material by more than 20 MPa.

Composition weight %	2CrMoNiWV Steel Ferrite 96.62%	M_2C 1.42%	$M_{23}C_6$ 1.96%	Proposed Weld Ferrite 98.64%	$M_{23}C_6$ 1.36%	$3\frac{1}{2}$NiCrMoV Steel Ferrite 95.93%	M_7C_3 0.74%	$M_{23}C_6$ 3.20%	V_3C_2 0.13%
Carbon	0.003	9.013	5.046	0.002	5.014	0.007	8.670	5.077	13.584
Silicon	0.259	–	–	0.406	–	0.313	–	–	–
Manganese	0.677	3.230	0.001	1.014	0.001	0.376	5.323	0.003	–
Sulphur	0.016	–	–	0.010	–	0.016	–	–	–
Phosphorus	0.016	–		0.010	–	0.016	–	–	–
Nickel	0.776	0.006	–	2.028	–	3.648	–	–	–
Chromium	1.029	38.753	28.336	1.187	31.496	0.589	47.895	18.843	–
Molybdenum	0.112	28.727	17.034	0.346	19.030	0.038	2.166	13.954	–
Vanadium	0.045	19.833	–	–	–	0.023	–	–	86.418
Copper	0.207	0.009	–	–	–	0.208	–	–	–
Tin	0.021	–	–	–	–	0.021	–	–	–

Table 7.3: Proportions and chemical compositions of phases in the base steels and the weld.

7.12 Dilution Effects

To examine the effect of dilution during the welding process, the mechanical properties of two intermediate compositions were found. These were chosen as 50:50 mixtures by composition of the weld and parent material, as shown in Table 7.4

Variable weight %	2CrMoNiWV +Weld	$3\frac{1}{2}$NiCrMoV +Weld	Variable weight %	2CrMoNiWV +Weld	$3\frac{1}{2}$NiCrMoV +Weld
Carbon	0.15	0.16	Chromium	1.85	1.6
Silicon	0.315	0.35	Molybdenum	0.725	0.55
Manganese	0.85	0.7	Vanadium	0.16	0.065
Sulphur	0.0125	0.0125	Copper	0.10	0.10
Phosphorus	0.0125	0.0125	Tungsten	0.326	–
Nickel	1.375	2.75	Oxygen	0.03	0.03

Table 7.4: Chemical compositions of the regions of dilution between the two parents and the proposed weld.

The predicted mechanical properties for the diluted regions are compared to the predicted properties of the weld in the Figure 7.4. It can be seen that the strength of these diluted regions would be too large, compared to the required specification. This is primarily due to the exceptionally large carbon concentrations of the base steels in comparison to the weld. In practice, this is unlikely to be a problem if the dilution is spread into a large pool of weld metal, as is the case is submerged arc welding.

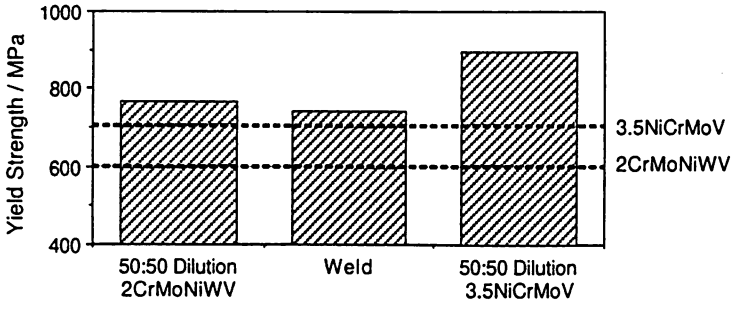

Figure 7.4a: Predicted yield strength for the composition showing 50:50 dilution between weld and parents.

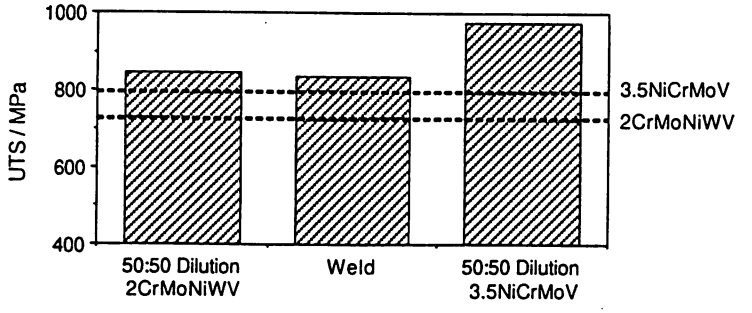

Figure 7.4b: Predicted UTS for the composition showing 50:50 dilution between weld and parents.

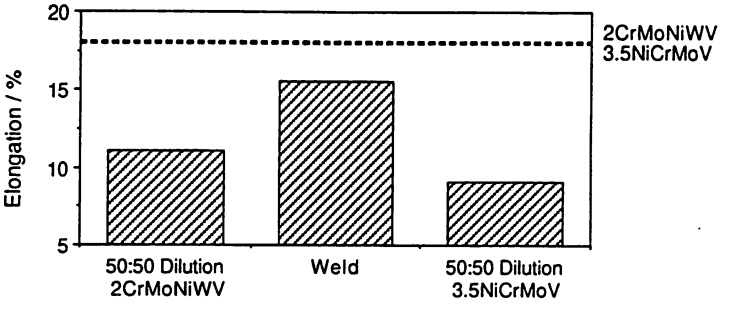

Figure 7.4c: Predicted elongation for the composition showing 50:50 dilution between weld and parents.

7.13 Weld Manufacture

Electrodes were manufactured by Oerlikon to the specifications (Figure 7.5). The chemical composition of the weld deposited using these electrodes is given in Table 7.5.

FACT SHEET

LINKWELD

* PARSONS POWER GENERATION SYSTEMS LTD
* OERLIKON WELDING LTD
* UNIVERSITY OF CAMBRIDGE

PUBLICATIONS

1 **Seth, Conroy and Goulette**
"Market forces and turbine materials innovations."
Third International Charles Parsons Turbine Conference: Materials Engineering in Turbine and Compressors.
Institute of Materials, April 1995.

---

2 **Cool and Bhadeshia**
"Prediction of Martensite start temperature of power plant steels."
Materials Science and Technology, volume 12 number 1, pp 40-44 January 1996.

---

3 **Cool, Bhadeshia and MacKay**
"Modelling the mechanical properties in the HAZ of power plant steels – 1 Bayesian neural network analysis of proof strength."
Mathematical Modelling of weld phenomena III. Institute of Materials (in press)

---

4 **Cool and Bhadeshia**
"Austenite formation in 9Cr1Mo type power plant steels."
Science and Technology of Welding and Joining (in press).

---

5 **Bhadeshia**
"Calculation of microstructure and properties of steel welds."
Griffith Conference on Fracture, 1995.

---

6 **Summerfield, Cool, Keville and Bhadeshia**
"Computer modelling of low alloy steel welds."
Welding and Metal Fabrication pp 23-24 January 1996.

---

7 **Cool, Bhadeshia and MacKay**
"The yield and ultimate tensile strength of steel welds."
Materials Science and Engineering (in press).

---

8 **Race and Bhadeshia**
"Precipitation sequence during carburization of Cr-Mo Steels."
Materials Science and Technology volume 8 pp 875-992 October 1992.

ENHANCED ENGINEERING MATERIALS

PARSONS POWER GENERATION SYSTEMS LIMITED
Heaton Works, Newcastle upon Tyne NE6 2YL
Telephone: 0191 265 0411 Telex: 53109 (CAP G) Fax: 0191 265 7610

FACT SHEET

LINKWELD

* PARSONS POWER GENERATION SYSTEMS LTD
* OERLIKON WELDING LTD
* UNIVERSITY OF CAMBRIDGE

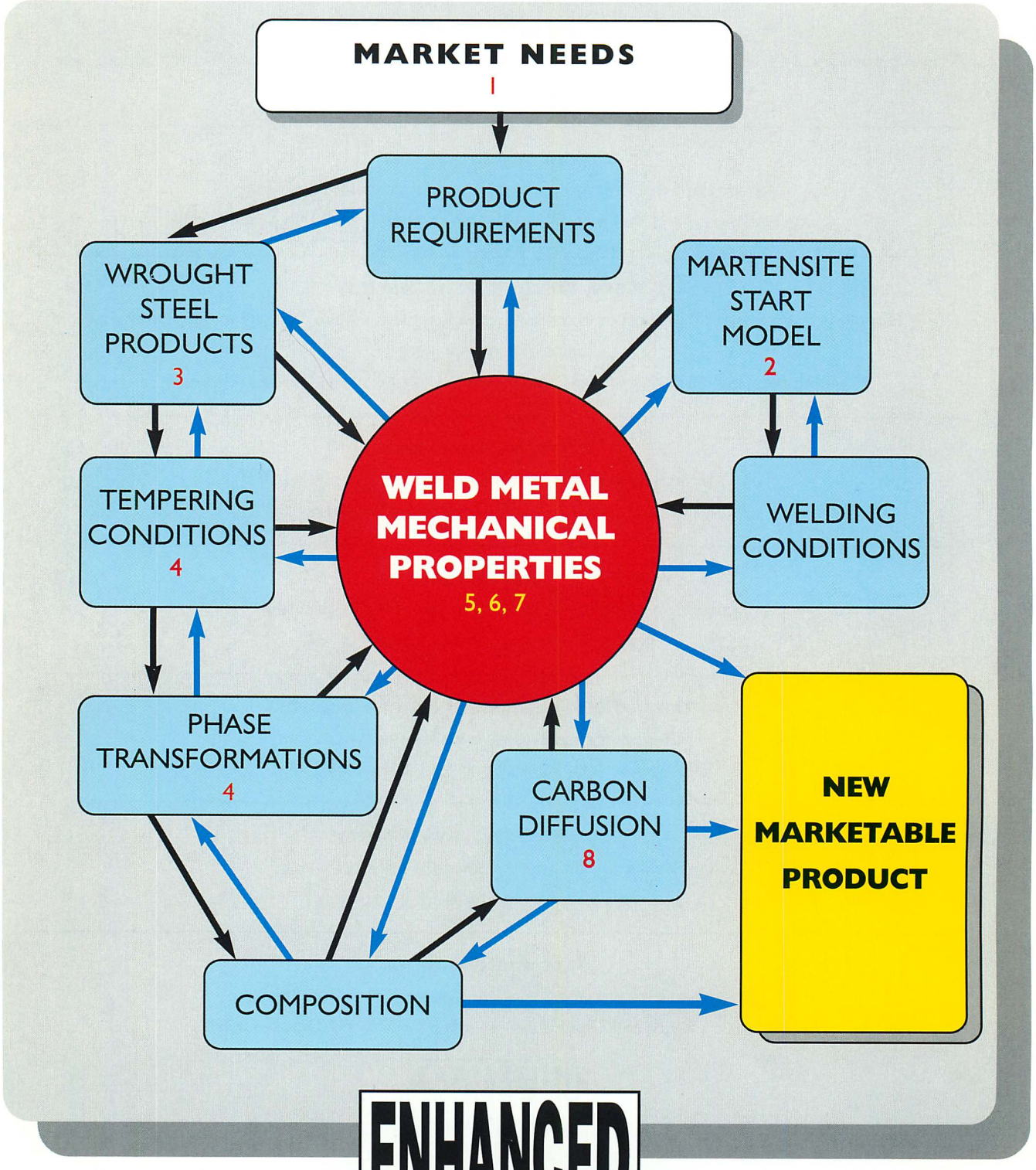

ENHANCED ENGINEERING MATERIALS

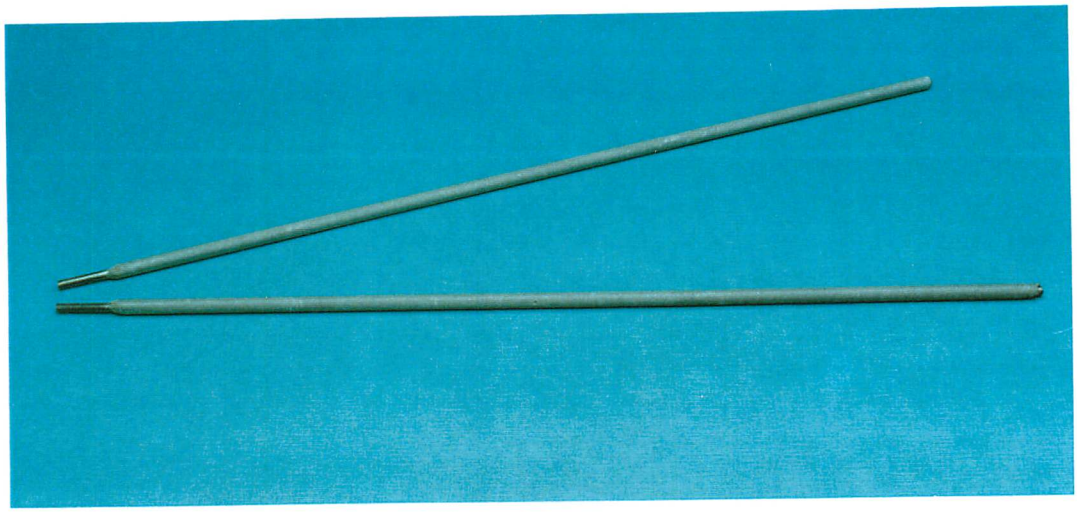

Figure 7.5: Welding electrodes.

A multipass butt weld was prepared between 2CrMoNiWV and $3\frac{1}{2}$NiCrMoV steels laid on a mild steel base plate (Figure 7.6). A buttering layer of 2Cr1Mo weld metal was set down before the experimental electrodes to combat diffusion. After welding, Quantovac and LECO chemical analysis checks were carried out on the weld metal of the weldment, sufficiently distant from the parent materials to avoid any dilution. It was observed that the measured composition differed slightly from that of the target weld. The two sets of values are compared in Table 7.5.

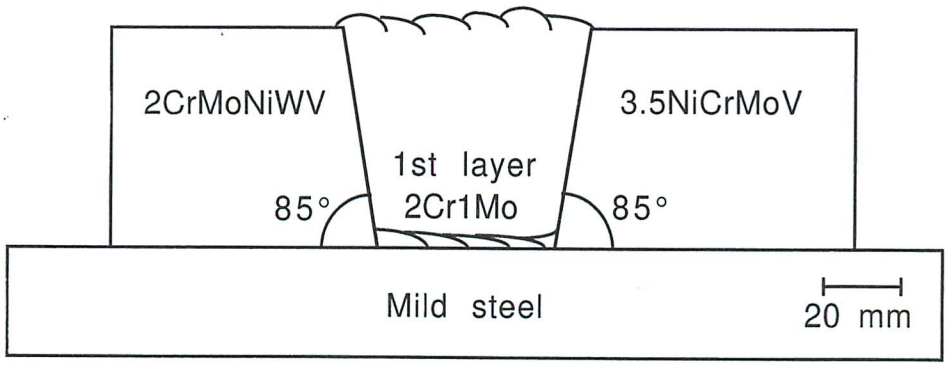

Figure 7.6: Schematic of the butt weld.

Although small, and within the tolerance limits, these differences in composition would alter the input values for the model, so a recalculation of the properties using the measured data for the butt weld compositions was carried out. These are presented in the following discussion.

7.14 Experimental Results

To ensure consistency, all mechanical properties were measured from the same multipass butt weld deposit, which was large enough to be sliced into sections for the tempering trials. Three different tempering treatments were carried out on the butt weld. All heat treatments were for eight hours, and

Variable	Target	Butt Weld	Variable	Target	Butt Weld
Carbon weight %	0.07	0.08	Copper weight %	–	0.03
Silicon weight %	0.4	0.43	Cobalt weight %	–	<0.01
Manganese weight %	1.0	1.02	Tungsten weight %	–	<0.01
Sulphur weight %	0.01	0.004	Titanium p.p.m.w.	–	<50
Phosphorus weight %	0.01	0.007	Boron p.p.m.w.	–	<5
Nickel weight %	2	2.23	Niobium p.p.m.w.	–	80
Chromium weight %	1.6	1.86	Oxygen p.p.m.w.	300	430
Molybdenum weight %	0.6	0.71	Nitrogen p.p.m.w.	50	100
Vanadium weight %	–	0.01	Aluminium weight %	0.015	n/a

Table 7.5: Chemical compositions of the proposed and actual weld.

the three temperatures chosen were the tempering temperature 650 °C ±50 °C to either side of this. All weld metal tensile and Charpy specimens were machined from the as-welded and the heat treated samples of the butt weld deposit, sufficiently far away from the base plate and parent materials to avoid any dilution. Mechanical tests were carried out to assess the properties of the material.

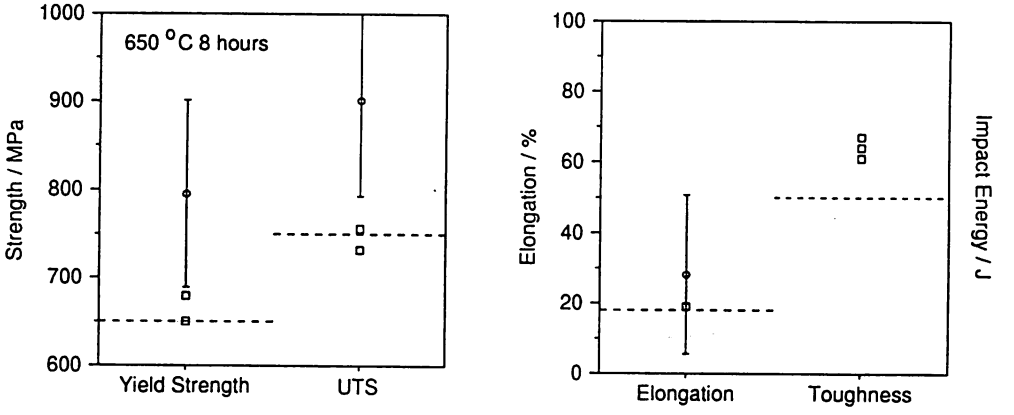

Figure 7.7a: The predicted, target and measured values for the mechanical properties of the weld at the proposed heat treatment temperature. The error bars represent 95 % confidence limits. No predicted values are provided for the Charpy toughness.

The results are presented in Figure 7.7, which shows the calculated data with 95 % confidence limits, the target values (indicated by dashed horizontal lines) and some experimental data. The predicted results in this and following figures are the new predictions made with the *actual* composition of the weld as presented in Table 7.5. The as-welded strength was very high, consistent with the expected martensitic structure and the calculated strength. After tempering, the strength was observed to drop gently at first, and then quite sharply for the 700 °C treatment. The modelling has tended to

overestimate the strength, but the target values are all met by the new electrode, which has an unusual chemical composition, and whose characteristics are not familiar to the neural network models. No toughness predictions have been provided because of the large error bars as mentioned above. However, it is encouraging to note that the target has been met.

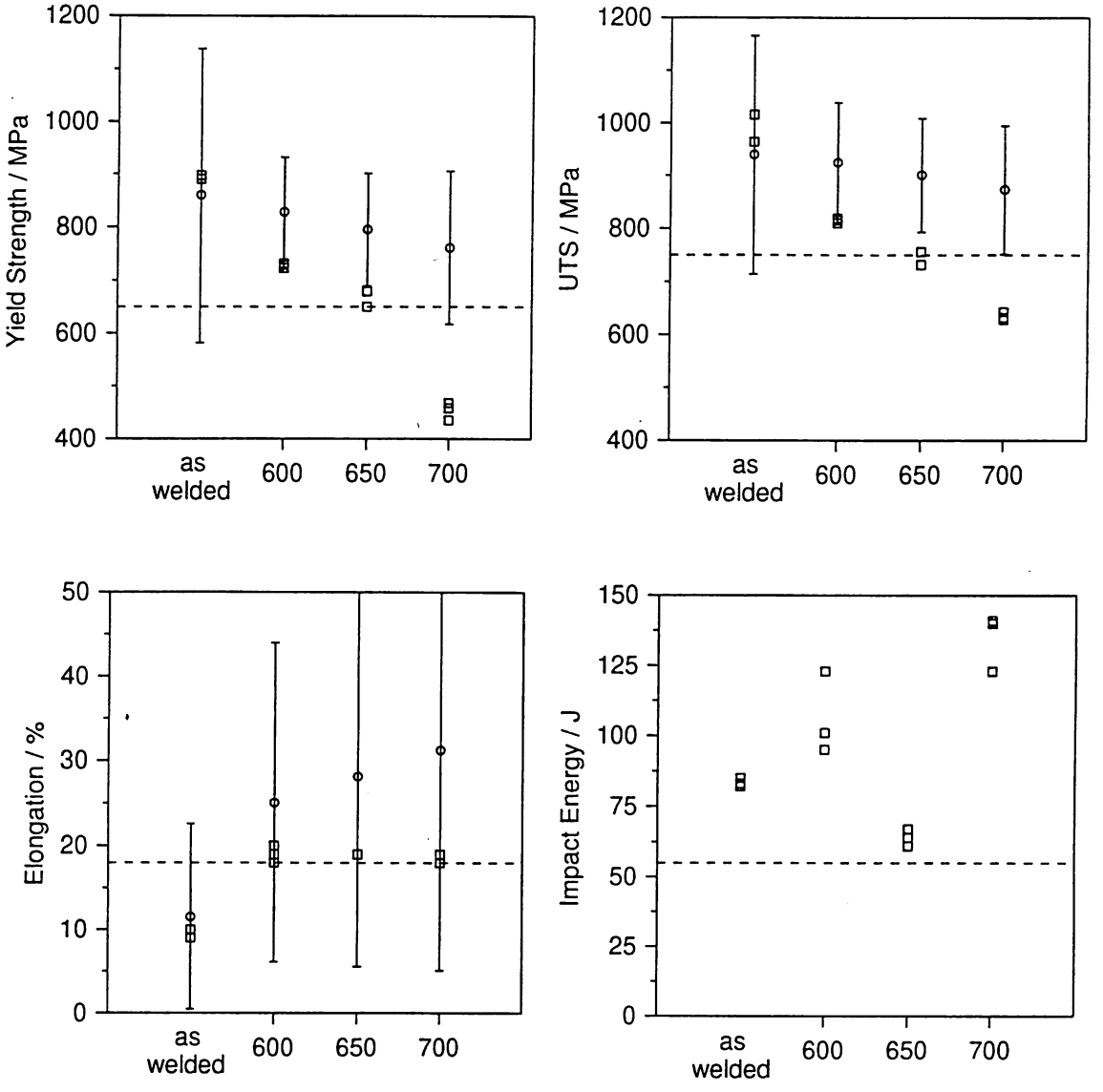

Figure 7.7: The target, predicted and measured trends of the mechanical properties for variations in tempering temperature. (a) Yield strength (b) UTS (c) Elongation (d) Toughness. The boxes represent experimental values from the butt weld, and the error bars show the predicted values (2σ) and the dotted horizontal lines indicate the target values.

A full set of data are similarly presented in Figure 7.7b. It is exciting that the as-welded mechanical properties are excellent and agree well with predictions. Even the toughness in this high strength as-welded condition is found to be excellent. This, combined with the 650 °C tempering data make the new electrode acceptable for the technological application for which it was invented, although full scale component welding tests remain to be done in the near future.

Further examination of Figure 7.7b reveals that the new weld is more sensitive to tempering than expected from the predictions. The decrease in strength with tempering is larger than expected, particularly for the 700 °C heat treatment. This discrepancy suggested a need for experimental investigation.

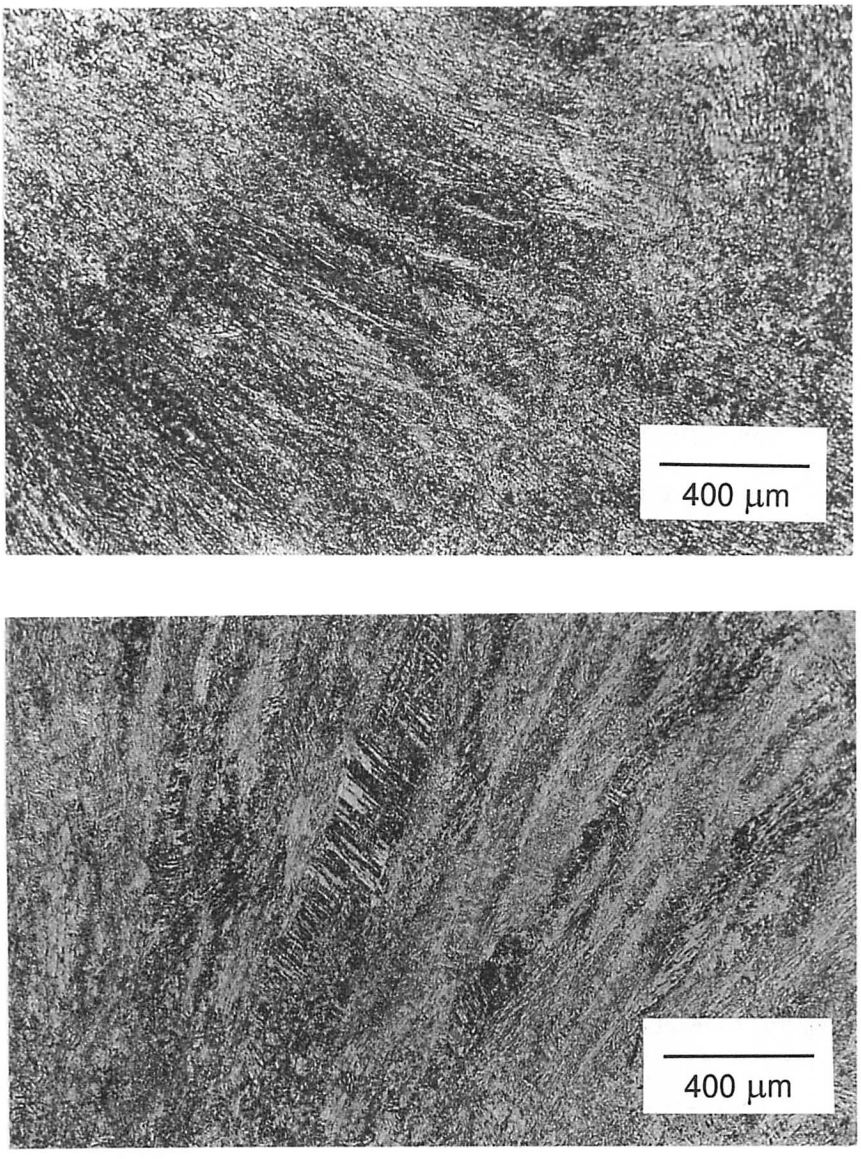

Figure 7.7a: Optical microscopy of (top) as-welded and (bottom) 600 °C heat treated specimens.

Optical microscopy soon revealed the reason for the sharp drop in strength following tempering at 700 °C (Figure 7.7). The as-welded microstructure consists of martensite and subsequent tempering has only a minor effect in the optical microstructure. However, for the highest tempering temperature there is the onset of recrystallisation, which causes the sharp drop in yield strength. Coarse ferrite grains form in bands parallel to the solidification front in each bead, with a spacing less than the size of the bead. This is almost certainly because of minor variations in chemical composition as the solidification velocity is influenced by corresponding uncontrolled variations in the welding parameter [Davies and

Garland, 1975]. The segregated (depleted) regions presumably have a lower Zener pinning force, and therefore recrystallise first. The recrystallisation is expected to spread throughout the microstructure with further tempering.

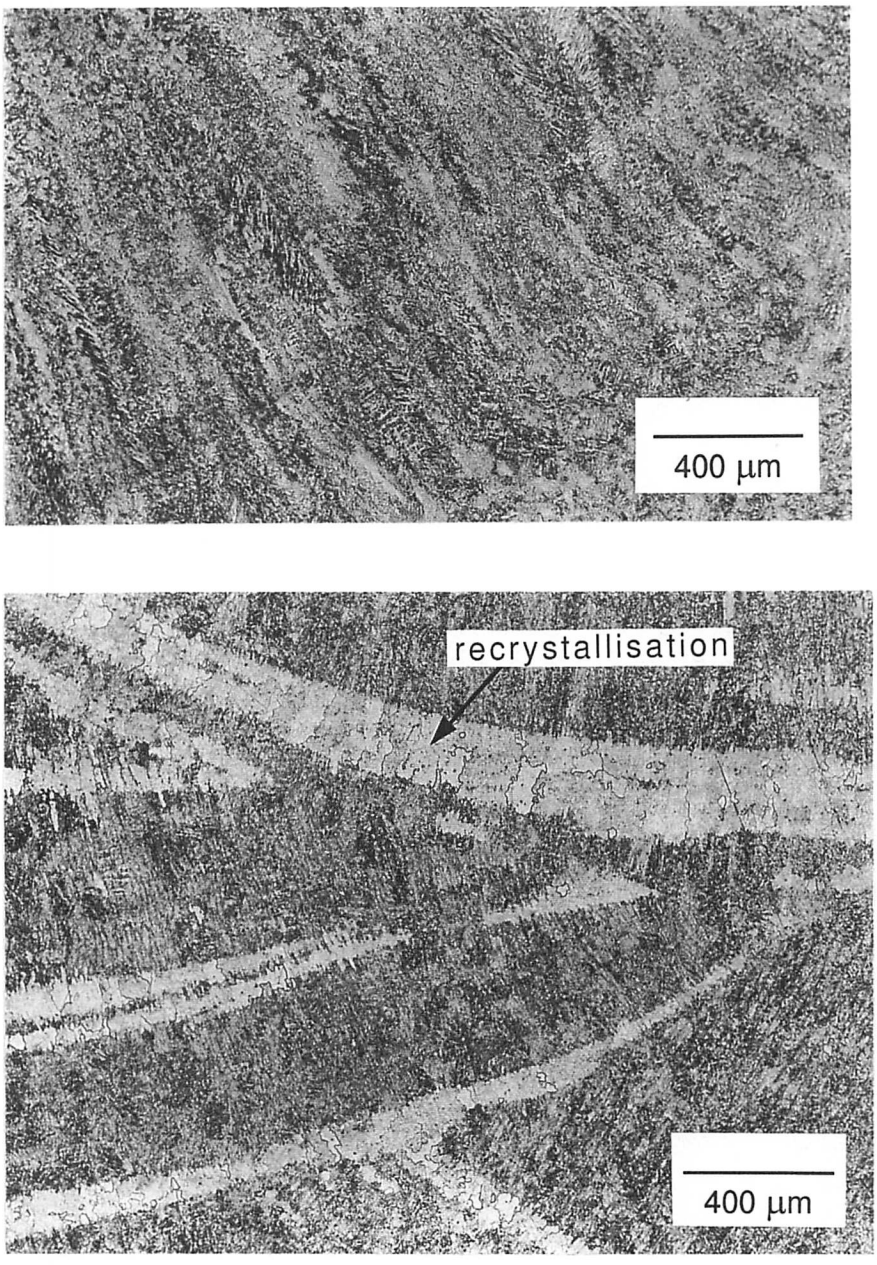

Figure 7.7b: Optical microscopy of (top) 650 °C and (bottom) 700 °C heat treated specimens.

It is interesting that the discrepancy between the calculated and measured values is smaller for the UTS than for the yield strength for all of the cases considered Figure 7.7b. This is because in an inhomogeneous microstructure which is partially recrystallised, yielding happens first in the very soft component, thereby indicating a low stress for the initiation of plastic flow [Bhadeshia and Edmonds, 1980]. Deformation beyond yield then spreads throughout the microstructure so that the UTS is less

affected by the soft regions.

7.14.1 Scanning Electron Microscopy

The fracture surfaces of the failed Charpy specimens were studied using scanning electron microscopy (Figure 7.8). The as-welded specimen and those heat treated at 600 °C and 650 °C showed ductile cleavage, whilst the sample tempered at 700 °C showed a brittle region on a large scale. It was not clear how the brittle zone corresponded to the recrystallisation bands observed optically, but the exercise confirmed the unsuitability of such a severe temper.

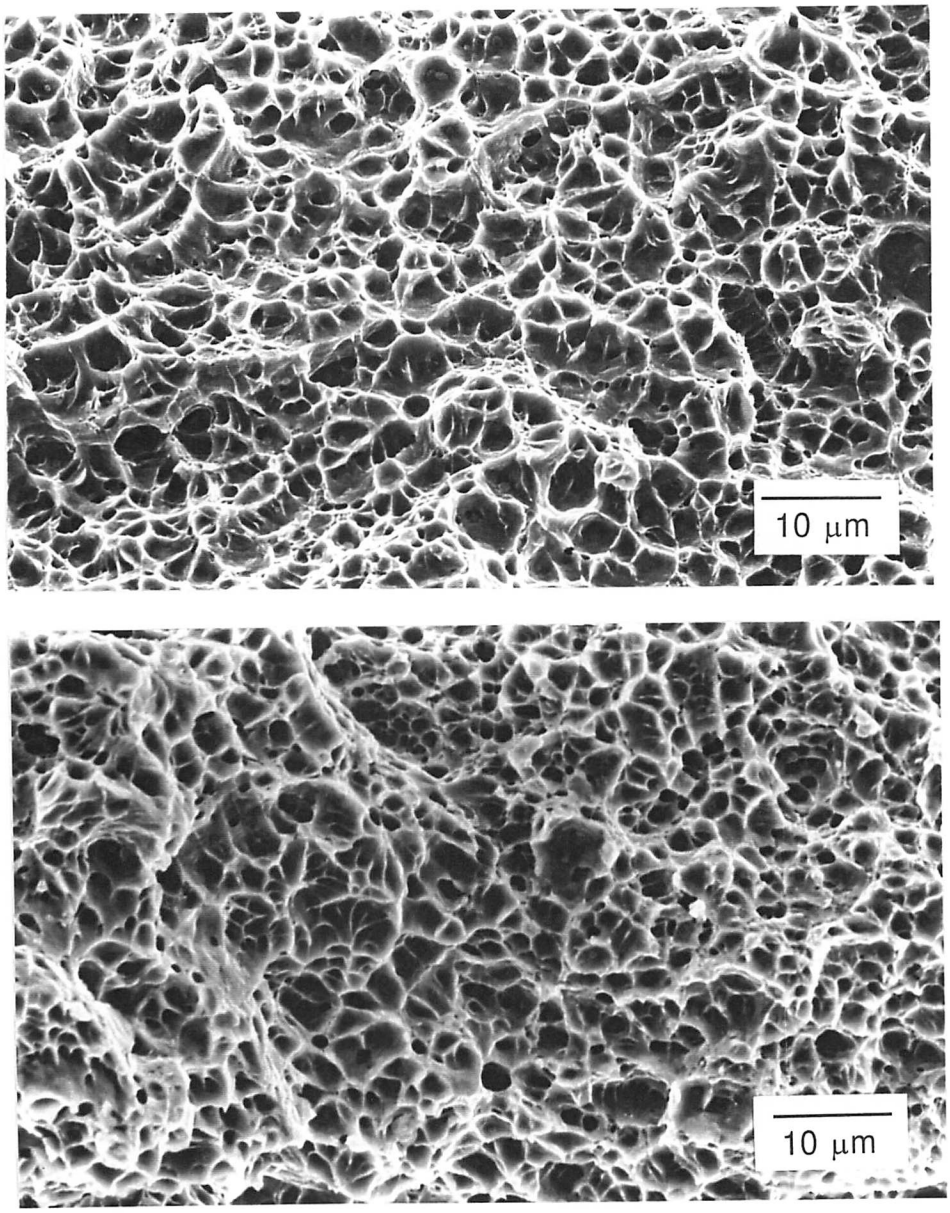

Figure 7.8a: Scanning electron microscopy of the fracture surfaces of (top) as-welded and (bottom) 600 °C heat treated specimens.

7.14.2 Hardness Testing

Hardness traverses using a 10 kg weight were carried out on the butt weld in both the as-welded

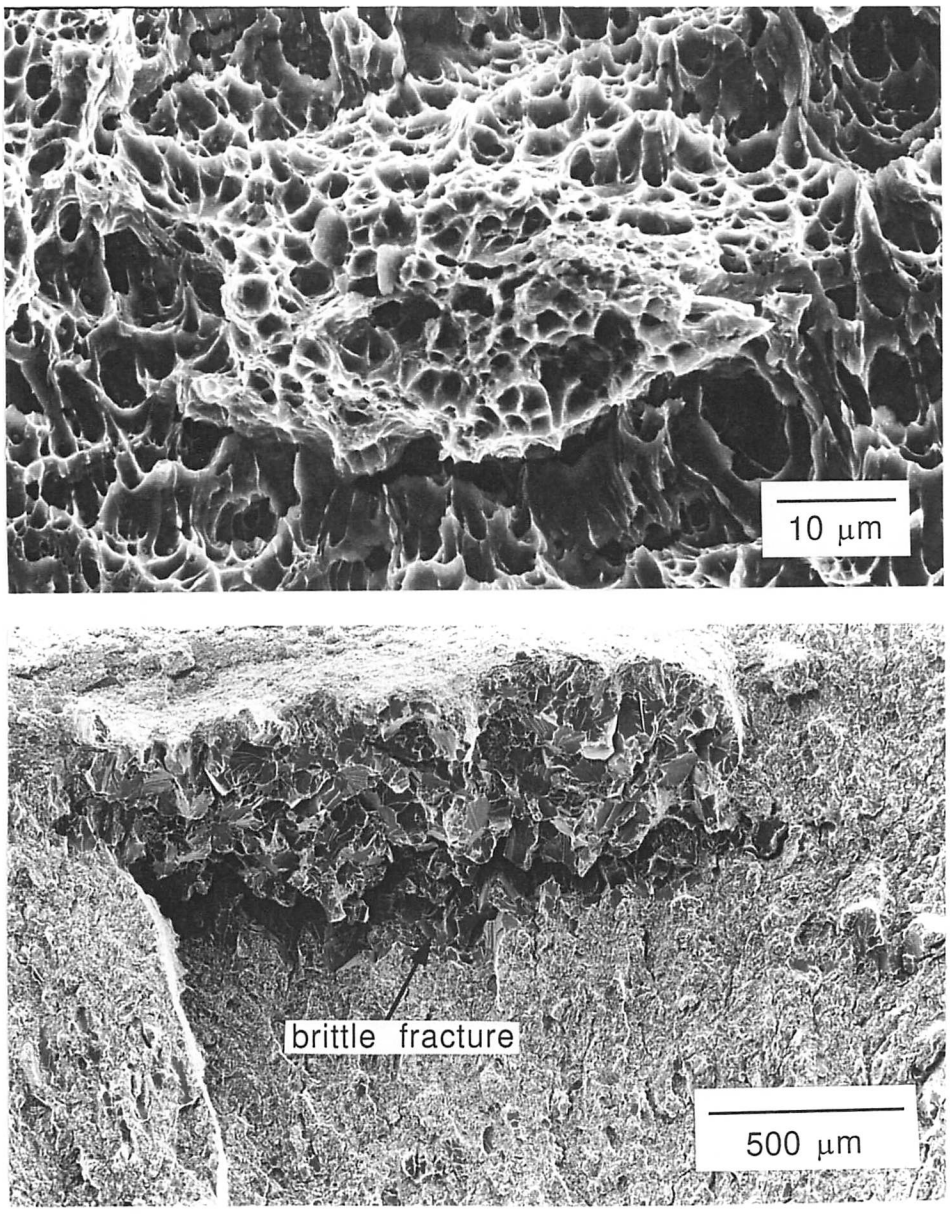

Figure 7.8b: Scanning electron microscopy of the fracture surfaces of (top) 650 °C and (bottom) 700 °C heat treated specimens.

and the 650 °C, 8 hours heat treated condition. The as results are presented in Figure 7.9 and Table 7.6. The high hardness of the weld in the as-welded sample provided further evidence of martensite.

Vicker's hardness tests using a load of 2.5 kg were carried out on the sample which had been tempered at 700 °C for eight hours. The measurements (Table 7.7) revealed that the banded recrystallised regions were much softer than the surrounding matrix, confirming the recrystallisation.

7.14.3 Transformation Temperatures

The *Thermecmastor-Z* thermomechanical simulator was used to measure the M_S temperature of an all weld metal deposit, to compare to a prediction made for the actual weld composition, using the M_S model described in Chapter 2. The predicted value of 374 °C compares with the three measured experimental values of 438, 435, and 438 °C. It is suspected that the measured values may be higher

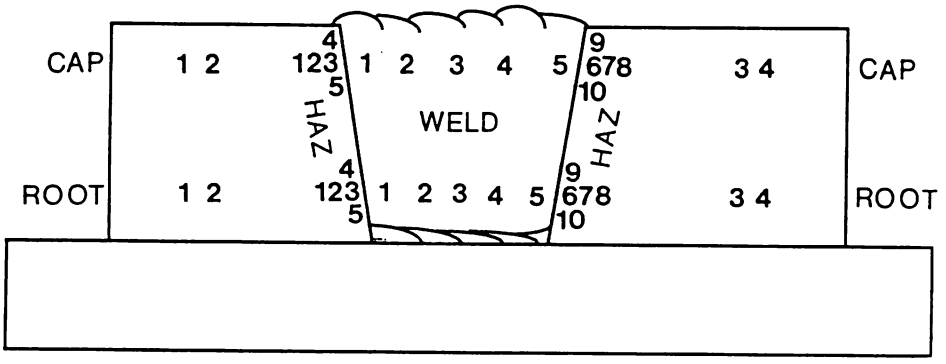

Figure 7.9: Hardness test positions for the heat treated weld. Positions for the as-welded sample are identical for the parent and the heat affected zone, but accomodate six evenly spaced tests across the cap of the weld, instead of five.

	As-welded						650 °C, 8 hours					
Test	**Cap**			**Root**			**Cap**			**Root**		
Position	HAZ	Weld	Parent	HAZ	Weld	Parent	HAZ	Weld	Parent	HAZ	Weld	Parent
1	311	325	258	297	294	258	242	245	251	225	228	251
2	397	297	254	376	314	238	294	240	242	266	238	245
3	441	333	276	429	292	285	322	219	245	319	262	251
4	468	311	270	429	283	287	317	225	249	333	230	245
5	441	370		417	345		342	243		317	238	
6	459			405			294	256		333		
7	459			380			254			294		
8	363			336			224			245		
9	464			394			292			304		
10	413			405			287			299		

Table 7.6: Hardness test results for the as-welded condition.

	Martensitic Region	Recrystallised Region
Hardness	254, 254, 243, 251, 240	157, 159, 151, 160, 162
Mean hardness	248	158

Table 7.7: Hardness test results for the sample heat treated at 700 °C for eight hours.

than those calculated because of the presence of chemical segregation. Ac_1 and Ac_3 temperatures were

also measured to give some insight into the phase diagram of this new composition. The results are presented in Table 7.8.

As was expected and observed for all other austenite transformations measured as part of this research (Chapter 4), an increase in the heating rate lead to an increase in the austenite transformation temperatures. As expected, the temperatures were comfortably high enough for the post weld heat treatment not to induce austenitisation.

Heating Rate °C s^{-1}	Ac_1 °C	Ac_3 °C
5	790	872
10	802	891
20	811	900

Table 7.8: Martensite and austenite transformation results for the new weld.

7.15 Summary

A novel electrode with an unusual chemistry has been designed without the benefit of the usual matrix of tests. The electrode meets the technological targets. Tests outside the range of engineering requirements revealed a higher sensitivity to tempering than expected. Even this proved to be useful in that it suggested specific experiments which revealed partial recrystallisation at high temperatures. Although not necessary for the application, this problem can be resolved by adding small quantities of vanadium for pinning boundaries.

A submerged arc version of the alloy has now been made. Preliminary tests are very promising, and arrangements are in hand for full scale component trials.

CHAPTER EIGHT

Further Work

Neural network analysis has been found to be a useful method for understanding the relationship between chemical composition, heat treatment and the elementary mechanical properties of steel weld metals. The models produced to date are unique in their ability to estimate these properties quantitatively; they have relied on the availability of data in the literature. Further data are constantly being reported and accumulated, so that the analysis will be repeated periodically to ensure that the models are firmly based.

A welded joint is more than just the weld metal. The heat affected zone is often a limiting factor. A very large database on the mechanical properties of wrought steels of the kind used commonly in the power generation industry has already been compiled and assessed for accuracy. It is proposed to use this along with the neural network method to understand and estimate the properties of the weld heat affected zone. Preliminary work on the approach to be used has already been published [Cool *et al.*, 1996].

The models developed are now being used routinely in industry. This will in addition be used to assess new research programmes being proposed, for example, the Technology Foresight Programme, where steels are to be designed for use at temperatures as high as 650 °C for prolonged periods typical in power plant. To do this also requires a model for creep so that the neural network approach could be very useful.

Some of the new welding alloys of untypical chemical composition have emerged from the work, but the alloys have not yet been characterised apart from the generation of routine data. Detailed metallography using transmission electron microscopy is necessary to understand the tempering behaviour and long term stability to multiple heat treatments of the type needed occasionally during repairs. It would be interesting in this respect to design an alloy which would be resistant to several stress relief heat treatments so that corrective welding operations can be carried out without any exaggerated loss of mechanical properties.

Finally, it is evident from this work that a number of relationships have been predicted which are not well understood. This is particularly the case for elongation and toughness data. Systematic experiments are necessary to determine whether the input parameters are sufficient to describe all the variations, or whether it is the noise in the experimental data which lead to uncertainties in predictions.

APPENDIX ONE

FORTRAN Program to Calculate M_S Temperature

Introduction

This appendix outlines the necessary inputs to calculate the martensite-start temperature as a basis of free energy and composition, and presents a computer program for carrying out the calculation. It is presented using documentation defined in the MAP format [Bhadeshia, 1995].

In order to have the correct inputs to the program, it is necessary to use the National Physical Laboratory's phase diagram simulation package, MTDATA [1996] for determination of certain parameters.

MAP FORTRAN LIBRARY

Program MAP_MS

0. Provenance of Source Code

T. Cool, Phase Transformations Group, Department of Materials Science and Metallurgy, University of Cambridge, Cambridge, U.K.

1. Purpose

To estimate the M_S temperature of an alloy steel as a function of the free energy, calculated from the chemical composition.

2. Specification

This is a self-contained program.

3. Description

The program reads in the chemical composition of a steel and thermodynamic results from MTDATA, calculated for a steel of the same composition. MTDATA is a computer based package used for thermodynamic predictions. It is used here to predict the free energy of austenite, and that of ferrite of the same composition, over a range of temperatures. The program calculates the free energy due to the composition of the steel after Ghosh and Olson [1993, 1994], and the free energy chance for the austenite $\rightarrow$ ferrite transformation over the temperature range, including a Zener ordering term. Equating these two values allows the martensite-start temperature to be calculated.

4. References

1. T. Cool, PhD Thesis, University of Cambridge, 1996

2. G. Ghosh and G. B. Olson, Proceedings of ICOMAT '92, International Conference on Martensitic Transformations, Monterey Institute for Advanced Studies, California, U.S.A. 353–358, 1993

3. G. Ghosh and G. B. Olson, Acta Metallurgica et Materialia **42** 3361–3370, 1994

4. T. Cool and H. K. D. H. Bhadeshia, Materials Science and Technology, **12** 40–44, 1996

5. MTDATA, Metallurgical Thermochemistry and Thermodynamic Database, National Physical Laboratory, Teddington, U. K., 1996

5. Parameters

Input parameters

J6 - integer
an identification number for the alloy

C(1) - double precision
Carbon composition in weight %. 0 <C(1)< 2

C(2) - double precision
Silicon composition in weight %. 0 <C(2)< 3.5

C(3) - double precision
Manganese composition in weight %. 0 <C(3)< 5

C(4) - double precision
Nickel composition in weight %. 0 <C(4)< 6

C(5) - double precision
Molybdenum composition in weight %. 0 <C(5)< 5.6

C(6) - double precision
Chromium composition in weight %. 0 <C(6)< 15.5

C(7) - double precision
Vanadium composition in weight %. 0 <C(7)< 1.8

C(8) - double precision
Copper composition in weight %. 0 <C(8)< 1.5

C(9) - double precision
Tungsten composition in weight %. 0 <C(9)< 18

C(10) - double precision

Niobium composition in weight %. 0 <C(10)< 1.5

C(11) - double precision

Nitrogen composition in weight %. 0 <C(11)< 1.5

C(12) - double precision

Cobalt composition in weight %. 0 <C(12)< 3.5

Y - real

Experimental M_S value in °C. If no value is available, a zero is requested as an input.

J7 - integer

The number of temperatures at which the free energies of austenite and ferrite have been calculated using MTDATA. Work in this thesis has used 25 temperatures at 25 °C intervals.

T(n) - double precision array

The temperature(s) in Kelvin at which MTDATA has been run. n=1–J7

D(n) - double precision array

The ferrite free energies at the corresponding temperatures, T(n). These are determined from MTDATA by allowing only the ferrite phase to exist at the range of temperatures.

E(n) - double precision array

The austenite free energies at the corresponding temperatures, T(n). These are determined from MTDATA runs at the same temperatures, allowing only the austenite phase to exist.

Output parameters

FE

Predicted free energy due to composition [Ghosh and Olson, 1993, 1994] with K_1 = 1010 kJ mol^{-1} (new value).

L1

M_S predicted from the free energy (new K_1) without consideration of the Zener ordering term.

L2

M_S predicted from the free energy (new K_1) with inclusion of the Zener ordering term.

FFE

Predicted free energy due to composition [Ghosh and Olson, 1993, 1994] with K_1 = 683 kJ mol^{-1} (old value).

L3

M_S predicted from the free energy (old K_1) without consideration of the Zener ordering term.

L4

M_S predicted from the free energy (old K_1) with inclusion of the Zener ordering term.

6. Error Indicators

User is warned if he attempts to input a composition outside a range specific to each element (indicated above).

7. Accuracy

8. Further Comments

9. Example

9.1 Program data

J6 = 1
C(1) = 0.08
C(2) = 0.43
C(3) = 1.02
C(4) = 2.23
C(5) = 0.71
C(6) = 1.86
C(7) = 0.01
C(8) = 0.03
C(9) = 0
C(10) = 0.008
C(11) = 0.01
C(12) = 0
Y = 0
J7 = 25
T(1) = 973.0000
D(1) = -7.8159414481E+05
T(2) = 948.0000
D(2) = -7.5085427769E+05
T(3) = 923.0000
D(3) = -7.2071918466E+05
T(4) = 898.0000

D(4) = -6.9117439454E+05
T(5) = 873.0000
D(5) = -6.6220894490E+05
T(6) = 848.0000
D(6) = -6.3381478019E+05
T(7) = 823.0000
D(7) = -6.0598629400E+05
T(8) = 798.0000
D(8) = -5.7871998519E+05
T(9) = 773.0000
D(9) = -5.5201420414E+05
T(10) = 748.0000
D(10) = -5.2586897107E+05
T(11) = 723.0000
D(11) = -5.0028585226E+05
T(12) = 698.0000
D(12) = -4.7526788374E+05
T(13) = 673.0000
D(13) = -4.5081953488E+05
T(14) = 648.0000
D(14) = -4.2694670623E+05
T(15) = 623.0000
D(15) = -4.0365675818E+05
T(16) = 598.0000
D(16) = -3.8095856840E+05
T(17) = 573.0000
D(17) = -3.5886261742E+05
T(18) = 548.0000
D(18) = -3.3738110299E+05
T(19) = 523.0000
D(19) = -3.1652808518E+05
T(20) = 498.0000
D(20) = -2.9631966529E+05
T(21) = 473.0000
D(21) = -2.7677420306E+05
T(22) = 448.0000
D(22) = -2.5791257808E+05
T(23) = 423.0000
D(23) = -2.3975850300E+05
T(24) = 398.0000
D(24) = -2.2233889775E+05

T(25) = 373.0000
D(25) = -2.0568433547E+05
E(1) = -7.8112221055E+05
E(2) = -7.4897941982E+05
E(3) = -7.1721440685E+05
E(4) = -6.8583476688E+05
E(5) = -6.5484851561E+05
E(6) = -6.2426412408E+05
E(7) = -5.9409055753E+05
E(8) = -5.6433731864E+05
E(9) = -5.3501449600E+05
E(10) = -5.0613281854E+05
E(11) = -4.7770371666E+05
E(12) = -4.4973939142E+05
E(13) = -4.2225289286E+05
E(14) = -3.9525820922E+05
E(15) = -3.6877036873E+05
E(16) = -3.4280555638E+05
E(17) = -3.1738124832E+05
E(18) = -2.9251636733E+05
E(19) = -2.6823146333E+05
E(20) = -2.4454892401E+05
E(11) = -2.2149322170E+05
E(22) = -1.9909120393E+05
E(23) = -1.7737243695E+05
E(24) = -1.5636961299E+05
E(25) = -1.3611903445E+05

10. Auxiliary Routines

The subroutines called by this program are

REED
REEDI
BOUND
ADD

11. Keywords

martensite transformation, steel

Program Listing

```
C This program uses the output from MTDATA to predict the change in free energy
C for the ferrite → austenite transformation, and hence the Ms temperature
C using Ghosh and Olson's equation.
      IMPLICIT REAL*8(A-H,L-Z),INTEGER(I,J,K)
      DIMENSION AR(100),WT(100),AT(100),ML(100),T60(100)
      DIMENSION ZENER(100),EE(100),EENEW(100),EEOLD(100)
      DOUBLE PRECISION C(100),D(100),E(100),F(100),G(100),T(100)
      DOUBLE PRECISION TC(100),H(100)
      WRITE(*,715)
715   FORMAT(////19X,' Identification Number ?')
      CALL REEDI(J6)
C Carbon
      WRITE(*,707)
707   FORMAT(19X,' Carbon wt.% ?')
      CALL REED(C(1))
      IF(C(1) .LT. 0.0D+00 .OR. C(1) .GT. 2.0D+00)
     &CALL BOUND(C(1),0.1D-03,2.0D+00)
C Silicon
      WRITE(*,708)
708   FORMAT(19X,' Silicon wt.% ?')
      CALL REED(C(2))
      IF(C(2) .LT. 0.0D+00 .OR. C(2) .GT. 3.5D+00)
     &CALL BOUND(C(2),0.0D+00,3.5D+00)
C Manganese
      WRITE(*,709)
709   FORMAT(19X,' Manganese wt.% ?')
      CALL REED(C(3))
      IF(C(3) .LT. 0.0D+00 .OR. C(3) .GT. 5.0D+00)
     &CALL BOUND(C(3),0.0D+00,5.0D+00)
C Nickel
      WRITE(*,710)
710   FORMAT(19X,' Nickel wt.% ?')
      CALL REED(C(4))
      IF(C(4) .LT. 0.0D+00 .OR. C(4) .GT. 6.0D+00)
     &CALL BOUND(C(4),0.0D+00,6.0D+00)
C Molybdenum
      WRITE(*,711)
711   FORMAT(19X,' Molybdenum wt.% ?')
      CALL REED(C(5))
      IF(C(5) .LT. 0.0D+00 .OR. C(5) .GT. 5.6D+00)
     &CALL BOUND(C(5),0.0D+00,5.6D+00)
C Chromium
      WRITE(*,712)
712   FORMAT(19X,' Chromium wt.% ?')
      CALL REED(C(6))
      IF(C(6) .LT. 0.0D+00 .OR. C(6) .GT. 15.5D+00)
     &CALL BOUND(C(6),0.0D+00,15.5D+00)
C Vanadium
      WRITE(*,713)
```

```
713  FORMAT(19X, ' Vanadium wt.% ?')
     CALL REED(C(7))
     IF(C(7) .LT. 0.0D+00 .OR. C(7) .GT. 1.8D+00)
    &CALL BOUND(C(7),0.0D+00,1.8D+00)
C Copper
     WRITE(*,714)
714  FORMAT(19X, ' Copper wt.% ?')
     CALL REED(C(8))
     IF(C(8) .LT. 0.0D+00 .OR. C(8) .GT. 1.5D+00)
    &CALL BOUND(C(8),0.0D+00,1.5D+00)
C Tungsten
     WRITE(*,700)
700  FORMAT(19X, ' Tungsten wt.% ?')
     CALL REED(C(9))
     IF(C(9) .LT. 0.0D+00 .OR. C(9) .GT. 18.0D+00)
    &CALL BOUND(C(9),0.0D+00,18.0D+00)
C Niobium
     WRITE(*,701)
701  FORMAT(19X, ' Niobium wt.% ?')
     CALL REED(C(10))
     IF(C(10) .LT. 0.0D+00 .OR. C(10) .GT. 1.5D+00)
    &CALL BOUND(C(10),0.0D+00,1.5D+00)
C Nitrogen
     WRITE(*,716)
716  FORMAT(19X, ' Nitrogen wt.% ?')
     CALL REED(C(11))
     IF(C(11) .LT. 0.0D+00 .OR. C(11) .GT. 1.5D+00)
    &CALL BOUND(C(11),0.0D+00,1.5D+00)
C Cobalt
     WRITE(*,717)
717  FORMAT(19X, ' Cobalt wt.% ?')
     CALL REED(C(12))
     IF(C(12) .LT. 0.0D+00 .OR. C(12) .GT. 3.5D+00)
    &CALL BOUND(C(12),0.0D+00,1.5D+00)
C
C if there is an experimentally determined value for Ms then this bit of the
C program reads it in, and if there isn't, it tactfully skips the step
     WRITE(*,718)
718  FORMAT(19X, ' Input experimental Ms value in Centigrade. (0 if none)')
     CALL REED(Y)
     IF(Y .LT. 0.0D+00 .OR. Y .GT. 1.5D+09)
    &CALL BOUND(Y,0.0D+00,1.5D+09)
C
C now to convert from wt.% to mole fraction
C relative atomic masses of the elements in order
```

```
C C,Si,Mn,Ni,Mo,Cr,V,Cu,W,Nb,N,Co,Fe
      AR(1)=12.0111
      AR(2)=28.0855
      AR(3)=54.938
      AR(4)=58.71
      AR(5)=95.94
      AR(6)=51.996
      AR(7)=50.9415
      AR(8)=63.546
      AR(9)=183.85
      AR(10)=92.9064
      AR(11)=14.0067
      AR(12)=58.993
      AR(13)=55.847
C
      DO 22 i=1,13
       wt(i)=c(i)
22    CONTINUE
C
      DO 50 KK=1
       WT(13)=100.0D0-ADD(WT,13)
C
       DO 10 I=1,13
        ML(I)=(WT(I))/AR(I)
10     CONTINUE
       SUM=ADD(ML,13)
       DO 11 J=1,13
        AT(J)=(ML(J))/SUM
11     CONTINUE
C
       C(13)=WT(13)
C
C This section inputs the temperature values and the appropriate ferrite and
C austenite free energies.
       WRITE (*,100)
100    FORMAT (19X, ' How many temperature values ?')
       CALL REEDI(J7)
       WRITE (*,101)
101    FORMAT (19X, ' First temperature in Kelvin ?')
       CALL REED(T(1))
       WRITE (*,201)
201    FORMAT (19X, ' Ferrite free energy at this temperature? ')
       CALL REED(D(1))
       DO 37 K=2,J7
        WRITE (*,102)
102     FORMAT (19X, ' Next temperature in Kelvin ?')
        CALL REED(T(K))
        WRITE (*,202)
202     FORMAT (19X, ' Ferrite free energy at this temperature ?')
        CALL REED(D(K))
```

```
 37     CONTINUE
        DO 38, K=1,J7
         WRITE (6,578) T(K)
 578     FORMAT (19X,F8.0, ' Kelvin')
         WRITE (*,103)
 103     FORMAT (19X, ' Austenite free energy at this temperature ?')
         CALL REED(E(K))
 38     CONTINUE
 C
        WRITE (6,*) 'Composition of sample',J6
        WRITE (6,997) 'Element ','C','Si','Mn','Ni','Mo','Cr',
       &'V','Cu','W','Nb'
       &,'N','Co','Fe'
        WRITE (6,998) 'Wt%          ',(WT(I),I=1,13)
        WRITE (6,999) 'At fract. ',(AT(J),J=1,13)
 50    CONTINUE
 997   FORMAT (A10,16A8)
 998   FORMAT (A10,16F8.4)
 999   FORMAT (A10,16F8.4)
 C
 C This simply converts Kelvin to Centigrade
       DO 87 K=1,J7
        TC(K)=T(K)-273.0
 87    CONTINUE
 C
 C This provides the conversion factor from kg to moles
       DO 99 K=1,16
        H(K)=C(K)*AR(K)
        P=P+H(K)
 99    CONTINUE
 C
 C This calculates the change in free energy using the data in J/kg, and
 C converts this value to J/mole using the conversion factor calculated above.
       DO 39 K=1,J7
        F(K)=D(K)-E(K)
        G(K)=(F(K))*P/100000.0
 39    CONTINUE
 C
 C This do loop is commented out in co13xbothk.for
       DO 49 K=1,J7
        WRITE (6,900) TC(K),G(K)
 900    FORMAT (10X,F8.0,' Centigrade',10X,F10.2,' J/mol')
 49    CONTINUE
 C
       WRITE (6,*) ' '
 C
```

```
C this bit calculates Olson's equation for the weight% given
      FD=-(683.3+4009*AT(1)**(0.5)+1879*AT(2)**(0.5)+1980*AT(3)**(0.5))
      FF=-(172*AT(4)**(0.5))
      FG=-(1418*AT(5)**(0.5)+1868*AT(6)**(0.5)+1618*AT(7)**(0.5))
      FH=-(752*AT(8)**(0.5))
      FI=-(714*AT(9)**(0.5)+1653*AT(10)**(0.5))
      FJ=-(3097*AT(11)**(0.5))
      FE=FD+FF+FG+FH+FI+FJ
      WRITE (6,*) '***NEW K1***'
      WRITE (6,*) 'Predicted free energy due to comp = ',FE,' J/mol'
      WRITE (6,*) ' '
C This section is the Zener ordering term, as a function of Carbon
      DO 79 K=1,J7
       T60(K)=T(K)*(1-AT(1))/(28080*AT(1))
       IF (T60(K) .GT. 1.0) GOTO 14
       IF (T60(K) .GT. 0.25) GOTO 17
       ZZ1=0.2307+42.7974*T60(K)-233.8631*((T60(K))**2)
       ZZ2=645.4485*((T60(K))**3)-954.3995*((T60(K))**4)
       ZZ3=711.8095*((T60(K))**5)-211.5136*((T60(K))**6)
       ZEN1=ZZ1+ZZ2+ZZ3
       ZZ11=-2.6702+45.6337*T60(K)-225.3965*((T60(K))**2)
       ZZ22=567.7112*((T60(K))**3)-771.6466*((T60(K))**4)
       ZZ33=538.1778*((T60(K))**5)-151.3818*((T60(K))**6)
       ZEN2=ZZ11+ZZ22+ZZ33
       GOTO 16
       ZEN2=1
       ZEN1=3.295
16     AA=((ZEN2*AT(1))**2)*(-50898.56)/(1-AT(1))
       BB=ZEN1*T60(K)*AT(1)*0.6623741
       ZENER(K)=AA+BB
       ZENER(K)=ZENER(K)*4.187
       GOTO 19
14      ZENER(K)=0
19      YY=1
79     CONTINUE
C
      DO 44 K=1,J7
       EENEW(K)=ZENER(K)+G(K)
44     CONTINUE
C
      WRITE (6,*) ' '
C
      WRITE (6,*) 'Without Zener ordering'
C
C This do loop calculates an approximate prediction for the Ms temperature,
C on the basis of Olson's equation, and the MTDATA output.
C Assuming delta G (G(K)) and Ms free energy are equal, it also assumes a
C linearity between temperature/free energy data.
```

```
C A more accurate value may obviously be gained from plotting a graph of the points.
      DO 18 K=1,(J7-1)
       IF (G(K) .GT. FE .AND. FE .GT. G(K+1)) THEN
        MIN=TC(K+1)
        MAX=TC(K)
        MING=G(K+1)
        MAXG=G(K)
       ELSE
       ENDIF
18    CONTINUE
      L1=MIN+ ((FE-MING)*(MAX-MIN)/(MAXG-MING))
      WRITE (6,*) ' '
      WRITE (6,675) L1
675   FORMAT (10X,'Ms (new) approximately ',F8.0,' Centigrade')
C
      WRITE(6,*) ' '
C
      WRITE(6,*) 'With Zener ordering'
C
C This do loop calculates an approximate prediction for the Ms temperature,
C on the basis of Olson's equation, and the MTDATA output. It also incorporates
C the Zener ordering term.
C Assuming delta G (G(K)) and Ms free energy are equal, it also assumes a
C linearity between temperature/free energy data.
C A more accurate value may obviously be gained from plotting a graph of the points.
      DO 73 K=1,(J7-1)
       IF (EENEW(K) .GT. FE .AND. FE .GT. EENEW(K+1)) THEN
        MIN=TC(K+1)
        MAX=TC(K)
        MING=EENEW(K+1)
        MAXG=EENEW(K)
       ELSE
       ENDIF
73    CONTINUE
      L2=MIN+ ((FE-MING)*(MAX-MIN)/(MAXG-MING))
      WRITE (6,*) ' '
      WRITE (6,678) L2
678   FORMAT (10X,'Ms (new) approximately ',F8.0,' Centigrade')
C
      WRITE(6,*) ' '
C
```

```
C this bit calculates Olson's equation for the weight% given with the old K1
      FFD=-(1010+4009*AT(1)**(0.5)+1879*AT(2)**(0.5)+1980*AT(3)**(0.5))
      FFF=-(172*AT(4)**(0.5))
      FFG=-(1418*AT(5)**(0.5)+1868*AT(6)**(0.5)+1618*AT(7)**(0.5))
      FFH=-(752*AT(8)**(0.5))
      FFI=-(714*AT(9)**(0.5)+1653*AT(10)**(0.5))
      FFJ=-(3097*AT(11)**(0.5))
      FFE=FFD+FFF+FFG+FFH+FFI+FFJ
      WRITE (6,*) '***OLD K1***'
      WRITE (6,*) 'Predicted free energy due to comp = ',FFE,' J/mol'
      WRITE (6,*) ' '
C
      DO 444 K=1,J7
       EEOLD(K)=ZENER(K)+G(K)
444   CONTINUE
C
      WRITE (6,*) ' '
C
      WRITE (6,*) 'Without Zener ordering'
C
C This do loop calculates an approximate prediction for the Ms temperature,
C on the basis of Olson's equation, and the MTDATA output.
C Assuming delta G (G(K)) and Ms free energy are equal, it also assumes a
C linearity between temperature/free energy data.
C A more accurate value may obviously be gained from plotting a graph of the points.
      DO 118 K=1,(J7-1)
       IF (G(K) .GT. FFE .AND. FFE .GT. G(K+1)) THEN
        MIN=TC(K+1)
        MAX=TC(K)
        MING=G(K+1)
        MAXG=G(K)
       ELSE
       ENDIF
118   CONTINUE
      L3=MIN+ ((FFE-MING)*(MAX-MIN)/(MAXG-MING))
      WRITE (6,*) ' '
      WRITE (6,676) L3
676   FORMAT (10X,'Ms (old) approximately ',F8.0,' Centigrade')
C
      WRITE(6,*) ' '
C
      WRITE(6,*) 'With Zener ordering'
C
C This do loop calculates an approximate prediction for the Ms temperature,
C on the basis of Olson's equation, and the MTDATA output. It also incorporates
C the Zener ordering term.
C Assuming delta G (G(K)) and Ms free energy are equal, it also assumes a
C linearity between temperature/free energy data.
```

```
C A more accurate value may obviously be gained from plotting a graph of the points.
      DO 773 K=1,(J7-1)
        IF (EEOLD(K) .GT. FFE .AND. FFE .GT. EEOLD(K+1)) THEN
         MIN=TC(K+1)
         MAX=TC(K)
         MING=EEOLD(K+1)
         MAXG=EEOLD(K)
        ELSE
        ENDIF
773     CONTINUE
      L4=MIN+ ((FFE-MING)*(MAX-MIN)/(MAXG-MING))
      WRITE (6,*) ' '
      WRITE (6,679) L4
679   FORMAT (10X,'Ms (old) approximately ',F8.0,' Centigrade')
C
      WRITE(6,*) ' '
C
C this bit prints out whether there is an experimental value or not
      IF(Y .LT. 0.1D+00) THEN
       WRITE(6,*) 'No experimental data was provided for comparison'
      ENDIF
      IF(Y .GT. 0.0D+00) THEN
       WRITE(6,994) Y
994   FORMAT('Experimental Value   ',10X,F10.2,' Centigrade')
      ENDIF
C
      STOP
      END
C-------------------------------------------------------
      SUBROUTINE REED(A)
      DOUBLE PRECISION A
996   READ(*,*,ERR=999)A
      GOTO 998
999   WRITE(*,997)
997   FORMAT(19X,' Incorrect Input. Try again'/)
      GOTO 996
998   RETURN
      END
C-------------------------------------------------------
      SUBROUTINE REEDI(I)
      INTEGER I
996   READ(*,*,ERR=999)I
      GOTO 998
999   WRITE(*,997)
997   FORMAT(19X,' Incorrect Input. Try again'/)
      GOTO 996
998   RETURN
      END
C-------------------------------------------------------
      SUBROUTINE BOUND(A,B,C)
      DOUBLE PRECISION A,B,C
```

```
2     WRITE(*,1)B,C
1     FORMAT(12X,' Input value out of bounds'/
     &14X,' The limits are ',D12.4,' to ', D12.4/)
      CALL REED(A)
      IF(A .LT. B .OR. A .GT. C)GOTO 2
      RETURN
      END
C-----------------------------------------------------
      DOUBLE PRECISION FUNCTION ADD(X,I)
      IMPLICIT DOUBLE PRECISION (A-H,L-Z)
      INTEGER I
      DIMENSION X(100)
      A=0.0D0
      DO 12 I1=1,I
      A=A+X(I1)
12    CONTINUE
      ADD=A
      END
```

APPENDIX TWO

Yield Strength Committee Model Weights

The weights for all models making up the yield strength committee which have been trained using the *entire* dataset. These weights describe each trained network.

-0.171546	-0.00225139	-0.0970205	-0.0300255	-0.0633371	-0.00429571	0.0388401
-0.276171	-0.798268	-0.106679	-0.128003	-0.07281	0.222673	0.324986
0.0424416	-0.0428604	0.171731	0.127469	-0.581542	-0.163026	0.144293
0.016795	-0.141619	0.0484977	0.0786442	0.0212737	0.0325292	0.00343047
-1.16545	-0.0758439	-0.0670774	0.0399578	0.247083	0.338366	0.0107962
-0.0347937	0.199963	-0.0188507	-0.31864	-0.308316	0.255493	-0.00444168
0.025369	-0.039484	-0.136707	0.0123413	0.0539999	-0.184229	0.0590583
-0.00584449	-0.0974913	-0.0842608	-0.0758818	0.147873	0.025533	0.0139334
0.0317911	0.163918	-0.500529	0.0556693	-4.0902	-11.317	8.05724
			9.29007			

Table A2.1: The weights for the highest ranked yield strength model (3 hidden units, random number seed of 35). The data are arranged in a continuous horizontal sequence in the following order: $\theta_1^{(1)}$, $w_{1,1}^{(1)} \ldots w_{1,19}^{(1)}$, $\theta_2^{(1)}$, $w_{2,1}^{(1)} \ldots w_{2,19}^{(1)}$, $\theta_3^{(1)}$, $w_{3,1}^{(1)} \ldots w_{3,19}^{(1)}$, $\theta^{(2)}$, $w_1^{(2)} \ldots w_3^{(2)}$.

1.5294	0.130644	0.159576	0.129336	0.0617725	4.25782	1.02219
-0.536674	-1.92137	0.546298	0.714566	-1.66812	-3.26685	-0.0639273
-0.124555	0.447275	1.54761	0.501745	-1.83306	-0.73649	2.53948
0.0837894	0.763305	0.576838	-1.48212	2.05231	0.212393	2.52537
1.99737	1.02329	0.46945	-0.946581	-2.82259	0.219534	-0.119991
1.33101	1.26448	-0.194266	-0.04004	0.0472404	1.44837	-0.0902397
0.630194	0.0726304	-2.43426	4.066	-0.409978	-2.3393	0.838061
0.110044	0.620535	0.824383	-1.13547	0.0976623	0.263277	1.46608
3.11664	0.072773	-0.254449	-0.0203781	-0.745496	0.486221	0.640586
			-0.422727			

Table A2.2: The weights for the second highest ranked yield strength model (3 hidden units, random number seed of 50). The data are arranged in a continuous horizontal sequence in the following order: $\theta_1^{(1)}$, $w_{1,1}^{(1)} \ldots w_{1,19}^{(1)}$, $\theta_2^{(1)}$, $w_{2,1}^{(1)} \ldots w_{2,19}^{(1)}$, $\theta_3^{(1)}$, $w_{3,1}^{(1)} \ldots w_{3,19}^{(1)}$, $\theta^{(2)}$, $w_1^{(2)} \ldots w_3^{(2)}$.

1.52771	0.130892	0.158762	0.129669	0.028678	4.28128	1.02017
-0.537522	-1.91699	0.544957	0.710081	-1.65936	-3.27051	-0.0623858
-0.126148	0.448406	1.55414	0.503071	-1.83626	-0.735993	2.54129
0.085005	0.761328	0.57517	-1.47947	2.05066	0.212981	2.52377
1.99755	1.02311	0.466991	-0.927745	-2.83122	0.216813	-0.117682
1.32788	1.26225	-0.194948	-0.0385676	0.0470837	1.45127	-0.0896011
0.628999	0.0700215	-2.43563	4.06835	-0.406778	-2.34629	0.843195
0.111985	0.616167	0.842021	-1.14799	0.0940677	0.267963	1.46457
3.11701	0.0720523	-0.253438	-0.0195078	0	0	0
0	0	0	0	0	0	0
0	0	0	0	0	0	0
0	0	0	-0.745237	0.486101	0.640934	-0.42255
			0			

Table A2.3: The weights for the third highest ranked yield strength model (4 hidden units, random number seed of 35). The data are arranged in a continuous horizontal sequence in the following order: $\theta_1^{(1)}$, $w_{1,1}^{(1)} \ldots w_{1,19}^{(1)}$, $\theta_2^{(1)}$, $w_{2,1}^{(1)} \ldots w_{2,19}^{(1)}$, $\theta_3^{(1)}$, $w_{3,1}^{(1)} \ldots w_{3,19}^{(1)}$, $\theta_4^{(1)}$, $w_{4,1}^{(1)} \ldots w_{4,19}^{(1)}$, $\theta^{(2)}$, $w_1^{(2)} \ldots w_4^{(2)}$.

-0.107965	0.0573655	-0.0613495	0.0288485	-0.000134314	0.00305974	0.0836847
0.0406543	-0.516705	-0.0964365	0.100146	-0.000725501	-0.0179112	-0.162536
-0.00557001	-0.0338045	0.0765412	-0.0264282	-0.290584	-0.244032	0.0910335
0.10959	0.0518192	0.00783204	0.00286686	0.000667963	0.107157	0.232409
0.118248	-0.0299825	-0.386075	0.000558905	-0.141753	-0.21818	0.00222818
-0.00391664	0.054927	0.0493295	-0.228877	-0.274673	0.0367457	0.023917
0.0695565	-0.038123	-0.00490637	-0.000783721	0.0255852	-0.00878945	0.241244
0.0320366	-0.294835	-0.000885827	-0.0191008	-0.0335813	0.0193123	0.0221419
-0.0392133	0.0783278	-0.591047	-0.0773039	0.111396	0.0174837	0.0352805
0.0270851	0.00128652	0.00482311	-0.0037441	0.205378	0.340798	0.0452223
-0.129257	-0.000542862	-0.113091	-0.00296279	-0.0146525	0.0160665	0.0117534
-0.0158564	0.621586	0.0665543	1.50679	29.4869	-27.9551	31.4683
			33.6464			

Table A2.4: The weights for the fourth highest ranked yield strength model (4 hidden units, random number seed of 5). The data are arranged in a continuous horizontal sequence in the following order: $\theta_1^{(1)}$, $w_{1,1}^{(1)} \ldots w_{1,19}^{(1)}$, $\theta_2^{(1)}$, $w_{2,1}^{(1)} \ldots w_{2,19}^{(1)}$, $\theta_3^{(1)}$, $w_{3,1}^{(1)} \ldots w_{3,19}^{(1)}$, $\theta_4^{(1)}$, $w_{4,1}^{(1)} \ldots w_{4,19}^{(1)}$, $\theta^{(2)}$, $w_1^{(2)} \ldots w_4^{(2)}$.

-0.463083	0.0139331	1.38713	0.126085	0.166394	0.224425	0.696231
0.228694	-2.49771	0.0490209	2.80412	-0.727356	-1.13542	-0.692619
-1.35559e-05	0.181066	-0.650902	-0.0167849	-0.0147237	-0.676583	0.115048
0.0127762	-1.36156	-0.00308982	-0.196379	-0.0954772	-0.62722	0.348801
2.97001	0.1547	-3.08881	-0.12653	0.0709729	0.750029	-3.5612e-05
-0.050513	0.6152	-0.0190338	-0.0116097	0.713112	-0.142552	2.72956
			2.65188			

Table A2.5: The weights for the fifth highest ranked yield strength model (2 hidden units, random number seed of 50). The data are arranged in a continuous horizontal sequence in the following order: $\theta_1^{(1)}$, $w_{1,1}^{(1)} \ldots w_{1,19}^{(1)}$, $\theta_2^{(1)}$, $w_{2,1}^{(1)} \ldots w_{2,19}^{(1)}$, $\theta^{(2)}$, $w_1^{(2)}$, $w_2^{(2)}$.

APPENDIX THREE

Ultimate Tensile Strength Committee Model Weights

-0.545033	-0.0064281	-0.126882	0.0330432	-0.0662099	0.167478	-0.00908487
-0.321078	0.0692095	0.144995	0.0257678	0.000139848	0.000106472	-0.093284
-0.0112513	-0.0188631	0.0317367	-0.107515	0.212019	0.0367566	0.0271643
-0.0661274	0.732212	-0.0151088	-0.0346088	0.117374	0.127426	0.192166
0.0632741	-0.223416	0.0733402	0.256446	0.0661928	8.89202e-05	-0.000106467
-0.148686	0.0250997	0.0861742	0.0664669	-0.0324574	0.180785	-0.0734655
-0.0350267	-0.317535	-0.2994	-0.00220252	0.149785	0.101062	0.218229
-0.0652287	0.0972585	0.184202	6.75444e-05	0.0967146	0.0461672	0.000105812
0.000105008	-0.0536363	0.0387114	0.101838	0.0403639	0.0940998	-0.0696791
-0.126964	-0.0783781	-0.144771	10.5165	7.70683	-7.1856	7.16927

Table A3.1: The weights for the highest ranked ultimate tensile strength model (3 hidden units, random number seed of 35). The data are arranged in a continuous horizontal sequence in the following order: $\theta_1^{(1)}, w_{1,1}^{(1)} \ldots w_{1,21}^{(1)}, \theta_2^{(1)}, w_{2,1}^{(1)} \ldots w_{2,21}^{(1)}, \theta^{(2)}, w_1^{(2)}, w_2^{(2)}$.

-0.16122	0.0407871	-0.00909901	0.0169438	0.136259	0.0888185	-0.0175177
0.103726	-0.0131323	0.0872891	0.0239744	-0.000826904	-0.00130356	0.215996
0.0496323	0.0167179	0.020286	-0.0135664	0.15469	0.480376	-0.0368901
-0.0747955	-0.172081	0.0897425	-0.0361481	-0.0489297	-0.208196	-0.20474
-0.0579633	-0.0637738	0.0294171	-0.0906785	-0.0646641	0.000636431	0.000926244
0.272689	-0.00147277	0.0826351	-0.0207208	0.0221835	0.0285505	0.626368
0.214549	0.0752131	-0.152502	0.0364549	-0.0374196	-0.0411478	-0.160239
0.0319428	-0.017594	0.270243	-0.0164737	0.0443762	0.125007	0.000464847
0.000679067	0.537775	-0.0794043	-0.181952	0.0278522	-0.0711348	0.194159
0.12131	-0.197654	0.0873153	-0.00618774	0.0566016	-0.0517417	-0.0930999
-0.549828	-0.349333	-0.0361367	0.083644	0.0601097	-0.173143	-0.0972791
-0.000566209	-0.000780473	0.155943	-0.14056	0.0876987	-0.0118004	-0.0137913
-0.245168	-0.184675	0.0144672	0.207809	-0.317642	-0.0111103	0.0198983
0.0313242	-0.010758	-0.0342228	0.0349095	0.139498	0.0299207	0.0334859
-0.0761596	0.000590194	0.000840134	-0.283084	-0.0157624	0.152502	0.027587
-0.00533164	-0.201626	-0.333052	-0.135756	0.0294736	2.85903	-11.038
	8.00081	5.57286	-7.80338	7.66909		

Table A3.2: The weights for the second highest ranked ultimate tensile strength model (5 hidden units, random number seed of 35). The data are arranged in a continuous horizontal sequence in the following order: $\theta_1^{(1)}, w_{1,1}^{(1)} \ldots w_{1,21}^{(1)}, \theta_2^{(1)}, w_{2,1}^{(1)} \ldots w_{2,21}^{(1)}, \theta_3^{(1)}, w_{3,1}^{(1)} \ldots w_{3,21}^{(1)}, \theta_4^{(1)}, w_{4,1}^{(1)} \ldots w_{4,21}^{(1)}, \theta_5^{(1)}, w_{5,1}^{(1)} \ldots w_{5,21}^{(1)}, \theta^{(2)}, w_1^{(2)} \ldots w_5^{(2)}$.

-0.0911319	-0.0467519	-0.185872	0.0542093	0.139544	0.112131	-0.00884624
-0.159532	0.0762567	-0.0752384	0.0329026	-6.76202e-05	-0.000832395	0.10332
0.0176329	0.457008	-0.0952556	0.307908	0.0127599	0.00153671	-0.0344478
0.0353183	-0.0293909	0.0921828	0.23866	-0.157204	-0.254759	-0.301421
-0.132347	0.373071	0.0449085	-0.0840789	-0.0743927	0.000103465	0.00130424
0.0281757	-0.0607581	0.0845989	0.030228	-0.144532	-0.0989584	0.407892
0.121197	0.072573	-0.0334251	0.117165	0.091334	0.0607349	-0.329338
-0.150816	-0.0344293	0.0254348	0.0643187	0.0170009	0.0785463	-0.000140272
-0.0022139	-0.140086	0.0239122	0.247511	0.0303347	-0.204584	-0.128115
0.108966	-0.00901446	-0.00418695	-0.0371955	-0.0101928	0.270777	-0.147764
0.10708	-0.10376	-0.0364737	0.156751	-0.0886395	0.031076	-0.118679
-0.000104144	-0.00229921	0.0265603	0.00725928	-0.340225	0.0552878	-0.179458
0.118286	0.295933	0.166681	-0.13071	-0.276006	-0.0461078	-0.00489961
0.136872	0.263665	0.188504	0.0881901	-0.397621	-0.0242848	0.111534
0.0567841	0.000213839	0.00178291	-0.0580242	0.13678	0.2538	-0.0149016
0.0369014	0.18085	0.00767431	0.0329047	-0.177406	1.52726	-8.9659
	9.70672	-8.12352	-10.5055	9.05696		

Table A3.3: The weights for the third highest ranked ultimate tensile strength model (5 hidden units, random number seed of 5). The data are arranged in a continuous horizontal sequence in the following order: $\theta_1^{(1)}, w_{1,1}^{(1)} \ldots w_{1,21}^{(1)}, \theta_2^{(1)}, w_{2,1}^{(1)} \ldots w_{2,21}^{(1)}, \theta_3^{(1)}, w_{3,1}^{(1)} \ldots w_{3,21}^{(1)}, \theta_4^{(1)}, w_{4,1}^{(1)} \ldots w_{4,21}^{(1)}, \theta_5^{(1)}, w_{5,1}^{(1)} \ldots w_{5,21}^{(1)}, \theta^{(2)}, w_1^{(2)} \ldots w_5^{(2)}$.

-0.341103	0.000208627	-0.0366557	-0.0943532	-0.0174077	-0.00562245	-0.0421953
0.20631	-0.0645495	-0.180316	-0.0477751	-0.0148117	0.00120155	0.0953614
-0.0794944	-0.0461336	-0.0320866	-0.00411833	-0.072802	0.0127794	-0.00137493
0.233802	-0.626333	0.00772527	0.0703737	0.140811	0.042378	-0.0220453
0.071239	-0.280358	0.105118	0.256957	0.0726967	0.0224132	0.000835579
-0.14672	0.101595	0.060798	0.0549941	0.00194871	0.0995868	-0.0181281
	-0.000927529	-0.236674	9.49514	9.69405	11.3157	

Table A3.4: The weights for the fourth highest ranked ultimate tensile strength model (2 hidden units, random number seed of 35). The data are arranged in a continuous horizontal sequence in the following order: $\theta_1^{(1)}, w_{1,1}^{(1)} \ldots w_{1,21}^{(1)}, \theta_2^{(1)}, w_{2,1}^{(1)} \ldots w_{2,21}^{(1)}, \theta^{(2)}, w_1^{(2)}, w_2^{(2)}$.

APPENDIX FOUR

Elongation Committee Model Weights

1.63729	0.154138	-0.270472	-0.0810972	1.40933	0.749691	5.63063e-05
0.670304	-0.00421304	8.77637e-06	-0.0617053	-1.08297	-0.733283	0.535769
0.076743	-0.47886	0.365962	-0.240763	-0.220445	-0.101777	-0.00752344
	0.00097048	1.66408	0.80988	-1.14361		

Table A4.1: The weights for the highest ranked elongation model (1 hidden unit, random number seed of 50). The data are arranged in a continuous horizontal sequence in the following order: $\theta_1^{(1)}, w_{1,1}^{(1)} \ldots w_{1,22}^{(1)}, \theta^{(2)}, w_1^{(2)}$.

1.63729	0.154138	-0.270472	-0.0810972	1.40933	0.749691	5.63063e-05
0.670304	-0.00421304	8.77637e-06	-0.0617053	-1.08297	-0.733283	0.535769
0.076743	-0.47886	0.365962	-0.240763	-0.220445	-0.101777	-0.00752344
	0.00097048	1.66408	0.80988	-1.14361		

Table A4.2: The weights for the second highest ranked elongation model (1 hidden unit, random number seed of 15). The data are arranged in a continuous horizontal sequence in the following order: $\theta_1^{(1)}, w_{1,1}^{(1)} \ldots w_{1,22}^{(1)}, \theta^{(2)}, w_1^{(2)}$.

1.63729	0.154138	-0.270472	-0.0810972	1.40933	0.749691	5.63063e-05
0.670304	-0.00421304	8.77637e-06	-0.0617053	-1.08297	-0.733283	0.535769
0.076743	-0.47886	0.365962	-0.240763	-0.220445	-0.101777	-0.00752344
	0.00097048	1.66408	0.80988	-1.14361		

Table A4.3: The weights for the third highest ranked elongation model (1 hidden unit, random number seed of 35). The data are arranged in a continuous horizontal sequence in the following order: $\theta_1^{(1)}, w_{1,1}^{(1)} \ldots w_{1,22}^{(1)}, \theta^{(2)}, w_1^{(2)}$.

1.63729	0.154138	-0.270472	-0.0810972	1.40933	0.749691	5.63063e-05
0.670304	-0.00421304	8.77637e-06	-0.0617053	-1.08297	-0.733283	0.535769
0.076743	-0.47886	0.365962	-0.240763	-0.220445	-0.101777	-0.00752344
	0.00097048	1.66408	0.80988	-1.14361		

Table A4.4: The weights for the fourth highest ranked elongation model (1 hidden unit, random number seed of 40). The data are arranged in a continuous horizontal sequence in the following order: $\theta_1^{(1)}, w_{1,1}^{(1)} \ldots w_{1,22}^{(1)}, \theta^{(2)}, w_1^{(2)}$.

1.63729	0.154138	-0.270472	-0.0810972	1.40933	0.749691	5.63063e-05
0.670304	-0.00421304	8.77637e-06	-0.0617053	-1.08297	-0.733283	0.535769
0.076743	-0.47886	0.365962	-0.240763	-0.220445	-0.101777	-0.00752344
	0.00097048	1.66408	0.80988	-1.14361		

Table A4.5: The weights for the fifth highest ranked elongation model (1 hidden unit, random number seed of 5). The data are arranged in a continuous horizontal sequence in the following order: $\theta_1^{(1)}$, $w_{1,1}^{(1)} \ldots w_{1,22}^{(1)}$, $\theta^{(2)}$, $w_1^{(2)}$.

1.63729	0.154138	-0.270472	-0.0810972	1.40933	0.749691	5.63063e-05
0.670304	-0.00421304	8.77637e-06	-0.0617053	-1.08297	-0.733283	0.535769
0.076743	-0.47886	0.365962	-0.240763	-0.220445	-0.101777	-0.00752344
	0.00097048	1.66408	0.80988	-1.14361		

Table A4.6: The weights for the sixth highest ranked elongation model (1 hidden unit, random number seed of 100). The data are arranged in a continuous horizontal sequence in the following order: $\theta_1^{(1)}$, $w_{1,1}^{(1)} \ldots w_{1,22}^{(1)}$, $\theta^{(2)}$, $w_1^{(2)}$.

0.88167	0.149517	0.0151697	0.0129692	0.335026	0.00392999	-0.0511173
1.21241	0.0175067	-0.0467438	-0.000104062	0.0077249	-0.00956263	0.35758
-0.00951728	-0.00204085	0.0849073	0.0956826	-0.761419	-0.508334	-0.735911
0.00113289	-0.0902916	-0.81098	-0.0720458	-0.0211654	0.00213147	0.0495388
-0.00163021	0.0276734	-0.385251	-0.0884199	-0.136684	-0.00144756	0.0177207
-0.0172987	-0.184275	-0.0093803	-0.0125923	0.130897	-0.123881	0.383453
0.387762	0.557174	0.00253247	-0.0851067	-1.36555	-0.0815129	0.0268461
-0.0218758	-0.519388	-0.0013435	-0.00147399	-0.922479	0.0693961	0.16083
0.000284554	0.00654317	-0.00461379	-0.225933	-0.00949491	0.0068156	-0.318388
0.0485314	0.380421	0.154403	0.112262	0.0031324	0.00544869	7.98685
		6.35459	8.7227	8.12829		

Table A4.7: The weights for the seventh highest ranked elongation model (3 hidden units, random number seed of 100). The data are arranged in a continuous horizontal sequence in the following order: $\theta_1^{(1)}$, $w_{1,1}^{(1)} \ldots w_{1,22}^{(1)}$, $\theta_2^{(1)}$, $w_{2,1}^{(1)} \ldots w_{2,22}^{(1)}$, $\theta_3^{(1)}$, $w_{3,1}^{(1)} \ldots w_{3,22}^{(1)}$, $\theta^{(2)}$, $w_1^{(2)} \ldots w_3^{(2)}$.

0.88167	0.149517	0.0151697	0.0129692	0.335026	0.00392999	-0.0511173
1.21241	0.0175067	-0.0467438	-0.000104062	0.0077249	-0.00956263	0.35758
-0.00951728	-0.00204085	0.0849073	0.0956826	-0.761419	-0.508334	-0.735911
0.00113289	-0.0902916	-0.81098	-0.0720458	-0.0211654	0.00213147	0.0495388
-0.00163021	0.0276734	-0.385251	-0.0884199	-0.136684	-0.00144756	0.0177207
-0.0172987	-0.184275	-0.0093803	-0.0125923	0.130897	-0.123881	0.383453
0.387762	0.557174	0.00253247	-0.0851067	-1.36555	-0.0815129	0.0268461
-0.0218758	-0.519388	-0.0013435	-0.00147399	-0.922479	0.0693961	0.16083
0.000284554	0.00654317	-0.00461379	-0.225933	-0.00949491	0.0068156	-0.318388
0.0485314	0.380421	0.154403	0.112262	0.0031324	0.00544869	7.98685
		6.35459	8.7227	8.12829		

Table A4.8: The weights for the eigth highest ranked elongation model (3 hidden units, random number seed of 50). The data are arranged in a continuous horizontal sequence in the following order: $\theta_1^{(1)}$, $w_{1,1}^{(1)} \ldots w_{1,22}^{(1)}$, $\theta_2^{(1)}$, $w_{2,1}^{(1)} \ldots w_{2,22}^{(1)}$, $\theta_3^{(1)}$, $w_{3,1}^{(1)} \ldots w_{3,22}^{(1)}$, $\theta^{(2)}$, $w_1^{(2)} \ldots w_3^{(2)}$.

0.88167	0.149517	0.0151697	0.0129692	0.335026	0.00392999	-0.0511173
1.21241	0.0175067	-0.0467438	-0.000104062	0.0077249	-0.00956263	0.35758
-0.00951728	-0.00204085	0.0849073	0.0956826	-0.761419	-0.508334	-0.735911
0.00113289	-0.0902916	-0.81098	-0.0720458	-0.0211654	0.00213147	0.0495388
-0.00163021	0.0276734	-0.385251	-0.0884199	-0.136684	-0.00144756	0.0177207
-0.0172987	-0.184275	-0.0093803	-0.0125923	0.130897	-0.123881	0.383453
0.387762	0.557174	0.00253247	-0.0851067	-1.36555	-0.0815129	0.0268461
-0.0218758	-0.519388	-0.0013435	-0.00147399	-0.922479	0.0693961	0.16083
0.000284554	0.00654317	-0.00461379	-0.225933	-0.00949491	0.0068156	-0.318388
0.0485314	0.380421	0.154403	0.112262	0.0031324	0.00544869	7.98685
		6.35459	8.7227	8.12829		

Table A4.9: The weights for the ninth highest ranked elongation model (3 hidden units, random number seed of 40). The data are arranged in a continuous horizontal sequence in the following order: $\theta_1^{(1)}$, $w_{1,1}^{(1)} \ldots w_{1,22}^{(1)}$, $\theta_2^{(1)}$, $w_{2,1}^{(1)} \ldots w_{2,22}^{(1)}$, $\theta_3^{(1)}$, $w_{3,1}^{(1)} \ldots w_{3,22}^{(1)}$, $\theta^{(2)}$, $w_1^{(2)} \ldots w_3^{(2)}$.

1.52934	0.842658	0.00763292	0.000626582	0.575709	1.76476e-05	-0.00934563
-0.012752	-0.0218797	-4.50097e-06	0.00195792	0.0182485	0.00388389	1.30363
-0.00274639	0.00405458	0.790024	0.0195902	-0.688101	-0.10193	-0.643422
-0.00795733	0.0664209	-1.40359	-0.571502	0.0136467	0.000949231	-0.454338
1.93989e-05	0.0075802	-0.0138852	0.0119805	-5.24641e-06	0.00324197	0.0325499
0.00640393	-0.945455	-0.00436165	0.00588677	-0.56252	0.00822007	0.473832
0.0781074	0.443773	-0.0100259	-0.184774	2.87075	6.0364	9.88388

Table A4.10: The weights for the tenth highest ranked elongation model (2 hidden units, random number seed of 50). The data are arranged in a continuous horizontal sequence in the following order: $\theta_1^{(1)}$, $w_{1,1}^{(1)} \ldots w_{1,22}^{(1)}$, $\theta_2^{(1)}$, $w_{2,1}^{(1)} \ldots w_{2,22}^{(1)}$, $\theta^{(2)}$, $w_1^{(2)}, w_2^{(2)}$.

0.88167	0.149517	0.0151697	0.0129692	0.335026	0.00392999	-0.0511173
1.21241	0.0175067	-0.0467438	-0.000104062	0.0077249	-0.00956263	0.35758
-0.00951728	-0.00204085	0.0849073	0.0956826	-0.761419	-0.508334	-0.735911
0.00113289	-0.0902916	-0.81098	-0.0720458	-0.0211654	0.00213147	0.0495388
-0.00163021	0.0276734	-0.385251	-0.0884199	-0.136684	-0.00144756	0.0177207
-0.0172987	-0.184275	-0.0093803	-0.0125923	0.130897	-0.123881	0.383453
0.387762	0.557174	0.00253247	-0.0851067	-1.36555	-0.0815129	0.0268461
-0.0218758	-0.519388	-0.0013435	-0.00147399	-0.922479	0.0693961	0.16083
0.000284554	0.00654317	-0.00461379	-0.225933	-0.00949491	0.0068156	-0.318388
0.0485314	0.380421	0.154403	0.112262	0.0031324	0.00544869	7.98685
		6.35459	8.7227	8.12829		

Table A4.11: The weights for the eleventh highest ranked elongation model (3 hidden units, random number seed of 50). The data are arranged in a continuous horizontal sequence in the following order: $\theta_1^{(1)}$, $w_{1,1}^{(1)} \ldots w_{1,22}^{(1)}$, $\theta_2^{(1)}$, $w_{2,1}^{(1)} \ldots w_{2,22}^{(1)}$, $\theta_3^{(1)}$, $w_{3,1}^{(1)} \ldots w_{3,22}^{(1)}$, $\theta^{(2)}$, $w_1^{(2)} \ldots w_3^{(2)}$.

1.52934	0.842658	0.00763292	0.000626582	0.575709	1.76476e-05	-0.00934563
-0.012752	-0.0218797	-4.50097e-06	0.00195792	0.0182485	0.00388389	1.30363
-0.00274639	0.00405458	0.790024	0.0195902	-0.688101	-0.10193	-0.643422
-0.00795733	0.0664209	-1.40359	-0.571502	0.0136467	0.000949231	-0.454338
1.93989e-05	0.0075802	-0.0138852	0.0119805	-5.24641e-06	0.00324197	0.0325499
0.00640393	-0.945455	-0.00436165	0.00588677	-0.56252	0.00822007	0.473832
0.0781074	0.443773	-0.0100259	-0.184774	2.87075	6.0364	9.88388

Table A4.12: The weights for the twelfth highest ranked elongation model (2 hidden units, random number seed of 40). The data are arranged in a continuous horizontal sequence in the following order: $\theta_1^{(1)}$, $w_{1,1}^{(1)} \ldots w_{1,22}^{(1)}$, $\theta_2^{(1)}$, $w_{2,1}^{(1)} \ldots w_{2,22}^{(1)}$, $\theta^{(2)}$, $w_1^{(2)}, w_2^{(2)}$.

0.875064	0.146739	0.0142797	0.0127131	0.327083	0.00461617	-0.0485897
1.20065	0.0147705	-0.0447336	-6.82392e-05	0.00761233	-0.00968848	0.350626
-0.00907756	-0.00198469	0.0836625	0.0939901	-0.750179	-0.495806	-0.718516
0.000918248	-0.0909517	-0.808926	-0.0703016	-0.0213713	0.0026763	0.0593876
-0.00163857	0.0276183	-0.369993	-0.0897013	-0.136185	-0.00150871	0.0169561
-0.0171528	-0.180091	-0.00904761	-0.0130981	0.136346	-0.12279	0.373593
0.380064	0.546129	0.00224655	-0.0843507	-1.33113	-0.0807122	0.025942
-0.0214072	-0.504757	-0.00152557	-0.00185584	-0.912996	0.0694843	0.15237
0.000340223	0.00662406	-0.00494845	-0.221741	-0.00900197	0.00700077	-0.308425
0.0440781	0.382118	0.155967	0.122742	0.00308551	0.00962997	0
0	0	0	0	0	0	0
0	0	0	0	0	0	0
0	0	0	0	0	0	0
0	8.17243	6.59659	8.90523	8.46649	0	

Table A4.13: The weights for the thirteenth highest ranked elongation model (4 hidden units, random number seed of 5). The data are arranged in a continuous horizontal sequence in the following order: $\theta_1^{(1)}$, $w_{1,1}^{(1)} \ldots w_{1,22}^{(1)}$, $\theta_2^{(1)}$, $w_{2,1}^{(1)} \ldots w_{2,22}^{(1)}$, $\theta_3^{(1)}$, $w_{3,1}^{(1)} \ldots w_{3,22}^{(1)}$, $\theta_4^{(1)}$, $w_{4,1}^{(1)} \ldots w_{4,22}^{(1)}$, $\theta^{(2)}$, $w_1^{(2)} \ldots w_4^{(2)}$.

1.52934	0.842658	0.00763292	0.000626582	0.575709	1.76476e-05	-0.00934563
-0.012752	-0.0218797	-4.50097e-06	0.00195792	0.0182485	0.00388389	1.30363
-0.00274639	0.00405458	0.790024	0.0195902	-0.688101	-0.10193	-0.643422
-0.00795733	0.0664209	-1.40359	-0.571502	0.0136467	0.000949231	-0.454338
1.93989e-05	0.0075802	-0.0138852	0.0119805	-5.24641e-06	0.00324197	0.0325499
0.00640393	-0.945455	-0.00436165	0.00588677	-0.56252	0.00822007	0.473832
0.0781074	0.443773	-0.0100259	-0.184774	2.87075	6.0364	9.88388

Table A4.14: The weights for the fourteenth highest ranked elongation model (2 hidden units, random number seed of 15). The data are arranged in a continuous horizontal sequence in the following order: $\theta_1^{(1)}$, $w_{1,1}^{(1)} \ldots w_{1,22}^{(1)}$, $\theta_2^{(1)}$, $w_{2,1}^{(1)} \ldots w_{2,22}^{(1)}$, $\theta^{(2)}$, $w_1^{(2)}$, $w_2^{(2)}$.

0.875064	0.146739	0.0142797	0.0127131	0.327083	0.00461617	-0.0485897
1.20065	0.0147705	-0.0447336	-6.82392e-05	0.00761233	-0.00968848	0.350626
-0.00907756	-0.00198469	0.0836625	0.0939901	-0.750179	-0.495806	-0.718516
0.000918248	-0.0909517	-0.808926	-0.0703016	-0.0213713	0.0026763	0.0593876
-0.00163857	0.0276183	-0.369993	-0.0897013	-0.136185	-0.00150871	0.0169561
-0.0171528	-0.180091	-0.00904761	-0.0130981	0.136346	-0.12279	0.373593
0.380064	0.546129	0.00224655	-0.0843507	-1.33113	-0.0807122	0.025942
-0.0214072	-0.504757	-0.00152557	-0.00185584	-0.912996	0.0694843	0.15237
0.000340223	0.00662406	-0.00494845	-0.221741	-0.00900197	0.00700077	-0.308425
0.0440781	0.382118	0.155967	0.122742	0.00308551	0.00962997	0
0	0	0	0	0	0	0
0	0	0	0	0	0	0
0	0	0	0	0	0	0
0	8.17243	6.59659	8.90523	8.46649	0	

Table A4.15: The weights for the fifteenth highest ranked elongation model (4 hidden units, random number seed of 35). The data are arranged in a continuous horizontal sequence in the following order: $\theta_1^{(1)}$, $w_{1,1}^{(1)} \ldots w_{1,22}^{(1)}$, $\theta_2^{(1)}$, $w_{2,1}^{(1)} \ldots w_{2,22}^{(1)}$, $\theta_3^{(1)}$, $w_{3,1}^{(1)} \ldots w_{3,22}^{(1)}$, $\theta_4^{(1)}$, $w_{4,1}^{(1)} \ldots w_{4,22}^{(1)}$, $\theta^{(2)}$, $w_1^{(2)} \ldots w_4^{(2)}$.

0.88167	0.149517	0.0151697	0.0129692	0.335026	0.00392999	-0.0511173
1.21241	0.0175067	-0.0467438	-0.000104062	0.0077249	-0.00956263	0.35758
-0.00951728	-0.00204085	0.0849073	0.0956826	-0.761419	-0.508334	-0.735911
0.00113289	-0.0902916	-0.81098	-0.0720458	-0.0211654	0.00213147	0.0495388
-0.00163021	0.0276734	-0.385251	-0.0884199	-0.136684	-0.00144756	0.0177207
-0.0172987	-0.184275	-0.0093803	-0.0125923	0.130897	-0.123881	0.383453
0.387762	0.557174	0.00253247	-0.0851067	-1.36555	-0.0815129	0.0268461
-0.0218758	-0.519388	-0.0013435	-0.00147399	-0.922479	0.0693961	0.16083
0.000284554	0.00654317	-0.00461379	-0.225933	-0.00949491	0.0068156	-0.318388
0.0485314	0.380421	0.154403	0.112262	0.0031324	0.00544869	7.98685
		6.35459	8.7227	8.12829		

Table A4.16: The weights for the sixteenth highest ranked elongation model (3 hidden units, random number seed of 35). The data are arranged in a continuous horizontal sequence in the following order: $\theta_1^{(1)}$, $w_{1,1}^{(1)} \ldots w_{1,22}^{(1)}$, $\theta_2^{(1)}$, $w_{2,1}^{(1)} \ldots w_{2,22}^{(1)}$, $\theta_3^{(1)}$, $w_{3,1}^{(1)} \ldots w_{3,22}^{(1)}$, $\theta^{(2)}$, $w_1^{(2)} \ldots w_3^{(2)}$.

0.875064	0.146739	0.0142797	0.0127131	0.327083	0.00461617	-0.0485897
1.20065	0.0147705	-0.0447336	-6.82392e-05	0.00761233	-0.00968848	0.350626
-0.00907756	-0.00198469	0.0836625	0.0939901	-0.750179	-0.495806	-0.718516
0.000918248	-0.0909517	-0.808926	-0.0703016	-0.0213713	0.0026763	0.0593876
-0.00163857	0.0276183	-0.369993	-0.0897013	-0.136185	-0.00150871	0.0169561
-0.0171528	-0.180091	-0.00904761	-0.0130981	0.136346	-0.12279	0.373593
0.380064	0.546129	0.00224655	-0.0843507	-1.33113	-0.0807122	0.025942
-0.0214072	-0.504757	-0.00152557	-0.00185584	-0.912996	0.0694843	0.15237
0.000340223	0.00662406	-0.00494845	-0.221741	-0.00900197	0.00700077	-0.308425
0.0440781	0.382118	0.155967	0.122742	0.00308551	0.00962997	0
0	0	0	0	0	0	0
0	0	0	0	0	0	0
0	0	0	0	0	0	0
0	8.17243	6.59659	8.90523	8.46649	0	

Table A4.17: The weights for the seventeenth highest ranked elongation model (4 hidden units, random number seed of 40). The data are arranged in a continuous horizontal sequence in the following order: $\theta_1^{(1)}, w_{1,1}^{(1)} \ldots w_{1,22}^{(1)}, \theta_2^{(1)}, w_{2,1}^{(1)} \ldots w_{2,22}^{(1)}, \theta_3^{(1)}, w_{3,1}^{(1)} \ldots w_{3,22}^{(1)}, \theta_4^{(1)}, w_{4,1}^{(1)} \ldots w_{4,22}^{(1)}, \theta^{(2)}, w_1^{(2)} \ldots w_4^{(2)}$.

0.881778	0.149079	0.0150108	0.0129649	0.333917	0.00405523	-0.0502317
1.21186	0.0162867	-0.0474532	-9.25712e-05	0.00767695	-0.00958434	0.356515
-0.00945074	-0.00195533	0.0865262	0.0949511	-0.75927	-0.5033	-0.728624
0.00104946	-0.0914394	-0.815179	-0.0711924	-0.0213195	0.00235899	0.0541426
-0.00162737	0.0274486	-0.376486	-0.0887954	-0.136325	-0.00144802	0.0176411
-0.017358	-0.182327	-0.00932709	-0.0127907	0.131945	-0.123168	0.377956
0.383002	0.549563	0.00249548	-0.0852401	-1.35162	-0.0818593	0.0266826
-0.0219188	-0.518937	-0.00138906	-0.00163904	-0.926713	0.0700123	0.159504
0.000289716	0.0066333	-0.00469452	-0.226271	-0.0093178	0.00688777	-0.317378
0.0473581	0.384103	0.155525	0.116715	0.00315488	0.00729588	0
0	0	0	0	0	0	0
0	0	0	0	0	0	0
0	0	0	0	0	0	0
0	0	0	0	0	0	0
0	0	0	0	0	0	0
0	0	0	0	0	0	0
0	0	0	0	0	0	0
0	0	0	0	0	0	0
0	0	0	0	0	0	0
0	0	0	0	0	7.99344	6.38805
	8.8046	8.10836	0	0	0	

Table A4.18: The weights for the eighteenth highest ranked elongation model (6 hidden units, random number seed of 5). The data are arranged in a continuous horizontal sequence in the following order: $\theta_1^{(1)}$, $w_{1,1}^{(1)} \ldots w_{1,22}^{(1)}$, $\theta_2^{(1)}$, $w_{2,1}^{(1)} \ldots w_{2,22}^{(1)}$, $\theta_3^{(1)}$, $w_{3,1}^{(1)} \ldots w_{3,22}^{(1)}, \theta_4^{(1)}, w_{4,1}^{(1)} \ldots w_{4,22}^{(1)}, \theta_5^{(1)}, w_{5,1}^{(1)} \ldots w_{5,22}^{(1)}, \theta_6^{(1)}, w_{6,1}^{(1)} \ldots w_{6,22}^{(1)}, \theta^{(2)}$, $w_1^{(2)} \ldots w_6^{(2)}$.

0.874771	0.146805	0.0143466	0.0127059	0.326812	0.00456246	-0.0487417
1.20019	0.0150525	-0.0445665	-7.05789e-05	0.00760997	-0.00967737	0.350917
-0.00910323	-0.00198949	0.0832326	0.0941308	-0.750475	-0.496713	-0.720022
0.000940908	-0.0905226	-0.808176	-0.0705199	-0.021279	0.00261591	0.0580307
-0.00167358	0.0276319	-0.372788	-0.0894525	-0.135815	-0.001506	0.0169479
-0.0171231	-0.180711	-0.00905881	-0.0130589	0.135577	-0.122805	0.374914
0.380954	0.547552	0.00228048	-0.0842315	-1.33499	-0.0806494	0.0259863
-0.0214429	-0.505422	-0.00153593	-0.00185373	-0.912332	0.0695398	0.152854
0.000340595	0.00659408	-0.00489067	-0.221723	-0.00901903	0.00702048	-0.309064
0.0445361	0.381375	0.155368	0.121302	0.00307887	0.00928373	0
0	0	0	0	0	0	0
0	0	0	0	0	0	0
0	0	0	0	0	0	0
0	0	0	0	0	0	0
0	0	0	0	0	0	0
0	0	0	0	0	0	0
0	0	0	8.1733	6.59471	8.90735	8.45815
		0	0			

Table A4.19: The weights for the nineteenth highest ranked elongation model (5 hidden units, random number seed of 5). The data are arranged in a continuous horizontal sequence in the following order: $\theta_1^{(1)}$, $w_{1,1}^{(1)} \ldots w_{1,22}^{(1)}$, $\theta_2^{(1)}$, $w_{2,1}^{(1)} \ldots w_{2,22}^{(1)}$, $\theta_3^{(1)}$, $w_{3,1}^{(1)} \ldots w_{3,22}^{(1)}$, $\theta_4^{(1)}$, $w_{4,1}^{(1)} \ldots w_{4,22}^{(1)}$, $\theta_5^{(1)}$, $w_{5,1}^{(1)} \ldots w_{5,22}^{(1)}$, $\theta^{(2)}$, $w_1^{(2)} \ldots w_5^{(2)}$.

0.875064	0.146739	0.0142797	0.0127131	0.327083	0.00461617	-0.0485897
1.20065	0.0147705	-0.0447336	-6.82392e-05	0.00761233	-0.00968848	0.350626
-0.00907756	-0.00198469	0.0836625	0.0939901	-0.750179	-0.495806	-0.718516
0.000918248	-0.0909517	-0.808926	-0.0703016	-0.0213713	0.0026763	0.0593876
-0.00163857	0.0276183	-0.369993	-0.0897013	-0.136185	-0.00150871	0.0169561
-0.0171528	-0.180091	-0.00904761	-0.0130981	0.136346	-0.12279	0.373593
0.380064	0.546129	0.00224655	-0.0843507	-1.33113	-0.0807122	0.025942
-0.0214072	-0.504757	-0.00152557	-0.00185584	-0.912996	0.0694843	0.15237
0.000340223	0.00662406	-0.00494845	-0.221741	-0.00900197	0.00700077	-0.308425
0.0440781	0.382118	0.155967	0.122742	0.00308551	0.00962997	0
0	0	0	0	0	0	0
0	0	0	0	0	0	0
0	0	0	0	0	0	0
0	8.17243	6.59659	8.90523	8.46649	0	

Table A4.20: The weights for the twentieth highest ranked elongation model (4 hidden units, random number seed of 15). The data are arranged in a continuous horizontal sequence in the following order: $\theta_1^{(1)}$, $w_{1,1}^{(1)} \ldots w_{1,22}^{(1)}$, $\theta_2^{(1)}$, $w_{2,1}^{(1)} \ldots w_{2,22}^{(1)}$, $\theta_3^{(1)}$, $w_{3,1}^{(1)} \ldots w_{3,22}^{(1)}$, $\theta_4^{(1)}$, $w_{4,1}^{(1)} \ldots w_{4,22}^{(1)}$, $\theta^{(2)}$, $w_1^{(2)} \ldots w_4^{(2)}$.

0.874771	0.146805	0.0143466	0.0127059	0.326812	0.00456246	-0.0487417
1.20019	0.0150525	-0.0445665	-7.05789e-05	0.00760997	-0.00967737	0.350917
-0.00910323	-0.00198949	0.0832326	0.0941308	-0.750475	-0.496713	-0.720022
0.000940908	-0.0905226	-0.808176	-0.0705199	-0.021279	0.00261591	0.0580307
-0.00167358	0.0276319	-0.372788	-0.0894525	-0.135815	-0.001506	0.0169479
-0.0171231	-0.180711	-0.00905881	-0.0130589	0.135577	-0.122805	0.374914
0.380954	0.547552	0.00228048	-0.0842315	-1.33499	-0.0806494	0.0259863
-0.0214429	-0.505422	-0.00153593	-0.00185373	-0.912332	0.0695398	0.152854
0.000340595	0.00659408	-0.00489067	-0.221723	-0.00901903	0.00702048	-0.309064
0.0445361	0.381375	0.155368	0.121302	0.00307887	0.00928373	0
0	0	0	0	0	0	0
0	0	0	0	0	0	0
0	0	0	0	0	0	0
0	0	0	0	0	0	0
0	0	0	0	0	0	0
0	0	0	0	0	0	0
0	0	0	8.1733	6.59471	8.90735	8.45815
		0	0			

Table A4.21: The weights for the twenty-first and final highest ranked elongation model (5 hidden units, random number seed of 5). The data are arranged in a continuous horizontal sequence in the following order: $\theta_1^{(1)}, w_{1,1}^{(1)} \ldots w_{1,22}^{(1)}, \theta_2^{(1)}, w_{2,1}^{(1)} \ldots w_{2,22}^{(1)}, \theta_3^{(1)}, w_{3,1}^{(1)} \ldots w_{3,22}^{(1)}, \theta_4^{(1)}, w_{4,1}^{(1)} \ldots w_{4,22}^{(1)}, \theta_5^{(1)}, w_{5,1}^{(1)} \ldots w_{5,22}^{(1)}, \theta^{(2)}, w_1^{(2)} \ldots w_5^{(2)}$.

APPENDIX FIVE

Charpy Toughness Committee Model Weights

0.625471	-0.202414	0.844923	-0.0353495	0.333065	-0.245596	-0.020394
0.03891	-0.149788	0.363143	0.0254333	-0.0330975	1.02302	0.427016
-1.0857	0.0362138	0.0607974	-0.170669	-0.478539	0.137054	-1.26259
1.02608	-1.94728	-0.221472	-0.527141	1.40518	-0.0296882	0.371384
0.118592	0.4347	0.286814	0.323894	0.106105	0.0827958	-0.0161477
0.74046	-0.90933	-0.431415	0.310117	-0.00599675	-0.180139	0.49932
-0.173028	-0.299233	-1.38363	-0.321973	0.435868	0.521256	1.67011
0.305019	-0.246198	0.387895	0.742993	-0.279362	0.646736	0.145328
-0.0332281	0.0107727	0.224969	-0.332954	-0.141027	0.437644	0.0710098
0.242739	-0.0766462	-0.123131	0.169574	-0.986036	-0.0524459	-1.12208
-0.938813	-2.02375	-0.258414	0.0649272	0.0742159	-0.604282	-0.303976
-1.0137	0.0443474	-0.0963418	-0.00844874	-0.349477	-0.70704	0.36149
-0.217857	-0.0467665	-0.257146	0.692221	0.29424	-0.633021	0.842695
-0.428972	1.19595	1.04493	-0.975559	0.204711	-0.144633	-0.726627
-0.099252	-0.325883	-0.077934	0.20275	-0.00466453	-0.00680664	-0.926814
-0.892913	1.19514	-0.0121532	-0.0577351	0.0442162	-0.522409	0.193243
1.11322	0.526944	2.38201	0.210575	0.188841	-0.444425	0.164299
-0.0241106	0.0322701	0.0713464	-0.603055	-0.372817	0.081256	-0.124816
0.010279	-0.227963	0.644424	-0.0773946	0.0909428	0.0974278	0.177542
-0.179101	0.270833	-0.696108	1.13636	-1.05483	-0.765953	-2.15322
	4.0828	-4.63483	-2.76754	1.86301	3.76891	

Table A5.1: The weights for the highest ranked toughness model (6 hidden units, random number seed of 100). The data are arranged in a continuous horizontal sequence in the following order: $\theta_1^{(1)}, w_{1,1}^{(1)} \ldots w_{1,22}^{(1)}, \theta_2^{(1)}, w_{2,1}^{(1)} \ldots w_{2,22}^{(1)}, \theta_3^{(1)}, w_{3,1}^{(1)} \ldots w_{3,22}^{(1)}, \theta_4^{(1)}, w_{4,1}^{(1)} \ldots w_{4,22}^{(1)}, \theta_5^{(1)}, w_{5,1}^{(1)} \ldots w_{5,22}^{(1)}, \theta_6^{(1)}, w_{6,1}^{(1)} \ldots w_{6,22}^{(1)}, \theta^{(2)}, w_1^{(2)} \ldots w_6^{(2)}$.

0.469554	-0.0502405	0.343047	0.19549	0.175047	-0.473726	0.130475
-0.0418146	-0.0635287	-0.0538669	0.0648491	-0.00558674	-0.703425	0.229683
-0.0122026	0.077717	-0.140186	-0.45719	0.346023	-0.471372	0.498953
0.598267	-1.16299	-0.535317	-0.0913416	-0.028293	1.34882	0.190195
0.991838	0.213733	0.295389	0.0770165	0.0985613	-0.166238	0.00114156
-2.41595	-0.245352	0.104854	-0.0246569	0.000599015	-0.820058	0.808575
	0.198887	-0.0403925	-0.111755	1.36187		

Table A5.2a: The weights for the second highest ranked toughness model (14 hidden units, random number seed of 40). The data are arranged in a continuous horizontal sequence in the following order: $\theta_1^{(1)}, w_{1,1}^{(1)} \ldots w_{1,22}^{(1)}, \theta_2^{(1)}, w_{2,1}^{(1)} \ldots w_{2,22}^{(1)}$.

0.816856	0.852088	-1.18608	-0.0469947	0.273446	-1.53052	-0.0861486
0.0678708	0.0433118	-0.072114	0.112526	-0.00473539	-0.0660165	-0.29858
0.107513	0.0193701	-0.112811	0.322976	-1.29314	0.097058	-0.184541
0.775305	2.25195	-0.00661654	0.205042	0.000961076	-0.389744	0.105174
-0.718809	-0.194874	0.0577662	0.0106161	-0.0273071	0.0555005	0.0129673
-0.46042	-0.261526	0.0397649	-0.0447727	-0.151146	-0.355521	0.221986
-0.449259	0.25493	1.88945	-0.159821	0.134959	0.93357	-0.535735
0.427395	-0.279158	-0.481252	-0.225018	0.0595499	0.0266659	-0.0868712
-0.00717643	-0.00480066	-1.77169	0.806801	0.035668	-0.0612036	-0.00159039
-0.181043	-0.401953	-0.181304	0.315526	0.936213	0.862866	-0.41377
0.2179	0.0120201	1.48148	-0.371524	0.718466	-0.0504834	0.141665
-0.0933917	0.0546242	0.148505	0.0340734	-2.24754	0.708987	0.0514048
-0.068087	0.107306	0.405332	0.179074	-0.152475	0.848719	-1.10751
0.382457	0.145277	0.490221	-0.087829	-0.480942	0.0160029	0.237282
0.0394834	-0.158829	-0.0812175	0.0466994	0.0639584	0.00997372	1.31263
0.532767	-0.0149404	-0.0331908	0.0324263	-0.384091	-0.856753	0.161201
-0.0329705	-1.714	-1.97724	0.333222	-0.359431	0.0225839	-1.00857
-0.145994	-1.2376	0.152573	0.0168186	0.00659675	-0.236603	0.172944
-0.00794832	2.45269	-0.382786	-0.0079042	-0.00706483	-0.025179	0.307136
-0.395854	-0.16046	-0.159144	-0.350488	-1.49531	0.308397	-0.213244
-0.282753	1.86657	0.0595676	0.413132	-0.0481661	-0.0197746	-0.0313611
0.0410866	-0.014087	-0.00127196	-1.41897	-0.989702	-0.0164266	0.0954107
0.0340657	-0.0871527	0.342423	-0.476377	0.64595	-1.33316	0.680625
-0.0226159	-0.0543284	-0.497971	0.267231	-0.0945974	-0.780321	0.199009
-0.417724	-0.147336	-0.183007	0.0617899	-0.0222121	-1.50097	1.17275
-0.114317	0.0557866	-0.133182	-0.171673	0.157861	-0.0540976	-0.284695
1.34047	-0.153788	0.298855	0.58584	0.874329	-1.07773	0.0378907
-0.00764788	-0.298027	0.157234	0.10952	0.0557496	-0.186933	-0.0197605
1.11937	0.789039	-0.0732941	0.0754433	0.0422081	0.0579526	-0.451545
0.0580272	0.555438	-0.429015	-0.176169	0.92753	-0.359572	0.0327102
-0.333013	0.0130862	0.804016	-0.0964566	-0.123252	0.0747801	0.1187
-0.176006	0.00727801	1.30321	-0.735758	0.129839	-0.152773	0.0417153
0.0280647	0.166968	0.0958088	-0.74532	0.49825	1.07623	0.908342
0.398326	-0.65799	0.356007	-0.190864	-0.101518	-0.261333	-0.0951049
0.000755163	0.0677465	-0.0770426	-0.0113173	-0.502721	-0.35446	0.0286646
-0.153731	-0.0945714	0.0601459	-0.294913	-0.394174	0.0394237	1.33782
			2.1637			

Table A 5.2b: The weights for the second highest ranked toughness model (14 hidden units, random number seed of 40). The data are arranged in a continuous horizontal sequence in the following order: $\theta_3^{(1)}, w_{3,1}^{(1)} \ldots w_{3,22}^{(1)}, \theta_4^{(1)}, w_{4,1}^{(1)} \ldots w_{4,22}^{(1)} \ldots\ldots \theta_{13}^{(1)}, w_{13,1}^{(1)} \ldots w_{13,22}^{(1)}$.

0.276048	0.484394	-0.0419397	-1.33178	0.00313581	0.871083	0.0682771
0.0446734	-0.0178607	0.0716875	-0.0203449	0.0048965	-0.368177	1.76367
0.0332424	-0.123248	0.0118276	-0.0713461	-0.200124	0.429835	-0.408772
2.68141	-0.581742	0.940661	-8.35699	5.75617	5.51516	8.36113
-4.93221	7.99628	2.4125	8.91663	8.54745	7.01464	6.12497
		6.9927	-7.76225	5.17823		

Table A 5.2c: The weights for the second highest ranked toughness model (14 hidden units, random number seed of 40). The data are arranged in a continuous horizontal sequence in the following order: $\theta_{14}^{(1)}$, $w_{14,1}^{(1)} \ldots w_{14,22}^{(1)}$, $\theta^{(2)}$, $w_1^{(2)} \ldots w_{14}^{(2)}$.

-0.614856	1.02916	-0.292528	1.39797	-0.61411	0.347673	-0.11822
0.0674189	0.250112	0.100811	-0.736708	0.00346872	-0.523629	-0.171485
0.0280949	0.0586859	0.104732	-0.42169 -	0.404704	-0.0484208	0.113765
-0.659006	0.696868	-0.84443	-0.231113	-0.200484	-0.0378387	0.643618
0.156378	-0.0132425	0.188299	-0.0596366	-0.839056	-0.00484588	-0.00934897
0.18409	-0.648929	0.00397402	0.0304926	0.219121	-0.458205	0.121978
0.0252207	0.251809	-0.42863	2.52931	-0.144947	0.160286	-0.502665
-0.0539332	0.279614	0.0218227	-0.216484	0.586124	0.16371	-0.346849
0.203088	-0.0150155	0.41459	-0.0639245	0.479224	0.104229	-0.0295318
-0.441751	-0.248683	-0.126129	0.525436	-0.621601	1.60658	-0.727777
-0.469678	-0.47007	-1.18913	-0.332892	-0.247644	-0.0784335	-0.041689
-0.135355	-0.294563	-0.0886584	0.00827439	-0.0801124	0.049992	0.0569388
0.107551	0.0474349	-0.234752	0.00393369	-0.214516	-0.332667	-0.0203208
-1.51496	0.128965	0.0630023	0.399254	-2.80362	-0.0484016	-0.326462
0.350342	0.236853	0.263526	0.566807	-0.179871	0.0214791	0.0383902
2.1333	-0.0841479	0.0254139	0.120534	0.395104	-0.239931	0.0912426
0.417327	0.268644	-1.2111	-0.487951	0.181293	-0.0384289	0.978792
1.14671	-0.0058125	-0.119454	0.621175	0.285936	-0.321135	0.320267
-0.00212759	0.407439	-0.741742	0.0363595	0.0475047	0.0593542	0.0207415
-0.595825	0.292936	-0.205754	-0.0669106	-2.44783	-0.212002	-0.803572
0.578538	-1.42104	0.41517	-0.552337	0.467546	-0.398458	0.0709529
0.803243	-0.58838	-0.00644819	0.214081	-1.66976	0.683675	-0.101062
0.149985	0.0307298	0.269533	0.0511302	0.388093	1.15646	0.00589268
-0.249593	-1.23187	-0.194345	-0.280422	0.32532	-0.324884	-0.085332
-0.0691636	-0.396847	0.371047	0.280556	0.00110306	-0.0967508	0.383081
-0.00705494	0.162403	0.325406	0.30242	0.0993031	-0.0667573	-0.24418
		0.137998	1.83326			

Table A5.3a: The weights for the third highest ranked toughness model (17 hidden units, random number seed of 5). The data are arranged in a continuous horizontal sequence in the following order: $\theta_1^{(1)}$, $w_{1,1}^{(1)} \ldots w_{1,22}^{(1)}$, $\theta_2^{(1)}$, $w_{2,1}^{(1)} \ldots w_{2,22}^{(1)} \ldots\ldots \theta_8^{(1)}$, $w_{8,1}^{(1)} \ldots w_{8,22}^{(1)}$.

-0.169875	-0.783946	0.310444	-0.195068	0.50462	0.377732	0.407837
-0.208479	0.437426	0.793338	-0.0799172	0.0043102	-0.251405	-3.55103
0.338933	0.164117	-0.0382573	0.0342126	0.231579	0.0354466	-0.466081
0.31013	-0.306957	1.08607	-1.56516	-0.098294	-2.25832	-0.172362
-0.0480348	0.215619	-0.653199	0.300093	-0.771978	0.412377	-0.0225972
-0.242447	1.39636	-0.031275	-0.236657	0.136925	0.437093	-0.34929
-0.352292	-0.191897	1.34951	-2.31438	-1.27409	-0.82501	0.107506
0.519821	1.29968	0.285405	0.100605	0.00708861	-0.411054	-0.251829
0.05194	0.00857459	-0.469969	-3.88297	-0.199369	-0.00666369	-0.362674
0.0875091	1.02047	0.0687771	-0.504264	-0.0423455	-0.812806	1.08366
2.17936	-0.452137	1.13988	0.584935	-0.178567	0.663723	-0.00478273
0.338366	0.0668866	-0.0910848	-0.00436658	0.619732	-2.26813	-0.0308758
0.0154461	-0.0828617	-0.140964	-0.499514	0.0281246	-0.327617	-1.13947
4.2238	-0.221556	-0.406183	-0.396784	0.294338	0.326377	0.0345239
-0.226669	0.489261	0.40024	-0.326156	0.299378	0.00903229	-0.134686
0.877192	0.0810146	-0.176258	0.208891	0.941953	-0.761059	0.0189504
-0.00792134	0.507433	-3.54439	0.109257	-1.28557	-0.0220706	-2.43715
0.654846	0.175422	0.24111	0.0624647	-0.119463	-0.174432	0.192473
-0.00741214	0.144737	-0.0201889	-0.220711	0.263997	0.167314	-0.0243716
-0.0605181	-0.23194	-0.306073	0.438751	-2.61583	-0.229013	0.396472
-0.271793	2.21418	0.0303813	-0.43318	0.321642	-0.0364566	0.366517
-0.514867	0.0890184	-0.00323342	0.443572	-2.6298	-0.350164	0.00231367
0.0929542	-0.460272	-0.215418	-0.0395911	-0.998937	-0.328113	1.00797
-1.50131	0.599997	0.0514374	1.86128	0.147616	1.59407	-0.0442286
-0.190086	-0.0400507	0.504477	0.408892	0.0143568	0.895901	-3.57634
0.368255	0.0672786	-0.0866924	-0.351098	0.226275	0.199162	-0.355538
-0.657186	-1.1849	0.280955	0.190221	0.279151	-1.19009	-0.17327
-0.919528	0.0756099	0.160658	0.2572	-0.455567	0.521251	-0.00636719
0.703556	-0.286453	-0.325552	0.0221193	0.0238372	-0.0683968	-0.171166
0.502096	-0.817694	-0.0786382	0.174447	-0.21242	-5.8534	3.79263
-4.0083	4.32264	-3.36428	6.21204	-3.10821	-2.57831	5.65535
-3.33061	-4.13077	1.41807	-3.23636	-2.70708	-4.29771	-4.55873
			-4.17289			

Table A 5.3b: The weights for the third highest ranked toughness model (17 hidden units, random number seed of 5). The data are arranged in a continuous horizontal sequence in the following order: $\theta_9^{(1)}, w_{9,1}^{(1)} \ldots w_{9,22}^{(1)}, \theta_{10}^{(1)}, w_{10,1}^{(1)} \ldots w_{10,22}^{(1)} \ldots\ldots \theta_{17}^{(1)}, w_{17,1}^{(1)} \ldots w_{17,22}^{(1)}, \theta^{(2)}, w_1^{(2)} \ldots w_{17}^{(2)}$.

0.224276	-0.922683	0.391506	-1.22803	-0.920178	-0.395075	-0.21259
0.311908	0.255478	0.154679	-0.039839	-0.00407927	-0.315711	1.81072
-0.0333061	0.207428	-0.052736	1.09148	-0.529177	0.283421	-0.256637
0.340051	-2.59724	0.94546	-2.07236	0.0424057	0.151976	0.237154
-0.563558	0.00219558	-0.11242	0.27389	-0.608431	0.211644	-0.0179791
0.143694	2.42648	-0.0610537	0.0394116	0.274066	0.862721	0.129963
-0.0418321	0.406089	0.409771	-2.69126	-0.616159	0.132158	-0.288074
1.47099	-0.00395189	0.116664	0.47491	-0.319157	-0.198399	-0.403152
0.158871	-0.0202793	-0.0281721	-1.25826	-0.518549	-0.0649973	0.0839444
-0.281084	1.75937	-0.104363	-0.27811	0.133202	2.38642	-0.801353
-0.200118	0.159064	-0.166098	-0.0583316	0.809114	-0.588466	0.305999
-0.24319	0.0321361	0.201095	0.00712936	-0.322684	-3.86552	-0.302271
-0.149636	0.342127	0.347751	1.07372	-0.104522	-0.639932	0.159182
-0.0163986	-0.839242	-2.34461	-0.74874	-0.112333	0.293696	0.632076
0.180234	0.654849	0.145784	0.0201701	-0.0197928	-0.0232143	-0.115945
-1.58816	0.223152	-0.0276328	0.681822	0.530944	0.68311	0.015556
0.498621	0.125791	-2.31483	-0.181811	-1.68976	-0.472379	0.519245
0.677379	-0.442833	-0.147631	-0.317241	0.182578	0.475888	0.0154266
0.0318098	0.531954	0.0832674	-0.533043	-0.324893	0.745514	-0.34914
-0.0456408	-0.138355	-0.648093	0.464127	-2.22968	-0.693678	-0.993906
0.0797501	-0.17514	0.0723646	-0.556946	-0.0446372	0.142129	0.0440012
0.767644	0.110908	0.0414103	0.247926	-0.138487	-0.365703	0.018392
0.116543	-0.357394	-1.13484	0.0842664	-1.0175	0.202825	-1.49922
-0.930893	-0.431487	0.299766	-0.103213	0.334593	0.924457	-0.459258
-0.783817	-0.299005	0.467759	0.265207	0.0205866	-0.41656	-2.77812
0.0790643	-0.109101	-0.143994	0.232089	0.341619	0.0998081	-0.508507
0.656355	-1.11511	1.16343	0.277496	-0.649742	-0.112678	-0.0136209
-1.13845	0.117578	0.0435992	0.167158	-0.051263	0.220573	-0.0244722
0.325778	1.53819	0.22228	-0.0832293	0.00280035	-1.00379	0.808849
0.110467	0.761873	-0.17994	2.82973	0.716401	-0.390935	-1.16246
0.534208	-0.0775261	0.290002	-0.200558	0.220483	0.0204095	0.0274744
-0.197068	-0.048798	0.111921	0.109214	-0.0409363	-0.070937	0.582597
0.381579	0.147619	-0.32857	0.299933	-0.177565	-2.43132	1.16616
-0.132512	-0.195466	0.14435	0.0873223	-0.231619	0.223493	0.174525
-0.00956762	0.730667	0.171805	-0.022366	-0.236853	-0.127333	0.0752682
0.0334657	-0.319091	0.802482	-0.784436	-0.00521487	-0.606268	0.292295
			-2.86028			

Table A5.4a: The weights for the third highest ranked toughness model (17 hidden units, random number seed of 5). The data are arranged in a continuous horizontal sequence in the following order: $\theta_1^{(1)}, w_{1,1}^{(1)} \ldots w_{1,22}^{(1)}, \theta_2^{(1)}, w_{2,1}^{(1)} \ldots w_{2,22}^{(1)} \ldots\ldots \theta_{11}^{(1)}, w_{11,1}^{(1)} \ldots w_{11,22}^{(1)}$.

-0.263005	-0.189438	0.0334802	-1.0964	0.052349	-0.401208	-0.328675
-0.0901085	0.235153	0.489379	-0.0549939	0.00584576	0.300946	0.166831
0.169645	0.0634695	0.168912	-0.654228	-2.16493	0.0468689	0.172784
-0.103413	-2.36139	-0.718525	-1.58306	-0.393674	-0.167764	0.430142
0.856362	0.149253	0.017781	-0.187115	0.224944	0.275921	0.0223534
0.183188	-1.76362	0.615216	0.0578224	-0.166886	0.337838	0.166241
0.0851703	-0.123865	0.244691	-1.19589	0.486867	-1.85501	-0.352622
0.260448	-0.497242	-1.05167	-0.446292	-0.546531	0.10862	0.157216
-0.0779422	-0.0034212	-0.249822	4.13147	0.0167581	0.230056	0.244699
-0.283281	-0.385923	-0.0801639	1.83297	0.504785	-2.15476	0.457026
-3.56788	4.15919	-4.1215	-3.56298	4.40325	-4.55811	6.24877
5.50511	3.02402	3.36642	-3.62385	-3.87175	-5.83356	-2.65877

Table A 5.4b: The weights for the third highest ranked toughness model (17 hidden units, random number seed of 5). The data are arranged in a continuous horizontal sequence in the following order: $\theta_{12}^{(1)}, w_{12,1}^{(1)} \ldots w_{12,22}^{(1)}, \theta_{13}^{(1)}, w_{13,1}^{(1)} \ldots w_{13,22}^{(1)}, \theta_{14}^{(1)}, w_{14,1}^{(1)} \ldots w_{14,22}^{(1)}, \theta^{(2)}, w_1^{(2)} \ldots w_{14}^{(2)}$.

0.568271	0.0722919	0.530982	0.39989	0.0322204	0.45186	-0.105967
0.435091	0.586885	0.354105	-0.0303509	0.00519444	-0.618756	0.182118
0.014789	0.0465998	0.00533521	-0.324182	0.119407	0.329268	-0.772432
0.412186	-0.259826	0.00304543	0.247168	0.605576	0.389335	0.0648854
-0.0970288	-0.208555	0.0549875	0.493291	0.197394	-0.104869	-0.00659174
-0.423863	0.00722941	0.459406	-0.308703	-0.0112246	-0.371759	0.0305808
0.325011	-0.789798	0.887043	-0.296547	-0.116225	0.162401	0.0535268
-0.0487667	0.00232706	-0.457793	-0.105947	-0.402281	-0.115107	-0.203395
-0.0710261	0.000225363	0.284297	-0.216689	0.423963	-0.290207	0.0580683
0.0119704	-0.129926	-0.0492247	0.0449812	0.534716	-0.167591	2.7846
		-9.92231	9.23913	-8.40654		

Table A5.5: The weights for the fifth highest ranked toughness model (3 hidden units, random number seed of 50). The data are arranged in a continuous horizontal sequence in the following order: $\theta_1^{(1)}, w_{1,1}^{(1)} \ldots w_{1,22}^{(1)}, \theta_2^{(1)}, w_{2,1}^{(1)} \ldots w_{2,22}^{(1)}, \theta_3^{(1)}, w_{3,1}^{(1)} \ldots w_{3,22}^{(1)}, \theta^{(2)}, w_1^{(2)} \ldots w_3^{(2)}$.

REFERENCES

Abe, F. and Nakazawa, S., (1992)
Metallurgical Transactions A **23A** 3025–3034
The Effect of Tungsten on Creep Behaviour of Tempered Martensitic Steels.

Adam, W., Mischok, W., Wellnitz, G., Zschau, M. and Niederhoff, K., (1995)
Böhler Welding Publication
Welding of New Types of Steel for Power Plant Construction.

Alberry, P. J. and Gooch, D. J., (1985)
Welding and Metal Fabrication **53** 332–336
12CrMoV Status Review.

Alekseev, A. A., Shevchenko, G. A., Pokhodnya, I. K. and Yurlov, B. V., (1991)
Doc II-A-845-91 Kiev, USS Academy of Sciences, USSR National Welding Committee
Effect of Copper on Structure and Properties of Multilayer CMnNi Weld Metal.

Andrews, K. W., (July 1965)
Journal of the Iron and Steel Institute **203** 721–727
Empirical Formulae for the Calculation of Some Transformation Temperatures.

Aplin, P. F. and Middleton, C. J., (April 1990)
Steam Plant for the 1990s I. Mech. E. Conference **C386/010** 149–160
The Development of High Strength 9Cr Steels for Steam Based Power Plant for the 1990s.

Arnfelt, H., (1928)
Journal of the Iron and Steel Institute **XVIL** 1–21

Ashby, M. F. and Jones, D. R. H., (1980)
Engineering Materials 1 — An Introduction to their Properties and Applications Pergamon Press

Bain, E. C. and Paxton, H. W., (1961)
Alloying Elements in Steel ASM Publication

Baker, R. G. and Nutting, J., (1959)
Journal of the Iron and Steel Institute **192** 257–268
The Tempering of 2-1/4Cr1Mo Steel After Quenching and Normalising.

Barnes, A. M., (May, 1994)
TWI Research Board Document 7224.01/94/813.02
The Influence of Composition on Microstructural Development and Toughness of Modified 9 % Cr 1 % Mo Weld Metals.

Batte, A. D., Murphy, M. C., and Stringer, M. B., (1978)
I. Mech. E. Steam Turbines for the 1980s Conference Proceedings, London 81–91
Developments in High Temperature Steam Turbine Materials' Technology.

Batte, A. D. and Murphy, M. C., (1979)
Metals Technology **5** 450–413
The High Strain High Temperature Fatigue Properties of a $1\frac{1}{2}$CrMoV Steam Turbine Casing Steel.

Beech, S. M., Greenwell, B. S. and New, P., (1990)
I. Mech. E. Steam Plant for the 1990s Conference Proceedings **C386/042** 81–88
Future Developments in Materials for Turbine Generators.

Berger, C., Beech, S. M., Mayer, K. H., Scarlin, R. B. and Thornton, D. V., (September 1994)
12th International Forgemasters Conference, Chicago
High Temperature Rotor Forgings of High Strength 10% CrMoV Steels.

Bertilsson, J. E. and Berg, U., (1980)
Brown Boveri Report 5-160–5-180
Steam Turbine Rotor Reliability — Built up vs Welded vs Monoblock.

Bhadeshia, H. K. D. H. and Edmonds, D. V., (1980)
Metal Science **14** 41–49
Analysis of the Mechanical Properties and Microstructure of a High Silicon Dual Phase Steel.

Bhadeshia, H. K. D. H., (1981a)
Metal Science **15** 175–177
Driving Force for Martensitic Transformation in Steels.

Bhadeshia, H. K. D. H., (1981b)
Metal Science **15** 178–180
Thermodynamic Extrapolation and Martensite-Start Temperature of Substitutionally Alloyed Steels.

Bhadeshia, H. K. D. H. and Middelton, C., (1982)
Central Electricity Generating Board Internal Report
Martensitic Transformation in 12CrMoV Steels.

Bhadeshia, H. K. D. H., (1992)
Bainite in Steels, Institute of Materials, London

Bhadeshia, H. K. D. H. and Svensson, L.-E., (1993)
Mathematical Modelling of Weld Phenomena, eds Cerjak, H. and Easterling, K. E. Institute of Materials Press 109–180
Modelling the Evolution of Microstructure in Steel Weld Metal.

Bhadeshia, H. K. D. H., MacKay, D. J. C. and Svensson, L.-E., (1995)
Mqaterials Science and Technology **11** 1046–1051
Impact Toughness of C-Mn Steel Arc Welds — Bayesian Neural Network Analysis.

Bhadeshia, H. K. D. H., (1995a)
Materials World 128–130
Transparent Steel — The Teaching of Creative Design.

Bhadeshia, H. K. D. H., (1995b)
Proceedings of the Griffith Conference on Fracture in press
Calculation of Microstructure and Properties of Steel Welds.

Bhadeshia, H. K. D. H., (1995c)
MAP — Materials Algorithms Project

Blondeau, R., Boulisset, R., Ramson, L., Kaplan, D., and Roesch, L., (September 1984)
Proceedings of the 5th International Conference 1257–1289
Cold Forming and Welding Behaviours of Heavy Plate Steels for Pressure Vessel Applications.

Böhler Welding, (October, 1993)
Product Information Data Sheet 145
Filler Metals for the Steel X 10 CrMoVNb 91 W-Nr 1.4903 and Grade P91/T91 acc. to ASTM/ASME.

Boniszewski, T., (October, 1979)
The Metallurgist and Materials Technologist 567–578
Manual Metal Arc Welding — Old Process, New Developments

Bosansky, J. and Evans, G. M., (1992)
Welding International **6** 997–1002
Relationships Between the Properties of Weld Metals Microalloyed with V and Nb, their Structure and Substructure.

British Standard EN 499, (1995)
Specification for Covered Carbon and Carbon Manganese Steel Electrodes for Manual Metal Arc Welding.

British Standard 2633, (1987)
Specification for Class I Arc Welding of Ferritic Steel Pipework for Carrying Fluids.

British Standard 3605, (1991)
Austenitic Stainless Steel Pipework and Tubes for Pressure Purposes.

Buchi, G. J. P., Page, J. H. R. and Sidey, M. P., (March, 1965)
Journal of the Iron and Steel Institute 291–298
Creep Properties and Precipitation Characteristics of 1%Cr-Mo-V Steels.

Carapella, L. A., (1944)
Metals Progress **46** 108
Computing A" or M_S (Transformation Temperature on Quenching) from Analysis

Chandel, R. S., Orr, R. F., Gianetto, J. A., McGrath, J. T., Patchett, B. M. and Bicknell, A. C., (1985)
Physical Metallurgy Research Laboratories Report ERP/PMRL 85-16(OP-J)
The Microstructure and Mechanical Properties of Narrow Gap Welds in 2.25Cr1Mo Steel.

Cool. T., Bhadeshia. H. K. D. H. and MacKay, D. J. C., (1996)
Mathematical Modelling of Weld Phenomena III eds Cerjak, H. and Bhadeshia, H. K. D. H. Institute of Materials Press, London
Modelling the Mechanical Properties in the HAZ of Power Plant Steels. I: Bayesian Neural Network Analysis of Proof Strength.

Cornwell, J. F. and Pollard. G., (1971)
British Steel Report MG/44/71
Structural Aspects of Creep in 1%Cr$\frac{1}{2}$%Mo and 2$\frac{1}{4}$%Cr1%Mo Steels.

Cunha, P. C. R., Pope, A. M., and Nobrega, A. F., (1982)
Second International Conference on Offshore Welded Structures
Fracture Toughness of Weld Metals for Brazilian Offshore Platforms.

Davies, G. J. and Garland, J. G., (1975)
International Metallurgical Reviews **20** 83–106
Solidification Structures and Properties of Fusion Welds.

Davin, C., (October, 1994)
Linkweld '93 Progress Report **1**

Davin, C., (January, 1995)
Linkweld '93 Progress Report **3**

Day, R. V., (March, 1965)
Journal of the Iron and Steel Institute 279–284
Intercrystalline Creep Failure in 1%CrMo Steel.

Dien, W., (1973)
Brown Boveri Review **9-73** 427–430
Welded Turbine Shafts.

Dieter, G. E., (1988)
Mechanical Metallurgy, McGraw-Hill

Dittrich, S. and Große-Wordemann, J., (1986)
Thyssen Schweißtecknik GMBH report
2$\frac{1}{4}$Cr-1Mo Filler Metals with High Toughness Properties after Step Cooling.

Dittrich, S. and Heuser, H., (1986)
Thyssen Schweißtecknik GMBH report
SMAW of P91 Piping with Optimised Filler Metals.

Dyson, D. J. and Holmes, B., (1970)
Journal of the Iron and Steel Institute **208** 469–474
Effect of Alloying Additions on the Lattice Parameter of Austenite.

Easterling, K. E., (1983)
Introduction to the Physical Metallurgy of Welding Butterworths

Eaton, N. F. and Glossop, B. A., (1970)
Proceedings of the Conference on the Welding of Creep Resistant Steels, Cambridge, UK **Paper 9** 6–10
The Welding of Dissimilar Creep-Resisting Ferritic Steels.

Elsender, A., Gallimore, R., Murphy, M. C. and Poynton, W. A., (February 1978)
Metals Technology 45–56
Strength and Toughness of 3.5Ni-Cr-Mo-V Steam Turbine and Generator Rotor Forgings.

EPRI, (1989)
Electric Power Research Institute Report Summary

ESAB Report, (1981)
RC81033

ESAB Report, (1982)
RR82011

Es-Souni, M., Beaven, P. A. and Evans, G. M., (1990)
Oerlikon Schweißmitteilungen 48 **123** 15–31
Microstructure and Mechanical Properties of Cu-Bearing MMA CMn Weld Metals.

Evans, G. M., (1978)
Oerlikon Schweißmitteilungen 36 **82** 4–19
Effect of Manganese on the Microstructure and Properties of All-Weld Metal Deposits.

Evans, G. M., (1979)
Oerlikon Schweißmitteilungen 37 **87** 17–31
Effect of Interpass Temperature on the Microstructure and Properties of C-Mn All-Weld Metal Deposits.

Evans, G. M., (1980)
Oerlikon Schweißmitteilungen 38 **92** 20–35
Effect of Heat Input on the Microstructure and Properties of C-Mn All-Weld Metal Deposits.

Evans, G. M., (1982a)
Oerlikon Schweißmitteilungen 40 **99** 17–31
The Effect of Carbon on the Microstructure and Properties of C-Mn All-Weld Metal Deposits.

Evans, G. M., (1982b)
Oerlikon Schweißmitteilungen 40 **100** 25–35
The Effect of Iron Powder in Basic Low Hydrogen All-Positional Electrodes.

Evans, G. M., (1983)
Oerlikon Schweißmitteilungen 41 **103** 15–27
The Effect of Stress Relieving on the Microstructure and Properties of C-Mn All-Weld Metal Deposits.

Evans, G. M., (August/September 1989)
Welding and Metal Fabrication 346–358
Effect of Chromium on the Microstructure and Properties of CMn All-Weld Metal Deposits.

Evans, G. M., (1990a)
Oerlikon Schweißmitteilungen 48 **122** 18–35
The Effect of Nickel on the Microstructure and Properties of CMn All-Weld Metal Deposits.

Evans, G. M., (1990b)
Oerlikon Schweißmitteilungen 48 **124** 15–31
The Effect of Aluminium on the Microstructure and Properties of CMn All-Weld Metal Deposits.

Evans, G. M., (1991a)
Oerlikon Schweißmitteilungen 49 **126** 18–33
The Effect of Vanadium in Manganese Containing MMA Weld Deposits.

Evans, G. M., (1991b)
Oerlikon Schweißmitteilungen 49 **127** 24–39
The Effect of Niobium in Manganese Containing Weld Metal Deposits.

Evans, G. M., (1992a)
Oerlikon Schweißmitteilungen 50 19–34
The Effect of Titanium in Manganese Containing MMA Weld Deposits.

Evans, G. M., (December 1992b)
Welding Journal 447s–454s
The Effect of Titanium on SMA CMn Steel Multipass Deposits.

Evans, G. M., (1994a)
Oerlikon Report
Effects of Alloying Elements on Mod 9Cr1Mo Weld Deposits.

Evans, G. M., (1994b)
Oerlikon Schweißmitteilungen 21–39
Microstructure and Properties of Ferritic Steel Welds Containing Al and Ti.

Evans, G. M., (1994c)
Oerlikon Report
Effect of Boron on 9Cr1Mo Weld Metal.

Evans, G. M., (1995)
personal communication to H. K. D. H. Bhadeshia

Fisher, J. C., (1949)
Metals Transactions **185** 688–690
The Free Energy Change Accompanying the Martensite Transformation in Steels.

Foldyna, V. and Kuboň, Z., (1993)
COST 501 Report
Creep Resistant Chromium Steels — Metallurgical Understanding.

Fuji Electronic Industrial Co. Ltd., (1986)
Thermecmastor-Z Instruction Manual

Garland, J. G. and Kirkwood, P. R., (1975a)
GS/PROD/643/1/75/C
The Influence of Vanadium on Submerged Arc Weld Metal Toughness.

Garland, J. G. and Kirkwood, P. R., (1975b)
Metal Construction 320–330
Toward Improved Submerged Arc Weld Metal.

Ghosh, G. and Olson, G. B., (1993)
Proceedings of ICOMAT '92, International Conference on Martensitic Transformations, Monterey Institute for Advanced Studies, California, U.S.A. 353–358
Solid Solution Strengthening and Kinetics of Martensite Transformation in Fe Base Alloys.

Ghosh, G. and Olson, G. B., (1994)
Acta Metallurgica et Materialia **42** 3361–3370
Kinetics of fcc-bcc Heterogeneous Martensite Nucleation — Critical Driving Force for Athermal Nucleation.

Gorton, O. K., (1975)
Materials in Power Plant **Series 3** 44–51
Fabrication Aspects for Steels of Boiler Construction.

Graham, M. R., (April 1975)
Materials in Power Plant, Institute of Metals Spring Residential Course 115–119
Turbine Generator Materials.

Graham, F. N. and Barnes, D. C., (April 1990)
Steam Plant for the 1990s I. Mech. E. Conference **C386/045** 319–324
The Use of Direct Numerical-Controlled Milling Machines for Steam Turbine Blade Production.

Grange, R. A. and Stewart, H. M., (1946)
Transactions of the American Institute of Mining and Metallurgical Engineers **167** 467–501
The Temperature Range of Martensite Formation.

Gretoft, B., Bhadeshia, H. K. D. H. and Svensson, L.-E., (1986)
Acta Sterologica **5/2** 365–371
Development of Microstructure in the Fusion Zone of Steel Welds.

Haigh, R. H., (1996)
PhD Thesis, University of Birmingham
Development of Microstructure in Modified 9Cr1Mo Steel Weldments.

Hald, J., (1994)
EPRI Report
Materials Comparison Between NF616, NCM12A and TB12M, III: Microstructural Stability and Ageing.

Harris, P. and Lee, E. H., (February 1962)
British Welding Journal 60–69
Some Aspects of Welding in Steam Turbines.

Hohn, A., (1973)
Brown Boveri Review **9-73** 404–416
Rotors for Large Steam Turbines.

Honeycombe, R. W. K. and Bhadeshia, H. K. D. H., (1995)
Steels: Microstructure and Properties Second Edition

Hrivňák, I, (1985)
International Journal of Pressure Vessels and Piping **20** 223–237
A Review of the Metallurgy of Heat Treatment of Welded Joints.

Hrivňák, I, (1987)
International Institute for Welding Document IX-G-319/c-87 1–61
Guide to the welding and weldability of Cr-Mo and Cr-Mo-V heat resistant Steels.

Hunt, A. C., Kluken, A. O. and Edwards, G. R., (January 1994)
Welding Journal 9s–15s
Heat Input and Dilution Effects in Microalloyed Steel Weld Metals.

Ichikawa, K., Hori, Y., Sudea, A. and Kobayashi, J., (March 1992)
Nippon Steel Corporation Report
Toughness and Creep Strength of Mod. 2.25Cr 1Mo Steel Weld Metal.

Inagaki, M. Okane, I. and Nakajima, M., (1966)
Transactions of National Research Institute for Metals Volume 8 **4** 34–47
Influence of Heat Treatment on Creep Rupture Strength of Welded Joint of $2\frac{1}{4}$Cr1Mo Steel.

Irvine, K. J., Crowe, D. J. and Pickering, F. B., (August 1960)
Journal of the Iron and Steel Institute **196** 386–405
The Physical Metallurgy of 12% Chromium Steels.

Irvine, K. J., Pickering, F. B. and Garstone, J., (September 1960)
Journal of the Iron and Steel Institute **196** 66–81
The Effect of Composition on the Structure and Properties of Martensite.

Iwanaga, K., Ishiki, Y.,Mimuro, H. and Ohji, A., (April 1990)
Steam Plant for the 1990s I. Mech. E. Conference **C386/001** 25–30
General Planning and Construction of the 700 MW Unit with Enhanced Steam Conditions.

Jaffee, R. I., (1989)
EPRI Superclean Rotor Steels, Workshop Proceedings, Sapparo, Japan. ed. R. I. Jaffee Pergamon Press 3–27
Development of Superclean Rotor Steels.

Jorge, J. C. F., Rebello, J. M. A, and Evans, G. M., (1993)
IIW Document II-A-880-93
Microstructure and Toughness Relationship in CMnCr All-Weld Metal Deposits.

Kaufmann, L. and Cohen, M., (1958)
Progress in Metal Physics 7 165

Kikutake, T., Okamoto, K., Yamanaka, K., Nakao, H., Horii, Y. and Sugioka, I., (1984)
Pressure Vessel Technology Volume 2. Materials and Manufacturing. Proceedings of the Fifth International Conference, San Fransisco 1188–1209
Heavy Section 2.25Cr-1Mo Steel Plate Manufactured by Newly Developed Refining System.

Kluken, A. O., Siewert, T. A., and Smith, R., (1994)
Welding Journal 193s–199s
Effects of Copper, Nickel and Boron on Mechanical Properties of Low Alloy Steel Weld Metals Deposited at High Heat Input.

Knott, J. F., (1973)
Fundamentals of Fracture Mechanics Butterworths, London

Koçak, M., Petrovski, B. I., Richter, E. and Evans, G. M., (1994)
OMAE Volume III Materials Engineering ASME 277–289
Influence of Titanium and Nitrogen on the Fracture Properties of Weld Metals.

Kung, C. Y. and Rayment, J. J., (February 1982)
Metallurgical Transactions A **13A** 328–331
An Examination of the Validity of Existing Empirical Formulae for the Calculation of M_S Temperature.

Lancaster, J. F., (1993)
Metallurgy of Welding Fifth Edition, Chapman and Hall

LECO Corporation, (1979)
LECO CS-044 Product Details

Leslie, W. C., (1981)
The Physical Metallurgy of Steels McGraw Hill

Levine, E. and Hill, D. C., (1977a)
Metal Construction **9** 346-353
Toughness in HSLA Steel Weldments.

Levine, E. and Hill, D. C., (1977b)
Metallurgical Transactions A **8A** 1453
Structure-Property Relationships in Low Carbon Weld Metal.

Lord, M., (June 1996)
Dissertation for the Certificate of Postgraduate Studies in Natural Sciences University of Cambridge
The Design and Modelling of Ultra-High Strength Steel Weld Deposits.

Lundin, C. D., Kruse, B. J. and Pendley, M. R., (1982)
Welding Research Bulletin **277**
High Temperature Properties of $2\frac{1}{4}$Cr1Mo Weld Metal.

Lüthy, A., (June 1968)
Welding Journal 461–474
Some Advantages of Welding Turbine Rotors.

MacKay, D. J. C., (1992a)
Neural Computation 4 **3** 415–447
Bayesian Interpolation.

MacKay, D. J. C., (1992b)
Neural Computation 4 **3** 448–472
A Practical Bayesian Framework for Backprop Networks.

MacKay, D. J. C., (1992c)
Neural Computation 4 **5** 698–714
The Evidence Framework Applied to Classification Networks.

MacKay, D. J. C., (March 1993)
Darwin College Journal 81.

MacKay, D. J. C., (March 1995)
University of Cambridge Programme for Industry — Modelling Phase Transformations in Steels
Bayesian Non-Linear Modelling with Neural Networks.

Martinez, R., Cassanelli, A. N., Gonzalez, J. C., Patchett, B. M., Mejias, H. D. and de Vedia, L. A., (1990)
Proceedings, Recent Trends in Welding Science and Technology
Development of an AWS E90T1-B3 Type Flux Cored Electrode for Welding 2.25%Cr-1%Mo Steel.

Marriott, J. B. and Greenfield, P., (1988)
COST Publication, eds Marriott, J. B. and Pithan, K.
A Review of the Properties of 9–12 % Cr Steels for use as HP/IP Rotors in Advanced Steam Turbines.

MTDATA, (1996)
Metallurgical Thermochemistry and Thermodynamic Database, National Physical Laboratory, Teddington, U. K.

Natsume, S. and Gotoh, A., (April 1990)
The Fifth International Symposium of the Japan Welding Society 639–644
Effects of Chemical Compositions on Tensile Properties of Weld Metals for Modified 2.25Cr-1Mo Steels.

Naylor, D. J., (February 1993)
Materials World 109–110
Exploiting High Temperature Steels.

Nehrenberg, A. E., (1946)
Transactions of the American Institute of Mining and Metallurgical Engineers **167** 494-498
Discussion arising from Grange and Stewart's work.

Olson, G. B. and Cohen, M., (1976)
Metallurgical Transactions A **7A** 1897–1923
A General Mechanism of Martensitic Nucleation: Part I General Concepts and the FCC → HCP Transformation. Part II FCC → BCC and Other Martensitic Transformations. Part III Kinetics of Martensitic Nucleation.

Olson, G. B., (1995)
Private communication to H. K. D. H. Bhadeshia

Orr, J., Burton, D. and Rasche, C., (November 1992)
The Manufacture and Properties of Steel 91 for the Power Plant and Process Industries ECSC Information Day, Dusseldorf **Paper 2.3**
The sensitivity of microstructure and the mechanical properties of Steel 91 to initial heat treatments.

Orr, J. and Burton, D., (1993)
Ironmaking and Steelmaking 20 **5** 333–337
Development, Current and Future use of Steel 91.

Panton-Kent, R., (1989)
Welding Institute Research Report, No. 404/1989, TWI, Abington, Cambridge
Weld Metal Hydrogen Cracking Behaviour Microstructure and Hardness of MMA Welded 9Cr1Mo Steels.

Panton-Kent, R., (1990)
Welding Institute Members Report **429** 3–20
Weld Metal Toughness of MMA Electron Beam Welded Modified 9%Cr1%Mo Steel.

Park, S. and Svensson, L-E., (1990)
ESAB Report
Estimation of the Microstructure and the Strength of Low-Alloy Cored Wire Weld Deposits, Using a Computer Model.

Parker, J. D. and Parsons, A. W. J., (1994)
International Journal of Pressure Vessels and Piping **57** 345–352
The Tempering Performance of Low-Alloy Steel Weldments.

Patriarca, P., (1976)
Nuclear Technology **28** 516–536

Patterson, J. D., (1981)
The Joining of Metals, Practice and Performance, Volume II 227–244
The Effects of Composition on the Strength and Fracture Toughness of C-Mn Submerged Arc Weld Metal.

Payson, P. and Savage, C. H., (1944)
Transactions of the American Society of Metals **33** 261–280
Martensite Reactions in Alloy Steels.

Philip, T. V., (1983)
Materials Handbook, ASM **9th edition** 421–443
Ultrahigh-Strength Steels.

Pickering, F. B., (1978)
Physical Metallurgy and the Design of Steels Applied Science Publishers

Porter, D. A. and Easterling, K. E., (1992)
Phase Transformations in Metals and Alloys. Second Edition Chapman and Hall

Race, J. M., (1992)
PhD Thesis, University of Cambridge
Carbon Diffusion Across Dissimilar Steel Welds.

Raiter, V. and Gonzalez, J. C., (1989)
Canadian Metallurgical Quarterly 28 **2** 179–185
Influence of Molybdenum on the Microstructure and Properties of Weld Metal With Different Manganese Contents.

Ridley, N., Maropoulos, S. and Paul, J. D. H., (March 1994)
Materials Science and Technology **10** 239–249
Effects of Heat Treatment on Microstructure and Mechanical Properties of Cr-Mo-3.5Ni-V Steel.

Robson, J. D. and Bhadeshia, H. K. D. H., (1996)
Materials Science and Technology in press
Modelling Simultaneous Kinetics in Power Plant Steels, Part II.

Rollason, E. C., (1961)
*Metallurgy for Engineers, Third Edition*Edward Arnold, London

Rowland, E. S. and Lyle, S. R., (1945)
Metal Progress **47** 907–912
Measurement of Case Depths by Martensite Formation.

Sahay, S. K., Bhadeshia, H. K. D. H. and Honeycombe, R. W. K., (1992)
Materials Science and Engineering **A157** 101–105
Carbide Precipitation and the Nucleation of Allotriomorphic Ferrite in an Fe–W–C Steel.

Sawada, S. Suzuki, K. and Watanabe, J., (1977)
ASME, Ed. G. V. Smith
Application of Advanced Vacuum Carbon Deoxidised Steels to Heavy Forgings. Effects of Melting and Processing Variables on the Mechanical Properties of Steel.

Schinn, R. and Schieferstein, U., (1970)
Int. Forgemasters Conf. Terni 25–70
Properties of High Temperature 1%CrMoV Steels for HP and IP Rotors.

Schuller, H. J., Haigh, L. and Woitscheck, A., (1974)
Der Machineshaden **47** 1–13
Cracking in the Weld Region of Shaped Components in Hot Steam Lines.

Sikka, V, K., Ward, C. T. and Thomas, K. C., (1983)
Ferritic Steels for High Temperature Applications, ASM, Metals Park, Ohio, U.S.A. 65–84

Slater, L., (1993)
M. Sc. Thesis, School of Industrial and Manufacturing Science, Cranfield Institute of Technology
The Weldability of 2%CrMoNiWV Creep Resisting Steel.

Steven, W. and Haynes, A. G., (August 1956)
Journal of the Iron and Steel Institute **183** 349–359
The Temperature of Formation of Martensite and Bainite in Low Alloy Steels. Some Effects of Chemical Composition.

Still, J. R. and Rogerson, J. H., (July 1978)
Metal Construction 339–341
The Effect of Ti and B Additions to Multipass Submerged Arc Welds in 50D Plate.

Surian, E., Trotti, J., Herrera, R. and de Vedia, L. A., (June 1991)
Welding Journal 133s–140s
Influence of Carbon on Mechanical Properties and Microstructure of Weld Metal from a High Strength SMA Electrode.

Svensson, L-E. and Gretoft, B., (December 1990)
Welding Journal 454s–461s
Microstructure and Impact Toughness of CMn Weld Metals.

Svensson, L-E., (1994)
Control of Microstructure and Properties in Steel Arc Welds, CRC Press, London. 188

Swift, R. A. and Rogers, H. C., (April 1973)
Welding Journal 145s–172s
Embrittlement of 2.25Cr-1Mo Steel Weld Metal by Postweld Heat Treatment.

Thomson, R. C. and Bhadeshia, H. K. D. H., (April 1992)
Metallurgical Transactions A **23A** 1171–1179
Carbide Precipitation in 12Cr1MoV Power Plant Steel.

Viswanathan, R. and Beck, C. G., (1975)
Metallurgical Transactions A **6A** 1997–2003
Effect of Aluminium on the Stress Rupture Properties of CrMoV Steels.

Watson, M. N., Harrison, P. L. and Farrar, R. A., (March 1981)
Welding and Metal Fabrication 101–108
How Niobium Influences SA Mild Steel Weld Metals.

Weisman, J. and Eckart, L. E., (1985)
Modern Power Plant Engineering Prentice Hall

Westinghouse Electric Corporation, (1981)
EPRI CS-1967, Project 912-1
Steam Turbine Blades: Considerations in Design and a Survey of Blade Failures.

Wolstenholme, D. A., (1974)
Marchwood Engineering Laboratories Report R/M/N746
Hardness and Strength of 2Cr1Mo Manual Metal Arc Weld Metals.

Wyatt, L. M., (1976)
Materials of Construction for Steam Power Plant Applied Science Publishers Ltd., London

Yokoyama, T., (1959)
Bull. Fac. Eng. Yokohama National University 7 27

Zener, C., (1946)
Transactions of the American Institute of Mining and Metallurgical Engineers **167** 550–583
Kinetics of the Decomposition of Austenite.